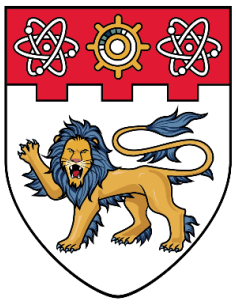

NANYANG TECHNOLOGICAL UNIVERSITY
SINGAPORE

Nature-Inspired Lightweight Auxetic Structures for Enhanced Stiffness and Absorption Capacity

Zhang Ee Teng

School of Mechanical and Aerospace Engineering

15 November 2023

Nature-Inspired Lightweight Auxetic Structures for Enhanced Stiffness and Absorption Capacity

Zhang Ee Teng

School of Mechanical and Aerospace Engineering

A thesis submitted to the Nanyang Technological University in partial fulfilment of the requirement for the degree of

Doctor of Philosophy

15 November 2023

Statement of Originality

I hereby certify that the work embodied in this thesis is the result of original research, is free of plagiarised materials, and has not been submitted for a higher degree to any other University or Institution.

15 November 2023

. . . . . .

Date

. . . . . .

Zhang Ee Teng

Supervisor Declaration Statement

I have reviewed the content and presentation style of this thesis and declare it is free of plagiarism and of sufficient grammatical clarity to be examined. To the best of my knowledge, the research and writing are those of the candidate except as acknowledged in the Author Attribution Statement. I confirm that the investigations were conducted in accord with the ethics policies and integrity standards of Nanyang Technological University and that the research data are presented honestly and without prejudice.

19 December 2023

. . . . . .

Date

. . . . . .

Ng Bing Feng

Authorship Attribution Statement

The content of this thesis, in majority, comprises of reproduction of the author's own published and own contribution in collaborated publications. Thus, the following research outcomes indicated in this thesis shall representatively acknowledge and reference the associated research results upfront. As such, the author refrains from referencing them in this work.

This thesis contains material from four paper(s) published in the following peer-reviewed journal(s) in which I am listed as an author.

Chapter 3 is published as E. T. Zhang, H. Liu, and B. F. Ng, "Novel arc-shaped ligaments to enhance energy absorption capabilities of re-entrant anti-trichiral structures," Compos. Part B Eng. DOI: 10.1016/j.compositesb.2021.109366

To which the contributions of the thesis author are as follows:

- Conceptualization, methodology, validation, investigation, data curation, writing, visualization

Chapter 4 is published as E. T. Zhang, H. Liu and B. F. Ng, "Mechanics of Re-Entrant Anti-Trichiral Honeycombs with Nature-Inspired Gradient Distributions," Int. J. Mech. Sci.

To which the contributions of the thesis author are as follows:

- Conceptualization, methodology, validation, investigation, data curation, writing, visualization

Chapter 5 is published as H. Liu, E. T. Zhang, G. Wang, and B. F. Ng, "In-plane crushing behavior and energy absorption of a novel graded honeycomb from hierarchical architecture," Int. J. Mech. Sci. DOI: 10.1016/j.ijmecsci.2022.107202 and H. Liu, E. T. Zhang, and B. F. Ng, "In-plane dynamic crushing of a novel honeycomb with functionally graded fractal self-similarity," Compos. Struct. DOI: 10.1016/j.compstruct.2021.114106

To which the contributions of the thesis author are as follows:

- Validation, investigation, data curation, review and editing, visualization

15 November 2023

. . . . . .

Date

. . . . . .

Zhang Ee Teng

Table of Contents

Nomenclature

List of Symbols	
ε_x	Strain in x direction
ν_{xy}	Poisson's ratio
x_i	Average deformed width between x_{i1} and x_{i2}
x_0, y_0	Original width, height
ρ_p	Density of material
σ	Stress
ε_p	Strain
η	Energy Absorption Efficiency
ε_D	Densification Strain
γ	Fractal parameter
σ_{pl}	Plateau stress in i-th gradient layer of graded hierarchical honeycomb
σ_p^{sub}	Yield stress of the substructure
σ_{mat}	Yield stress of the base material
$\bar{\rho}_{sub}$	Relative density of the substructure

σ_{st_i}	Static plateau stress
σ_{dy_i}	Dynamic plateau stress
$\overline{\rho_t}$	Relative density of the i-th gradient layer of the graded hierarchical structure
ε_{dy}	Densification strain for i-th gradient layer

List of Abbreviations

NPR	Negative Poisson's Ratio
AM	Additive Manufacturing
REAT	Re-entrant anti-trichiral
SEA	Specific Energy Absorption
SS	Stress-Strain
EA	Energy Absorption
PPR	Positive Poisson's Ratio
BBC	Body-centered cubic
MCF	Mean Crushing Force
CFE	Crushing Force Efficiency
FDM	Fused Deposition Modelling

SLA	Stereolithography
ABS	Acrylonitrile Butadiene Styrene
DLP	Digital Light Processing
PR	Poisson's Ratio
FD	Force-displacement
RD	Relative density
PCF	Peak Crushing Force
FE	Finite Element
Dc	Single ligament downward curved REAT
Uc	Single ligament upward curved REAT
Dc+C	Combination of downward curved and straight ligament REAT structure
Uc+C	Combination of upward curved and straight ligament REAT structure
Dc+Uc	Combination of downward and upward curved ligament REAT structure
UC-P	Unidirectionally graded chiral with positive gradient
UC-N	Unidirectionally graded chiral with negative gradient

BC-P	Bi-idirectionally graded chiral with positive gradient
BC-N	Bi-idirectionally graded chiral with negative gradient
UH-P	Unidirectionally graded height with positive gradient
UH-N	Unidirectionally graded height with negative gradient
BH-P	Bi-idirectionally graded height with positive gradient
BH-N	Bi-idirectionally graded height with negative gradient
Ui	Unidirectionally increasing in curvature gradient from bottom to top of Uc structure
Ud	Unidirectionally decreasing in curvature gradient from bottom to top of Uc structure
Bi	Bidirectionally increasing in curvature middle layer of Uc structure
Bd	Bidirectionally decreasing in curvature gradient from middle layer of Uc structure
Ui-R=2 or Ui-2	Unidirectionally increasing in curvature gradient from bottom to top of Uc structure with its radius kept at 2mm
Ud-R=2 or Ud-2	Unidirectionally decreasing in curvature gradient from bottom to top of Uc structure with its radius kept at 2mm
US	Uniform self-similarity

TH	Traditional honeycomb
AG-I	Asymmetric graded self-similarity honeycomb with increasing fractal parameter from top to bottom of the structure
AG-II	Asymmetric graded self-similarity honeycomb with decreasing fractal parameter from top to bottom of the structure
SG-I	Symmetric graded self-similarity honeycomb with increasing fractal parameter from middle of the structure
SG-II	Symmetric graded self-similarity honeycomb with decreasing fractal parameter from middle of the structure
UH_TRI	Uniform hierarchy honeycomb with triangular substructure
UH_HEX	Uniform hierarchy honeycomb with hexagonal substructure
NGH_TRI	Negative gradient hierarchical honeycomb with triangular substructure of decreasing hierarchy from the top to the bottom of the structure
NGH_HEX	Negative gradient hierarchical honeycomb with hexagonal substructure of decreasing hierarchy from the top to the bottom of the structure

PGH_TRI	Positive gradient hierarchical honeycomb with triangular substructure of increase hierarchy from the top to the bottom of the structure
PGH_HEX	Positive gradient hierarchical honeycomb with hexagonal substructure of increase hierarchy from the top to the bottom of the structure
ReC	3D re-entrant lattice of conventional straight struts
ReM	3D re-entrant lattice with straight struts modified to bent inward
VP	Vertical printing direction
HP	Horizontal printing direction

Abstract

Bio-organisms often exhibit curved-like, graded and hierarchical structures which significantly contribute to their exceptional mechanical adaptability and performances in diverse range of environmental conditions. These structures offer lightweight properties alongside enhancements to crashworthiness and impact resistance. In this thesis, we delve into the development of innovative materials by mimicking the structural designs from nature, emphasizing on the exploration of lightweight solutions for applications across various domains. Specifically, through the introduction of curved ligaments, gradient variations and hierarchical arrangements, this thesis will demonstrate improvements to the mechanical properties and energy absorption (EA) capabilities of honeycomb structures.

Firstly, the use of arc-shaped ligaments in re-entrant anti-trichiral (REAT) structures introduces unique deformation patterns through the rotation of cylinders, contact interactions, and petal-like cell interactions. Experimental and Finite Element Analysis (FEA) demonstrate the positive influence of curved ligaments on elastic modulus, Poisson's ratio (PR), plateau stress, and SEA capabilities. The findings reveal significant improvements in normalised Young's modulus and SEA with the introduction of combined curved ligaments (Dc + Uc) design. Further parametric studies highlight the influence of ligament curvature and cylinder diameter on mechanical properties and deformation patterns.

The gradient-based approach in the design of REAT honeycombs represents an innovative method to enhance certain mechanical properties. Traditionally, gradients in these structures have been introduced through variations in thickness. However, this thesis explores an alternative by varying the cylindrical diameter (chiral) and the height of the unit cell. This shift from the conventional thickness-based gradient approach has shown to offer promising improvements in the mechanical properties of REAT structures, including elastic stiffness, SEA

(SEA), and densification strain. In contrast to the thickness-based gradient approach, which often results in layer-by-layer collapse due to significant stiffness differences between layers, the geometrical gradient approach utilizes variations in Poisson's ratio between layers as the primary mechanism for deformation. In comparison to their uniform counterparts, chiral-based gradient REAT structures exhibited a sustained increase in the quasi-plateau stage and a relative constant EA efficiency at 25% more efficient than the base REAT structure.

While the results for chiral-graded REAT structures were promising, height-based graded REAT did not reveal any dramatic improvements. Here, different variations in curvature and layer arrangements are investigated, which include conventional REAT structures, those with arc-shaped ligaments, and graded REAT designs. Negligible differences in mechanical performance are observed among the structures due to similar elastic and plastic deformation behaviors. In addition, improvements in plateau stress and elastic stiffness are observed in REAT structures with smaller cylindrical sizes and graded curvature. However, a consistent curvature with varied radius only showed marginally enhanced stiffness. This suggests that exploring simultaneous variations in cylindrical size and curvature could unveil more complex deformation behaviors, indicating a direction for future studies using advanced optimization methods like particle swarm optimization.

Expanding on the idea of functional grading approach, a series of novel fractal honeycombs are proposed by combining functionally graded and fractal self-similarity features. These structures are generated by varying the fractal parameter in each layer of the traditional self-similar honeycombs. The proposed structures exhibit notable improvements in EA and MCF as compared to traditional honeycombs. Additionally, the introduction of different gradient distributions allows for controlled deformation patterns during dynamic crushing.

Building on the foundation of hierarchical architectures in nature, a novel graded hierarchical honeycomb is further proposed. By replacing cell walls of regular honeycombs with triangular

and hexagonal sub-structures, and varying the hierarchical length ratio in each layer, the structure exhibits enhanced crashworthiness behaviors. The graded hierarchical honeycombs demonstrate a progressive deformation model under different impact velocities, revealing three distinct plateau stages during in-plane crushing. The triangular sub-structure exhibits superior EA compared to the hexagonal sub-structure, resulting in an increased SEA of up to 32.2% compared to uniform hierarchical honeycombs.

Finally, a new hybrid 3D auxetic structure along with its variant are investigated for both quasi-static and dynamic compression properties. Drawing inspiration from biological structures with hierarchical configurations, the investigation seeks to develop an auxetic structure with superior or equivalent properties to those derived from 2D designs, optimizing for dynamic loading conditions. The designs are based on existing literature and tested to evaluate their performance in different planes and printing directions. In the design of 3D structures, it's crucial to optimize the cell design to effectively manage EA in dynamic loading situations. Although maximizing EA in these scenarios is challenging due to the limited impact energy, leveraging the auxetic effect—which requires less compression, can be highly beneficial. For dynamic impacts, it is recommended to prioritize the ease of deformation in the auxetic design. In contrast, when dealing with quasi-static loading scenarios, the focus should remain on enhancing the auxetic effect itself. This approach ensures that the 3D structures are designed to efficiently manage different types of loading conditions.

In essence, this thesis presents a comprehensive exploration into design and optimization of honeycomb structures, providing novel insights into improve mechanical properties, responses and EA capabilities. The combinations of approaches inspired from natural bio-organisms and their mechanisms paves the way for a future of lightweight EA systems for enhanced safety and protection performance.

Acknowledgement

I would like to wholeheartedly acknowledge my supervisor Dr. Ng Bing Feng for his consistent support, guidance and encouragement throughout this research which pushed me to these achievements. His time, suggestions and expertise are of upmost value to the success of this work. At the same time, I would also like to thank Dr. Liu Hu for his suggestions and guidance through my collaboration with him.

I am also grateful to Dr. Rob Hewson and Dr. Ajit Panesar for their inspiration and guidance during my exchange with Imperial College London for their guidance and inspiration to the advancement of this research.

Furthermore, I am also grateful to my colleagues, Mr. Wong Zheng Xiong, Mr. Quah Tan Kai Noel, Mr. T. Thanaraj, Mr. Tay Wei Shian, Mr. Zeng Zhuohong and Mr. Yan Yunhao for their help, assistance and enthusiasm.

In addition, I would like to express my gratitude towards the support of the technical staffs at the department of Singapore Center for 3D Printing and Mechanical School of Aerospace and Engineering, Mr. Daniel Yeo Yin Ping, Mr. Tan Yong Sheng Andrew, Mr. Tan Ngee Kwan, Mr. Seet Thian Beng, Mr. Ng Tian Seng and Mr. Ang Hanlin.

Lastly, I am grateful to the Singapore Center for 3D Printing, the Department of Mechanical School of Aerospace and Engineering as well as Nanyang Technological University, Singapore for the scholarship and research funding.

Table of Figures

List of Tables

Chapter 1 Introduction

1.1 Background and Motivation

Nature, with its enormous collection of meticulous organization of cellular structures, has always been a remarkably rich source of inspiration for innovation. This has led to the initial development of honeycomb structures and subsequent advancements in other lightweight materials derived from microstructural arrangements and configurations in other organisms. The intricacy in the efficient arrangement of cellular structures have received substantial amount of attention leading to development of bio-inspired honeycomb structures.

Auxetic materials, recognized for its negative Poisson's ratio (NPR), have become a substantial consideration when designing lightweight structures. Their unique mechanical properties, now supported by the emergence of 3D printing technologies (additive manufacturing(AM)) pave the way for fabrication of complex novel geometries whose fabrication cannot be mimicked by conventional manufacturing techniques. Despite their advantage, these materials suffer from low stiffness as the by-product of substantial presence of porosity that restricts their structural applications. Consequently, enhancing the stiffness and other performance parameters of auxetic materials is paramount to widen their application in various engineering sectors.

Historically, research in auxetic structures or even conventional lattice structures has largely been centered around designs involving straight ligaments which only scratched the surface of the full potential these materials may offer. By borrowing the concepts from nature, a myriad of complex configurations evolved over millions of years to adapt to a variety of harsh environments can be applied to augment the performance of these structures.

The concept of incorporating curvature, both in-plane and out-of-plane, into ligaments of auxetic structures is a relatively unexplored area of research. Inspired by its natural form, this approach had been applied to limited numbers of structures such as re-entrant and hexachiral

honeycombs but only through simulation. The use of transversely curved ligaments combined with additional design parameters, allows for more extensive modifications and fine-tuning of deformation and mechanical responses whose range can be broadened behind what can be achieved with traditional honeycomb designs with straight ligaments. To author's knowledge, no studies examined the influence of the direction and degree of curvature in ligaments on re-entrant anti-trichiral (REAT) honeycomb structures.

Furthermore, nature presents itself with other intriguing configurations such as the hierarchical structures and gradient-based structural approach which are common across multiple scales in organisms. While each configuration had been a subject of extensive research and analysis, there had been limited exploration into combined effect of integrating two configurations together. This includes combinations such as hierarchical with gradient, curvature with gradient or hierarchical with curvature.

1.2 Objectives and Scope

The main objective of this thesis is to explore and validate the potential enhancements in mechanical properties, such as in-plane stiffness, various stages of deformation, NPR and specific energy absorption (SEA), of REAT structure by first incorporating curvature and gradient individually before combining the two designs together. The study will then delve into combinational impact of integrating two configurations namely, hierarchical with gradient, curvature with gradient and hierarchical with curvature. The ultimate goal is to broaden the application of auxetic materials by offering various novel routes to design and optimization of lightweight energy absorption (EA) systems.

To fulfil the objective, the following scopes of works are defined:

1. Exploring the Design Space:

To investigate various design aspects of auxetic structures, focusing on curved ligaments, gradient-based approaches, and hierarchical geometries. This involves examining parameters such as curvature direction and degree, ligament designs (single and double), and the impact of varying geometries, including fractal self-similarity and functionally graded structures.

2. Numerical Demonstration and Analysis:

   To model these designs numerically to understand their deformation patterns, stress-strain relationships, PR-strain curves, and mechanical performance. This includes studying the effects of curvature, gradient distributions, and hierarchical architectures on these parameters.

3. Experimental Validation:

   To conduct experimental tests, such as 3D printing of unit cell structures and quasi-static compression tests, to validate the numerical models. This involves comparing the experimental results with the numerical predictions for various designs, including graded hierarchical honeycombs.

4. Combined Performance Exploration:

   To evaluate the combined performance of these designs in terms of mechanical response and SEA. This will involve comparing different ligament designs, examining the role of node diameters in petal-shaped ligaments, and assessing the performance of structures under various crushing velocities.

1.3 Organizations

With close reference to the research mindmap shown in Figure 1.1 below, this thesis will consist of nine chapters as follows:

- Chapter 1 details the background, objectives and scopes of the research.

- Chapter 2 provides in-depth review of auxetic structures, covering their unique properties, various designs, deformation mechanisms, and applications. This chapter also delves into the role of these structures in bio-inspired applications.
- Chapter 3 entails information with regards to methodology used in carrying out the studies detailed in the later chapters.
- Chapter 4 introduces the use of arc-shaped ligaments to improve the SEA of REAT structures. It discusses the numerical methods used, the physical experimental setup, and validates the numerical results with experimental findings.
- Chapter 5 presents the delves into the application of a bio-inspired gradient distribution to conventional REAT structures, examining their mechanical properties. Key focus areas include the analysis of stress-strain(SS) curves, NPR, and SEA.
- Chapter 6 expands further by introducing a gradient-based approach applied to REAT structures with arc ligaments. It concludes with remarks on the work done on this novel structure and suggestions for future research directions.
- Chapter 7 discusses two innovative graded hierarchical honeycomb structures featuring self-fractal similarities and sub-structures.
- Chapter 8 introduces a 3D star sub-cell hybrid hierarch re-entrant whose anisotropic performances are characterized by both quasi-static and dynamic loading at two different loading orientations and printing directions.
- Chapter 9 summarizes the key findings and contributions. It also outlines potential areas for future research, building on the work presented in the thesis.

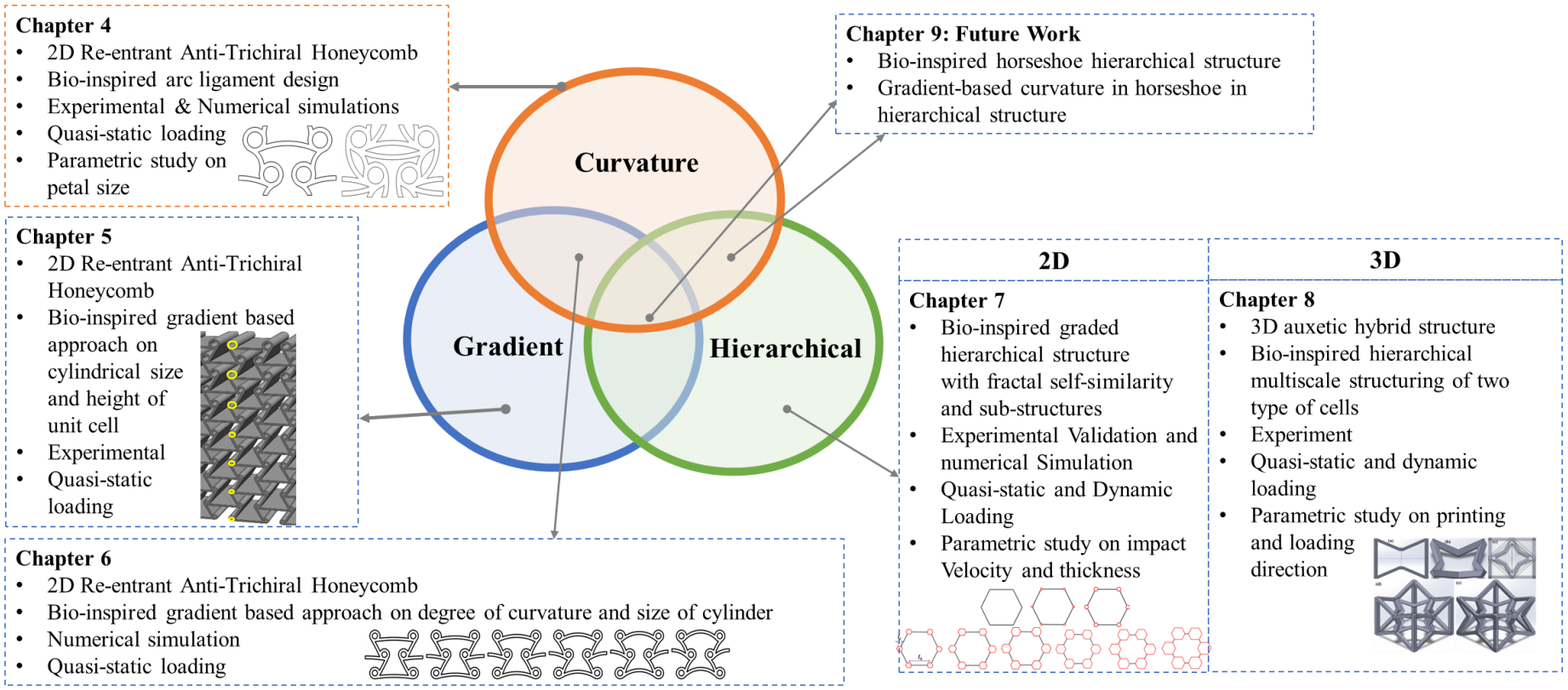

Figure 1.1. Research Mindmap capturing the entire scope of this thesis.

Chapter 2 Literature Review

2.1 Overview of Metamaterials

2.1.1 Conventional Auxetic Materials and Related Structural Enhancement

Auxetic cellular solids with NPR have exhibit unique and superior mechanical properties which include improvement in shear modulus [1], enhancement to indentation resistance [2], increase in fracture toughness [3], lowering of bulk modulus [4] and excellent EA capabilities [5]. This unique and counterintuitive property of the material will result in its lateral contraction when compressed or lateral expansion when stretched longitudinally, as illustrated in Figure 2.1. Generally, structures exhibiting auxetic properties are made up of re-entrant, chiral and hierarchical structures, where extensive studies have been performed [6]–[8] for potential engineering applications in automotive, medical, defence, sports and aerospace industries [6], [9]–[12]. Among them, the re-entrant and chiral auxetic structures are particularly interesting as their deformation mechanisms are attributed to the bending of ligaments and rotation of cylinders, respectively. This creates the opportunity to investigate the integration of both structures by exploiting the possible advantages of ligament and hinge design to seek further enhancements to mechanical properties.

First proposed by L.J. Gibson and M.F. Ashby [4], the re-entrant auxetic structure composed of periodically connecting hexagonal unit cells with two negative angles and whose effects were subsequently studied by Almgren [13] and Kolpakov [14] in conjunction with theoretical and experimental analysis of mechanical properties of beams in cellular honeycomb material [15]. The study concluded that two parameters namely wall thickness and cell-wall angles produced significant influence over the deformation modes, plateau stresses, and SEAs [16]–[18].

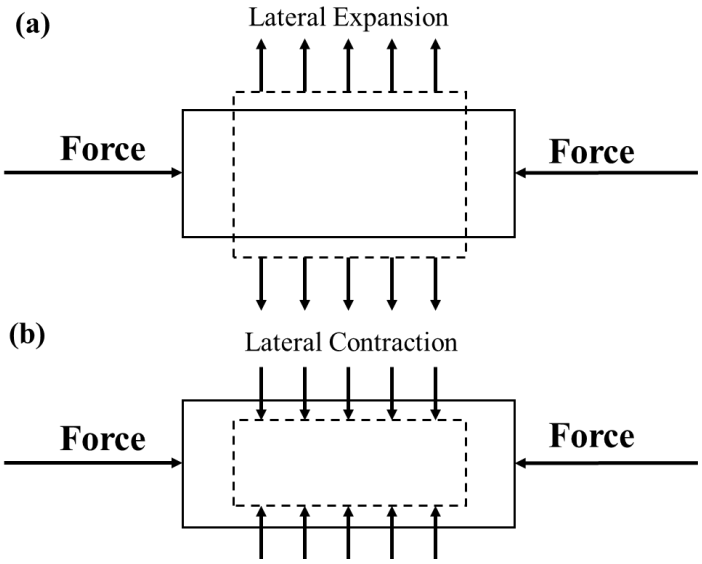

Figure 2.1. Schematic diagram illustrating (a) positive Poisson's ratio (PPR) of conventional material which contracts laterally as they are pulled apart, as compared with (b) NPR of auxetic materials [19] whose effect is opposite. The same is valid for compressive loading.

Furthermore, uni-directional arrangement in cell-wall angle [20] and bi-directional configuration in wall thickness [21] are capable of enhacing EA capabilities of re-entrant honeycomb through optimised configurations. Possessing excellent mechanical properties, re-entrant auxetic structures unfortunately also have drawbacks in having lower stiffnesses due to the significant presence of voids. Even though the voids can be effectively filled to improve mechanical properties while maintaining auxetic effects [22], this often compromise the strength to weight ratio [23]. Alternatively, partially solidifying the void region can improve mechanical properties which include the introduction of extra rib to the centre of re-entrant honeycomb unit cell for increased Young's modulus [24], the integration of rhombic honeycomb to achieve superior critical buckling strength [25], and the integration with thin plates to provide improvement in shear strength [26].

In another spectrum, chiral and anti-chiral honeycombs are another type of auxetic structures which distinguish themselves from re-entrant honeycomb by possessing an additional deformation mechanism in rotation of cylinders and cylinder-rotation induced ligament flexure in the deformation process [27]. Large, plastic deformation behaviours and EA performance of

the re-entrant and chiral-based auxetic materials were summarised in Zhang, Hu and You's review [28]. In re-entrant honeycombs, the negative Poisson's effect is predominately caused by the elastic and plastic bending of the ligaments during collapse while on the other hand, the same effect is generated by both the bending of ligaments but also the rotation of circular nodes or cylinders and ligaments about plastic joints. For re-entrant anti-trichiral honeycombs, the crushing stress and NPR effect of re-entrant anti-trichiral honeycomb under both small and large deformations were found to be significantly influenced by the variation of cell-geometry parameters [29], [30]. While its NPR effect is more prominent with the decrease of its ligament-ratio and the mean radius, the crushing stress increases with cell-wall thickness and decreases with ligament-length ratio. In addition, through numerical simulations and experiments, the in-plane elastic responses and relationships between variations in elastic constants and relative densities were established.

Separately, the introduction of novel structures through the replacement of walls with curved ligaments in splined re-entrant and enhanced splined re-entrant designs, have shown improvements to moduli in both the lateral and axial directions [31]. Through reinforcement of arch-like beams and soft hinges on re-entrant honeycomb, structural stiffnesses can be enhanced while retaining auxetic behaviours [32]. Similar to splined re-entrant structures, bio-inspired re-entrant arc-shaped honeycomb could improve impact EA abilities and crush uniformity [33]. Instead of replacing only the horizontal ligaments with elliptical pockets, the replacement of inclined walls of re-entrant honeycomb with double circular arc cell walls to create petal-like cells, produces plastic deformation as single sloped cell walls that facilitates EA [34]. Additionally, sinusoidally curved ligaments whose geometrical factors were also found to have profound effect on the anisotropy of the 2D lattice metamaterial [35]. The anisotropy in turn influences the amplitude/wavelength ratio and stiffness ratio between axial and transverse direction which ultimately define the auxeticity of the structure (i.e the NPR).

It was also found that transversely curved ligaments in tandem with additional design parameters allowed for more extensive modifications and fine-tuning of localized deformation in ligaments. This enabled tapping into extended envelope of mechanical responses that is not attainable by conventional chiral honeycomb design with flat ligaments [36]. Furthermore, curved ligaments may also be produced through controlled porosity via perforation method, which provides larger NPR and lower stress level as compared to conventional perforation shapes [37].

2.1.2 Bio-inspiration and REAT Structure

Honeycomb lightweight structures are prevalently applied in industries such as aerospace[38], automotive, marine, and civil engineering. Specifically, they are a suitable option for structural and human protection against impact and blast loadings[4], [5], [39]–[41] due to their high specific stiffness, strength, exceptional impact resistance, and EA capabilities[2], [42]–[44]. Alongside the well-documented forms of hexagonal[45][46], Kagome[47], circular[48] and triangle[49][50] honeycombs, nature has supplied a wide range of other bio-inspired concepts for design and optimization of lightweight lattice structures[9][51]. In particular, gradient-based distribution in nature has equipped animals, plants and significant number of organisms with superiority in adaptation and survivability in harsh environments through characteristics such as lightweight, shock and EA as well as crack resilience[52]. Influenced by the advantages of gradient distribution, it is possible to embody the concept into REAT honeycomb to enhance its mechanical performances. REAT possesses NPR and features a chiral-based structure derived from re-entrant hexagonal honeycombs. Each joint of the re-entrant unit cell comprises of a chiral, and each adjacent chiral is designed to be tangential to 3 ligaments on the same side[27][53].

Apart from many uniformly distributed lattice structures, novel class of architected mechanical metamaterials has been developed to produce superior compressive responses and EA

capability. Xu et al.[54] investigated the in-plane uniaxial compressive response and EA capacity of a novel hybrid configuration. The AuxHex structure exhibited superior stiffness, compressive strength and EA attributed to the stable and uniform deformation mode of its unit cell. The concept of AuxHex structure was then transformed into 3D lattice structure whose crushing deformation is stabilized by auxiliary structure, further enhancing the EA capacity[55]. On the other hand, tailorable PR, elastic modulus, and shear modulus were achieved through novel tetra-missing rib auxetic honeycomb by evolution of its elastic constant with geometrical variation[56]. Similarly, a novel class of chiral structure paired with hierarchical configuration was generated, which was capable of exhibiting auxetic behaviour as well as two types of deformation mechanisms[57]. While the PR is dependent on both the ratio of thickness as well as that of ligaments, the work also discovered regions where PR was independent of dimensions, which is important from the perspective of production as it would make PR insensitive to manufacturing defects.

Furthermore, high EA capability through multi plateau stress can be realized through a combination of different honeycomb structures with widely varying mechanical performances. For instance, Wang et al.[58] proposed integrating double arrowhead honeycomb with star-shaped honeycomb to produce two-stage plateau stress under low-velocity impact loading. Shen et al.[59] implemented vertex-based hierarchical technique onto re-entrant honeycomb structure to enhance its elastic modulus while keeping the PR stable over a wide range. On the other hand, an approach as simple as introducing strengthening ribs was able to increase Young's modulus by up to 200% in the strengthening direction without compromising on its auxetic property[60]. Additionally, tunability of stiffness was accomplished by tuning densification strain through re-entrant unit cells with different variable stiffness factors characterized by various densities added to the horizontal ligaments[61]. Besides modifying the horizontal ligaments, Qi et al.[62] designed re-entrant circular honeycomb with double

elliptical arc inclined walls to dissipate more energy. Results showed obvious plateau stage in a dynamic setting as well as higher stress level in the proximal end over distal end, revealing great potential for impact protection.

Furthermore, numerous structures that are inspired by biological creatures have also proven to provide superior mechanical responses over conventional structures. Zheng et al.[63] mimicked the structure of DNA to produce a helical structure whose mechanical properties were studied experimentally, numerically and theoretically. It was shown that connections between two intertwined helices was crucial to achieving stable chiral deformation. Taking chirality and twisting into consideration, a series of novel bio-inspired honeycomb structure with added twisted feature was fabricated. Three unit cells along each side with 30° twisted was found to have the highest compressive strength as well as SEA, which was attributed to uniform distribution of stress[64]. Ha et al.[65] evaluated the performance of a bio-inspired honeycomb sandwich panel based on the microstructure of a woodpecker's beak and revealed a positive correlation between SEA and cores with larger wave numbers and amplitude. By mimicking the internal structure of a turtle shell, Wu et al. [66] studied the dynamic responses of aluminum honeycomb sandwich structure with CFRP panel from which substantial improvement in crashworthiness was observed. On the other hand, CFRP can also contribute to the overall crashworthiness through interlayer design with sparsely distributed Aramid-pulp (AP) micro-/nano-fibers[67]. Similar improvement in both in-plane and out-of-plane crashworthiness with increasing level of hierarchy was concluded in a novel bio-inspired self-similar concentric auxetic reentrant and hierarchical honeycomb, respectively [67][68]. In addition, a bio-inspired hierarchical model mimicking microstructure of a horseshoe was proposed and its non-linear mechanical properties were analyzed to describe their dependences on the microstructure geometry[69]. A morning-glory inspired lattice structure was assembled to produce negative Poisson effect which is beneficial to SEA[70]. Remarkably, given the

geometry of the morning-glory unit cell, different types of cell-to-cell connections and thus cell distances were found to have profound effect on both the Poisson effect and EA efficiency. In stark contrast to conventional honeycombs which are made up of straight ligaments with sharp edges, most of the surfaces and cell walls of bio-inspired lattice structures with enhanced mechanical properties are curved in nature [63], [66], [68], [70]. This is further substantiated by bio-inspired re-entrant cell[33], novel re-entrant circular auxetic honeycombs[62] and novel REAT structure with arc-shaped ligaments[71].

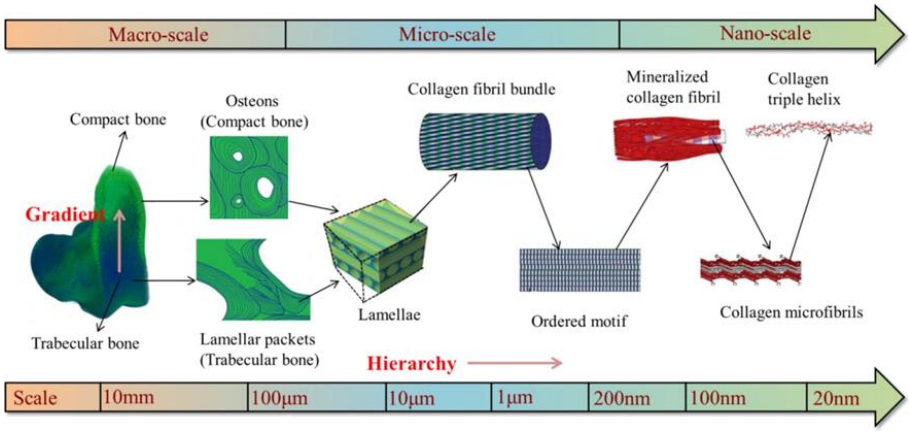

Figure 2.2. Bone structure exhibiting graded hierarchical distributed configuration [72]. As observed, the bone is made of both hierarchical and functionally graded microstructures.

Notably, nature-inspired gradient distribution exists more often than nature-inspired uniform distribution as the functionality demand varies across the interior of the structure. For example, bone structures have graded distribution that transits from the inner trabecular bone to the outer compact bone[72] which is illustrated in Figure 2.2 below. The structural composition of bamboo is also graded in nature as depicted in Figure 2.3(a), where the fiber bundles within the stem are compact and dense at the periphery and gradually becoming sparse towards the center, generating a gradient distribution of stiffness while keeping itself lightweight. Similarly, spider webs shown in Figure 2.3(d) feature a distinctive gradient variation in diameter, promoting tensile stiffness along the radial direction of the web[73]. Moreover, the special morphological gradient distribution in tubular density of equine hoof[74] and mineral

distribution in mantis shrimp's dactyl club[75] are particularly advantageous in providing longevity in fracture, crack and impact resistance.

Several research had successfully demonstrated the beneficial influence of adopting graded distribution into lightweight synthetic lattice structures. Gradient designs are generally accomplished by implementing a gradation of porosity which can be achieved through various methods including varying cell wall thickness and density [76]–[79] matrix of materials[80],[81] or microstructural composition[82] or geometrical parameters of unit cell[83]. For instance, in-plane graded honeycombs were found to improve the crushing strength and SEA by up to 70% compared to conventional honeycombs[84]. Moreover, graded cell wall honeycombs have a tendency to undergo localised deformation initially concentrated at the weakest layer, allowing controlled deformation, which may be valuable in niche applications[85]. The direction of the gradient also affects the performance of honeycombs[86]. Honeycombs with unidirectionally graded cell walls have lower crushing stress and lower energy dissipation as compared to their bidirectional graded counterparts. Other investigations [87]–[89] also confirmed the significant impact from the alteration of cell-wall thickness on mechanical properties over its traditional uniform counterparts. As these graded honeycombs exhibit PPR, the collapse in individual layers had no impact on the deformation of other layers. In contrast to the aforementioned layer-by-layer collapse, the horizontal shrinkage coming from auxetic structures (with NPR effect) that start in the weakest layer also affected other graded layers in their horizontal shrinkage before full densification [86].

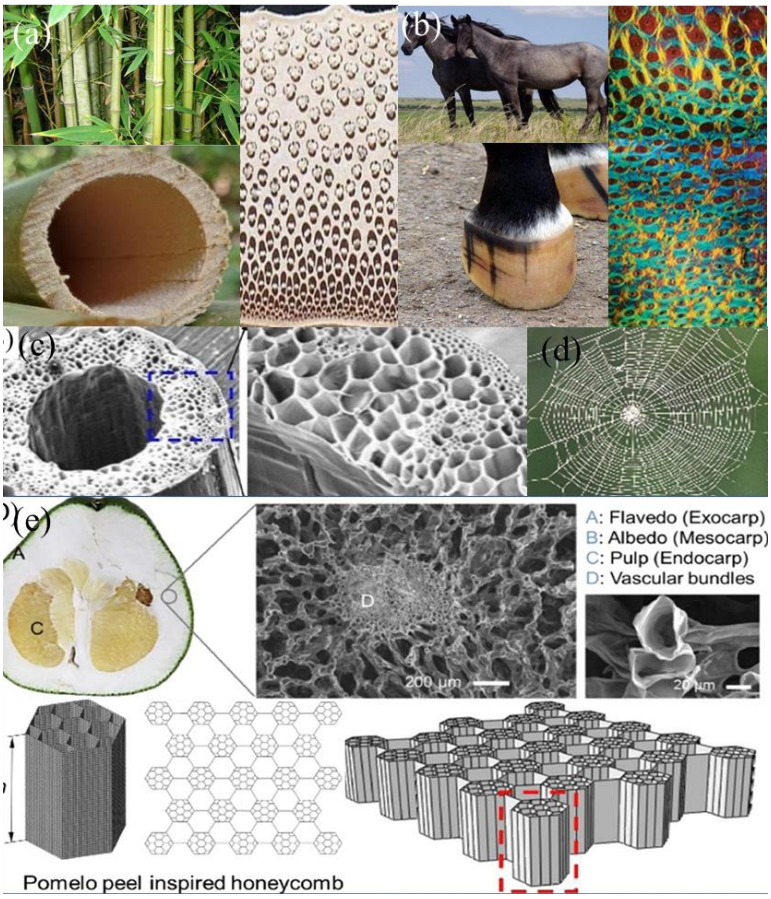

Figure 2.3. Illustration of (a) Graded distribution of vascular bundle density in bamboo stem, increasing from interior to outer periphery[90] inspiring height-based graded design in REAT structure. (b) Increased tubular density from inner-to-outer direction in horse hoof thickness[51]. (c) Stem exhibiting hierarchical configuration [91]. (d) Spider-web inspiring several orders of hierarchical honeycomb [92], And (d) Pomelo peel-inspired honeycomb [93].

Jiang et al.[94] proposed graded re-entrant circular honeycombs with both positive and negative gradient to improve mechanical properties over its uniform counterpart. It was concluded that multiple gradient layers can produce multiple plateau stages and notably, structures with positive gradient exhibited multi-plateau stages regardless of crushing velocity. Furthermore, a combination of gradient-based approach and hierarchical configuration were also adopted to develop a series of graded fractal honeycombs and graded hierarchical honeycombs which achieved significant improvements in the crashworthiness performance as well as SEA under various loading velocities [95][96].

Not limited to 2D lattice structures, graded distribution technique was also adopted in 3D lattice structures such as the body-centered cubic (BBC) lattice which demonstrated its versatility and

viability in enhancement of mechanical properties. Functionally graded BCC lattices produce distinctive SS behaviour with collapse in sequence through periodic weakening in layer[97]–[99]. Based on similar functionality to spider web, Liang et al.[100] proposed a bidirectionally graded configuration to a three-dimensional lantern-like lattice structure to achieve prominent enhancement to multi-directional crashworthiness. Gradient distribution was also introduced to thin walled tubed filled with three-dimensional arrowhead auxetic structure which exhibited even better EA and lower peak crushing force (PCF) when compared to its uniform counterpart[101], [102]. Likewise, comprehensive studies were conducted on both uniform and graded three-dimensional double-U hierarchical auxetic structures, which showed better high-speed compressive performance in terms of lower PCF and higher crushing force efficiency in negatively graded lattice over its uniform counterpart[103]. The effect of graded severity on short fibre reinforced Schwarz-P (SP), Gyroid and BCC was studied and found to have widely varying effects[104][105]. Results had shown that both moderate and severe grading has negative influence on the stiffness and EA on BCC as compared to positive impact on SP lattices. It is also worthwhile to note that gradient-based approach on auxetic structure tend to have better enhancement effect to their mechanical performance over the non-auxetic structures as the negative Poisson effect in one gradient layer tend to affect adjacent gradient layers, which implies increased mobilization of materials leading to better EA performances.

While extensive research has been conducted on the compressive performance of conventional REAT auxetic honeycombs[106], graded auxetic and non-auxetic honeycombs, there remains a significant research gap in the understanding of graded REAT honeycombs. Prior studies have primarily emphasized. Furthermore, majority of attention had been focused on thickness-based gradient to reproduce a layer-by-layer collapse with staircase effect in the plateau stage. However, this method may prove unsuitable for various practical applications, as it could result in inadequate EA capacity during early compression stage. Moreover, unnecessary

concentration of stress in the joints between transition in thickness could undermine the EA capability through increased fracture. Therefore, the present study draws inspiration from the gradient distribution in bamboo stems and horse hoof (Figure 2.3(a) and (b)) to expose innovative deformation modes in the auxetic nature of graded REAT honeycombs (excluding thickness gradients) that differentiate from the conventional collapse pattern. In the subsequent sections, a thorough analysis of the SS response, deformation pattern, NPR, EA, and crushing strength are discussed through extensive experiments conducted on the graded REAT honeycombs under quasi-static compression.

2.1.3 Honeycomb and Hierarchical Structures

It is well acknowledged that various forms of honeycomb structures can be designed and optimized as the key to achieving promising mechanical properties lies in its topological definition. Homing in on just the traditional hexagonal structures and leveraging on its benefits due to its prevalent adoption, the concepts of functionally grading and hierarchical architecture inspired from nature can be integrated and introduced with triangular and hexagonal substructural hierarchy. Furthermore, given the geometrical symmetry and simplicity of the hexagonal cell topology, a combination of functionally graded configurations and self-similarity can also be realized to further enhance the crashworthiness and EA of the structure.

Being the most adopted and researched cell topology till date, numerous theoretical and numerical studies confirmed the prominent crashworthiness performance under both in-plane [107][108][109]and out-of-plane[109], [110][111] dynamic loading. Furthermore, increasing the wall thickness can enhance the in-plane and out-of-plane performance[4][112], [113] which is similarly applicable with changes in cell wall angle and length to thickness ratio of the unit cells[114]. The influence also have positive impact on the enhancement to dynamic stress under high crushing speed due to contribution from the inertia force[115]. As such, hexagonal honeycomb was also widely deployed as material core to improve the mechanical performance

of lightweight sandwich structures[116]–[118]. To further transcend the performance limits of the hexagonal honeycomb, novel cell topologies have been rigorously proposed and introduced. For instance, nine honeycombs of various cell topologies were generated and compared based on their in-plane compressive performance and EA behaviors[119]. Yang et al.[120] introduced a variety of horseshoe-shaped honeycombs to improve out-of-plane crashworthiness behaviors by investigating a series of crashworthiness indicators such as the initial peak force, mean crushing force (MFC), crushing force efficiency (CFE) and SEA. In addition, Liu et al.[121] proposed a novel circular honeycomb made of semi-periodic sinusoidal beams to enhance in-plane stiffness strength. The global strain of the lightweight cellular structure was found to be to ten times larger than its raw material which demonstrated the potential of proposed structure for multifunctional in-plane morphing. Similar concepts were also presented through the use of multi-cell quadri-arc[122] and petal-shaped[107] mesostructures to achieve greater crashworthiness and EA behaviors of circular honeycombs. Performance over regular hexagonal honeycombs are obvious in quasi-static, low and medium velocity impact; however, the advantage starts to lose out due to increasingly dominant inertia effect in high velocity cases.

Lately, fabrication of honeycombs made of shape-memory materials were made possible by 4D printing technology to achieve reversibility in EA which enhance the reusability of lightweight structures after impact [123]–[125]. Furthermore, topological optimization[126] and shape optimization[127] were also proposed to design lightweight lattice structures with novel unit cell topologies. However, all of the aforementioned concepts are limited to single-order cellular configurations which underperforms in in-plane stiffness which may restrict their potential applications.

Besides directly manipulating the topologies of unit cell, bio-inspired concepts such as hierarchy had been well-sought after. There are specifically two types of hierarchical architecture, of which the first is generated by replacing the cell walls of regular honeycombs

with hexagonal[91][128][129], Kagome[47], triangular[130][131] or other topological tessellations. Through experiments and numerical simulations, it is well concluded and demonstrated that hierarchical configuration greatly improves mechanical and crashworthiness performance. Tao et al.[132] experimentally demonstrated the significant of hierarchical design in enhancing the in-plane compressive strength, SEA and CFE of 3D printed square hierarchical honeycombs. Furthermore, the level of hierarchy also produced a noticeable impact on the compressive behavior of the structures. Similarly in out-of-plane, Fan et al.[133] revealed the affirmative improvement in crushing performance of hierarchical tubular structures. Likewise, hierarchical design concept had been integrated into metamaterials which yielded similar enhancements in their mechanical performance[134].

While the first type of hierarchical structure reconstructs the cell wall with its unit cell geometry as illustrated by Figure 2.4(d), the second type of hierarchy is defined by replacing the vertices or nodes of the hexagon with smaller hexagon, which is also known as self-fractal similarity shown in Figure 2.4(b) and (c). Such design concept had been comprehensively investigated by Sun et al.[68], [135], [136] in the out-of-plane crushing which shown improvement in crushing resistance and EA over traditional honeycomb.

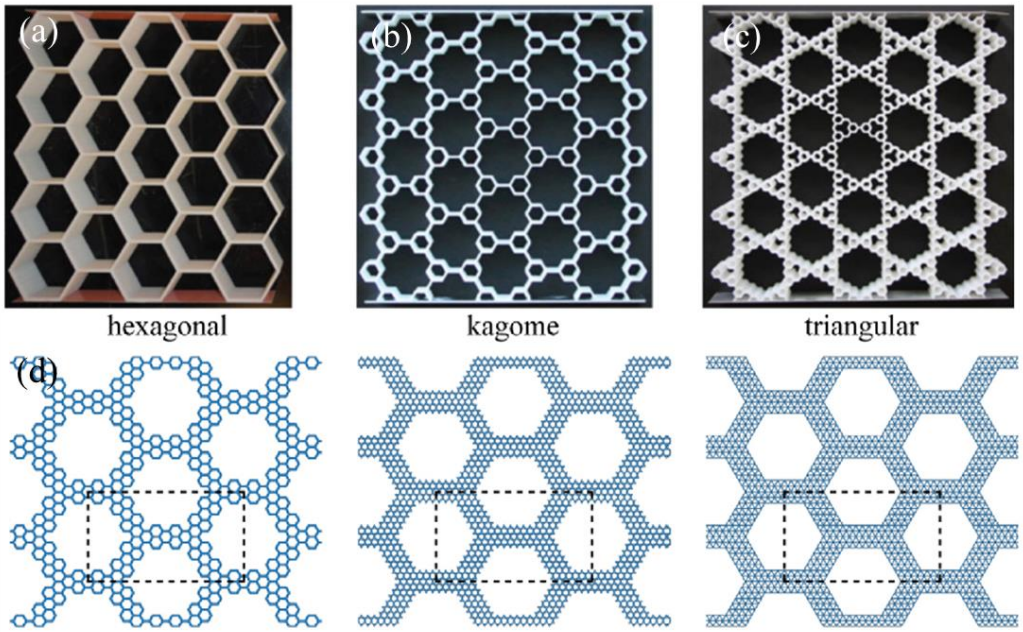

Figure 2.4. (a) Regular honeycomb and (b) hierarchical honeycomb with (b) first- and second order hierarchy and (d) hierarchical honeycombs made up of substructures [137].

The hierarchical concept is ideal for lightweight design for crashworthy structures as corresponding peak forces do not increase with density as compared to conventional honeycomb structure. The dynamic crushing characteristics influenced by self-similarity configuration were addressed by He at al.[138] whose study elucidated that self-similarity can offer drastic improvements to EA of honeycomb. Similar conclusions were drawn by other studies [139]–[142]. The prominent improvement in strength and stiffness of self-similar honeycomb over regular honeycomb was further clarified theoretically [139][137][143]. In addition, sandwich cores utilizing self-similar hierarchical honeycomb was also investigated to raise the loading bearing capacity under three-point bending [144]. Study had shown the tunability of mechanical properties of loading bearing structures are directly influenced by many factors such as cell size, shape pattern and level of hierarchy which is further tied to involvement of number of cells during deformation.

Apart from hierarchical construction, functionally graded honeycomb is another promising approach to achieve lightweight impact absorbers by integrating layers of honeycomb with

distinct characteristics of stepwise fashion to bring about unexpected mechanical features [85][85], [145]. Theoretical [146][147], numerical [148][149][85] and experimental [150] analysis were conducted to demonstrate the enhancement in mechanical properties over uniform counterpart. Currently, the most common approach to create graded honeycomb is to modify the cell-wall thickness in each layer which were concluded to enhance crushing behavior and EA capabilities [149]. The graded thickness approach had been further explored and adopted by several other studies [146], [151], [152], [153] to enhance the crushing properties of honeycombs. Interesting deformation feature characterized by double shock deformation is observed in experiment conducted on density graded honeycomb of which had contributed to improvement in EA capacity [154]. Apart from functional grading in wall thickness, the graded effect can also be achieved by changing the cell size in each layer. This is illustrated by continuously varying the cell sizes of Voronoi honeycombs [155]–[157] in which the new design offers advantages in impact resistance over the conventional porous structure. Graded multilayer sandwiches with corrugated cores of different cell profile were proposed by Cao et al.[158] to enhance EA efficiency. Similarly, Bai et al.[159] fabricated lattice with graded strategy through varied density and topological configurations which ultimately led to better absorption capability over uniform structures. Similar work is again conducted by Xiao et al.[160] whose graded micro-lattice structures showed promising impact protection system. Interestingly, it was also highlighted that continuous grading is better than stepwise grading system as the latter may lead to unfavorable secondary shock. The gradient distribution can also be obtained by taking into consideration the materials of different stiffness into structural design to produce a hybrid soft-hard lattice structure [161].

Given the following discussions and studies, self-similar hierarchy and gradient design strategies had been individually proven to be effective in redefining EA performances of the honeycomb structures. However, little is done to investigate their combined characteristics

adopted into one single honeycomb design. Therefore, new designs should not only take advantage of self-similarity hierarchy but also leverage on the functional gradient concept to enhance the dynamic crushing behavior of honeycombs. As such two novel designs will be introduced.

At the same time, in order to replicate the hierarchical characteristics of animal bones and plant roots in nature, hierarchical 3D lattice structures are designed to improve the mechanical properties of the traditional 3D lattice structure. Traditional 3D lattice structures include truss-based 3D lattices such as simple cubes [162][163], body-centered cubes[164][165][166], face-centered cubes[162][167], octet truss[168], [169], plate-based lattices [170]–[172] and shell-based 3d lattices[173]–[175]. When compared with conventional gyroid 3D structures, the mechanical properties of the two-order Gyroid lattice structure with very low density was found to have higher crushing strength than the single scale Gyroid lattice structure [176]. Similarly, a third-order lattice structure (Octahedron-octahedra-octahedra) and a second-order lattice structure (Octahedron-octahedra, Octet-octahedra, Octet-octets) was fabricated to reveal that the hierarchical structure had higher strength and stiffness than the non-hierarchical structure with no improvement in strength and stiffness of the structure beyond second order [177]. Lv et al.[178] studied the compressive mechanical performances of hierarchical octet structure by experiment and simulation, and found that the second-order structure was lower in SEA than that of the first-order structure, but higher than that of non-hierarchical structure. As far as research goes, the fortifications of 3d structures through hierarchical configurations are limited to non-auxetic structures as illustrated in the examples above. Thereby, drawing inspiration from the natural world, specifically from the varied hierarchical layers found in bone structures and plant systems, which are composed of distinct structural elements, the subsequent study proposes the incorporation of hybrid auxetic hierarchical 3d structures which uses more than one type of unit cells. The rationale behind this proposal is that such a combination of diverse

unit cells could potentially enhance the auxetic properties of the overall 3D structure, offering improved performance in applications where auxetic characteristics are beneficial.

Chapter 3 Methodology

This section covers the general methodologies and approaches used in validating various structural designs and materials employed in this research. The focus is on outlining the systematic comparison between experimental results and simulation, applicable to different chapters focusing on each distinct structures and materials. The choice of materials and fabrication techniques aligns with the specific requirements of each lattice structure.

3.1 Fabrication and Materials Characterization Techniques

The methodology recognizes the varying resolution requirements of different structures. For instance, simpler structures like the REAT can be fabricated using the FDM technique. In contrast, hierarchical structures with finer wall thicknesses are fabricated using Stereolithography (SLA) to cater to their intricate design needs. The difference in resolution requirements and structural complexities is exemplified in the Figure 3.1, contrasting conventional lattice structures with hierarchical ones .

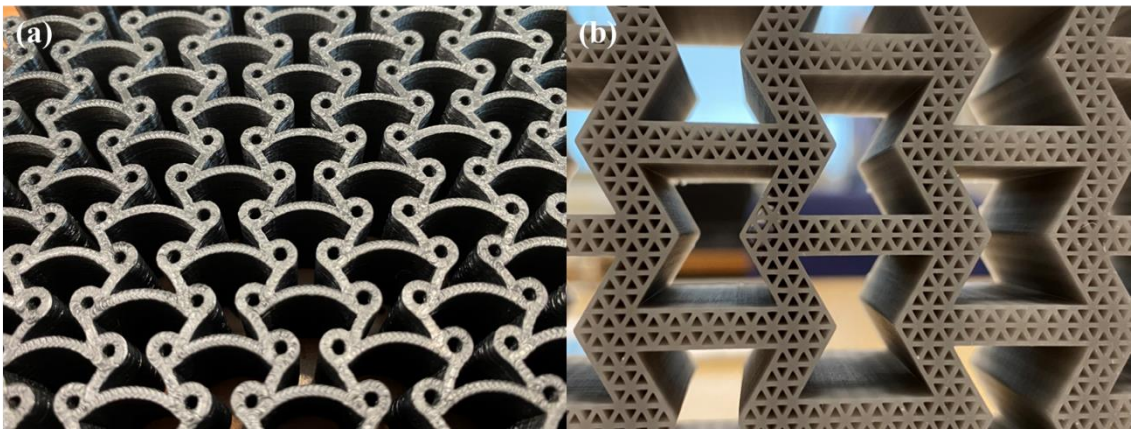

Figure 3.1. Illustration of complexity of structure between (a) honeycomb structure of 1mm in thickness by FDM technique as compared to (b) Hierarchical structure with significantly lower thickness at 0.3mm by SLA technique. Different printing techniques are deployed based on resolution requirements.

FDM is a widely used 3D printing technique that works by extruding thermoplastic filaments through a heated nozzle, depositing them layer by layer to build the desired structure. This method is particularly suitable for simpler lattice structures when compared with SLA. This is

due to the fact that FDM typically offers a lower resolution compared to SLA. The resolution is limited by the size of the extrusion nozzle commonly 0.4mm, which ultimately determines the minimum feature size and layer height. For structures that do not require extremely fine details, FDM provides a balance of resolution, strength, and material choice.

One inherent limitation of FDM is its difficulty in achieving complete fill in the wall thickness of printed structures. This challenge arises due to the nature of the FDM process, where material is extruded in a linear path, potentially leading to gaps or insufficient density in the walls shown in Figure 3.2(a). However, this issue can be effectively addressed by modifying the pre-print settings. Instead of employing a traditional linear trajectory for the print path, a wavy or zigzag pattern is used as seen in Figure 3.2(b). This adjustment allows the extruded material to overlap and interlock more effectively, thereby ensuring a more uniform and dense fill within the walls of the structure. This technique enhances the structural integrity and mechanical properties of the printed object, making FDM more versatile for a wider range of applications, particularly where wall density and strength are critical.

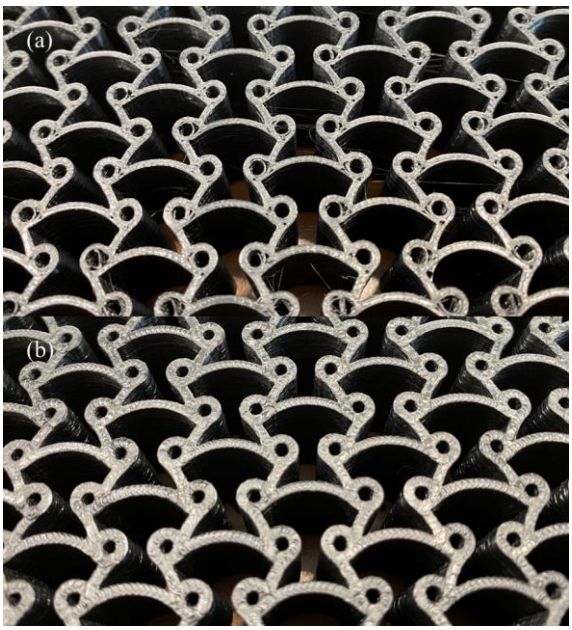

Figure 3.2. illustration of comparison between two lattice structures created using different printing trajectories. (a) displays a lattice printed with a linear path extrusion technique, where noticeable porosities are evident, particularly at the tangential attachments. These porosities are more pronounced due to the greater thickness at these points, which the linear path technique struggles to fill completely. In contrast, (b) shows a lattice structure

produced using a zigzag printing trajectory. This method results in a more uniform and thorough fill, effectively reducing the porosities and achieving better material distribution throughout the structure.

Even though the resolution requirements for FDM are comparatively lower, it is imperative that the walls of the lattice are properly filled with materials to avoid any porosity or void. This is crucial for ensuring the fidelity of the experimental results. Inadequate fill can lead to porosity or voids within the structure, which could significantly interfere with the validation of experimental results against simulations. Ensuring a complete and uniform fill is therefore not only a matter of structural integrity but also a key factor in the accuracy and consistency of experimental validation with simulated counterpart.

The material used to print lattices with FDM technique in the study is Acrylonitrile Butadiene Styrene (ABS). On the other hand, SLA is a 3D printing technique known for its high resolution and ability to produce intricate details. It works by using a laser to precisely cure liquid resin into solid form, layer by layer. This method is particularly advantageous for fabricating hierarchical structures with fine wall thicknesses and complex geometries as depicted in Figure 3.1Figure (b). However, SLA comes with its own set of challenges that can impact the performance of the final structure. Firstly, the performance of structures printed with SLA is heavily dependent on post-processing and curing procedures. Uniform curing is crucial, but it can be challenging to achieve, especially in dense or intricate structures. Sometimes, the inner parts of the lattice may not cure evenly due to limited light penetration. Flipping the sample during post-processing can help ensure more even curing across the lattice, but uniformity remains a limiting factor. Notably, the mechanical strength of the printed structure can be affected by the printing time and the number of lattices printed per batch.

An important empirical observation in SLA printing is the inverse relationship between the number of lattices printed per batch and their mechanical strength. It has been noted that as the number of lattices in a single printing batch increase, the mechanical strength of each lattice tends to decrease, given a constant curing time. For instance, a lattice printed individually may

exhibit higher strength compared to several lattices printed together in the same batch. This variation can be attributed to the time required for the laser to return to a specific layer, potentially affecting the bonding between layers. The longer the interval between the curing of successive layers, the greater the risk of inconsistencies in bonding, which can weaken the overall structure. Furthermore, post-processing steps, such as washing and curing, can further impact the consistency and mechanical properties of the printed structure. Inconsistent post-processing can lead to variations in material properties throughout the batch, affecting the reliability and predictability of the printed structures.

To address these challenges, SLA printing requires careful management of batch sizes, printing time and post-processing procedures. Understanding the impact of batch size on the mechanical properties is crucial for optimizing print runs, especially when strength and reliability are important to ensure the consistency of the results. Additionally, standardizing and meticulously executing post-processing steps can help ensure more consistent and predictable outcomes in correspondence to simulation.

In close similarity to SLA, Digital Light Processing (DLP) technology emerges as a notable counterpart to SLA. DLP operates on a similar principle of curing liquid resin using light, but it employs a different approach. Unlike SLA, which uses a laser to cure the resin, DLP utilizes a digital projector screen to flash a single image of each layer across the entire platform. This means it can cure entire layers of the resin simultaneously, often leading to faster print times compared to the point-by-point method of SLA. DLP can also achieve high-resolution prints with excellent surface finish, comparable to SLA. However, the quality of the final product is pre-determined by the projector's resolution and other settings just as cure time and layer thickness. Furthermore, in contrast with the point-by-point laser curing method used in SLA, the simultaneous curing process in DLP significantly reduces print times, especially when dealing with larger batches or taller structures. As aforementioned in the limitations of SLA,

the mechanical properties of a print can vary depending on the size of the batch and the printing time, DLP offers more consistent mechanical properties across different print jobs. This consistency is attributable to the uniform exposure each layer receives during the DLP printing process. As each layer is cured uniformly and simultaneously, there is less variation in bonding quality between layers, leading to more predictable and uniform mechanical characteristics in the final product. Therefore, the efficiency of DLP in curing entire layers at once not only speeds up the printing process but also makes it more scalable for larger production volumes. In essence, DLP technology, while offering advantages in terms of printing efficiency and consistency in mechanical properties, shares similar challenges with SLA related to support structures and orientation.

PolyJet 3D printing technology is renowned for its ability to print with high precision and detail, making it particularly suitable for complex and detailed prototyping. PolyJet works by jetting layers of curable liquid photopolymer onto a build tray. A UV light then cures these layers, building the object. This process allows for extremely high resolution and the ability to produce fine details, surpassing many other 3D printing technologies. One of the most significant advantages of PolyJet is its ability to blend the hardest and the softest materials to create a range of intermediate materials. This capability allows for extensive customization in the properties of the printed object, enabling the creation of parts with varying degrees of flexibility, transparency, and color in a single print, much applicable to achieving gradient characteristics in lattice structure. While PolyJet excels in printing intricate structures, it does face challenges similar to Stereolithography (SLA) when dealing with complex geometries that require support materials, especially for overhanging parts. The internal support materials can be particularly challenging to remove without damaging the main structure. This is a crucial consideration in both PolyJet and SLA, where delicate and detailed designs are often printed. In some cases, the post-processing required to remove these supports may risk damaging or breaking the finer

aspects of the main structure. A common strategy to mitigate this issue is to reorient the lattice structure during printing to reduce the need for supports however changing the orientation of a lattice structure to minimize support structures can significantly alter its mechanical performance. Since both PolyJet and SLA involve layer-by-layer deposition, the orientation of the layers is a critical factor in determining the strength and behavior of the final product given a fixed direction of compression.

Building upon the discussion of various 3D printing techniques utilizing polymer materials previously, Type IV tensile samples were fabricated to evaluate their mechanical properties in accordance with established standards. The testing process adhered to the ASTM D-638 Type IV standard for tensile properties of plastics[179]. The uniaxial tensile tests were performed using a Shimadzu 10kN universal testing machine, equipped with a video extensometer. This setup allowed for measurements of the material's response to tension. The tests were conducted at a controlled tensile speed of 5 mm/min, in accordance with the ASTM D-638 standard. Furthermore, for all lattices presented in this thesis, quasi-static compressions are also done using the Shimadzu 10kN universal testing machine. Detailed justification for the choice of materials and their characterization will be presented in the respective chapters later.

3.2 Performance Characterization

To evaluate and characterize the performance of the structures, several measures of mechanical properties such as the in-plane stiffness, plateau stress and SEA are considered [180]. The stress of the structure is obtained by dividing the reaction force on the bottom plate by the projected area (length of the structure multiplied by the out-of-plane thickness). The stiffness or the elastic moduli are defined by the gradient of the SS curve while its crushing strength is interpreted by the stable level of stress with increase in strain. Next, the Poisson’s Ratio (PR) of the structure can be evaluated by choosing four points on the honeycomb structure shown in Figure 3.3 and interpreting their displacements. The four corner points are generally located at

the joints of connections between ligaments and are chosen close to the middle of the sample to avoid interference from the boundary effects. In addition, these chosen points are the same across all the proposed design configurations with the difference being the curvature of the ligaments. The strains ε_x, ε_y and PR v_{xy} are expressed as:

$$\varepsilon_x = \frac{x_i - x_0}{x_0} \tag{3.1}$$

$$\varepsilon_y = \frac{y_i - y_0}{y_0} \tag{3.2}$$

$$v_{xy} = -\frac{\varepsilon_y}{\varepsilon_x} \tag{3.3}$$

where, with reference to Figure 3.3 x_i is the average deformed width between x_{i1} and x_{i2}, y_i is the average deformed height between y_{i1} and y_{i2}. x_0 and y_0 are the original width and height between the marked spots, respectively.

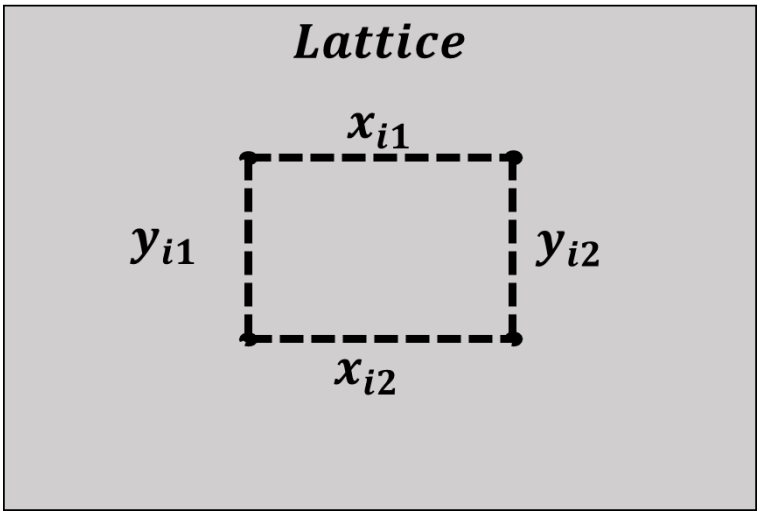

Figure 3.3. A general illustration of points of reference within a lattice in calculating the PRs of the structures.

The EA performance of the structures can be evaluated through the total EA, which is the area under the force-displacement (FD) curve shown in part of equation 3.4 where $F(s)$ is the instantaneous force that is a function of the compression displacement s. To eliminate the

effects of variation in mass across samples, EA can be divided by the corresponding mass (M) to obtain the SEA.

$$SEA(s) = \frac{EA(s)}{M} = \frac{\int_0^S F(s)ds}{M} \text{ Or } SEA(\varepsilon) = \frac{\int_0^{\varepsilon_p} \sigma \, d\varepsilon}{\rho_p} \tag{3.4}$$

Similarly, to prevent the over-influence of relative density (RD) over mechanical performances of various designs, the stress is normalized by the respective RD of every structure to eliminate any discrepancies. Furthermore, the EA performance of the structure should also be evaluated with the SEA, or the energy absorbed per unit mass of the structure. In order to accurately pinpoint the densification stage of each design, EA efficiency, also known as the energy absorbed per unit stress is used. The SEA which eliminates the variation of mass in total EA of various specimens, can be expressed through the total energy absorbed, which is the area under the FD graph divided by the mass of the structure expressed as above in equation 3.4.

Furthermore, SEA may also be expressed using SS curve normalised by density of the material, which is also expressed in equation 3.4 where σ and ε_p represent the instantaneous stress and strain, respectively and ρ_p is the density of the material.

A better gauge of the EA performance is the EA efficiency (η) which is defined as the energy absorbed up to a given nominal strain (ε_p) normalised by the corresponding stress value:

$$\eta(\varepsilon) = \frac{\int_0^{\varepsilon_p} \sigma \, d\varepsilon}{\sigma(\varepsilon_p)} \tag{3.5}$$

Furthermore, densification strain (ε_D) of a structure can be determined by the stationary point in the efficiency-strain curve where the efficiency is in global maximum, defined as:

$$\left.\frac{d\eta(\varepsilon)}{d\varepsilon}\right|_{\varepsilon=\varepsilon_D} = 0 \tag{3.6}$$

2.2.2 FE simulation methods

Furthermore, in order to comprehensively understand the crashworthiness of a structure, several other crashworthiness criteria, apart from SEA, which include PCF, MCF and CFE.

PCF reflects the maximum impact force where the higher PCF will lead to greater deceleration of the impact object and whose value, in the perspective of safety, should be kept as low as possible.

MCF represents the average force under the crushing process for a given displacement x as formulated:

$$MCF(x) = \frac{EA(x)}{x} \tag{3.7}$$

In general, the higher the MCF, the more efficient the crashworthiness performance of a structure [181].

Next, CFE indicates the uniformity of the force distributed over the deformation and is defined by [182]:

$$MCF = \frac{MCF}{PCF} \tag{3.8}$$

3.3 FE Analysis Setup

The series of studies discussed in the later chapters employ FE analysis to investigate the mechanical behavior and EA characteristics of specific lattice structures under compression. The analysis primarily utilizes the ABAQUS/Explicit solver, a tool for addressing complex dynamic and quasi-static problems. The essence of this methodology involves creating FE models, calibrating material properties, defining boundary conditions, and determining the optimal mesh size for accurate and efficient simulations.

The initial step of FE analysis cinvolves the development of FE models. These models are designed and exported in Solidworks and then imported into ABAQUS for detailed analysis.

The material properties from material characterization are calibrated based on experimental data. This calibration is crucial for accurately capturing the elastoplastic behavior of the polymer materials under load.

In the setup illustrated in Figure 3.4, both the top and the bottom plates are assumed to be analytically rigid. Even though shapes that can be defined with analytical rigid are limited, the compression plates can be aptly represented given their simple geometry. Furthermore, rigid bodies defined with analytical rigid surfaces are cheaper in terms of computational cost as compared to discrete rigid bodies. Results generated with analytical rigid bodies are generally smoother as less fluctuations are produced at the contact interaction between the mesh and surface in comparison to mesh-to-mesh interaction. Moreover, inaccurate solutions may be produced in discrete rigid bodies as a result of possible mesh penetration of master discrete rigid surfaces into deformable slave surfaces.

The bottom plate is fully constrained in all directions, while the top plate is allowed movement only in the y-direction. Additionally, constraints on honeycomb structure are applied to prevent out-of-plane buckling of the auxetic structure, which is vital for focusing only on the in-plane deformations.

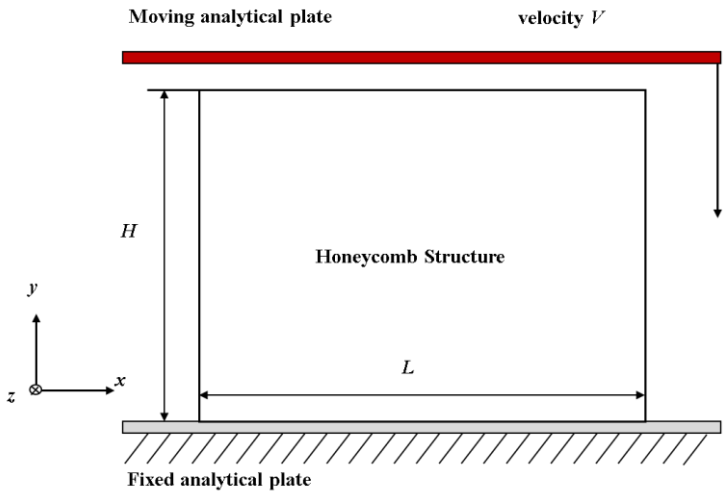

Figure 3.4 An illustration of simulation set up for FE analysis.

The simulation set up incorporate a general contact algorithm between the structure and compression plates, and a friction coefficient is set to simulate surface interactions. Mass scaling and smooth loading techniques are applied to handle the quasi-static nature of the problem efficiently. Similar to the experimental data extraction method for PR, unique nodes are chosen to calculate the PR through Eq. (3.3).

Another important aspect of FE is mesh sensitivity analysis. This approach involves testing various element sizes to find a balance between computational efficiency and the accuracy of results. This process ensures that the chosen mesh size is fine enough to capture the accurate details at a balance unnecessary usage of excessive resources and computational efficiency and speed.

The accuracy of the simulation results is verified by ensuring the kinetic energy remains negligible compared to the internal energy throughout the simulation [183].. This step is crucial to validate that the results are representative of quasi-static conditions. The method of validation involves comparing the SS curves obtained from the simulations with those derived from experimental data. A close agreement between the simulated and experimental curves would conclude that the FE model is able to accurately capture the elastoplastic behavior of the material. Furthermore, the deformation patterns predicted by the simulations are compared with experimental results. This comparison is critical in verifying the model's accuracy in predicting how the structure will deform under specific loading scenarios. Agreement in deformation patterns ensures that not only the material properties but also the boundary conditions and load applications in the model correctly mimic the experiment. Detailed justification for the choice of materials and their characterization will be presented in the respective chapters of this thesis.

To further elaborate on the FEA model, it is important to consider the loading strategies and solvers used, particularly for auxetic cellular structures undergoing large deformations. In these

cases, geometric nonlinearity should be considered. The convergence behavior of the simulations is closely related to the choice of loading strategies and solvers. Different solvers and loading techniques can significantly impact the accuracy and efficiency of the simulation. For example, using the ABAQUS/Explicit solver is beneficial for capturing the dynamic response and handling complex contact interactions.

Therefore, for the entirety of this thesis, ABAQUS Explicit is preferred over the Implicit solver for quasi-static loading conditions due to several key advantages, particularly in scenarios involving complex geometries and large deformations. The primary reason is its flexibility in handling severe nonlinearities, including contact and geometric nonlinearity, which are common in advanced material simulations like those of auxetic cellular structures. Unlike the Explicit solver, implicit solver can often struggle with convergence issues under such conditions. Furthermore, the Explicit solver can advance the solution in small, incremental steps, allowing it to capture the detailed progression of deformation and stress distribution fairly accurately as compared to implicit solver at a higher computational efficiency at a lower cost. This makes it particularly effective for problems where the structure experiences significant changes in geometry, as the Explicit solver can more easily track these changes without encountering convergence difficulties. Furthermore, the Explicit solver does not require the formation and solution of a global stiffness matrix, which not only reduces the computational cost and memory requirements but also avoids the iterative convergence process associated with Implicit methods. This characteristic is advantageous for simulations that involve complex contact interactions and large-scale interaction problems, as it simplifies the computational process and enhances stability. Although the Explicit solver is typically associated with dynamic problems, it can also be applied to quasi-static conditions through techniques like mass scaling and smooth loading to ensure that the dynamic effects remain negligible while maintaining computational efficiency. Consequently, ABAQUS Explicit

provides a more stable and reliable solution framework for quasi-static simulations of intricate and highly nonlinear material behaviors.

Chapter 4 Arc-shaped ligaments in REAT structure

In this chapter, novel REAT structures with (curvature) arc-shaped ligaments are proposed to enhance both the elastic modulus and EA capabilities through both experimental and numerical approaches. By first replacing straight ligaments with curved ligaments, unique deformation patterns are introduced through the rotation of cylinders, contact interaction between cylinder and ligaments, as well as petal-like cell interactions. Quasi-static compression reveals the effect of curvature along ligaments and their directions on the Young's modulus, PR, plateau stress and SEA capabilities. The primary finding is an improvement of up to eight times in normalized Young's modulus and up to four times in SEA with the introduction of combined curved ligaments (Dc+Uc) design. In addition, parametric studies on geometrical parameters of ligament curvature and cylinder diameter shows significant influence over mechanical properties and deformation patterns. This chapter sheds light on the development of novel REAT honeycombs that can be achieved through simple ligament modifications and combinational designs.

4.1 Design Approach

The objective of this chapter is to introduce and investigate the impact of arc-shaped ligaments on the mechanical properties of REAT honeycombs. The principle underlying this design approach is that the introduction of curvature to ligaments can enhance the mechanical properties, such as elastic modulus and EA, by altering the deformation mechanisms of the structure. The design methods involve replacing straight ligaments in conventional REAT honeycombs with curved ligaments to form novel unit cells, designing unit cells of various combinations of curved ligaments, utilizing both FE analysis and experimental methods to evaluate mechanical behavior of the designed structures and lastly, investigating the effect of

geometrical parameters such as ligament curvature and cylinder diameter on the mechanical properties.

Thus far, research into arc-shaped ligaments is still limited despite possible enhancements to mechanical properties as discussed earlier in literature review section 2.1.2. As such, this chapter seeks to contribute to the scientific understanding of curved ligaments by introducing the concept of arc shape to REAT honeycombs and unraveling their impact on PR, elastic modulus, plateau stress, EA, and deformation mechanisms.

The unit cells of the proposed novel honeycombs are designed based on the geometries of conventional or the control model as shown in Figure 4.1(a), where all the straight ligaments are replaced with half-waved arc ligaments. Given the constraint of tangential attachments, there are two possible ways the ligaments can be re-designed based on the direction of the curvature, leading to external and internal arc tangents highlighted in Figure 4.1(b)-(c), respectively. The naming convention of the proposed structures is based on the direction of curvature for the horizontal ligament.

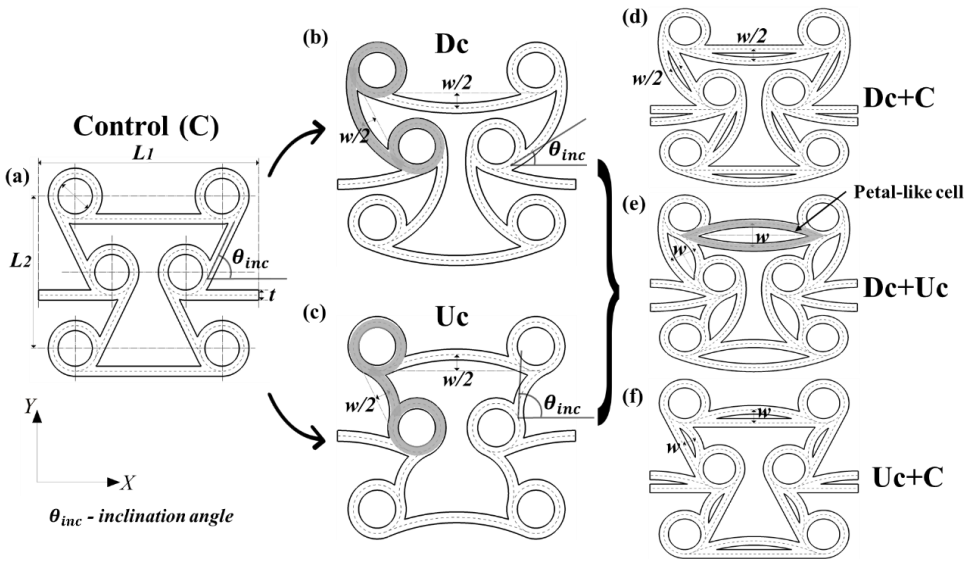

Figure 4.1. Schematics of cell geometries: (a) Conventional REAT honeycomb, also known as the control model (b) single rib downward-curved honeycomb (Dc) with external tangent arc highlighted (c) single rib upward-curved honeycomb (Uc) with internal tangent arc highlighted (d) double ligament combining downward-curved

and straight ligaments (Dc+C) (e) double ligament with downward-curved and upward-curved ligaments (Dc+Uc) and (f) double ligament with upward-curved and straight ligaments (Uc+C).

A systematic approach to the modifications of conventional REAT honeycombs is adopted following the approach to splined re-entrant designs by Zied and Osman [31] and Zhang et al. [33]. Firstly, modifications to the ligaments are performed by introducing curvature, namely Dc and Uc as shown in Figure 4.1(b)-(c), respectively. In this design, the straight ligaments are replaced with segments of a circle with curvature determined by the width "*w/2*", defined as the perpendicular distance between the midpoint of the straight ligament to the arc. It is important to note that the curvature of the curved ligaments between each design are different due to constraints set by the tangential attachment with the cylinders. With reference to external and internal tangent arc highlighted in grey in Figure 4.1(b) and (c), the distance between the attachments of the two ends of the upward curving ligament to the cylinders is shorter as compared to those of downward curving ligaments. Therefore, the actual lengths of the curved ligaments are different, and this difference will decrease with the reduction in diameter of the cylinder until the cylinders become a node which is basically a re-entrant design.

In the next step, the three designs of control, Dc and Uc are integrated to form double ligament designs. The design Dc+C comprise of an downward curving and straight ligament in Figure 1(d), Dc+Uc comprise of an upward and downward curving ligament in Figure 4.1(e), while Uc+C comprised of a upward curving and straight ligament in Figure 4.1(f). The RD of each structure is calculated from dividing the area of the unit cell configuration by the full area of the enclosing rectangle. The geometrical representations of the unit cells and their relative densities are illustrated in Table 4.1.

Table 4.1. Geometrical representations of unit cells and their relative densities. The RD is expressed as η = Acell/Arect, where Acell is area occupied by the unit cell configuration and Arect is area of the enclosed dotted rectangle.

Single Ligament Designs

C	Uc	Dc
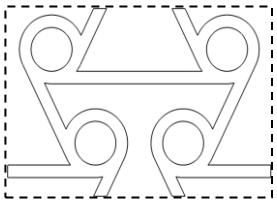	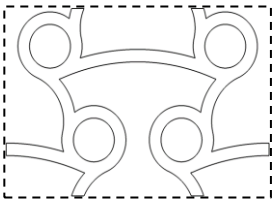	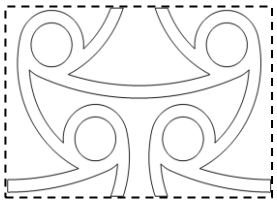
η = 0.303	η = 0.274	η = 0.355
Double Ligament Designs		
Uc+C	Dc+C	Dc+Uc
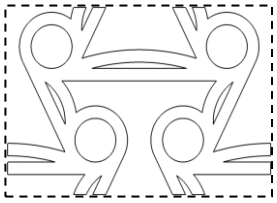	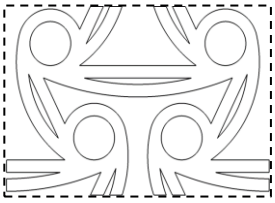	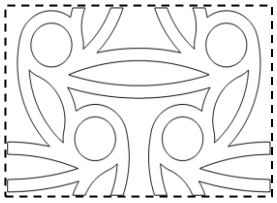
η = 0.404	η = 0.482	η = 0.445

4.2 Fabrication, FEA and Experimental Validation

The characterization of mechanical properties had been discussed in Chapter 3.2. However, with regards to NPR, extra step is taken to determine the number of unit cells to consider in the structure such that there is no edge or size effect on the PR, three different models of varying unit cell numbers are considered in Figure 4.2(b)-(d). The variation in PR for structures with 3×2, 5×4 (baseline) and 7×6 unit cells are compared in Figure 2(a). Significant edge effects on the calculated PR can be observed for the 3×2 model, as evident from the large fluctuations. This is in contrast to the relatively similar and stable PR in both the 5×4 and 7×6 models. Hence, the baseline model of 4×5 is deemed sufficient to estimate the effect of PR across different engineering strains.

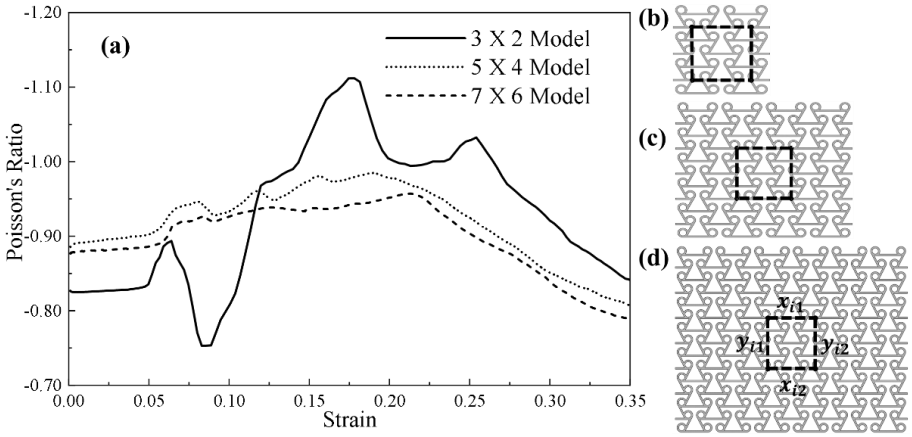

Figure 4.2. FE analysis model of REAT honeycomb of different cell numbers. (a) NPR vs engineering strain of the three models (b) 3×2 model (c) 5×4 model and (d) 7×6 model with points of reference illustrated in calculating the PRs of the structures.

Specific to this chapter of study, the models are developed using C3D8R quadrilateral 8 nodes linear brick with reduced integration shown in Figure 4.3 and mesh sensitivity is conducted based on control solid configuration in the quasi-static condition.

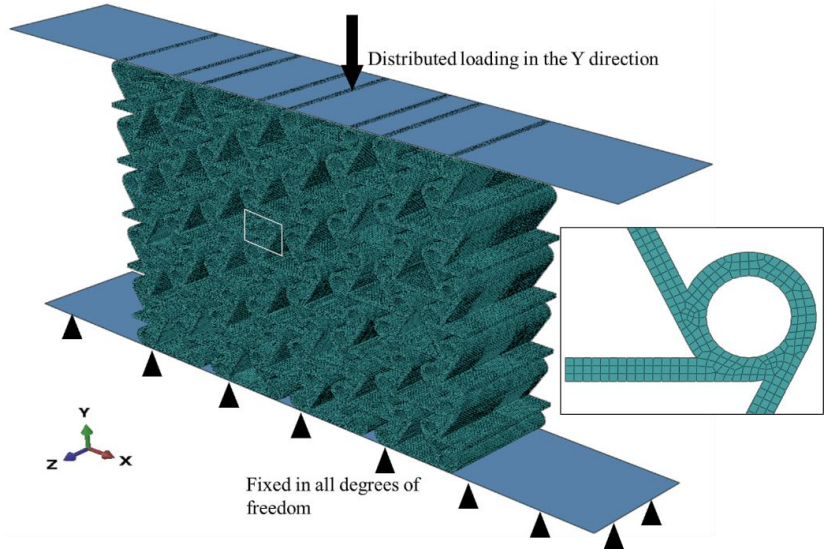

Figure 4.3. Numerical model with boundary conditions for the compression and a local diagram of the finite element mesh. The final element size is chosen to ensure there are at least three elements throughout the thickness.

Six different elements sizes, i.e., 0.8 mm, 0.6 mm, 0.4 mm, 0.35 mm, 0.3 mm and 0.2 mm are used for the convergence study. The force displacement diagram, internal energy to kinetic energy ratio as well as EA are compared. With consideration of computational efficiency and cost, an average size of 0.35 mm is adopted. Even though element size of 0.4 mm is sufficient for EA, there should be at least three elements across the thickness of the ligaments to produce

reliable and satisfactory outcomes [184]. Having less than three elements across the thickness will result in reduction in overall stiffness of the structure. Thus, an element size of 0.35mm is selected for the numerical modelling.

The REAT honeycomb or the control model samples were fabricated through material extrusion 3D printing, which were then subjected to compression tests where the results were used for validation of the FE analysis. The validated FE analysis approach was then used to evaluated newly proposed structures for further investigations. White Acrylonitrile Butadiene Styrene (ABS) polymer was used as base material for fabrication of the samples using Flashforge Dreamer NX. ASTM D-638 Type IV tensile samples were printed as well and the SS curve of the base material is plotted in Figure 4.4 below, exhibiting an approximate elastic-plastic property with Young's modulus of 1900 MPa and yield strength of 30 MPa.

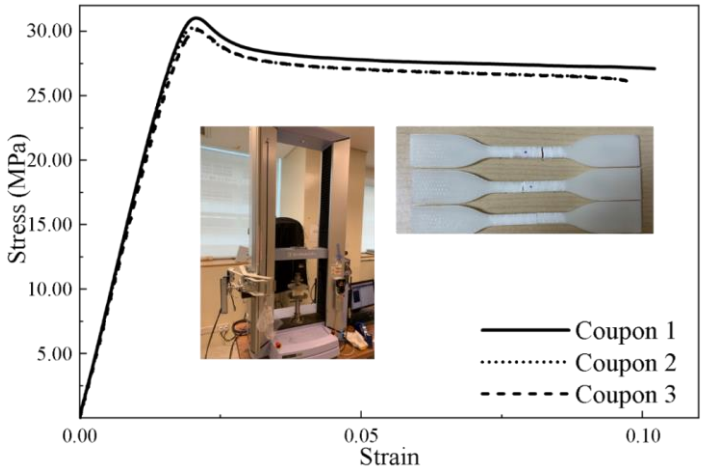

Figure 4.4. SS curve of the base material with insets showing experimental setup and specimen of base materials.

The control model contains three ligaments tangentially connected to each cylinder, namely, the horizontal ligament that is parallel to the *x*-direction and the two inclined ligaments at an angle. Referring to the schematics of cell geometries in Figure 4.1(a), the thickness t of both the ligaments and cylinders is set to be 1.0 mm. The mean diameter of the cylinders is 4.5 mm, cell repeat length L_1 is 22.5 mm and cell repeat width L_2 as 15 mm. w is set as 3.0 mm for

comparison between the proposed structures. The out-of-plane thickness of the honeycomb is 25 mm to prevent out-of-plane buckling.

For the compression test, the honeycomb sample was placed between two rigid plates with the bottom plate fixed and top plate crushing the honeycomb at a loading speed of 1 mm/min or strain rate of 0.0002 s^{-1} in the quasi-static experiment. The SS curve of the honeycomb is shown in Figure 4.6(b) with close similarity to the SS curve obtained by Hu et al. [29].

The compression test was recorded with a digital camera (Canon EOS 800D) and tangential joint areas were marked to monitor the deformation of the structure. The recordings were processed using MATLAB image processing tool, Image Viewer, to measure the variation in the longitudinal strain against the lateral strain.

The SS curve can be compartmentalized into four stages. According to the collapse process shown in Figure 4.6(a1) to (a4), no obvious severe deformation is observed. The ligaments deform elastically with slight flexure in the first stage where the stress increases linearly with strain. Under further compression, the honeycomb proceeds to the second stage as the stress remains fairly constant relative to strain. In this second stage, O′1 and O2 rotates anti-clockwise while O1 and O′2 rotates clockwise. Plastic hinges observed as small kinks on the inclined ligaments are formed at points A, A′, B and B′ shown in Figure 4.6(a2). As the compression advances into the third stage, more plastic hinges are formed at points C, C′, D and D′ in Figure 4.6(a3) as the cylinders come into contact with the horizontal ligaments. At the same time, the cylinders push the horizontal ligaments upwards, causing a rapid increase in stress as compared to strain. Apart from cylinder to ligament interaction before the start of fourth stage, cylinders O2 and its immediate neighbour O′2 also encounter with each other. Fractures were subsequently observed on the cell walls at the fourth stage of the compression as evident from the oscillation in stress with strain.

The SS relationship of the REAT structure from experiment and simulation shows good agreement up to 30% strain in Figure 4.6(b). Beyond which, the deviation is enlarged as the specimen starts to experience fractures in cell walls and delamination. The FEA model is developed under the assumption that the internal structure is fully solid. However, given that the extruder takes on a continuous path in the 3D printing of samples, it is not always possible to fully densify the thin walls especially at the connected regions between the cylinder and the ligaments. Nonetheless, a combination of extrusion width and precision is carefully selected to minimize the voids in the interior as much as possible. Furthermore, there are slight discrepancies between the experiment and simulation results between 15% and 25% strain, which may be attributed to the quasi-orthotropic behaviour of the ABS material [184]. In general, the deformation, SS curve and PR are in good agreement between experiments and simulations as shown in Figure 4.5 and Figure 4.6. Hence, mechanical properties up to 30% strain are taken into consideration for numerical analysis of the new designs.

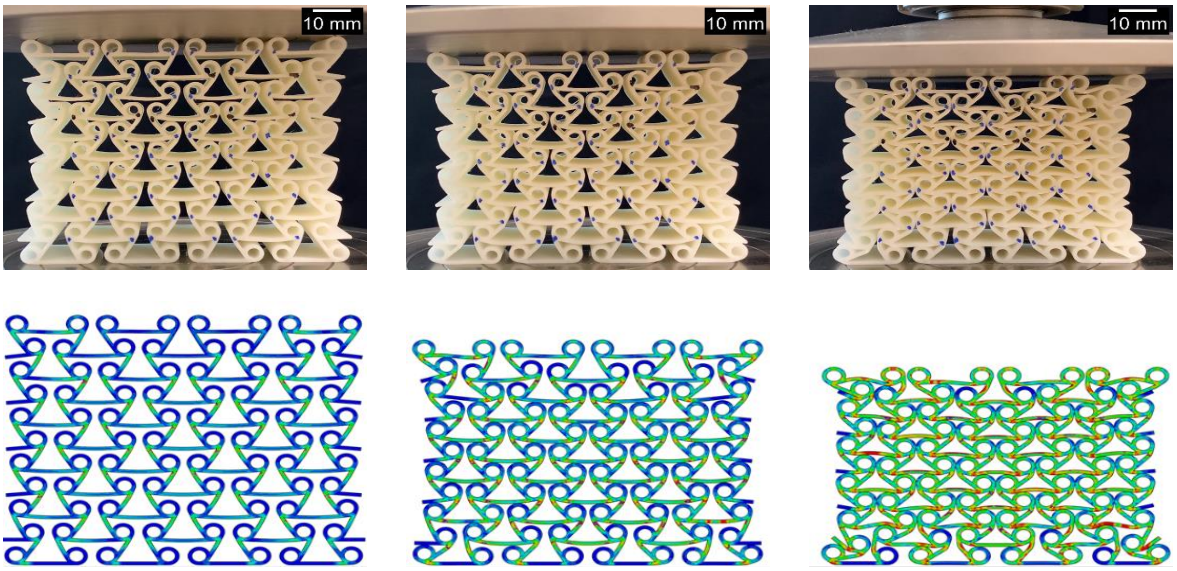

(a1) $\varepsilon = 0.10$ (a2) $\varepsilon = 0.15$ (a3) $\varepsilon = 0.25$

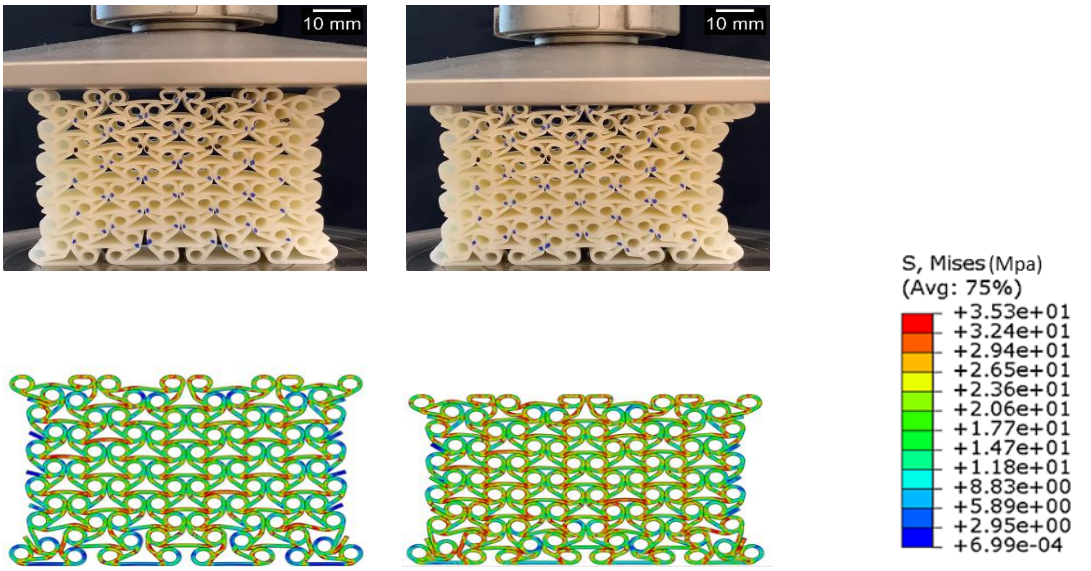

(a4) $\varepsilon = 0.30$ (a5) $\varepsilon = 0.35$

Figure 4.5. (a) Comparison of deformation patterns for REAT honeycomb between experiments (top) and simulations (bottom) up to 35% strain. Since fracture is not considered in the finite element analysis, a comparison between simulation and experiment at 35% strain shows the difference in results where fractures were present along the bottom-most and top-most row of unit cells of the experimental sample.

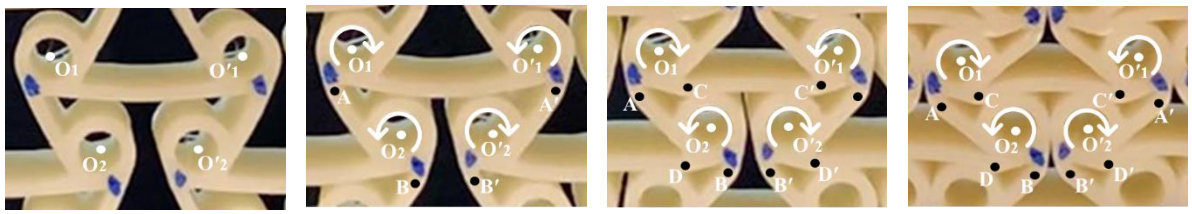

(a1) (a2) (a3) (a4)

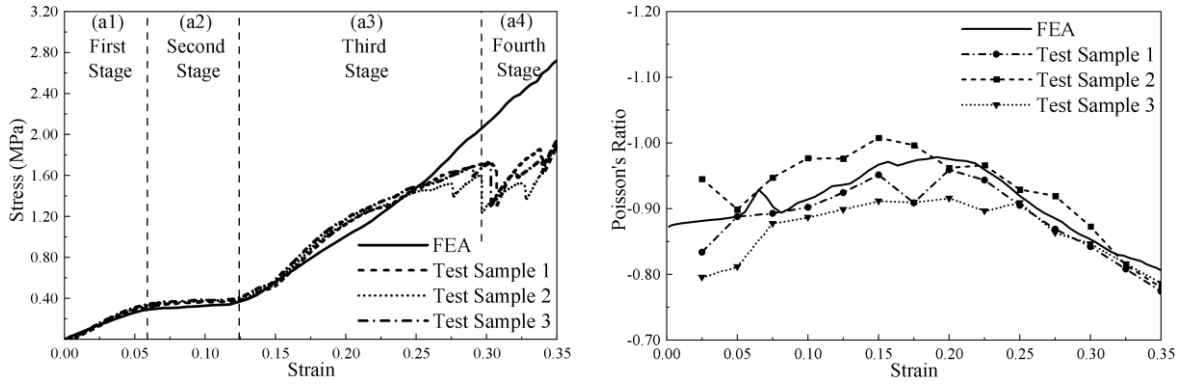

(b) (c)

Figure 4.6. Deformation process of the control model in experiment at various stages (a1) first stage, (a2) second stage, (a3) third stage and (a4) fourth stage. Comparison between experimental and FEA of REAT honeycomb for (b) SS relationship and (c) PR.

4.3 Results and discussions

4.3.1 Single ligament designs

The SS relationship, PR and Young's modulus normalised by RD for the single ligament designs (C, Uc and Dc models) are presented in Figure 4.7 and Table 4.1. All strains used in this discussion is engineering strain. The compartmentalization of the first three stages in the SS relationship (excluding fracture in the fourth stage) for the control model is used as baseline for comparison with Dc and Uc structures. For Dc model presented in Figure 4.7(b), the elastic modulus or the stiffness of the structure in the first stage is significantly lower than that in the control due to curvature in the ligaments. This is also demonstrated by the normalised Young's modulus of the Dc model from Table 2, which is four times lower than that of the control model.

Given the low incident angle θ_{inc} (Figure 4.1(b)) for Dc model, the inclined ligaments are not strong enough to both resist the compressive loading and induce drastic rotations in the cylinders. Little to no plastic deformation is observed in the inclined ligaments till approximately 18% strain. The contact between horizontal ligaments and the cylinders is observed to occur as early as around 5% strain in Dc (shown in deformation pattern of the representative unit cell in Figure 4.7(b)-A) compared to 12% to 13% strain in control as observed in Figure 4.7(a)-B. Upon further compression from 6% to 13% strain, the cylinders of Dc pushed the downward curving horizontal ligaments upwards, producing a deformation dominated by elastic bending that results in the linear increase in stress in Figure 4.7(b). However, the stress increment was reduced slightly between 13% to 17% strain, signifying the formation of energy dissipating plastic hinges as the rate of increase in stress with strain drops temporarily. The brief plateau stress, albeit not considered as a second stage, is caused by the straightening of the horizontal ligaments seen in Figure 4.7(b)-B and the initiation of upward flexing of the horizontal ligaments from the contact interaction with the cylinder in Figure 4.7(b)-C. Overall, the second stage is not present like the rest of the structures, as observed by

the lesser extent of formation of plastic hinges and the absence of plateau stress when compared to the control model. While formation of plastic hinges in the control model happens during the plateau stage, it only occurs during the third stage in Dc.

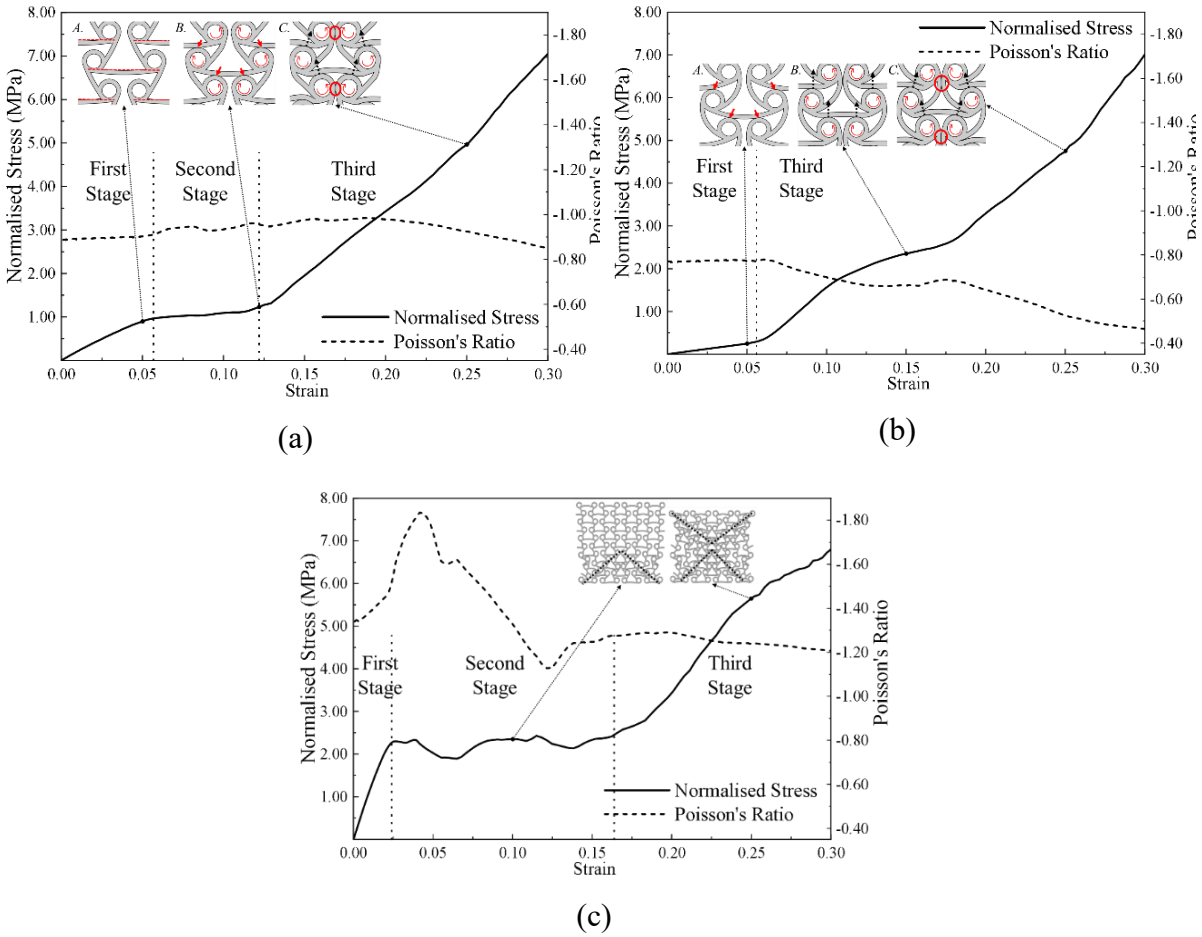

Figure 4.7. (a) FE simulated SS and PR-strain curve of control model. Inset shows simulated deformation pattern of individual cells: Inset A shows elastic flexure of ligaments in the first stage at 5% strain. Inset B shows rotation of cylinders, initiation of contact between cylinders and horizontal ligaments at 12.5% strain at the end of second stage. Solid red arrows indicate the point of contact between ligaments and cylinders. Inset C shows the rotation of cylinders and the upward flexing of horizontal ligaments at 25% strain with dotted black arrows illustrating the interaction between ligaments and cylinders after contact during the third stage. (b) FE simulated SS and PR-strain curve of Dc model. Inset shows simulated deformation patterns of individual cells: Inset A shows initiation of contact between cylinders and horizontal downward curving ligaments as marked by solid red arrows at 5% strain in the first stage. Inset B shows the rotation of cylinders and straightening of horizontal downward curving ligaments due to contact with cylinders at 15% strain with dotted black arrows specifying the interaction between the ligaments and the cylinders. Inset C shows the rotation of cylinders and the upward flexing of horizontal downward curving ligaments demonstrated at 25% strain. Dc structure lacks the second stage due to the absence of plateau stress. Note the difference in contact points between the circled ligament-ligament contact in Dc against control model. (c) FE simulated SS and Poisson's ratio-strain curve of Uc model illustrating the unique deformation within the entire structure at 10% strain in the second stage and 25% strain in the third stage. There is lack of uniformity in deformation unlike control and Dc models.

Conventionally, increase in stiffness of the structure is accompanied by the increase in RD. However, being 9.5% lower in RD than control model, Uc in Figure 4.7(c) exhibits much

greater in-plane stiffness that is six times that of the control model in terms of normalised Young's modulus. The Uc structure is more resistive to loading at the initial stage as its length of ligaments are shorter and incident angles are higher due to tangential attachment accompanied with the direction of curvature counteracting against the compression direction. In contrast to control and Dc models, the second stage for Uc extends significantly by the continual yet sequential formation of plastic hinges throughout the compression process in Figure 4.7(c). The unique deformation mechanism also results in more extensive rotation of cylinders about the plastic hinges.

Figure 4.8(b) illustrates the deformation process of the Dc model, indicating a uniform lateral contraction across the entire structure. On the other hand, for the Uc model, the base of the model contracts first by forming an inverted V (marked by black dotted lines in Figure 4.8(a) at 10% strain) followed by a V shape deformation at the top of the structure (marked by black dotted lines at 15% strain). The demonstrated sequential deformation mechanism initiates at the base, then at the top followed by the middle of the Uc structure, allowing consistent formation of plastic hinges as well as rotation of cylinder around them. This leads to significantly prolonged plateau stage between 2.5% to 17.5% strain. The third stage is also significantly delayed as the distance to contact between the cylinder and horizontal ligaments are larger.

Strain	nil	5%	10%	15%	25%
(a) Uc	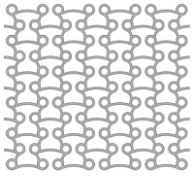	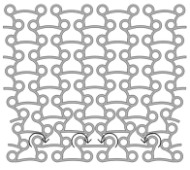	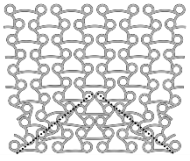	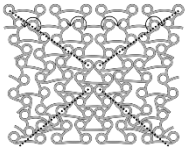	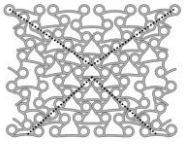

(b) Dc 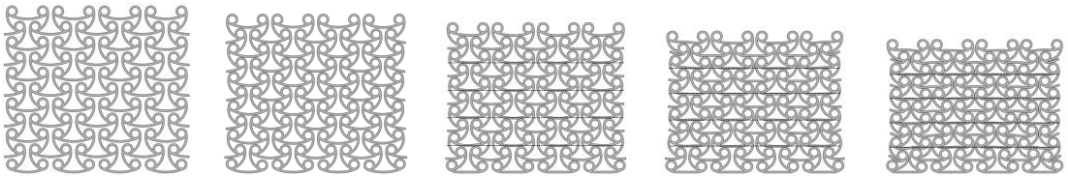

Figure 4.8. Deformation patterns of (a) Uc displaying the formation of inverted V deformation at the bottom of the structure at 10% strain, which is followed by a V deformation at the top of the structure at 15% strain to form a "X" deformation, and (b) Dc models illustrating an uniform deformation throughout the structure at different strains.

The PRs of both control and Dc models in the elastic range (first stage) start off and remain relative constant at about -0.90 and -0.80, respectively. The lower Poisson ratio in the first (elastic) stage of Dc than control is due to the smaller lateral contraction initiated by the lower stiff inclined downward curving ligaments as compared to the straight ligaments. The PR of the control model is relatively stable after the elastic portion with values ranging between -0.80 and -1.00 in Figure 4.7(a). Even though the cylinders begin to come into contact with the ligaments around 12.5 % strain, they are not laterally in contact with each other. Subsequently, the lateral gaps between the neighbouring cylinders are quickly closed off from the interaction with the horizontal ligaments as illustrated from Figure 4.7(a)-B to C, coupled with reduction in inclination angle of inclined ligaments. This allows for a more than proportionate increase in lateral strain as compared to longitudinal strain, leading to the peak of NPR at about 20% strain where cylinders establish lateral contact. On the other hand, the NPR of Dc in Figure 4.7(b) gradually drops throughout the compression process after the elastic range, starting from as early as 5% strain when the horizontal ligaments are in contact with the cylinders as a result of interaction between the downward curving horizontal ligaments and its immediate cylinders below in Figure 4.7(b)-A. The downward curvature of the horizontal ligament restricts the cylinders from laterally coming into contact with each other together with the limitation of the rotation of cylinders by the flexure in the middle of the inclined ligaments, thus leading to a smaller NPR than control model. It is also noted that the inclined ligaments in Dc are in contact with each other instead of the cylinders shown in Figure 4.7(b)-C.

Unlike control and Dc, a drastic range of NPR is observed for Uc in Figure 4.7(c). The NPR for Uc increases linearly in the first elastic stage and then peaks at a maximum NPR of -1.80 at 5% before exhibiting a non-linear behaviour in the second stage and dropping to -1.20 at the end of compression. The large and increasing NPR in the first elastic stage for Uc is attributed to the straightening of horizontal ligaments during the first stage coupled with the direction of curvature in the inclined ligaments which elicit a more drastic inward collapse of the structure facilitated by the rotation of the cylinders. The straightening of ligaments first started at the bottom of the structure, caused by the rotation of cylinders similar in direction to the cylinders in control and Dc as illustrated by the arrows in Uc at 5% strain in Figure 4.8(a). This deformation behaviour is not observed in Dc as the straightening of horizontal ligaments are only induced by the contact with cylinders.

Table 4.2. The normalised Young's modulus obtained for each design. The lowest normalised Young's modulus being Dc and the highest Dc+Uc. Uc achieved major improvement in Young's modulus of up to six times when compared with control model. Double ligaments generally produce higher normalised Young's modulus than their single ligaments counterparts.

Configuration	Control	Uc	Dc	Dc+C	Uc+C	Dc+Uc
Normalised Young's Modulus	19.3	114.2	4.98	34.1	157.5	162.1

4.3.2 Double ligaments

The SS and PR curves of the double ligament designs are illustrated in Figure 4.9 and Figure 4.10(b). The overall normalised elastic modulus of the double ligament structures is higher than the single ligaments except for Dc+C which is lower than Uc as shown in Tables 2 and 4. Dc+C exhibits similar trends as Dc where the contact between the horizontal ligaments and the cylinders are brought forward earlier as observed from the continuous increase in stress with strain in Figure 4.9(a). Dc+C model could not reproduce a SS curve with plateau stress but nevertheless the elastic modulus is higher than control model, which means there is

reinforcement to some extent. The lack of plateau stress in Dc+C is due to the short distance between horizontal ligaments and cylinders, as well as the double ligament design that doubles the thickness of connecting ligaments between cylinders. The gap between the straight and downward curved ligaments are small, which are closed quickly without any plastic deformation. Unlike Dc, the stress for Dc+C increases relatively linearly with strain after 7% strain. This is because the now thicker horizontal ligaments in Dc+C are harder to bend as well as the earlier third stage caused by increase in RD.

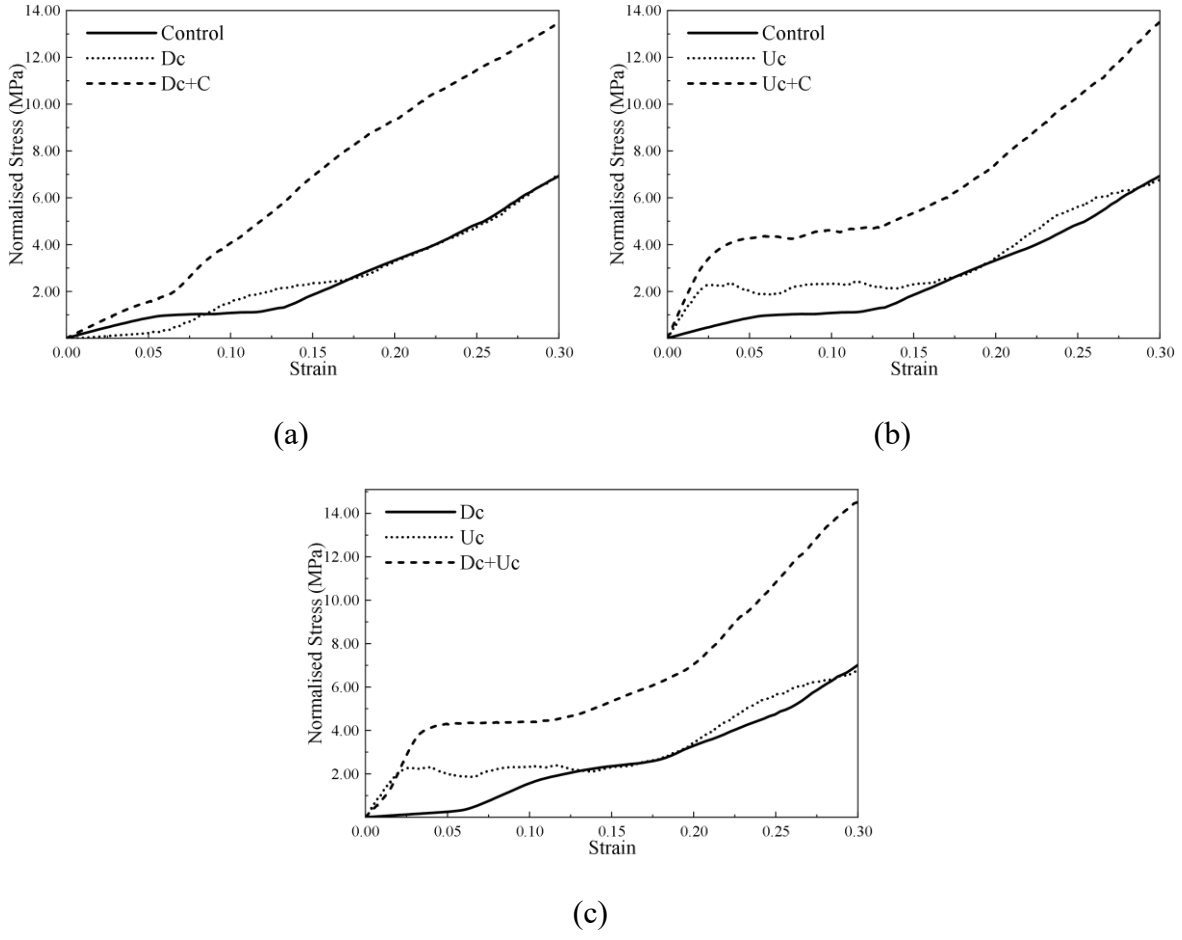

Figure 4.9. FE simulated SS curve of double-ligaments designs (a) Dc+C, (b) Uc+C and (c) Dc+Uc with their respective constituent single-ligament designs. All of the double-ligaments designs show some extent of reinforcement to the structure in terms of higher Young's modulus and crushing strength with increase in RD.

The combination of control and upward curvature ligaments in Uc+C generates SS curve of similar trends to Uc but at a higher elastic modulus and crushing strength in Figure 4.9(b). This

is due to the higher RD of the structure at the expense of reduction in length of plateau stage, which significantly impacts on the overall EA capability of the structure.

Finally, the elastic modulus of Dc+Uc design is higher than Uc design in Figure 4.9(c), proving the reinforcement of structure even if Dc ligaments with low stiffness are integrated. The presence of plateau stress implies that the structure is mainly driven by Uc ligaments due to its significantly higher elastic modulus than that of Dc. With reference to Figure 4.9(c), the crushing strength of Dc+UC is twice as much as that of Uc but at the cost of shorter plateau stage due to increased RD.

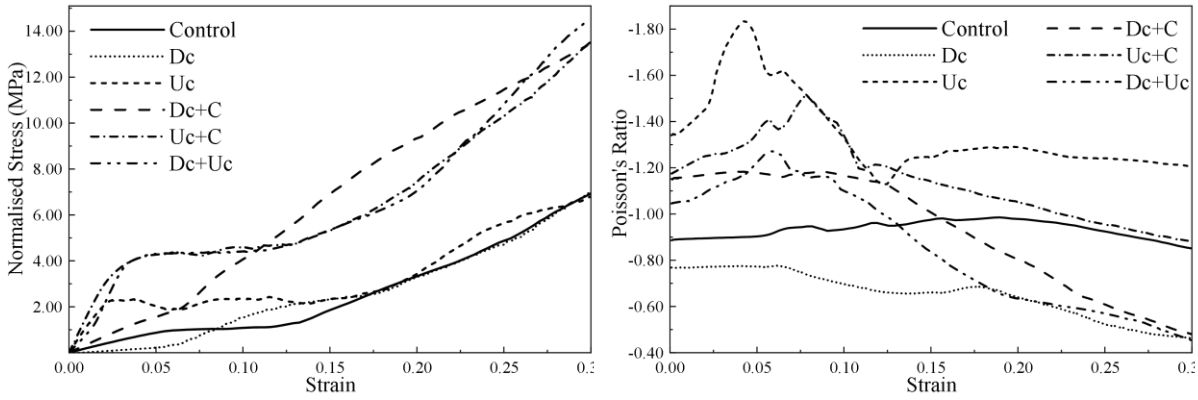

(a) (b)

Figure 4.10. (a) Combined normalised SS in which all of the double ligament designs except Dc+C exhibit larger crushing strength when compared to single ligament designs and (b) NPR-strain curve of both single and double ligament designs. Double ligament designs containing Uc as its constituent displayed characteristic of peak NPR, which implies that Uc ligaments play a significant role in determining the NPR of a structure.

In terms of NPR in Figure 4.10(b), all double ligament designs except Dc+C, which does not possess the Uc design, show linearly increasing NPR in the elastic stage. Taken into consideration of the NPR both in and outside the first (elastic) stage, it is ascertained that Uc ligaments play a significant role in influencing the NPR of the structure throughout the compression process.

Dc+C exhibits a higher starting NPR than Dc as the inclined ligaments are now more resistive to bending. This produces more horizontal tangential force that allows greater lateral contraction in the structure. As the effect generated by the stiffened inclined ligaments is

prolonged, Dc+C is also able to sustain a constant NPR after entry into the third stage at 5% strain. Furthermore, it experiences a much more drastic drop in NPR caused by the increase in RD and reduction in void spaces after entry into the third stage.

The trend of NPR in Dc+Uc resembles closely to that of Uc. This can be observed by the sharp increase in NPR and the momentary peak present in both Uc and Dc+Uc structures. Separately, the peak NPR of Dc+Uc is also lower than Uc due to the increased RD. The drop of NPR after the peak is drastically different in magnitude which can be explained by the difference in deformation mechanism and the way the NPR is calculated. As the lateral contraction is calculated based on the average between top and bottom width, the results are deemed fairly accurate for structures that contract uniformly which is the case for Dc+Uc. However, this is not the case for Uc where the deformation is observed to be sequential. If x_{i1} and x_{i2} from Figure 4.2 are to be plotted with global strain, we will see a rapid decrease in x_{i2} first followed by x_{i1}.

The deformation pattern of Uc+C bears resemblance to that of Uc but the sequence of deformation is different. For Uc, the deformation initiates with an inverted "V" at the bottom half while Dc+C initiates with a "V" at the top half at 10% strain. Subsequently at 15% strain, an inverted "V" deformation is formed at the bottom half of Uc+C, producing a "X" shaped deformation. Based on the NPR plotted against global strain in Figure 4.10(b), Uc+C is able to sustain an extended strain of large NPR and less drastic reduction in NPR across the compression process.

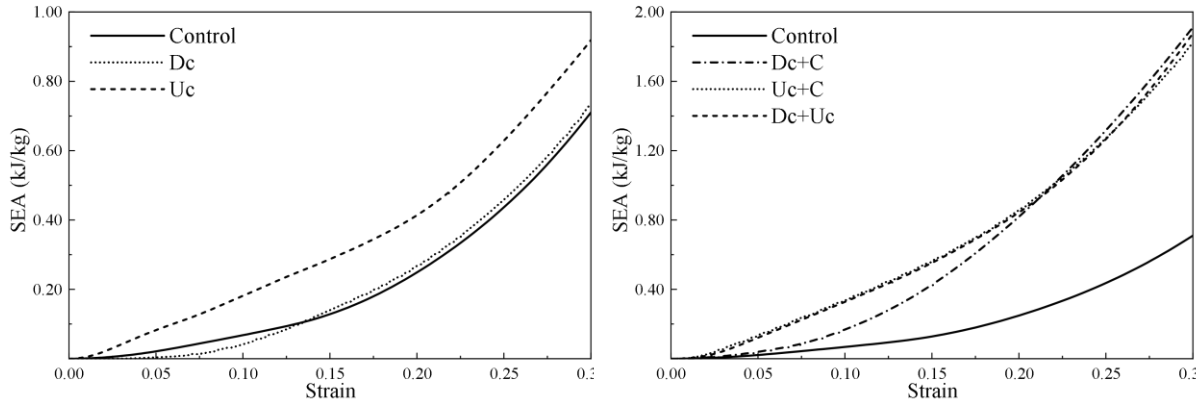

(a) (b)

Figure 4.11. (a) SEA-strain curves of the single ligament designs of which Uc not only has better overall SEA throughout the compression strain but also in the early stage of compression at lower strain. In contrast to Uc, both control and Dc have exponential increase in SEA which is lesser at the early strain and larger in the later strain. (b) SEA-strain curves of the double ligament designs where Dc+C shows similar SEA characteristic as control and Dc, while Dc+Uc and Uc+C both exhibits almost identical SEA.

The SEA of each structure against global strain is illustrated in Figure 4.11. Among the single ligament designs, Uc outperforms both the control and Dc models in SEA across the entire compression process. Furthermore, Uc demonstrates consistent EA as observed by its linear increment in EA based on the area under SS curve of Figure 4.11(a). When compared to Uc, control and Dc models are only able to achieve excellent EA capabilities after their entry into the third stage at about 12.5% and 5.5% strain, respectively, which is shown by the gradual increase in gradient of SEA curve with strain.

Among the double ligaments in Figure 4.11(b), despite Dc+C having similar SEA with Uc+C and Dc+Uc after 20% strain, its SEA is substantially lower before the 20% strain. This is attributed to the lower stiffness of the structure and the lack of second stage leading to a slow increase in SEA at the early stages of the compression followed by an increase in SEA at a much higher rate afterwards. Both Dc+Uc and Uc+C consisting of upward curvature ligaments show better performance in SEA capabilities throughout the compression as compared to the rest of the designs. Despite both Dc+Uc and Uc+C seemed to have relatively identical SEA through the entire compression process, the attributes to their SEA performance are vastly different. The performance in Uc+C mainly stems from the stiffening of the thickened

ligaments, whereas the performance of Dc+Uc arises from the petal-like cell (highlighted in Figure 4.1(e) formed by upward and downward curvature ligaments) flattening to induce more plastic deformation in the individual inclined circular arc ligaments.

4.3.3 Parametric study on Dc+Uc Design

In this section, parametric studies on the stiffness, plateau stress and SEA are carried out based on modifications to the design of Dc+Uc. Two separate parametric studies are conducted by varying the width *w* from 1 mm to 3 mm while keeping the diameter of the cylinders constant at 4.5 mm, and varying the diameter of cylinders from 1 mm to 4 mm while keeping the width constant at 3 mm. Due to the thickness of the ligament, the upper and lower ligaments are merged together at the width of 0.5 mm and 1 mm, and the structure becomes the control model when the width is reduced to zero. The geometric configuration of the unit cells involved in the parametric studies are listed in Table 3.

4.3.3.1 Variation in width

As shown in Table 4 and Figure 4.12(a), the in-plane stiffness, crushing strength and plateau stress generally increases with width. While the increase in crushing strength stems from the shortening of the Uc inclined ligaments as width is increased, the extension of plateau stress is the result of increased length of downward curvature ligaments which allows for more plastic deformation.

From the control model with no width to width of 3 mm, the curve for NPR in Figure 4.12(b) gradually switches from a relative stable NPR into possessing distinct peaks. These peaks also occurs earlier at around 6% strain for Dc+Uc 3 mm width as compared to occuring at 20% strain for the control model. Among the three structures with merged ligaments (width 0 mm to 1 mm), the NPR across the entire global strain generally increases with the overall stiffness of the structure due to the thickening of the ligaments. In the case of width between 1.5 mm

and 2.5 mm where the ligaments began to form petal-like cells, the peak NPR remains relatively constant but the global strain at which the maximum NPR is reached drops. The magnitude of peak NPR increases with width from 0 to 2 mm before decreasing from widths larger than 2 mm. The rate of decrease of NPR from the peak remained the same for widths above 2 mm.

Table 4.3. Geometric configurations of unit cells in the parametric studies conducted.

Variation in width keeping diameter constant		
w = 0.5	w = 1.0	w = 1.5
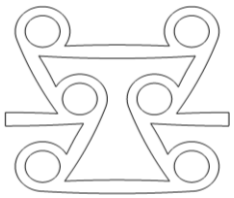		
w = 2.0	w = 2.5	w = 3.0 (baseline)
		
Variation in diameter keeping width constant		
D = 1.0	D = 2.0	D = 2.5
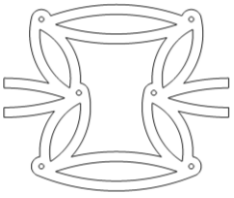	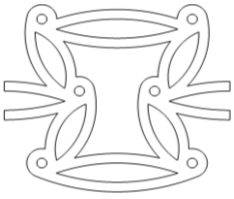	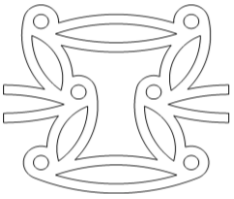
D = 3.0	D = 4.0	D = 4.5 (baseline)
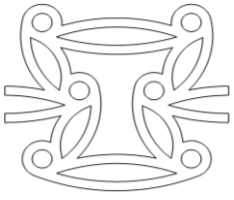	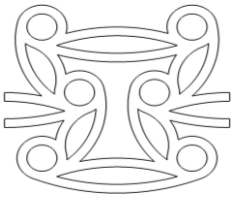	

Furthermore, approximately quadruple of SEA in control is observed as upward and downward curvature ligaments begin to form petal-like cells. Even when the ligaments are merged together at the width of 0.5 mm and 1 mm, the SEA doubles and triples that of the control model, respectively, due to increase in RD in Figure 4.12(c). Even though thickened ligaments prove to be a good way to increase SEA ability of the structure, they still do not possess decent SEA during the early stages of the compression. Comparing among structures with merged ligaments from 0 to 1 mm, a gradual increase in SEA at the early stage of the strain can be observed (elastic and plateau stage) in Figure 4.12(c). It is more evident when comparing Dc+Uc of width 1 mm with structures of larger width in which the rate of increase in SEA is higher at higher global strain but the lower at the smaller global strain. This explains the lack of decent EA capacity in the early stage as compared to the later stages of compression.

In addition, it can be observed from Figure 4.12(c) that the merged structure of width 1 mm has close similarity in the change of SEA with the split structure of width 1.5 mm. As width is increased, 1.5 mm is the first structure starting with split ligaments and possesses the longest upward curvature ligaments, resulting in lowest stiffness as compared to structures of higher width. Nevertheless, the elastic modulus of the structure of width 1.5 mm is larger than width 1 mm due to the emergence of upward curvature ligaments as well as the widening of the joint area. The plateau stress is also in close similarity due to the fact that the width is small enough that the separation is located more towards the middle of the ligaments such that the attachment area remains thickened. It is possible to assume that ligaments of 1.5 mm width are considered merged as the plastic hinges are mainly formed close to the attachment between ligaments and cylinders. The rate of increase in stress with strain during the third stage is higher in structures of width 1.5 mm due to the full-wave deformation mode in upward curvature ligaments, indicating a stronger EA closer to the third stage. For width larger than 1.5 mm, the slope for

SEA is also more constant for high strain rates as a result of the flattening and contraction of petal-like cells allowing for formation of more plastic hinges and hence better SEA.

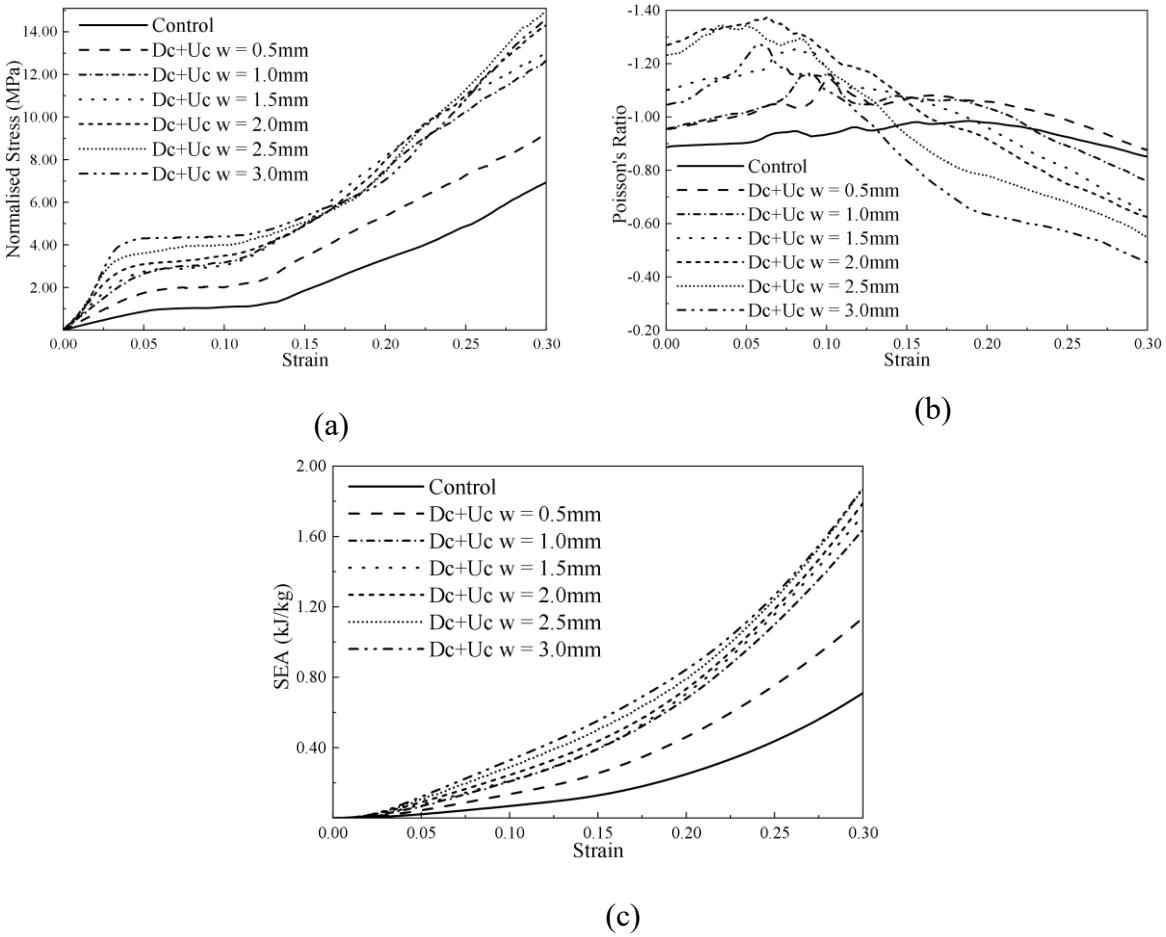

Figure 4.12. (a) SS which shows both increase in normalized Young's modulus (Table 4) and crushing strength. A further increase in length of plateau stress with width due to participation of more plastic deformation. (b) NPR-strain displaying an immediate transition from a stable NPR to one with distinct peaks. The peak value increases for width of 0.5 mm to 2 mm, which then decreases after 2 mm. A general increase in SEA can also be observed in (c) based on parametric studies of the width in Dc+Uc designs.

4.3.3.2 Variation in diameter

The SS curve, NPR and SEA for variation in diameter are shown in Figure 4.14. The elastic modulus of the structure is generally increased with increasing diameter, due to shortening of Uc inclined ligaments with larger diameter thus enhancing the overall stiffness of the structure. The normalized Young's modulus remained constant when the diameter increases from 4 mm to 4.5 mm, which may be due to the loss of rigidity in cylinders as they get larger. The plateau

stage is significantly lengthened with the reduction in diameter given that more space will be left for compression for more plastic and severe deformation to take place before the third stage. Furthermore, there is a transition of deformation mode with the change in diameter. At diameter of 1 mm, the structure, in the midst of its deformation, exhibits a "X" deformation in the middle of the structure at 15% strain in Figure 4.13(a). However, with reference to the same figure, the deformation differs drastically when diameter becomes 2 mm where a "V" shaped deformation is first formed at the top of the structure. Further compression produces an inverted "V" shaped deformation stacked on top of each other near the bottom of the structure as marked, which is in close similarity to deformation pattern found in Uc. In addition, the manner in which the cylinders and ligaments fold upon each other in the middle as they densify to fill the empty voids as compared to pure lateral cylinder-to-cylinder contact, elucidates the difference in length of the plateau stage. This effect becomes less prominent with increase in diameter as evident from reduction in the plateau stage in Figure 4.14(a). When diameter is at 3.0 mm, the structure is observed to deform uniformly in Figure 4.13(c). This is similar to what is observed in the deformation process of Dc in Figure 4.8(b) given the now shorter upward curvature ligaments that raised the overall stiffness of the structure.

Table 4.4. Summary the relative densities and normalized Young's modulus of the designs in the parametric study on width and diameter. For both variations, the normalised Young's modulus generally increase with increase in RD except for variation in width between 2.0mm and 3.0mm where RD remains almost constant while normalised Young's modulus increases.

	Variation in width keeping diameter constant					
Design	$w = 0.5$	$w = 1.0$	$w = 1.5$	$w = 2.0$	$w = 2.5$	$w = 3.0$
Relative Density	0.360	0.416	0.438	0.445	0.447	0.445
Normalized Young's modulus	38.35	60.95	68.41	90.30	113.15	162.14
	Variation in diameter keeping width constant					
Design	$D = 1.0$	$D = 2.0$	$D = 3.0$	$D = 4.0$	$D = 4.5$	
Relative Density	0.346	0.374	0.401	0.430	0.445	

Normalized Young's modulus	97.87	121.76	149.41	163.20	162.14

A variety of NPR is also observed with the change in diameter of the cylinders in Figure 4.14(b). Diameter between 1 mm and 3 mm shows NPR peaks of decreasing magnitude with increasing diameter. It is observed that the cylinders with diameter above 3 mm come into contact laterally with each other at earlier strain as compared to those with diameter of 1 mm and 2 mm. The structure also loses its distinct peak NPR when diameter is increased from 3 mm to 4 mm given the fact that the larger cylinders come into contact with the horizontal ligaments earlier at 14.5% strain as compared to 32% strain in smaller ones. As such, larger cylinders leave lesser room for the first two stages implying that the peak NPR is dependent on the lateral distance between the two cylinders. This explains that the structure with diameter of both 1 mm and 2 mm are able to achieve a much higher and distinct maximum NPR peak, which produces an obvious effect of folding cylinders and inclined ligaments folding on top of each other. The NPR peaks can be further explained by the neat and compact densification in structures of smaller diameters (Figure 4.13(a) and (b)) in contrast to structures of larger diameters (Figure 4.13(c)).

Lastly, the load bearing capacity of the structure increases with diameter due to the shortening of Uc inclined ligaments as diameter becomes larger in Figure 4.14(c). The increase in SEA with diameter in the early stage is minimal given the slight increase in elastic modulus of the structure. However, as the entry into the third stage becomes earlier with increasing diameter, the difference in SEA widened with further compression.

Given the existing parametric studies, it may be difficult to truly pinpoint an optimal structure owing to the numerous mechanical properties taken into consideration. For instance, to achieve a structure with long plateau stage and high Young's modulus, the structure may be equipped with smaller diameter and larger width. While larger plateau stage is often accompanied by

high EA, smaller diameter may compromise the absorption capability due to its lower crushing strength. Therefore, due to the immense number of offsetting factors, multi-objective optimization method such as the particle swarm optimization algorithm [185] can be utilized as further work to obtain an optimal structure.

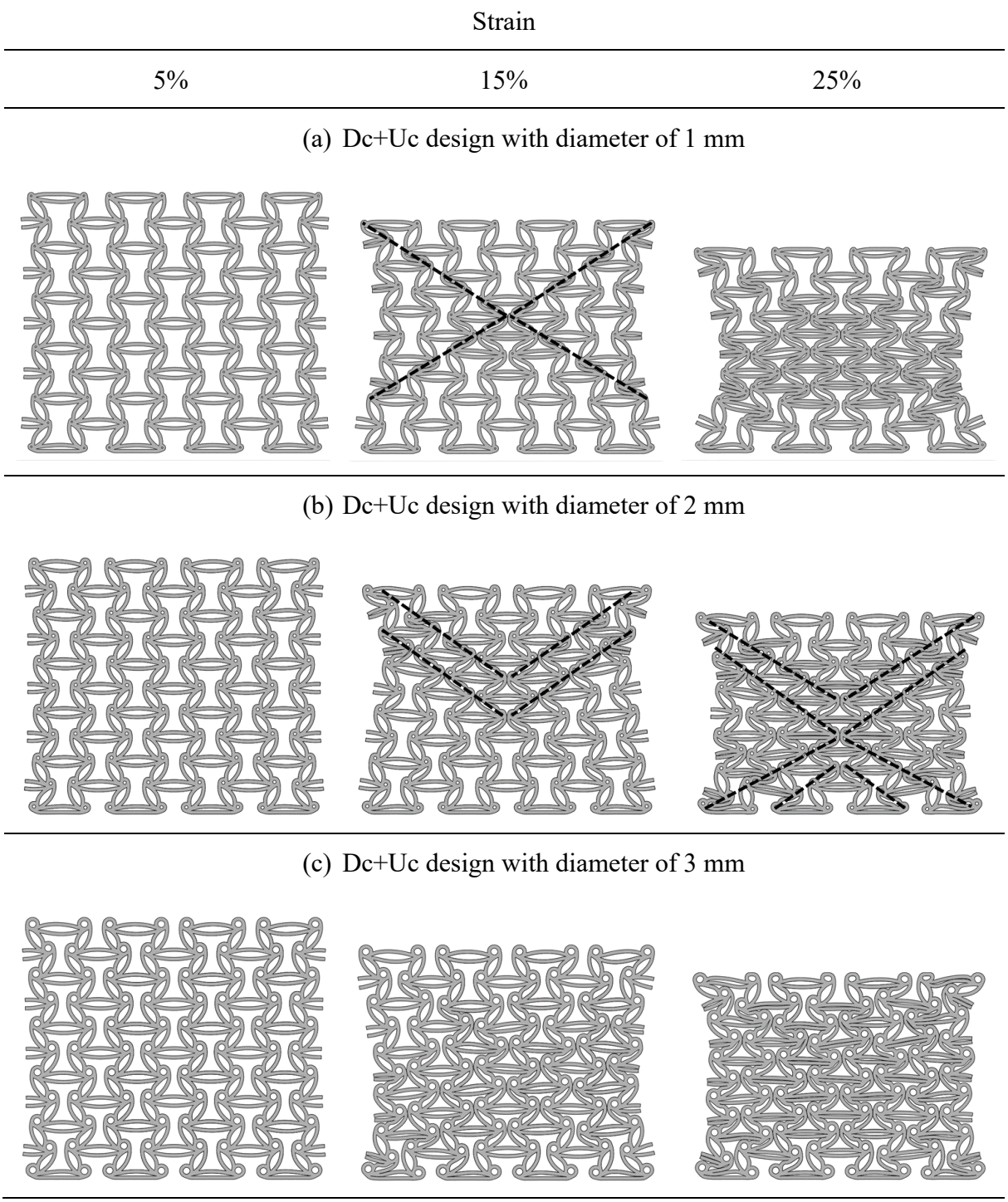

Figure 4.13. The deformation process of Dc+Uc design with diameter of (a) 1 mm, (b) 2 mm and (c) 3 mm at 5 %, 15 % and 25% strain. (a) The illustration of the formation of "X" deformation pattern marked by dotted line in

Dc+Uc design for diameter of 1 mm at 15% strain. (b) The entire transformation towards sequential double "V" at the top of the structure at 15% strain, followed by double inverted "V" formation at the bottom at 25% strain in Dc+Uc design for diameter of 2mm. (c) A relatively uniform deformation in design with diameter of 3mm as depicted by the uniform leftover porosity in each unit cell at 25% strain.

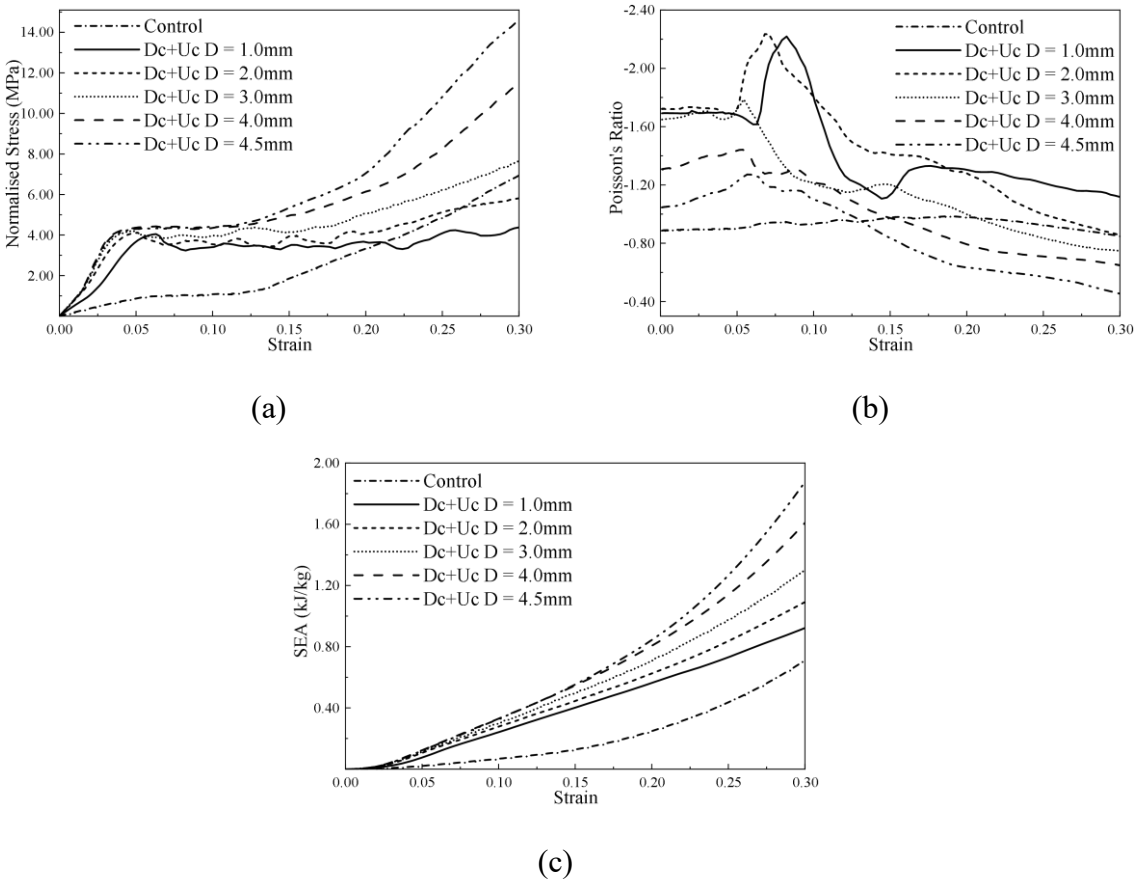

Figure 4.14. (a) Effect of diameter on SS curve with distinct shortening of plateau stage with increase in diameter due to the reduction in area of deformable porosity. (b) Effect of diameter on NPR-strain curve showing a sudden appearance of large NPR peak with small diameters. The NPR peaks gradually lose its distinctiveness, and the peak values decrease with larger diameters (c) Effect of diameter on SEA-strain curve revealing the stable increase in SEA in early strains but increasingly larger deviation in SEA with diameter.

4.4 Conclusion

By introducing arcs into ligaments of REAT honeycombs, five novel designs are conceptualised that exhibit significant improvements in mechanical properties including in-plane stiffness, SEA and plateau stress. In the single ligament designs, the geometrical arrangement of having upward curvature of ligaments (Uc), at a lower density, performs better than both the control and downward curvature of ligaments (Dc). Uc also exhibits unique deformation pattern together with a larger NPR range. In the double ligament designs, higher in-plane moduli and plateau stress are observed against conventional REAT honeycombs. In

particular, Dc+Uc can achieve approximately eight times the in-plane stiffness of the control model. Furthermore, the double ligament structure exhibits better SEA capabilities especially during the elastic and plateau stages. It is found that Dc+Uc has approximately four times more SEA than control model across the entire compression process.

Two parametric studies on varying the curvature of ligaments and cylinder diameter of the unit cells on Dc+Uc are carried out. It is observed that increasing diameter reduces the length of plateau stress while increasing width exhibit an opposing effect of increasing the length of plateau stress. Increasing width contributes to the increase in normalised Young's modulus of the structure due to shortening of Uc ligaments. Similarly, increasing diameter produces the same effect but only up to a certain limit as larger cylinder leads to loss of rigidity. In addition, variations of both parameters generate a wide range of PR with more prominent range observed for the change in the diameter of the cylinders.

Given the significant influence of geometrical parameters, an optimal combination of diameter and width can generate a structure that possesses high elastic modulus, extended plateau stage and high SEA especially in the early stages of strain. However, due to the presence of opposing effects between the parameters, further research will entail the use of optimization algorithm to generate an optimal structure. The present study sheds light on the development of novel REAT honeycombs that can be achieved through simple ligament modifications.

Chapter 5 Bio-inspired Gradient distribution approach on REAT structure

In this section, study on REAT has been extended to focus on the nature-inspired gradient-based approach to re-designing REAT honeycombs through extensive experimental quasi-static compression. Novel perspectives on REAT honeycomb are offered through the introduction of gradient distributions on two critical geometrical parameters, the cylindrical diameter (chiral) and height of the unit cell, rather than the traditional thickness-based gradient approach. Chiral-based gradient approach demonstrated clear advantages in elastic stiffness, SEA and densification strain over uniform REAT structures of constant geometrical parameters. These advantages are exhibited in their extended and constantly increasing quasi-plateau stage, consistent SEA especially during early stages of compression, and most importantly, the ability to maintain a relatively constant EA efficiency that is 25% more than that of the Base uniform REAT structure. Height gradient-based REAT structures, on the other hand, were able to leverage on associations between the NPR effect and height of unit cell to demonstrate notable deformation patterns across various portions of the structure. The present work reveals the performance enhancements through alternative gradient-based approaches over thickness-based gradient approaches and highlighted the differences in NPR between layers as the main driver of compressive collapse apart from the commonly concluded difference in RD.

5.1 Methodology

5.1.1 Design Strategy

This study presents the concept of graded REAT lattice structures, taking inspiration from the gradient distribution of vascular and tubular density observed in bamboo stems and horse hooves, as depicted in Figure 5.1(a) and (b), respectively. The radial dimensions of vascular density in bamboo stem bears significant resemblance to cylinders in a REAT unit cell shown

in Figure 5.1(b), which can also be discerned in the horse hoof. This inspires the introduction of unit cells of various cylindrical sizes assembled end-to-end in multicellular columns through tangential attachments between cylinders and inclined ligaments in which a fully graded REAT lattice structure is then formed by periodically arranging the multicellular columns in lengthwise direction. Furthermore, the gradient distribution in bamboo stem shown in Figure 5.1(a) may be evaluated as gradient distribution in distance between each layer of vascular or tubular density which could be applied to the height of unit cells.

REAT unit cells are typically defined by several parameters as shown in Figure 5.1(c). Key parameters include chiral radius r, cell wall thickness t, ligament length L_1 and L_2, and the resulting layer height h. In this study, REAT unit cells are assembled into a 6x8 layered honeycomb as shown in Figure 5.1(d). The honeycomb has an out-of-plane depth of 25mm, global height H of 75.8mm, and width W of 144mm. The global height may vary slightly in chiral-graded REAT structures, which are listed in Table A-1. By varying the parameters of chiral radius and unit layer height, graded REAT structures can be attained. A more detailed characterization of each design is documented in Table A-1 of the Appendix.

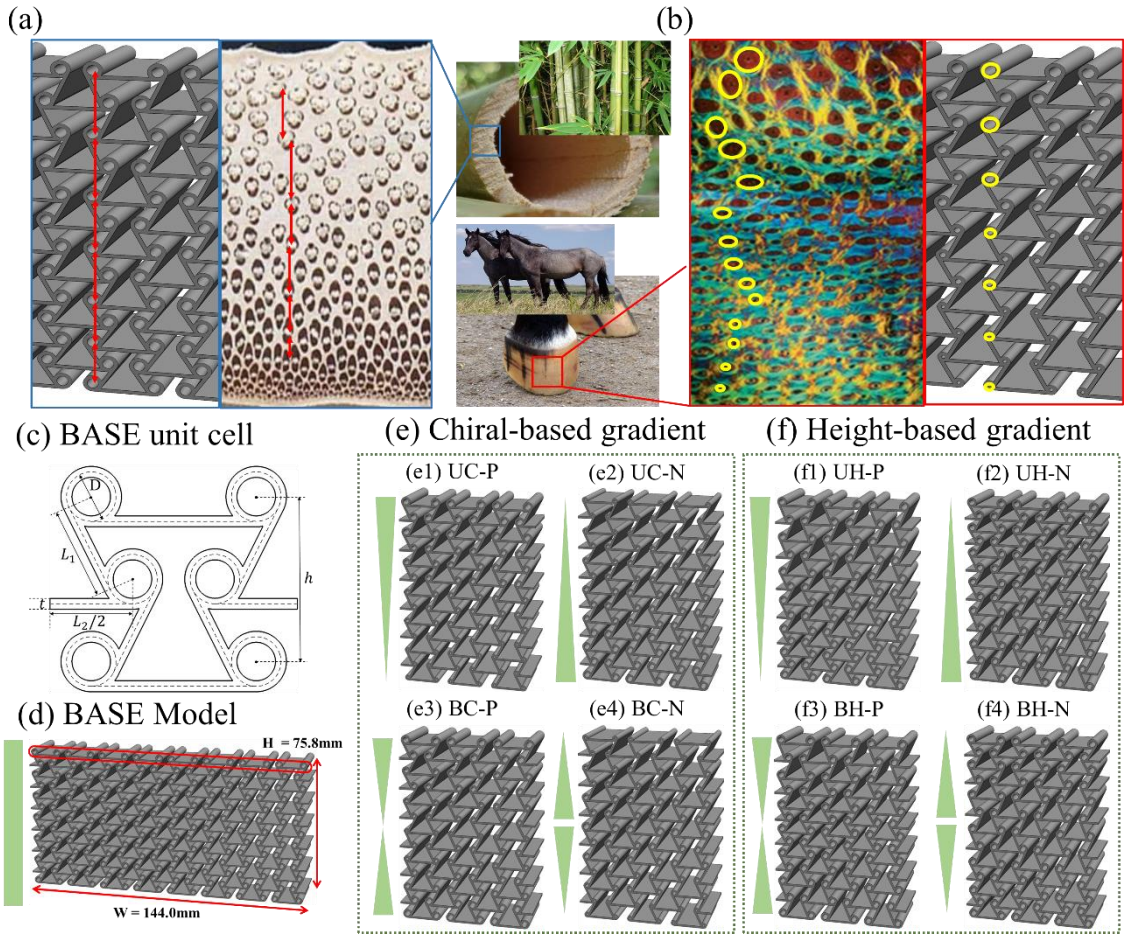

Figure 5.1. (a) Graded distribution of vascular bundle density in bamboo stem, increasing from interior to outer periphery[90] inspiring height-based graded design in REAT structure. (b) Increased tubular density from inner-to-outer direction in horse hoof thickness[51] which inspired the generation of graded distribution in size of cylinders in REAT structure. (c) Illustration of REAT unit cell with its geometrical parameters and (d) visualization of Base model with uniform distribution. One chiral layer is represented by red rectangle. (e) Gradient-based cylinder diameter approach in REAT structure: (e1) UC-P and (e2) UC-N - unidirectional, diameter change every three chiral layers where one chiral layer is a row of cylinders marked by red square in (d); (e3) BC-P and (e4) BC-N - bidirectional, diameter change every two chiral layers, varying from middle layer to both ends. Diameter changes in 0.5mm increments. (f) Gradient-based height variations in REAT structures: (f1) UH-P and (f2) UH-N - unidirectional, height change every unit cell layer from distal to proximal ends; (f3) BH-P and (f4) BH-N - bidirectional, height change every unit cell layer, increasing and decreasing from center two-unit cells. Height changes in 1.0mm increments.

Two types of graded REAT structures are proposed in this present study, namely gradient in diameter *D* and height *h*. Furthermore, two main gradient directions are incorporated: (1) unidirectional and (2) bidirectional gradient. The naming conventions for increasing and decreasing gradients or positive and negative gradients, respectively, are referenced from the layer at the distal end towards the proximal end for unidirectionally graded structures. The direction of gradient can be recognized by the green symbols to the left of each lattice shown

in Figure 5.1(d), (e) and (f). Therefore, given the naming convention, UC-P is expressed as Unidirectional graded Chiral with a Positive gradient whereas BC-P is Bidirectional graded Chiral with a Positive gradient. For bidirectional graded structures, positive and negative gradients are referenced symmetrically from the centre layer. Thus, bidirectionally graded structure with the largest cylindrical diameter and smallest cylinders towards the end of the lattice (Figure 5.1(e4)) is expressed as BC-N with a negative gradient. Then, BC-P with positive gradient will define a graded lattice with smallest cylinder in the middle and increasing cylinder sizes towards either end of the structure shown in Figure 5.1(e3). The naming conventions for graded chiral structure are identical for graded height REAT structures which are separately detailed in Figure 5.1(f).

5.1.2 Fabrication and Other Mechanical responses

In this study, the material selected for the analysis of REAT and its graded honeycomb structures is RGD-8530DM with elastic module of approximately 780 MPa with a density of 1.1 kg/mm^3, a mixture of two standard digital materials VeroWhite Plus and TangoPlus. The mixture is realised by multi-material capability of Stratasys Objet350 Connex3 Polyjet 3D printer. RGD-8530DM is chosen over the individual constituent standard materials because the combination will allow the RGD-8530DM to not only have higher stiffness over the soft TangoPlus but also greater fracture toughness over rigid VeroWhite Plus. Polyjet is a 3D printing technology that uses jetting heads to spray small droplets of photopolymer in layers that are instantly cured by ultraviolet lamps. The multi-jet printing technology is capable of printing resolutions between 16 to 50 μm which highly favours the demand for high dimensional accuracy[186], preventing inaccuracies of physical experimental validation due to unnecessary instability or premature fracture in any part of the honeycomb structure during quasi-static compression.

To ensure consistent results, all nine specimens were printed in one go and in three batches with the same cartridge, print time and post-processing. After printing, the specimens were left at room temperature to dry before the compression tests. The experimental setup is shown in Figure 5.2(a) and (b). Experiments on each design were repeated with three similar specimens and the results were shown to be consistent and documented in Figure A-1 to Figure A-9 in the Appendix. An average performance was taken from each design and then used for comparison. All design samples showed consistency except in Figure A-8 where slight discrepancy was observed between specimens due to instability in the middle layer with poor NPR. Furthermore, corresponding simulation setup, material characterization and experimental validation were done and presented in Appendix Figure A-10 and Figure A-11, respectively. Both experimental and simulation comparisons on the control REAT and one other random structure, UH-N are well within reasonable range and experiment is thus well validated.

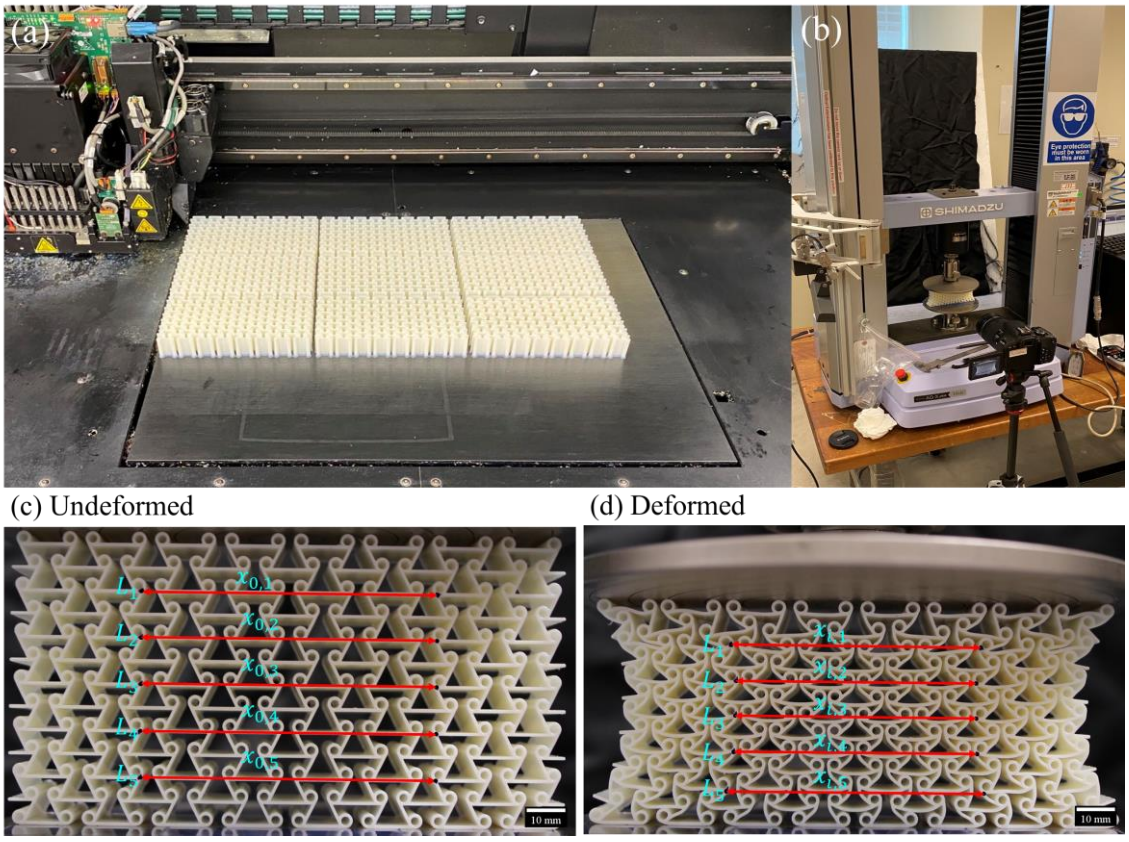

Figure 5.2. Fabrication, experimental setup, and NPR calculation of REAT designs. (a) All nine designs of REAT were 3D printed simultaneously using Stratasys Objet350 Connex3, ensuring consistency and repeatability of the

results. (b) Experimental setup for compression using Shimadzu 10kN universal test machine, recorded with a digital camera (Canon EOS 800D). Illustration of NPR calculation using images and marking on tangential joints located across the five levels between (c) undeformed and (d) deformed structure.

Unlike uniform lattice structures, the RD of a uniform REAT structure can be defined by the RD of a unit cell, but specifically for a gradient-based REAT structure, the RD will drastically vary across the direction of the gradient due to changes in cylinder diameter or height. Therefore, the RD of each design is evaluated with the help of a CAD software, using the area occupied by the structure divided by the rectangular area occupied by the entire structure. To prevent the over-influence of RD over mechanical performances of various designs, the stress is normalized by the respective RD of every structure to eliminate any discrepancies just as with other chapters.

Furthermore, in the previous chapter, the PR is calculated based on an enclosing rectangle within the structure to avoid the influence of boundary effect. The PR used in the previous work was a representative of the entire structure by taking the average of the directions. If the overall representation of NPR is used in this study, fine details on deformation within each layer of gradient distribution will be lost. Therefore, to distinguish and elucidate the various PR across different layers shown in Figure 5.2(c), the NPR is expressed as:

$$\varepsilon_{x,n} = \frac{x_{i,n} - x_{0,n}}{x_{0,n}} \tag{5}$$

$$\varepsilon_y = \frac{y_i - y_0}{y_0} \tag{6}$$

$$\nu_{xy,n} = -\frac{\varepsilon_{x,n}}{\varepsilon_y} \tag{7}$$

where, with close reference to Figure 5.2(c) and (d), x_o and x_i are the original and deformed width at each level n, respectively. ε_x and ε_y are the lateral and longitudinal strain of the overall structure, respectively.

5.2 Results and Discussion

The mechanical responses of all four graded REAT honeycombs under in-plane quasi-static compression is discussed. The deformation patterns, SS behaviour, EA performance, and change in PR are compared and analysed between different gradient parameters and gradient directions. This section is segmented into comparison between graded chiral structures and Base model, as well as between graded height structure and Base model.

5.2.1 Unidirectionally chiral gradient UC-P and UC-N

An in-depth summary of micro deformation of unit cells in the original REAT structure was detailed in our previous chapter. Here, for gradient-based REAT structures, both micro and meso-deformation will be used to evaluate the collapse pattern throughout the compression.

5.2.1.1 Mechanical responses from stress-strain

By introducing unidirectional gradient-based distribution in cylindrical diameter, several key observations were made in the elastic, plateau and densification stages based on the SS, SEA and EA efficiency curves. Initially, for all three structures, a uniform deformation begins to occur starting from 0 to 5% strain which signifies the elastic stage. This is generally observed when the inclined and horizontal ligaments undergo slight flexure under load.

After the elastic stage, the plateau stage is represented by plastic deformation in the inclined ligaments initiated by both the bending of ligaments and rotation of cylinders. The plastic deformation produced kinks on the upper portion of the inclined ligaments which can be observed specifically in the deformation process in Figure 5.3(b).

(a) 0% strain (b) 10% strain (c) 15% strain (d) 30% strain (e) 40% strain

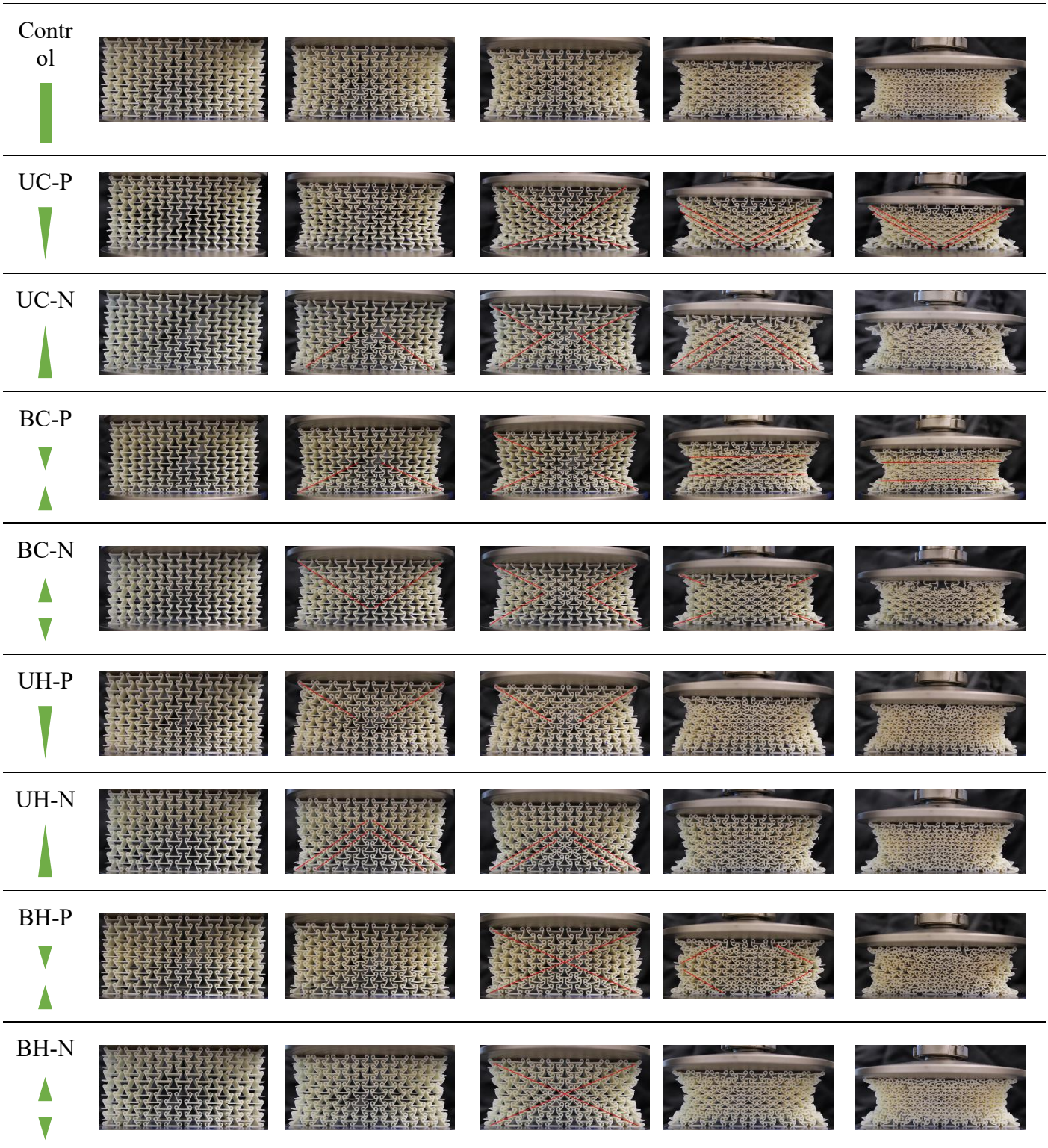

Figure 5.3. Deformation process comparison for all structures at strains of (a) 0%, (b) 15%, (c) 30%, and (d) 40%. Key differences in graded structures include skewed "X" and "V" deformations. Asymmetrical "X" formed due to earlier lateral contraction on one layer compared to others, observed around 15% strain. In later compression stages, stacked "V," inverted "V," "banded," and positive Poisson's effect deformations were observed.

Compared with Base model in Figure 5.4, the unidirectionally graded REAT structures started off with high plateau stress given the inverse relationship between cylindrical size and plateau

stress, and due to the deformation of smaller cylinders involved at the start of plateau stage which are evident in Figure 5.3(c) with UC-P producing a stronger lateral contraction at bottom portion of the structure. Unlike conventional auxetic structures such as the re-entrant, all three structures undergo a quasi-plateau stage of gradually increasing plateau stress.

The plateau stage itself also varies according to various gradient distribution in the REAT structure. Control REAT started off with flat plateau stage from 7.5 to 15% strain followed by a slight increase in stress before continuing off with gradually increasing plateau stress shown in Figure 5.4(a). The initiation of the increase in stress during the plateau stage at around 15% strain is caused by the contact between the cylinders and the downward flexed horizontal ligaments as substantiated in Figure 5.3(c). The plateau stress increased under further compression as the downward flexed horizontal ligaments resist against the upward pressure caused by the cylinders below them. The stress then briefly flattened off as horizontal ligaments lost their flexure as they are straightened at around 25% strain shown in Figure 5.4(a1). Similarly, both UC-P and UC-N possess a flat plateau stage which is longer as compared to Base model as the graded REAT has more porosity introduced by the smaller cylinders which means a greater displacement between the smaller cylinders and the horizontal ligaments above them allowing for more plastic deformation before contact and hence more extended plateau stage.

Between UC-N and control, both plateau stages show slight stress increase at 30% and 22.5% strain, respectively, as illustrated in Figure 5.4(a). The location of these instances of stress increase at different part of the plateau stage is attributed to the macro deformation mechanisms of the structures. Even though the contact between the horizontal ligaments and the larger cylinders of UC-N came as early as 17.5%, the stress increase was observed later as top layers with smaller cylinders underwent deformation until most of these cylinders are either in contact with adjacent counterparts or in contact with the horizontal ligaments above which can be seen

in the inset Figure 5.4(a2). The magnitude of stress increase is also larger due to the way larger cylinders and horizontal ligaments are in contact with one another in UC-N. The cylinders in Base model are very close and almost in touch with adjacent counterparts when the cylinders are in contact with the horizontal ligaments seen from Figure 5.4(a1), whereas on the other hand, seen from zoomed in inset Figure 5.4(a2), larger cylinders are adjacently far apart from each other when they are in contact with the horizontal ligaments. As the point of contact with ligaments are closer to the joints than towards the middle, the ligaments are thus even more resistive to upward force from the cylinders.

In contrast to both UC-N and control, UC-P did not experience any prominent brief stress increments during its plateau stage as depicted in Figure 5.4(a). Comparing with UC-N, UC-P at around 27.5% strain did not show any stress increments as there are no contact between larger cylinders at the top layers with the horizontal ligaments as illustrated in Figure 5.4(a3) which means there is still room for plastic deformation even though the smaller cylinders in the lower layers were in contact with the horizontal ligaments as the effect of cylindrical pressure against horizontal ligaments are less significant.

Ultimately, the characteristics of plateau stage are considered to be dependent on the overall deformation mechanism during the compression process. For instance, in a re-entrant with gradient -based thickness, its plateau stage is expected to have three flat plateau stages of consecutively higher stress assuming the stiffness of each gradient layer is drastically different given sufficient different in thickness between gradients. Conversely, uniform REAT structures have one single plateau stage of gradually increasing plateau stress. Again, unidirectional chiral-based gradient structures also have similar plateau stress to uniform REAT model but the sequence during the deformation process is drastically varied. From Figure 5.3(b) at 10% strain, the lower layers of UC-N started to collapse and laterally contract first, forming an marked inverted “V” deformation, followed by the lateral contraction of the top layer till points

of contact between cylinders and ligaments at 20% strain and finally the closing off of remaining porosities across the structure which produced the brief stress increase at the later part of the plateau stage. Correspondingly, the lower layers of UC-P also collapsed first as marked by the asymmetric red "X" in Figure 5.3(c), but the subsequent layers collapses and contract only after the cylinders in lower layers are in contact with one another or ligaments creating a more of layer-by-layer collapse creating a tapered "V" deformation which is most prominent in Figure 5.3(d) and (e). The phenomenon of brief stress increment was eliminated as it occurred only near the densification stage.

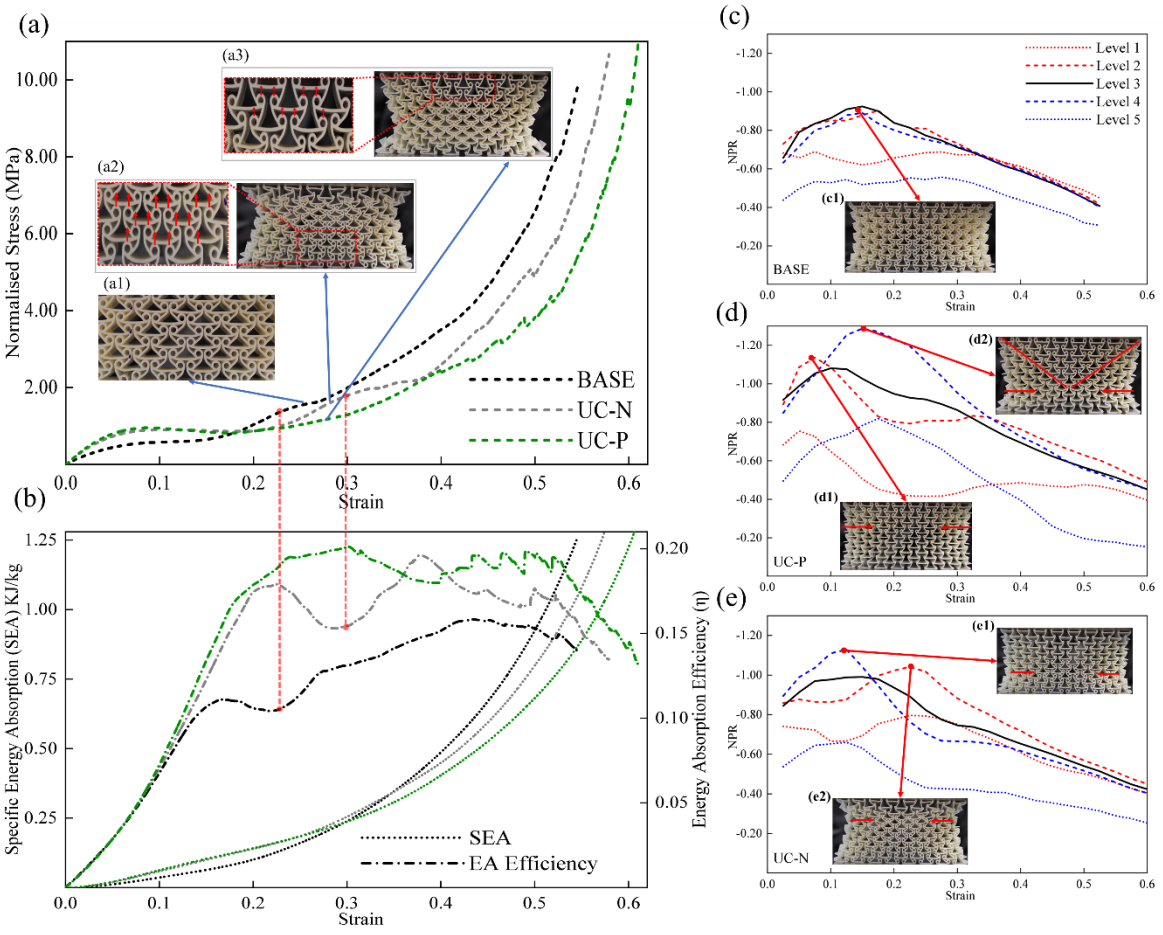

Figure 5.4. Performance comparison between Base model (uniform REAT) and unidirectionally chiral-graded REAT (UC-P and UC-N): (a) SS, (b) SEA-strain, and EA efficiency-strain curves. Unidirectional chiral-graded REATs exhibit higher starting plateau stress, better SEA in early compression, consistently higher EA efficiency, and higher densification strain. Short stress increments (black and grey dotted lines) caused by upward pressure from larger cylinders on horizontal ligaments briefly reduce EA efficiency. NPR-strain curves for (c) Base model, (d) UC-P, and (e) UC-N, showing NPR at five levels defined in (c), (d) and (e). Similar middle three levels NPRs indicate uniform deformation during compression (c1). Drastic NPR variation between levels enables sequential deformation. Self-initiated collapse in level 2 (d1) and level 4 (e1) shown for UC-P and UC-N, respectively.

Strong lateral contraction in level 4 of UC-P generates “V” deformation in (d2). And the PR of level 2 in UC-N increased due to presence of porosity in (e2).

5.2.1.2 Specific energy absorption and energy absorption efficiency

In terms of SEA, due to the more extended flat portion in the early portion of the plateau stage with higher plateau stress, both unidirectionally graded chiral REAT performed better in the early stages of compression between 0 to 30% strain by about 50% shown in Figure 5.4(b). Even though the uniform REAT structure performed better after 30% strain, majority of its SEA comes from the later stage of the compression close to the densification, meaning that the amount of useful EA is not more than that of graded REAT.

Furthermore, both graded REAT structures also performed better than the Base model as shown by their consistently high EA efficiency in Figure 5.4(b). However, the short stress increases in the plateau stress creates a dip in efficiency for control and UC-N at around 22 and 28% strain, respectively, marked by the red dotted vertical lines between graph (a) and (b) of Figure 5.4. Conversely, UC-P exhibited a more consistent EA efficiency due to its steady increase in plateau stress.

From the EA efficiency curve, it is also possible to see that the densification strain for control is much lesser than those of UC-N and UC-P. The EA efficiency of Base model reached its global maximum at around 42.5% strain which is in agreement with Figure 5.3(e) at 40% strain where there is little porosity left for deformation. Meanwhile, UC-P and UC-N had much greater densification strain both at around 50% strain. Although there is a global maximum in EA efficiency of UC-N at around 40%, Figure 5.3(e) showed that there are still porosity present in the structure for useful EA. The EA efficiency of both graded REAT structures drastically drops after 50% strain.

5.2.1.3 NPR Performance

Unlike original REAT model, the unidirectional distribution of graded chiral had a profound effect on the NPR effect across various layers within the structure. With regards to Figure 5.4(c), apart from levels 1 and 5 which are negatively affected by the boundary effect in the proximal and distal ends, the middle portion of the structure consisting of levels 2, 3 and 4 exhibit NPR that are very close to one another. This is indicative of uniform deformation which can also be seen in Figure 5.4(e1) as well as the compression process recorded in Figure 5.3. UC-P and UC-N, on the other hand, possess substantially differentiated NPR from different layers. They all display peaks at various strain, demonstrating a sequential collapse from one layer to another. However, this does not necessarily hints at a layer-by-layer collapse observed in thickness graded structure.

With close reference to levels 2, 3 and 4 first, UC-P started off the elastic stage with increasing NPR in all three layers of almost equal magnitude with slightly higher NPR effect in level 2 which demonstrates the lack of stiffness in layers with larger cylinder. Next, at 7.5% strain, the NPR of level 2 peaked before dropping off as illustrated in the NPR-strain graph in Figure 5.4(d) and flexure in ligaments displayed in Figure 5.4(d1). The NPR of level 2 was then overtaken by level 4, signifying the start of collapse in level 4, in which the NPR peaked up to a NPR of -1.3. This is evident from Figure 5.4(d2), which clearly shows a disproportionately larger lateral contraction (marked with a red arrow) in level 4 compared to other levels. Between around 10 and 30% strain, the NPR of level 3 is higher than level 2 but lower than level 4 due to interlayer influence from high NPR effect from level 4 as it is known that smaller cylinders exhibit stronger NPR effect than larger cylinders. For these three levels, all of them lose NPR at a constant rate implying that there was no lateral distance to cover between adjacent cylinders, leaving only the vertical displacement to condense which is apparent in Figure 5.3(d) of UC-P.

Again, considering the middle three levels, level 4 in the elastic stage began with higher NPR than level 2 and 3, indicating that in this case, larger cylinders have poorer stiffness when compared to other levels with smaller cylinders which is also true in UC-P albeit of smaller magnitude. The difference in magnitude may be due to UC-N having four chiral layers of largest cylinder while UC-P only has three.

In UC-N, the collapse of level 4 peaked at around 12.5% strain forming an inverted "V" deformation shown in Figure 5.4(e1) before dropping off till around 17.5% strain at which a turning point where level 2 started to show stronger NPR effect than level 4. This reversal is caused by the cylinders in the lower levels coming into contact with the horizontal ligaments instead of adjacent cylinders contacting one another. The mentioned contact restricted the further lateral contraction causing the NPR of level 4 to gradually drop. Subsequently, the NPR of level 2 peaked at around 22.5% strain shown in Figure 5.4(e2) before dropping after the adjacent cylinders close off the lateral displacement.

It is noted that level 1 and 5 of all three structures are distinctly lower than the other levels. Referring to the uniform REAT, despite being uniform in deformation, level 1 and 5 showed lower NPR due to the boundary effect from the proximal and distal ends. The influence from boundary effect is prevalent in the graded REAT structures due to the frictional contact between the structure and the compression plate. Undoubtedly, under the assumption of negligible friction, it is expected that level 5 consisting of the smallest cylinders should exhibit the strongest NPR effect regardless of sequence of collapse. Therefore, it is confirmed that unidirectionally graded chiral REAT structures deviate remarkably from uniform deformation while producing a drastically varying NPR among different level defined within the structure. It is also worth noting that the sequential deformation discussed in this work does not imply orderly collapse from top to bottom, instead, a collapse or lateral contract of one level may potentially has a interlayer propagation effect which initiates the contraction of another or an

initial collapse all by the layer itself due to its lack of stiffness or enhanced stiffness due to cylinder to ligament contact.

In essence, the sequential collapse from one layer to another is not driven by the stiffness difference between layers of varying cylindrical diameter. Rather, it's the NPR effect that drives this phenomenon. On the contrary, when considering a gradient-based distribution in thickness, the collapse becomes solely dependent on the stiffness variation. This variation arises from the drastic differences in relative densities among the layers. The creation of a gradient in chiral diameter introduces another dynamic. In this case, the difference in NPR between layers becomes more influential than the differences in RD and stiffness. This differential in NPR emerges as the main driver of deformation in graded chiral lattices.

5.2.2 Bidirectionally chiral gradient BC-N and BC-P

5.2.2.1 Mechanical responses from stress-strain

Much similar to unidirectionally chiral-graded REAT structure, both BC-N and BC-P are able to retain the gradually increasing plateau stress as well as higher elastic stiffness against Base model. Furthermore, brief stress increment and concentration are discovered in these structures.

Firstly, both plateau stages of the bidirectional chiral graded REAT structure started off relatively flat, with BC-P exhibiting a slightly higher plateau stress than BC-N after around 12% strain, as shown in Figure 5.5(a).This can be attributed to the fact that the bulk of deformation in BC-P involved smaller cylinders as compared to BC-N, as can be seen in Figure 5.5(a1), where a majority of deformation involved smaller cylinders. BC-N extended its plateau stage till around 30% strain before experiencing a brief stress increment caused by the interaction between largest cylinder in the middle chiral layer and the horizontal ligaments mentioned in the earlier section, as illustrated in Figure 5.5(a). On the other hand, BC-P produced a plateau stage with gradual increase in stress comparable to UC-P before exhibiting various catastrophic

fracture in the layers near the proximal and distal end of lattice marked by red circle in Figure 5.5(a1), leading to large drop in stress. As materials have higher fracture toughness, this shows that this design tends to produce various regions of high stress concentration leading to failure.

The major difference between the two plateau stages is the various locations where the collapse was initiated. The middle layer of BC-N with the largest cylinder collapsed first before top and bottom layers began to collapse simultaneously as observed in Figure 5.3(b) and (c). However, the pressure from the largest cylinders on its horizontal ligaments above had started just as the next biggest cylinders came into contact with the horizontal ligaments, and this caused a miniature stress increase at 27.5% strain. Interestingly, unlike all other graded structures, BC-N exhibited an obvious second plateau stress between 37.5% and 45% strain, strongly indicating the ongoing plastic deformation of top and bottom layers with smaller cylinders. This is substantiated by the presence of remaining porosity between adjacent cylinders, and between cylinders and horizontal ligaments that are above and below, as shown in Figure 5.3(d). The deformation is followed by the closing of these gaps observed in Figure 5.3(e).

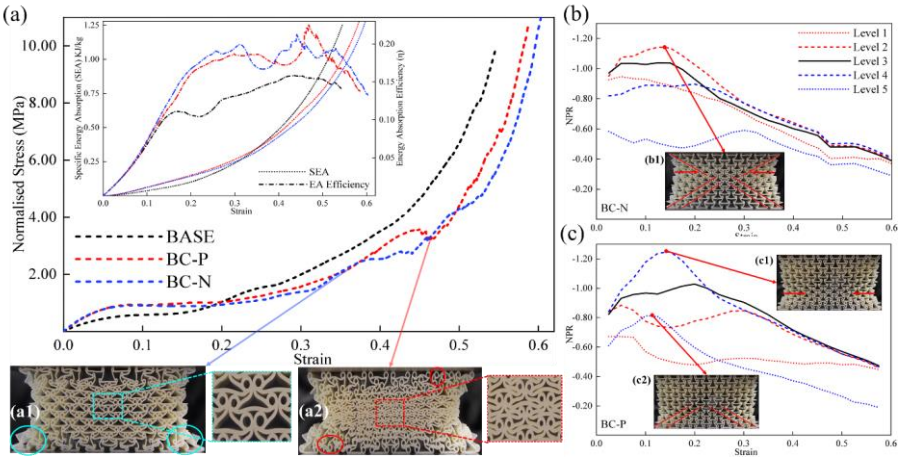

Figure 5.5. The following figure presents a summary of (a) SS curves, with an inset showing combined SEA and EA efficiency graphs. Bidirectionally chiral-graded REATs exhibit higher plateau stages than the Base model. Concentrated deformation in BC-P's middle leads to fractures near proximal and distal ends, while contact interaction between large cylinders and horizontal ligaments causes mini-stress increases, as observed in the Base and UC-N models. Though EA efficiency is higher than the Base model, densification strain of bidirectionally graded REATs is nearly equivalent. Graphs depict NPR-strain for (b) BC-N and (c) BC-P. Despite closely related NPRs between levels in BC-N, distinct inverted "V" and upright "V" deformations emerge, with level 2 peaking around 15% strain (b1). In contrast, significant NPR divergence between levels in BC-P results in pronounced deformations, especially when the spike in level 5's NPR at 10% strain creates an inverted "V" deformation in the

lower structure portion. This phenomenon carries over to level 4, forming a noticeable hourglass shape in the lower lattice section, while the top half shows little to no plastic deformation.

5.2.2.2 Specific energy absorption and energy absorption efficiency

The SEA of bidirectionally graded chiral REAT performed similar to that of unidirectionally graded chiral structure where more energy can be absorbed in the early stage of compression instead of having useful EA that are concentrated towards the densification stage in the Base model shown in Figure 5.4(b). Once again, the brief stress increments were accompanied by a significant drop in EA efficiency, as observed in BC-N, and are marked by the solid blue and red line between the SS curve and EA efficiency curve in Figure 5.5(a). Despite their higher EA efficiency, the densification strains in these structures are lower compared to their unidirectionally graded counterparts. Apart from global maximum defining the densification strain, analysis of its subsequent deformation after densification strain as well as the presence of fracture arising from failure to distribute stress throughout the structure are sufficient proof to conclude one's densification stage. For instance, the densification strain was concluded to be at the point where BC-P exhibited a sharp global maximum peak at 45% strain along with drastic drop in efficiency, coupled with Figure 5.5(a1) showing evidently compact middle layers, creating stress concentration in the layers whose movements are restricted by the boundary effect in the proximal and distal ends. Likewise, BC-N had its EA efficiency peaked at around 43% strain and subsequent deformation after this strain only involved further bending of ligaments within the protruding portion of the layer under the influence of boundary effect close to the distal end marked by the blue circle in Figure 5.5(a2). Thus, it is concluded that while bidirectional graded REAT structure offers good EA efficiency, their densification strain remains questionable in comparison to the uniform REAT structure.

5.2.2.3 NPR performance

Previously, peaks of various levels at different strains defined the sequence of deformation in the unidirectionally distributed chiral gradient REAT. Here, in the bidirectionally distributed chiral gradient, peaks are also observed, except that the peaks in BC-N are comparatively gentler, as depicted in Figure 5.5(b). During the elastic stage in BC-N, the NPR of level 4 started off lower than that of level 2 and 3, implying that the smaller cylinders in level 4 have inherently higher stiffness than the larger cylinders in level 3. Despite having the same cylinder size, level 2 experienced stronger NPR effect than level 4. This is due to the effect of interlayer influence caused by cylinders in level 3 coming into contact with horizontal ligaments. This carry-over effect did not affect the lower levels because given the structure of the REAT unit cell, it is not symmetrical, and the cylinders are directed upwards which causes them to be more prone to interact with ligaments above them instead of the ones below them. The NPR of level 2 peaked at around 15% strain, producing a “V” deformation at the top portion of the structure and a concurrent double inverted “V” deformation at the bottom portion of the structure shown in Figure 5.5(b1).

Notably, before level 2 peaked in its NPR, level 1 which is closest to the proximal end showed stronger NPR than level 4 which is further away from the boundary effect which can be explained by the interlayer influence effect caused by high NPR from level 2. It is also worthwhile to consider the fact that despite both proximal and distal ends possessing the smallest cylinders which is expected to show a substantial NPR effect, the NPR performance was poorer than the levels with larger cylinder which illustrate the detrimental impact of the boundary effect on the NPR performance. This is further substantiated by the lower NPR of level 1 and 5 compared to rest of the levels of control REAT given the uniformity in deformation. Furthermore, the boundary effect from the distal end is stronger than the proximal end, attributed to the larger surface area of contact between the plate and the lattice. Thus, the

presence of larger friction restricts the mobilization of bottom portion of the lattice as compared to the top portion. This is also partially the reason that inverted “V” deformation is more often observed than “V” deformation.

Conversely, a diversity of NPR between the middle three levels in BC-P was observed in the early stage of compression up to 25% strain. Between levels 2, 3 and 4, the deviation from one another widened as level 5 started to laterally contract till peak at approximately 12.5% strain where the cylinders of chiral layer 12 came into contact with the ligaments above. Despite not having a strong NPR effect given its proximity to distal end, the contraction in level 5 also initiated the lateral contraction in level 4 via the interlayer influence effect. Hence, the peak in NPR of level 5 at 10% shown in Figure 5.5(c2) forming an inverted “V” is sequentially followed by peak in NPR of level 4 at around 15% strain in Figure 5.5(c1). The strong NPR effect in level 4, in turn, was propagated over to level 3 but to a lower extent. It can be seen that the propagation effect gets weaker as cylinder size becomes smaller which is illustrated by the negligible effect of level 3 on level 2 whose NPR slightly dropped as level 3 increased. Furthermore, larger cylinders have greater propensity to rotate along with bending of ligaments whereas the rotational effect in smaller cylinders are less dominant as compared to bending of ligaments.

5.2.3 Height based gradient distribution in REAT

5.2.3.1 Stress-strain, mechanical responses, SEA, and absorption efficiency

Results from the experiments on gradient distribution in height on REAT had shown insignificant effect on the mechanical behaviour and EA capability. Considering all the layers in these four graded designs, the ratios of L_2 to L_1 fall between 1.5 and 2 which had been shown to have weaker dependence of the SS curve and the SEA on the ligament length ratio [30][106]. The insignificant impact by the graded distribution in height is illustrated in the following Figure 5.6. However, the deformation patterns of REAT with graded height distribution are

much more predictable and discernible. Cell layers with taller unit cells or smaller L_2/L_1 ratio contains larger displacement between the cylinders and the horizontal ligaments allowing for greater plastic moments and deformations. This is clearly observed in all height-graded REAT structures shown in Figure 5.5 where layers with greater height showed stronger lateral contraction than the layer with smaller height. It is also noted that BH-P exhibited higher plateau stage than the control REAT model and the rest of the height-graded structure shown in Figure 5.6(a) because due to the shorter displacement between cylinders and the horizontal ligaments in the middle layer, the cylinder to horizontal ligament contact came as early as 10% strain as illustrated in Figure 5.3(b) which caused the stress to start increasing after the elastic stage.

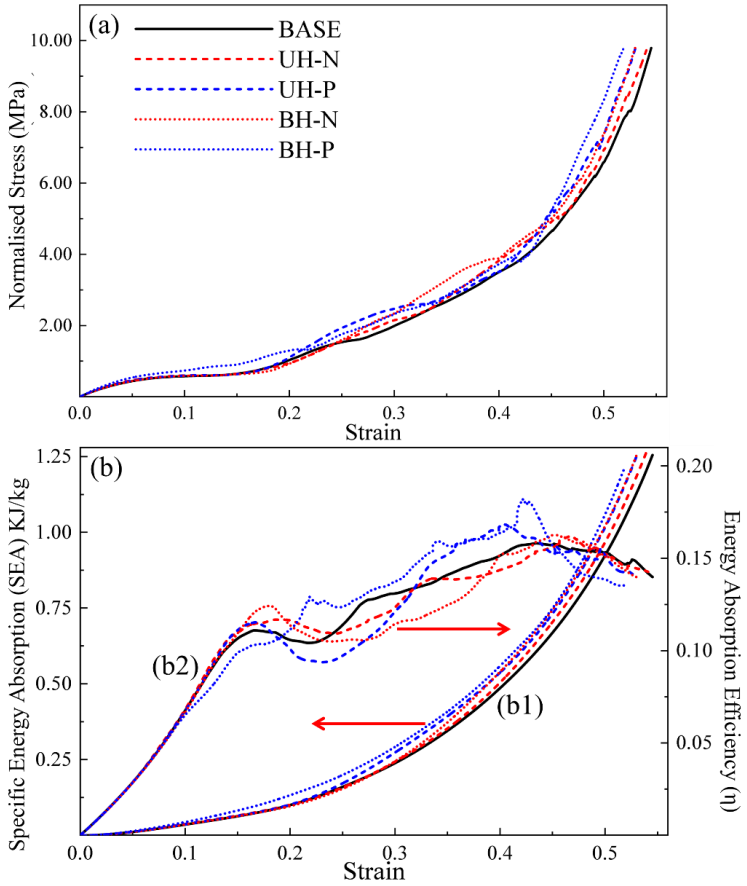

Figure 5.6. (a) SS comparison between Base model and height-based graded REAT structures, showing minimal impact of applying gradient Based approach in height on the SS performances. (b1) shows the SEA-strain of the structures in which, again, the EA capacity of the introducing gradient distribution in height is relatively similar to that of BASE model. (b2) illustrates the EA efficiency between the structures and again, variations are mostly similar, and all of the height graded REAT structure densifies at around 40-45% strain, close to Base model.

5.2.3.2 NPR performance

Despite the poor correlation between graded height and SS and EA performance, strong relationship between height and NPR exhibited drastic variations in NPR across various designs. This can be concluded in Figure 5.7 where NPRs of different levels are well distinguished from one another as compared to that of chiral-based graded REATs shown in Figure 5.4 and Figure 5.5. A well individualised NPR curve for each level in UH-P (Figure 5.7(a)) with level 1 having the stronger NPR effect followed by level 2, 3, 4 and finally 5. Whereas on the other hand, the trend in UH-N (Figure 5.7(b)) is reversed with level 4 (which is level 2 of UH-P) having the strongest NPR effect followed by 5, 3, 2 and 1. The reduction in NPR effect of level 5 of UH-N is due to the boundary effect on the distal end. Despite being influenced by boundary effect at proximal end, level 1 of UH-P continues to outperform the rest of the level. However, the same unit cell now near the distal end, with similar NPR trend, showed smaller NPR effect which goes to show the more detrimental impact of distal end over proximal end on the NPR effect. The significantly differentiated NPRs between levels created a tapered deformation through the outline of the unidirectionally graded REAT structures as illustrated in Figure 5.3 between 15 and 30% strain.

Notably bidirectional height graded REAT structures in Figure 5.7(c) and (d), the NPRs of levels with same unit cell configuration are almost equivalent of each other except for the level 1 and 5, implying that the NPR effect within each level was very much individualized unlike graded-chiral REAT structures where one level may have a profound interlayer influence over another depending on the size of the cylinders. As previously explained, the gradient distribution of cylindrical size every three chiral layers implies that the cylinders of various sizes may be shared between unit cells which makes the deformation within each level more interdependent. In contrast, even though the cylinders are shared between unit cells, the cylinder sizes are constant, and the geometrical change is discrete between layers of unit cells.

Furthermore, unlike unidirectional graded height, there are, to a certain extent, a detrimental impact on the neighboring levels can be deduced from Figure 5.7(c) where the performance of level 3 is poor given the smallest height of the unit cell being the weakest as well as the earlier contact between the cylinder and the horizontal ligaments heavily restricting the NPR effect. In addition, the NPRs of levels 2 and 3 of BH-P are much lower when compared with level 2 and 3 of Base model in Figure 5.4(a) while the NPRs of level 2 and 3 in BH-N are relatively similar to those of Base model. Even though it was discussed that the NPR of each level are distinct and individualized, the poor NPR effect of level 3 in BH-P could restrict its neighboring levels which can also be observed in the deformation process of BH-P in Figure 5.3 where a bulge in level 3 was much more obvious after 15% strain.

Overall, there is a lack of interdependence between SS and change in height of the unit cell due to the short range of L_2/L_1 ratio. However, despite the limited range in L_2/L_1 ratio, drastic range of NPR was observed between layers of various height configurations. Deformation pattern observed in height graded REAT was predictable as it is driven by the NPR effect of different layers.

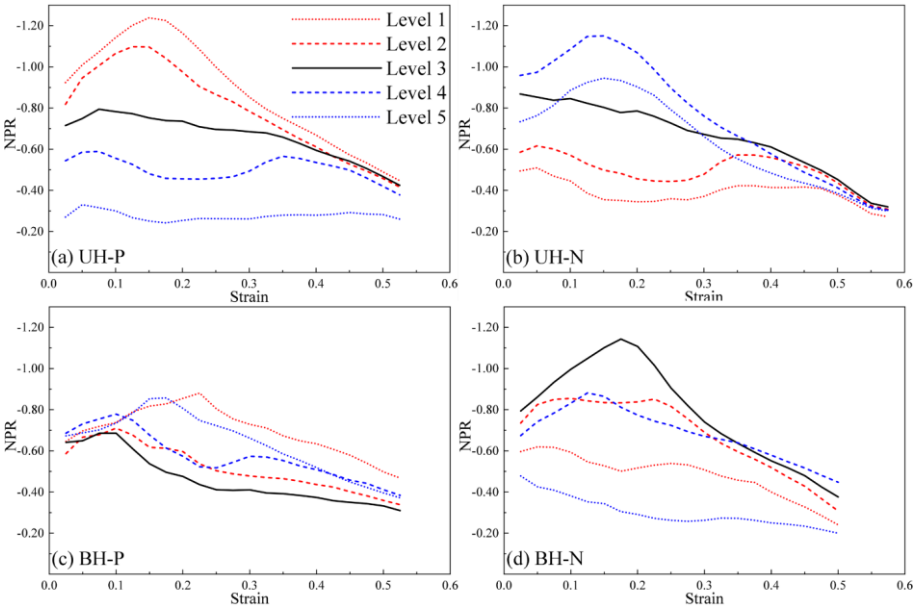

Figure 5.7. Summary of all NPR-strain of four height-graded REAT designs namely (a) UH-P, (b) UH-N, (c) BH-P and (d) BH-N. Except for BH-P, the NPRs of each layer are clearly separated indicating a significant relationship between height of the unit cell and its corresponding NPR effect.

5.2.4 Comparative Summary

A radar chart is shown in Figure 5.8 to compare the normalized performance between Base model and (a) chiral-graded and (b) height-graded REAT structures. The integration of the chiral-based gradient resulted in significant improvements, especially in areas such as elastic stiffness, plateau stress, and SEA during the early stage of compression. Even though the SEA is lower at the later stage of compression, this is offset by the extended densification strain and consistently higher EA efficiency. In contrast, height-graded REAT structures only produced stronger NPR effects with the rest of mechanical performances being fairly similar to Base model. BH-P is only distinguishable from the rest of height-graded structures due to the early collapse of the shortest unit cells in the middle layers, creating an early contact between cylinders and the horizontal ligaments, allowing the structure to skip the flat plateau stage and enter the stage with increasing stress.

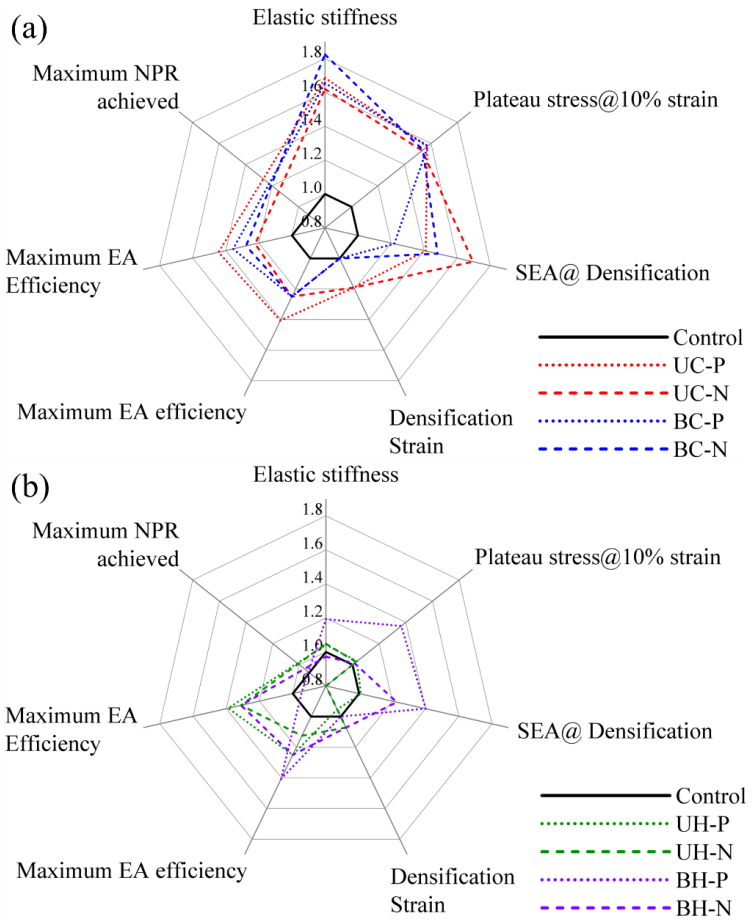

Figure 5.8. Radar chart illustrating the normalized comparison of key quantifiable performances between (a) chiral-graded REAT and (b) height-graded REAT structures, using Base model performance parameters. In (a), chiral-based gradient advantages over the Base model include higher elastic stiffness, higher plateau stress, and improved SEA at densification stage. Additionally, higher EA efficiency and a greater NPR effect are achieved through integrating a range of chiral diameters. For height gradient in (b), aside from the higher NPR effect, most mechanical performances are relatively close to the Base model, except for BH-N, which exhibits early cylinder-to-ligament interaction in layers with the shortest unit cell, bypassing the flat plateau stage.

The results of this study had demonstrated that the graded REAT structure especially the chiral-based graded REAT exhibited superior performance in terms of SEA compared to most other lattice structures found in literature illustrated in Figure 5.9. Notably, despite the enhanced mechanical properties, the density of the graded REAT structures remained around the average range. Furthermore, according to the Ashby plot, it is challenging to achieve a higher SEA while simultaneously keeping the density of the structure low especially for polymeric lattice structures. However, the promising performance of graded REAT structure indicate that advancing novel configurations by drawing inspiration from bio-structures may be possible in overcoming this limitation. This also suggests that there is potential room for further

exploration of bio-inspirated and its related development of lightweight lattice structures with improved SEA, tackling the challenges and trade-off between mechanical performance and density of the structures.

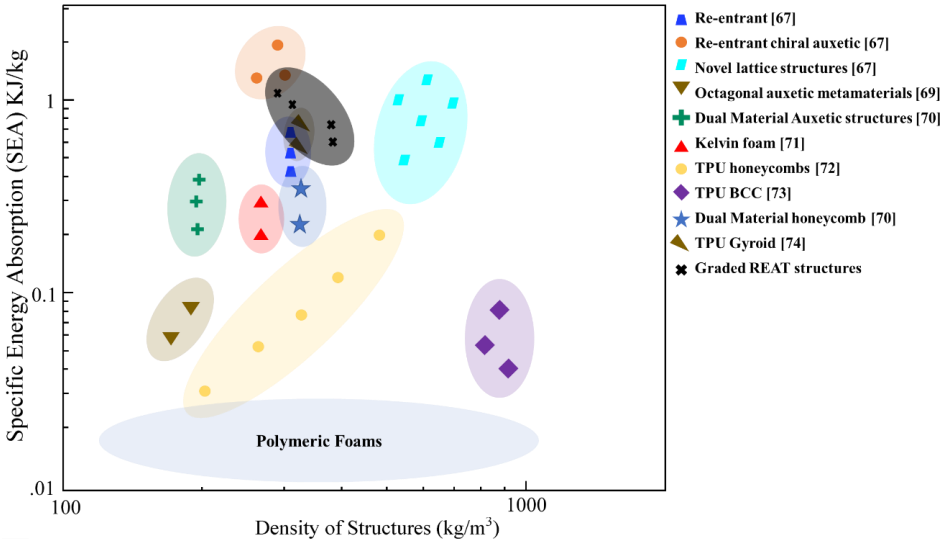

Figure 5.9. Ashby plots illustrated to compare SEA of graded REAT structures with various other lattice structures and foam in literature,[187]–[194]. The focus of the comparison was mainly on polymeric lattice structures rather than metallic lattices due to the significant differences in material properties between polymers and metals. Results indicated that graded REAT structure outperformed most of the lattice structures shown in terms of SEA while keeping their density close to average.

5.3 Conclusions

In this study, eight novel designs and Base model of REAT structures with gradient distribution based on cylindrical diameter and height were evaluated. For the gradient based on cylindrical diameter, the modified structures exhibited greater stiffness compared to the original Base REAT structure. These particular set of graded designs also had a more profound influence on the extension of their plateau stage, while maintaining a gradual increase in plateau stress, which is advantageous for consistent EA in both early and late stages of compression, at the same time, achieving a more stable and improved EA efficiency.

Moreover, significant variations in NPR were observed in the middle three levels of the graded chiral REAT structures. The differences in NPR effect outweighed the stiffness differences between layers, leading to sequential deformation rather than layer-by-layer collapse, as seen

in graded thickness structures driven by stiffness or RD differences in most literature. Additionally, effects of interlayer influence were identified between layers with larger cylinders, which had a greater impact on the overall structure compared to smaller cylinders. These interlayer influences were directional, owing to the geometrical configuration of REAT unit cells.

Regarding height-graded REAT structures, no drastic deviations were observed from the Base REAT model, except for the drastic NPR effect. This indicates a lack of interdependence between the height of the REAT unit cell and SS performance. This work provides insights into the mechanical responses of REAT structures with gradient-based configurations in cylinder diameter and height.

Chapter 6 Gradient Distribution Approach on Arc-shaped ligaments in REAT structure

In contrast to previous chapter, gradient-based approaches had been applied with the available geometrical parameters found in conventional REAT structure with straight ligaments. As such, the two main tuneable geometrical parameters are radius of the cylinder and the height of the unit cell. However, with the introduction of arc-shaped ligaments in the previous chapter, more tuneable geometrical parameters can thus be varied to expand the range of tunability in extra geometrical parameters such as the direction of curvature and degree of curvature.

6.1 Design Strategy

This section elucidates the design methodology for graded REAT featuring arc-shaped ligaments, aiming to manipulate the curvature degree of each curved ligament across the unit cell layers to achieve a graded curvature effect. Figure 6.1 visually represents this concept, showcasing a progression of curvature from one unit cell to another, increasing from left to right. By integrating this concept, series of designs are generated to evaluate the impact of utilizing gradient-based approach on curvature and its potential changes in combination with other parametric change such as the radius. It is also important to highlight that, as defined in Chapter 3 and illustrated in Figure 6.1(a) and (b), the REAT structure under examination exhibits a disparity in curvature between the inclined and horizontal ligaments. This discrepancy arises due to the tangential attachment, which is dependent on the distance between two cylinders. Concurrently, the horizontal and inclined arcs maintain an equal distance of w/2. Given that the horizontal ligament is twice the length of the inclined ligament, the horizontal arc has a lesser degree of curvature. In contrast, by eliminating the w/2 distance and allowing the arc to solely reference the horizontal ligaments—which are twice as long—the degree of curvature between the horizontal and inclined ligaments is equalized. The attachment points of

the cylinders connected by the inclined arc are subsequently adjusted to align with the horizontal arc and the cylinder's tangential attachment, as depicted in Figure 6.1(c).

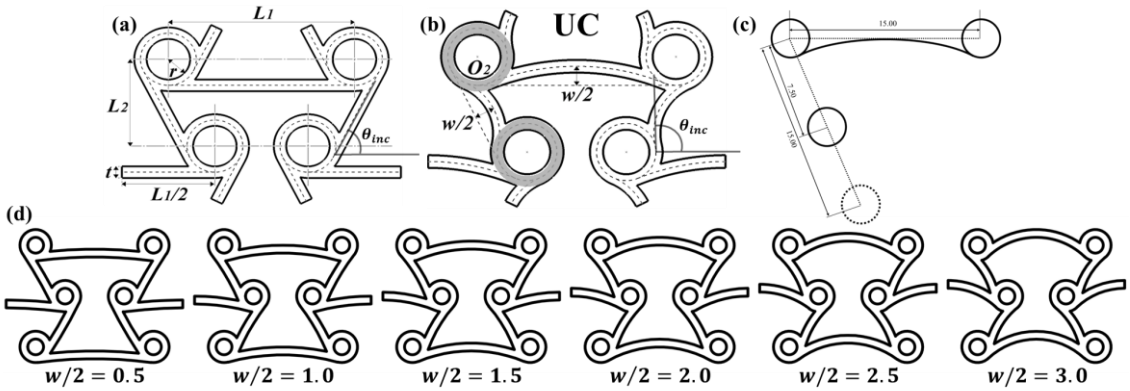

Figure 6.1. Unit cells of (a) Control and (b) UC with increasing degree of curvature from left to right shown in (d) which illustrates the degree of curvature being adjusted by increasing the value of w/2 at an increment of 0.5 from w/2=1 to 36 shown in unit cell of UC. However, to ensure equal degree of curvature, method of drawing is illustrated in (c) to show the new definition of curvature with only reference to the horizontal arc.

Consequently, the investigation commences with an exploration of four graded REAT curved honeycomb structures, encompassing two with unidirectional and two with bidirectional distributions of ligament curvature, as illustrated in Figure 6.2. The structures are systematically named to reflect their gradient distribution characteristics: 'U' denotes unidirectional, and 'B' denotes bidirectional. The second letter in each abbreviation indicates the direction of curvature change from the bottom to the top of the structure for unidirectional and from middle to both ends of the structures for bidirectional. This naming convention has been intentionally simplified to avoid any potential confusion with terminologies used in other chapters of this study.

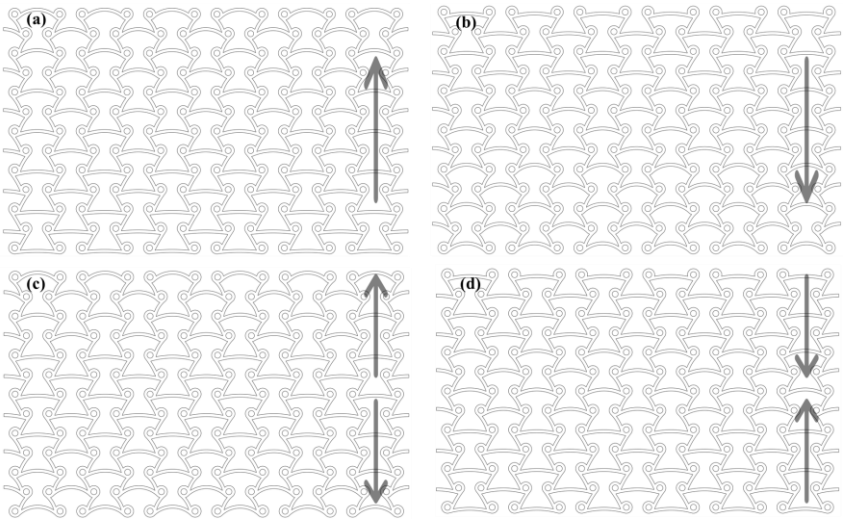

Figure 6.2. Illustration of four designs to be evaluated in this study. Two honeycombs are unidirectionally distributed with black arrow showing direction of increasing degree of curvature. Based on the direction of the increasing in curvature, the honeycombs are named as (a) Ui and (b) Ud with "U" indicating unidirectional gradient and "i" and "d" implying the increase and decrease in curvature from bottom to top, respectively. Subsequently, the bidirectionally distributed design are named as (c) Bi and (d) Bd.

6.2 Results and Discussion

This section delineates the mechanical behaviors of REAT under graded curvature conditions, utilizing four distinct design configurations. Each design is characterized by a unique gradient distribution, yet it is crucial to emphasize that these variations are derived from different arrangements of an identical set of layers with varying curvatures. When reconfigured, each design can be transformed into any of the others, highlighting their inherent similarity despite the apparent differences in gradient distribution. As illustrated by Figure 6.3, there is no significant difference between SS relationship. While acknowledging the inherent similarity in nature, the deformation observed may also elucidates the lack of discernable difference in the SS relationships across the designs. This also underscores the fact that despite the variation in structural configuration, the fundamental mechanical behaviors remain consistent in quasi-static compression.

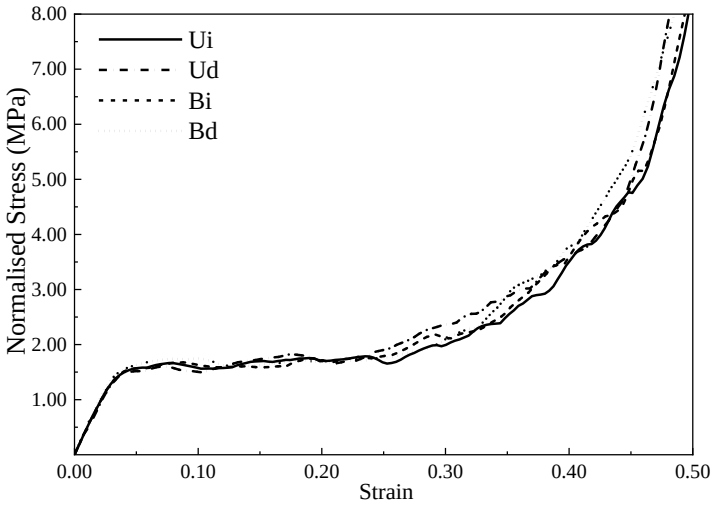

Figure 6.3. SS relationship between the four designs of REAT with graded curvature. There is no drastic difference between the four designs as it is noted that these variations essentially stem from different arrangements of the same set of layers of various curvatures.

Figure 6.4 provides additional substantiation to this observation, demonstrating a consistent initiation of plastic deformation in the layers characterized by the smallest curvature ligaments, subsequently progressing towards layers with larger curvature ligaments. This trend underlines the notion that ligaments with a larger curvature exhibit an increased resistance to compression compared to their straighter counterparts. However, an exception is observed in design Ud, where the plateau stress, occurring between strains of 0.25 and 0.35, is notably higher than in other designs. This is attributed to the premature collapse of a structurally stronger layer preceding the failure of a weaker one, resulting in a temporary increase in stress levels. The sequential collapse of layers is exemplified by design Bi, as shown in Figure 6.4(c). Here, the layer with the smallest curvature, and thus the weakest, succumbs first at a 15% strain. Despite the symmetrical gradation in curvature from the centre to the extremities of the structure, the lower layers yield prior to the upper layers, a behaviour that is evident at strains of 25% and 35%.

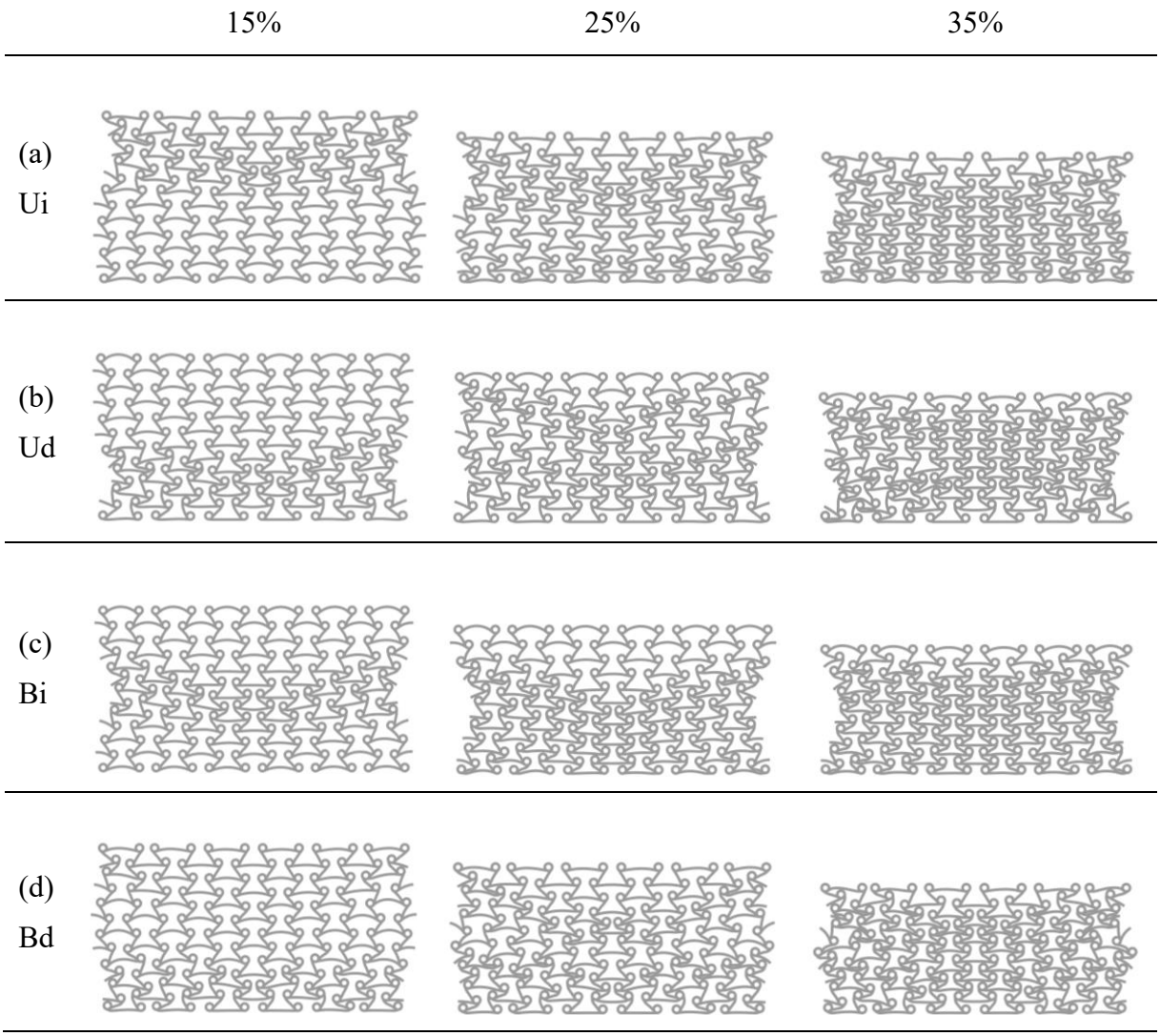

Figure 6.4. Deformation patterns for all four designs at three different strains of 15, 25, and 35%. The sequence of deformation is predictable as the layers with least curvature will collapse first followed by layers with greater curvature.

In comparison to REAT with graded curvature and a smaller radius of 2mm, the structure Ui-R=2, as observed in Figure 6.5, exhibits an elevation in plateau stress and an enhancement in structural stiffness. The diminished stiffness displayed by Ud-R=2 relative to Ui-R=2 is attributed to the interaction between the horizontal arc ligament and the top plate, as opposed to the cylinder, potentially compromising the structure's rigidity. Furthermore, there is a substantial increase in densification strain, shifting from 0.45 to approximately 0.6 strain. Consequently, reducing the cylinder size positively influences the mechanical response, enhancing stiffness, plateau stress, and densification strain. As explored in the parametric study in section 3.3.3, a reduction in cylinder size typically results in weaker stiffness due to the

shortening of ligaments generated from larger cylinders contributing to greater stiffness. However, in this graded scenario, the decrease in cylinder size in Ui-2 positively impacts the mechanical performance of the structure, despite a slight elongation of the arc ligament from the tangential attachment. Additionally, the deformation patterns of REAT with graded curvature and a cylinder size of 2mm, as illustrated in Figure 6.6 at 15% strain, clearly indicate that ligaments with lesser curvature are predisposed to collapse first, regardless of their position in the lattice. Although subsequent layers are expected to collapse in order of increasing curvature, this pattern does not hold true in both Figure 6.5 and Figure 6.6. This suggests a non-linear relationship between the curvature of the inclined ligaments and the stiffness of the structure at these two cylindrical sizes.

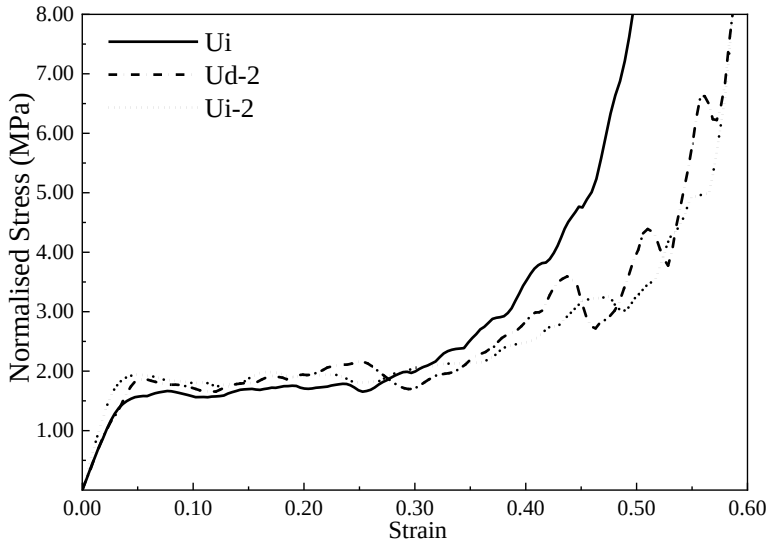

Figure 6.5. Comparison between graded REAT with curvature Ui of larger cylindrical diameter of 3mm and graded REAT with curvature Ud-2 and Ui-2 of cylindrical diameter of 2mm. Aside from the contact between horizontal arc ligaments and the top plate in Ud-2, Ui-2 in general exhibited better stiffness, higher plateau stress as well as larger densification strain as compared to graded counterpart with larger cylinder size.

Aside from the bidirectional graded REAT, unidirectional graded REAT structures across both cylindrical sizes initiated with collapse of ligaments with least curvature followed by a joint collapse of the layers with greater curvatures. Moreover, the horizontal ligaments appear to play a less significant role in the structure's stiffness, as stress concentration is predominantly observed in the inclined ligaments during the elastic stage of compression. Conversely, the

horizontal ligaments become more involved in the later stages of plastic deformation, participating in the straightening and downward flexure of ligaments and their subsequent contact interaction with the cylinder, which is delayed to the later stages of compression compared to straight ligaments.

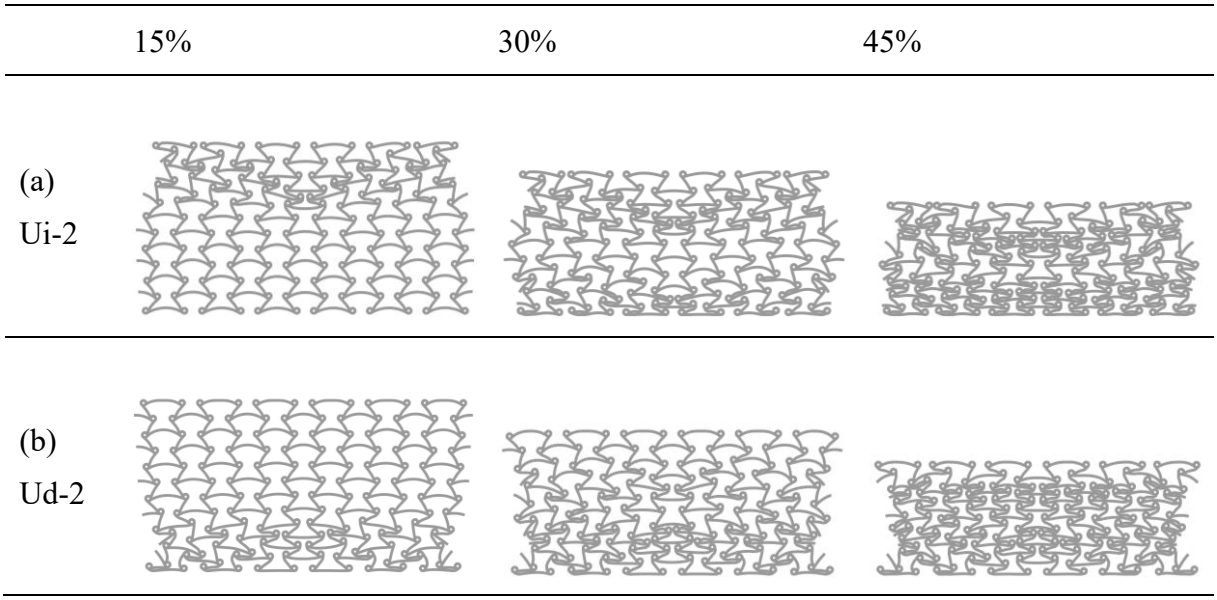

Figure 6.6. Deformation patterns of unidirectionally graded curvature REAT structures with cylindrical size of 2mm. Ligaments with least curvature is almost always expected to collapse first however, the layer-by-layer collapse is not in sequence as expected from increasing curvature.

Upon transitioning from a gradient in curvature with a cylindrical size of 3mm to a graded curvature with a cylindrical size of 2mm, a comparative analysis was conducted between the gradient in radius in REAT with constant curvature and the previously superior structure, which also possesses a graded curvature but with a cylindrical size of 2mm. Intriguingly, the plateau stress exhibited by both structures is relatively comparable. However, the structure denoted as Ud-r demonstrates a reduced stiffness in comparison to the other two structures. This is attributed to the initial deformation occurring in the lower layer, which is inherently less stiff than the subsequent gradient layers. In contrast, the structure labeled as Ud-i manifests a higher elastic stiffness than Ud-r. This is due to the gradient layer at which the initial collapse transpires, providing a stiffer response. As such, with reference to Figure 6.8, initiation of collapse for both structures, regardless of the strength of the bottom layer, consistently begins

at the bottom layer during the onset of compression. Given that a reduction in cylindrical size generally results in an increase in structural stiffness, the stiffness of Ui-r is consequently higher than that of Ud-r. The subsequent deformation follows a consistent pattern, with the initial collapse of the bottom layer leading to the collapse of the mid-layer which forms a tapered "V" deformation pattern, followed by plastic deformation in the undeformed region and eventual densification.

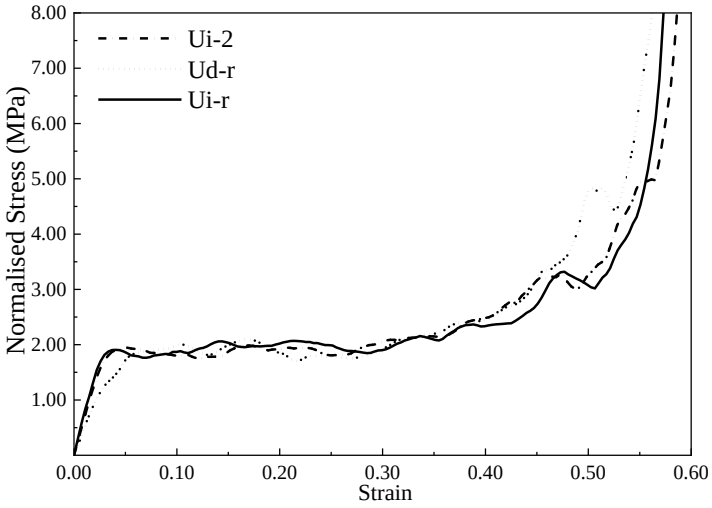

Figure 6.7. SS comparison between unidirectionally increase curvature with cylindrical size of 2mm and graded REAT structure with graded cylindrical size at constant curvature. Due to notable deformation, Ud-r has a lower stiffness as compared to Ud-i.

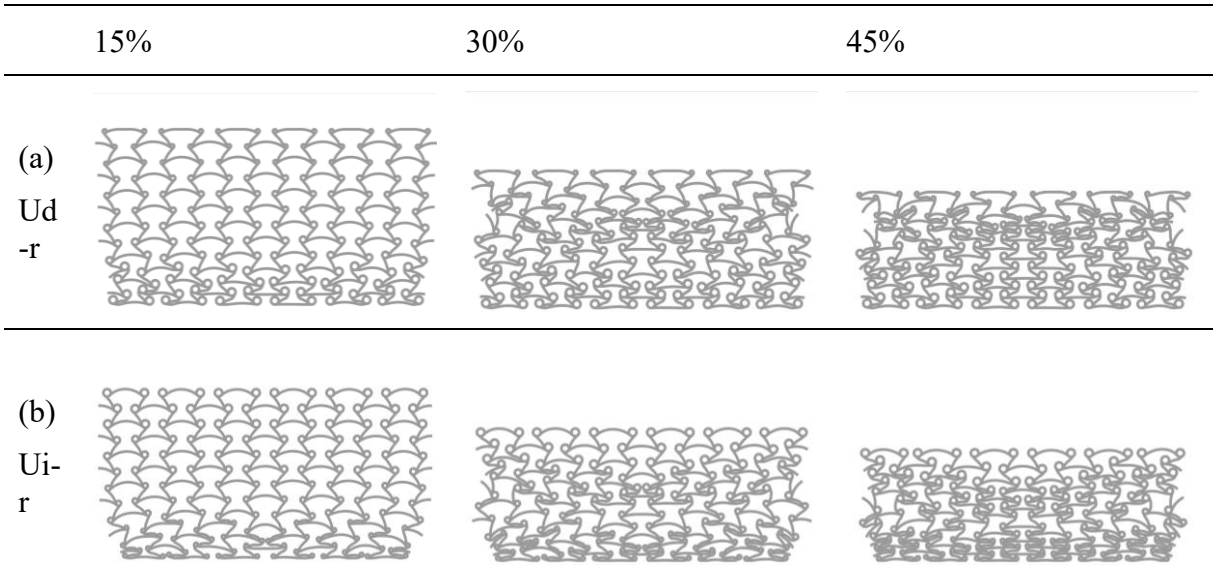

Figure 6.8. Deformation patterns of unidirectionally graded REAT structures with graded cylindrical size. Regard

6.3 Concluding Remarks

The investigation continues, building upon the insights gained in the previous two chapters, examining conventional REAT, REAT with arc-shaped ligaments, and graded REAT structures derived from conventional REAT geometrical parameters. The exploration commences with an analysis of the REAT structure featuring graded curvature, where the design methodology has been refined to ensure a uniform curvature across all layers.

Remarkably, there is an almost imperceivable difference between the graded structures, attributed to their analogous elastic and subsequent plastic deformation behaviours. Moreover, as all four structures incorporate identical gradient layers in their configuration, altering the arrangement of each gradient layer appears to have little to no substantial impact on the overall mechanical performance of the structures.

Subsequently, the focus is shifted towards REAT structures with a smaller cylindrical size and graded curvature, revealing enhancements in both plateau stress and elastic stiffness. Progressing further, the investigation reproduces the REAT structure with a constant curvature and varied radius, resulting in a marginal improvement in stiffness due to early deformation, though the plateau stress did not exhibit significant enhancement.

While the study provides valuable perspectives on the gradient-based approach, it may still be limited as it maintains a constant value for other significant geometrical parameters. A potentially more intriguing deformation behaviour might emerge if both the cylindrical size and curvature are varied simultaneously. However, given the extensive combinations and permutations of potential structures, a comprehensive analysis of this nature may be more suitably addressed in future research endeavours. Employing advanced optimization techniques, such as particle swarm optimization, could prove helpful in identifying the most optimal configuration combinations.

Chapter 7 Graded Hierarchical sub-structures and Graded Fractal Self-similarity

Apart from topological enhancements and subsequent integration with gradient based approach in conventional auxetic structure such as REAT structure as elucidated in the previous chapter, this study similarly proposes a series of novel fractal honeycombs based on the combination of functionally graded concepts with fractal self-similarity features, which are constructed by varying the fractal parameter in each layer of the traditional self-similar honeycombs.

Two graded fractal honeycombs with symmetric gradient and another two with asymmetric gradient are presented, and their dynamic crushing behaviors are numerically investigated. The numerical approach is first validated by comparing against theoretical and experimental data with good agreements achieved. Subsequently, it is demonstrated that the SG-I honeycomb can present the best EA behavior (89% higher than traditional honeycomb) for low velocity impact, while SG-II honeycomb performs the best for SEA (17% larger than traditional honeycomb) for high velocity impact. Furthermore, deformation patterns under dynamic crushing can be controlled by the design of graded fractal honeycombs through the introduction of different gradient distributions. The graded fractal honeycombs present significant improvements to the absorbed energy and MCF over traditional honeycombs, offering a new route to the design and optimization of future lightweight EA systems with improved safety protection performance.

Furthermore, inspired by nature, an innovative graded hierarchical honeycomb is proposed in this study to enhance its crashworthiness behaviors. The structure is created by replacing cell walls of regular honeycombs with triangular and hexagonal sub-structures and varying the hierarchical length ratio in each layer. The in-plane crushing performances of the graded hierarchical honeycombs are comprehensively analyzed and compared with their uniform hierarchical counterpart. The former exhibits a progressive deformation model under different impact velocities and three plateau stages can be observed under in-plane crushing loads

through theoretical predictions. The triangular sub-structure presents better EA than the hexagonal sub-structure, and its SEA is enhanced by up to 32.2% as compared to the uniform hierarchical honeycomb. The present study suggests that the combination of hierarchy and gradient is an effective strategy to improve the dynamic crushing behaviors of honeycombs, which can be further explored in protective devices to enhance their impact resistance.

7.1 Topological description of novel honeycomb structures

7.1.1 Novel honeycomb with functionally graded fractal self-similarity

The traditional fractal honeycomb, which is also known as the uniform self-similar (US) honeycomb, is constructed by replacing every vertex of the traditional hexagonal (TH) honeycomb with a narrowed hexagon. In a similar way, the higher-ordered fractal honeycomb can be achieved by altering all vertices of lower-ordered fractal honeycombs as narrowed hexagon [40]. In the present work, only the 1-st order fractal honeycomb with the wall angle of 120o is taken into account, and the representative unit for the traditional US honeycomb is exhibited in Figure 7.1. Let lh and lc denote the lengths of the cell wall of the regular hexagonal honeycomb and the cornered hexagon, respectively. Then, the fractal parameter γ = lc /lh can be introduced to represent the fractal behaviors, and its smallest and largest values are γ = 0 (reduced to TH honeycomb) and γ = 0.5, respectively, as shown in Figure 7.1.

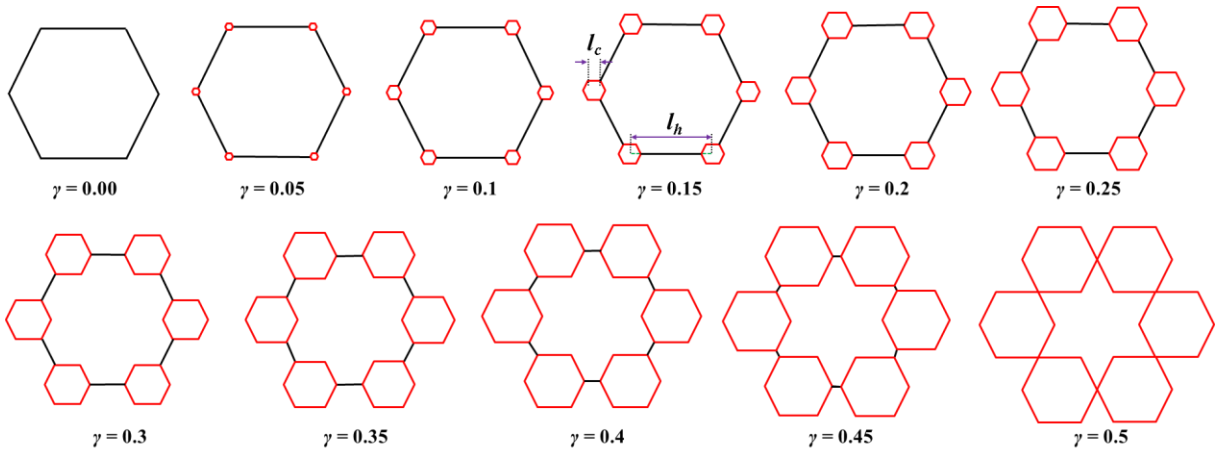

Figure 7.1. Representative unit cells of US honeycomb with various fractal parameters. From minimal value of γ = 0 represents TH honeycomb whose fractal cornered hexagonal at each vertex is considered to be a node, to maximal value of γ = 0.5 where straight ligaments of the honeycomb is completely replaced by the sub-structure honeycomb.

By varying the fractal parameter γ for each layer, the functionally graded fractal honeycomb can be achieved, as shown in Figure 7.2. Herein, four types of fractal honeycomb including two asymmetric and two symmetric graded distributions with a total layer number N = 10 are considered in the present study. For the asymmetric graded I (AG-I), the fractal parameter changes gradually from the bottom γ_1 = 0.5 to the top γ_{10} = 0.05 at regular intervals of step size Δγ = 0.05, while an opposite distribution for the fractal parameter is employed for the asymmetric graded II (AG-II). The subscript for the fractal parameter in γi denotes the i-th layer of the graded fractal honeycomb, numbered from the bottom upwards. For symmetric graded I (SG-I) type, the fractal parameter in the middle layer is γ_5 = 0.1, and it enlarges gradually to the top and bottom at regular intervals of step size Δγ = 0.1. On the other hand, for the symmetric graded II (SG-II), the fractal parameter in the middle layer is the largest at γ_5 = 0.5, which decreases gradually to the top and bottom at regular intervals of step size Δγ = 0.1.

For the TH honeycomb with wall thickness of t and wall length lh, its RD can be given as a function of t / lh, i.e., [30]

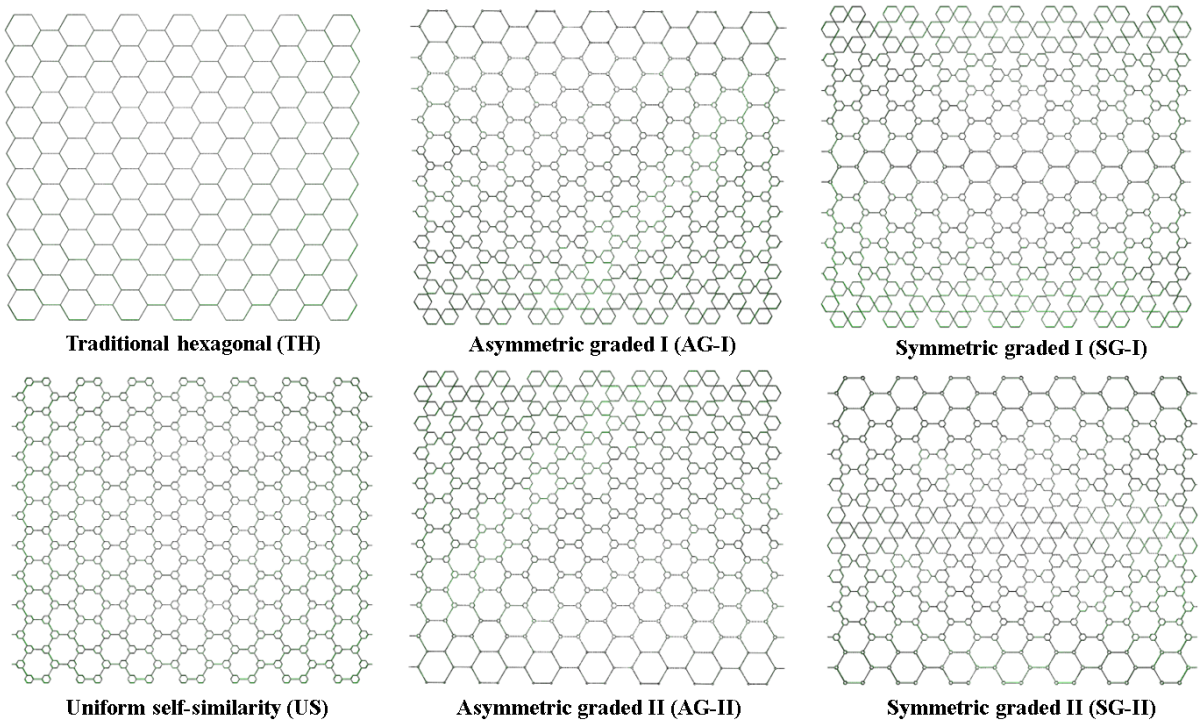

Figure 7.2. Geometrical configurations of graded fractal honeycombs. Graded strategy is achieved through unidirectional (asymmetric) and bidirectional (symmetric) arrangement of fractal parameters.

7.1.2 Graded honeycomb with hierarchical architecture

Configurations	Triangular Substructure	Hexagonal Substructure
	UH_TRI	UH_HEX
Uniform Hierarchy	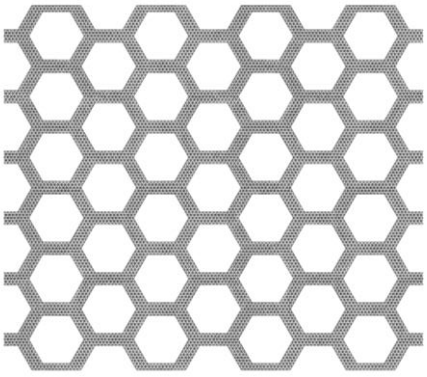	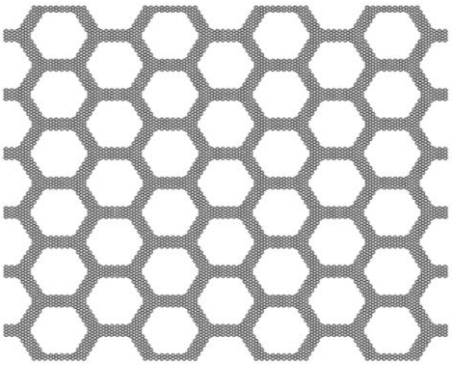
	NGH_TRI	NGH_HEX

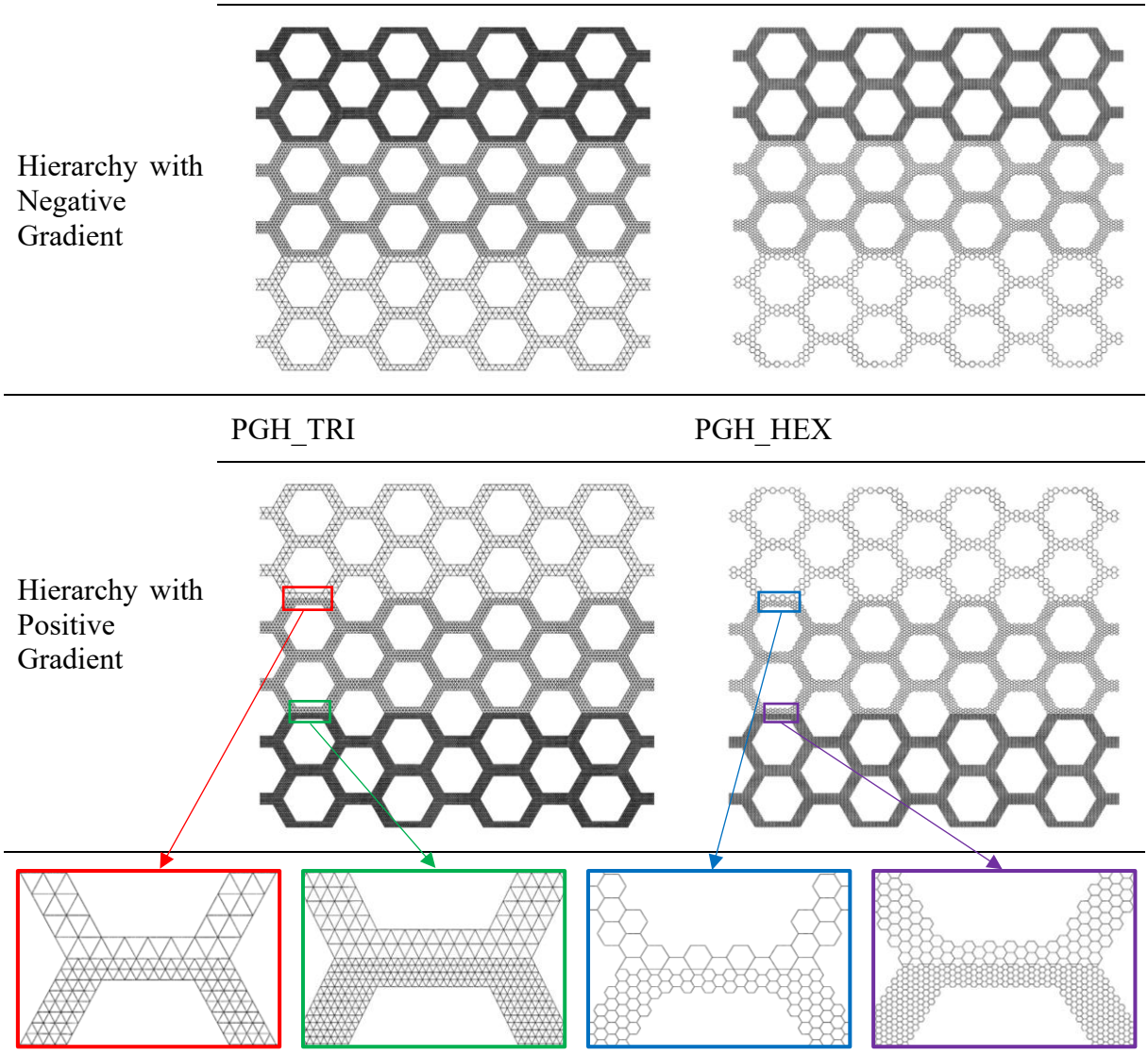

Figure 7.3. Illustration of graded hierarchical honeycomb with Triangular (-TRI) and hexagonal (-HEX) substructures. NGH is abbreviated to represent honeycomb of negative gradient in hierarchy with denser top layer and sparse bottom layer, while the opposite is denoted as PGH honeycomb with denser bottom and sparse top layer.

7.2 Theoretical Development, Fabrication and Validation

The following section builds upon the theorectical validation of experiment and simulation illustrated by Figure 7.4. The plateau stress of graded hierarchical structures under in-plane crushing is analyzed theorectically through the use of two-scale method introduced by Qian and Chen[139]. In this method, the substructures within the honeycomb is taken as homogenized solid yielding perfectly plastic behaviour. As such, simplifed model can be generated to represent the deformation modes shown in Figure 7.4 below. The inclined

ligaments marked by red lines undergoes plastic deformations characterized by bending by rotating about vertex A by an angle of $\theta = \pi/3$ towards horizontal and at the same time shortened by $\Delta L = |OA - OA'|$ during the compression. Hence, the inclined ligament is marked to deform from OA to OA′ during deformation as depicted in Figure 7.4 below. Therefore, the energy dissipation involes bending rotation of two plastic hinges at point A and B and the shortening deformation from AB to AB′. The following analysis is formulated by neglecting the PR effect of the structure as well as any formation of plastic hinges in the horizontal ligaments.

Due to the symmetrical nature of hexagonal unit cell, only half of the unit cell is taken into consideration, and so the external work imposed by half of the unit cell is calculated as:

$$W_{ext} = \frac{3}{2} N_i l_i b \sigma_{pl} \Delta \mathrm{y} \tag{7.1}$$

from which σ_{pl} is the plateau stress in i-th gradient layer of graded hierarchical honeycomb and $\Delta y = \sqrt{3} N_i l_i / 2$ denoting the displacement moved by the half unit cell when the plastic hinge (red) is deformed to horizontal position which then transforms W_{ext} into:

$$W_{ext} = \frac{3\sqrt{3} N_i l_i b}{4} \sigma_{pl} \tag{7.2}$$

Next, considering the rotation of two plastic hinges in a unit cell is given by $W_b = 2M_b \Delta\theta$ with $\Delta\theta = \pi/3$ and plastic bending moment generated by the plastic hinge:

$$M_b = 2 \int_0^{\frac{h}{2}} \sigma_p^{sub} b y \, \mathrm{d}y = \frac{1}{4} b h^2 \sigma_p^{sub} \tag{7.3}$$

in which σ_p^{sub} defines the yield stress of the substructure and b is the out-of-plane thickness of the honeycomb.

Originally, the substructure was assumed to be homogenized solid structure, now to release the assumption, its equilateral yield stress σ_p^{sub} can be estimated by

$$\sigma_p^{sub} = C_{sub}\bar{\rho}_{sub}^2\sigma_{mat} \tag{7.4}$$

where σ_{mat} is the yield stress of the base material. The coefficient C_{sub} denotes the relationship between in-plane equilateral stress and the RD of the pure triangular and hexagonal honeycombs. These coefficients were obtained throught FE simulations on parametric study on the equilateral yield stress of pure triangular and hexagonal honeycomb with various RD. The relationship is obtained through curve fitting of the FE results. This topic has been comprehensively analyzed by several researchers such as Gibson and Ashby[42] in which it systematically examine the mechanical responses of honeycombs with different cell geometries. Similarly, Qiao and Chen[139] and Qiu et al.[195] analyzed the collpase stress of equilateral triangular honeycomb and pure honeycomb, respectively. Both studies unanimously concluded that the equilateral yield stress is proportional to the second-order RD of pure triangular and pure hexagonal honeycombs. Hence, $C_{tri} = 0.534$[139] and $C_{hex} = 0.271$[195] as derived from these studies are deployed for triangular and hexgonal substructure, respectively.

Furthermore, $\bar{\rho}_{sub}$, the RD of substructure can be denoted as follows:

triangular substructure;

$$\bar{\rho}_{tri} = \frac{6t}{\sqrt{3}l_i} \tag{7.5}$$

hexagonal substructure;

$$\bar{\rho}_{hex} = \frac{2t}{\sqrt{3}l_i} \tag{7.6}$$

Therefore, the energy dissipated by the bending moment of the two plastic hinges can be formulated as:

$$W_{bend} = 2M_b\Delta\theta = \frac{\pi}{6}bh^2\rho_p^{sub} \tag{7.7}$$

The second part of energy dissipation is the shortening deformation OA calculated as $\Delta L = |AB - AB'| = N_i l_i(1 - cos\theta) = \frac{N_i l_i}{2}$. The plastic dissipation W_{short} can thus be derived as:

$$W_{short} = A\sigma_\rho^{sub}\Delta L = \frac{1}{2}N_i l_i hb\sigma_\rho^{sub} \tag{7.8}$$

Finally, by conservation of energy under the whole process would be denoted by:

$$W_{ext} = W_{bend} + W_{short} \tag{7.9}$$

Thus, by substituting the formulas discussed above into the above equation, the plateau stress can thus be finalised as:

$$\sigma_{pl} = \left[\frac{2}{3\sqrt{3}}\frac{h}{N_i l_i} + \frac{2\pi}{9\sqrt{3}}\frac{h^2}{(N_i l_i)^2}\right]\sigma_\rho^{sub} \tag{7.10}$$

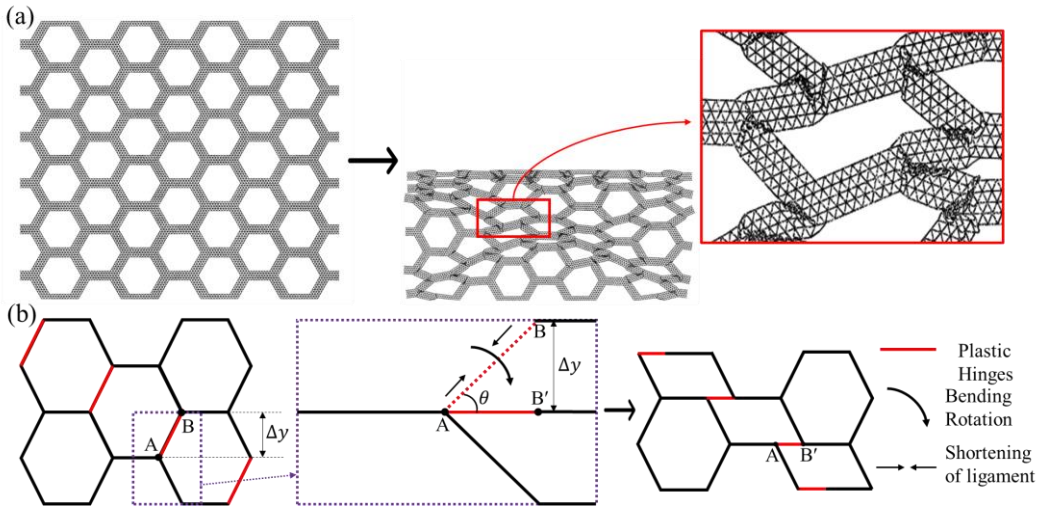

Figure 7.4. Schematic diagram for deformation mechanism for graded hierarchical honeycomb: (a) deformation pattern predicted by FE simulation that is simplified by (b) representative model for theoretical analysis.

Quasi-static compression experiments were carried out to provide a validation of the proposed FE simulation method using shell elements. Apart from fabrication of the honeycombs, some

dog-bone-shaped specimens were also printed by using SLA printing technology to obtain the material property of the base material, and dimension of the bone-shaped specimen is illustrated in Figure 7.5(a) below. The uniaxial tensile tests on the bone-shaped specimens were performed using the universal test machine with a tensile speed of 1 mm/min, and the specimens before and after tensile tests are shown in Figure 7.5(b). The SS curve of this base material is presented in Figure 7.5(c). From the figure, Grey-Pro resin exhibits a typical elastic-plastic property with Young's modulus $E = 1.1 \pm 0.2\,GPa$ and yield stress $\sigma_0 = 28.2 \pm 0.3\,MPa$.

The honeycomb samples were placed on a fixed plate and were crushed by a downward moving plate with a compression velocity of $2mm/min$. The FE-models with the same geometrical parameters and boundary conditions were established and discussed previously in section 2.2.2 to compare with the experimental results.

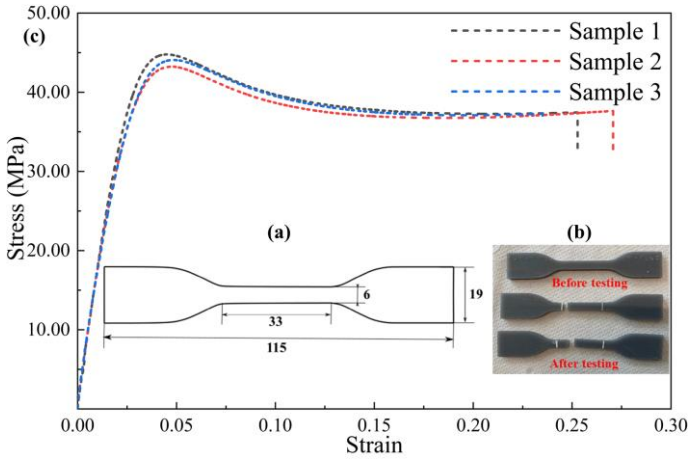

Figure 7.5. Tensile specimens for material characterization: (a) dimensions of tensile samples; (b) specimens before and after tensile tests; (c) SS curves of base material obtained from uniaxial tensile test.

In the case for hierarchical structures, computational investigations on the crashworthiness of hierarchical structures under dynamic loading are performed using nonlinear finite element software ABAQUS/Explicit as well. Shown in Figure 7.6 below, the hierarchical structure with size of L×H×Z is simulated, where L and H are the horizontal and vertical lengths of the structure, and Z being the out-of-plane thickness of the honeycomb. In Figure 7.6 (b) and (c),

the graded fractal honeycomb is composed of 13 cells in the horizontal direction and 10 cells in the -vertical direction and the graded hierarchical honeycomb with 7 unit cells in x-direction and 6 unit cells in y-direction, respectively.

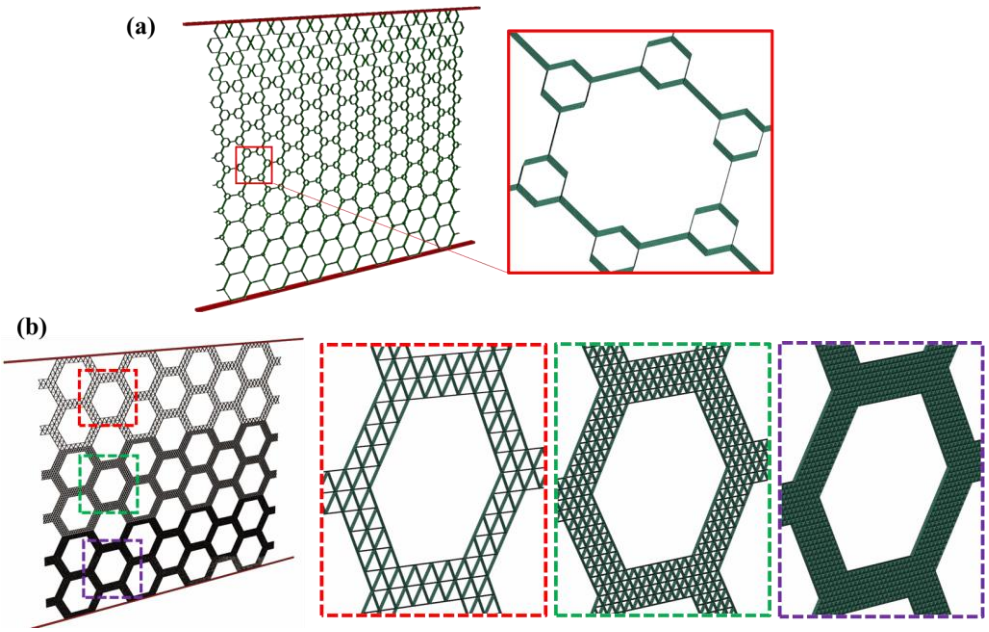

Figure 7.6. (a) Diagram of in-plane analysis of graded fractal honeycomb and (c) graded hierarchical honeycomb.

The honeycomb is meshed by using four-node, reduced-integration, shell elements (S4R), and an average element size of 0.2 mm is adopted for both structures shown in Figure 7.6. The honeycomb is being sandwiched between two analytically rigid blocks on top and bottom sides. The bottom block remains stationary while the top block moves down on the structure with a constant velocity varying between 3 m/s and 100 m/s in the simulations. A general contact "all with self" criterion is chosen to simulate the contact behavior between the honeycomb and rigid blocks as well as to prevent any interpenetration of folding walls during crushing. The general contact is more computationally efficient than surface-to-surface contact and self-surface contact definition as general contact automatically encompass the said criteria. At the same time, the frictional coefficient at all contact points is specified as 0.2 for the contact along tangential direction while contact along normal direction is set as "hard contact"[33][107]. As

observed from the experiment, linear, nonlinear and rotation deformations mostly appeared in-plane hence the deformation along its thickness (*z*-direction), the rotation about *x*- and *y*-directions for all nodes of the honeycomb are constrained while the deformation across *x*- and *y*- directions as well as rotation about *z*- direction are set free to accurately capture its in-plane deformation [33][107]. Therefore, to avoid any misrepresentation by potential out-of-plane buckling and eliminate boundary effects, the displacement for all nodes of the honeycomb along the out-of-plane direction is constrained to ensure the plane strain state of deformation.

Finally, to obtain a reasonable element size for the hierarchical honeycomb for the following simulation study, a mesh sensitivity analysis is performed firstly. Four different element sizes including 0.8 mm, 0.4 mm, 0.3 mm, and 0.2 mm are taken into consideration for the convergence study. The crushing velocity is set as v = 15m/s for all of the convergence analyses. As observed from Figure 7.7, the SS curve and the SEA-strain curve converges with refinement of element size. The deviations in the SS curve and the SEA-strain curve shrinks as the element size is reduced from 0.8mm to 0.3mm, which becomes even smaller when the element size is smaller than 0.3mm. To balance between computational efficiency and accuracy, element size of 0.2mm is adopted.

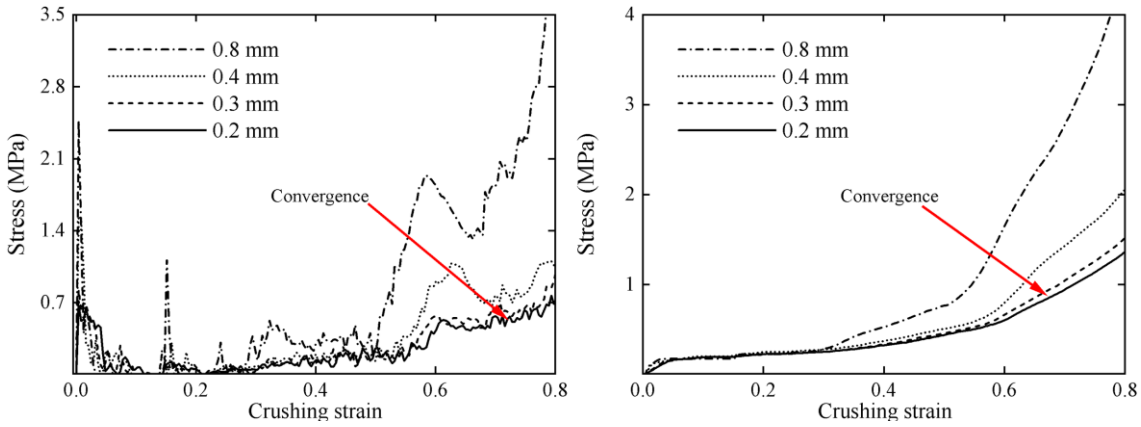

Figure 7.7. (a) SS and (b) SEA-strain curves for hierarchical honeycomb with different element sizes. Convergence is observed from 0.3 to 0.2mm wall thickness. The crushing strain for this chapter is defined as engineering strain.

The deformation modes of the hierarchical honeycombs at various engineering strains predicted by FE simulations and experiments are compared in Figure 7.8 below. The deformation patterns of UH-Hex and UH-Tri in the experiments are very well captured by the FE simulation, validating the latter's ability to provide computational analysis on crushing behaviors of hierarchical structures. In addition to comparison in deformation modes, the SS curves of UH-Hex and UH-Tri are also compared between simulation and experiments. Despite strong agreement in deformation modes, there is slight deviation between the experiment and FE simulation can be found in the elastic and densification region of the SS curve due to partial fracture of honeycomb samples not taken into consideration in the simulations.

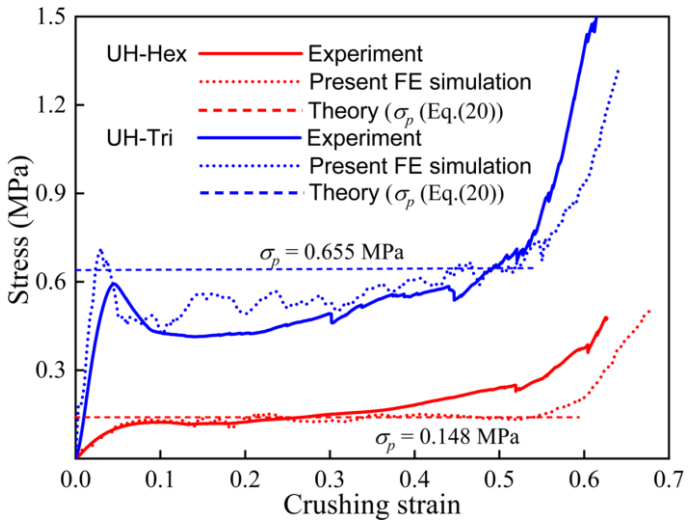

Figure 7.8. Validation between SSs of UH-Hex and UH-Tri honeycombs predicted by FE simulations and experiments. Significant agreement is observed between experiment, simulation and theoretical analysis. SS is segmented into three regions namely elastic, plateau and densification region as illustrated in the diagram. Slight deviation in elastic and densification region is observed due to fracturing of material in experiment not taken into account for FE simulation.

Nevertheless, the plateau stress and the overall SS curves from the experiment are fairly well-represented by the simulation and theoretical analysis which provide assurance that the FE method can provide satisfactory accuracy in subsequent analysis of crushing mechanisms of hierarchical honeycombs.

	Strain (ε)	Experiment	Simulation
UH-Hex	0.00	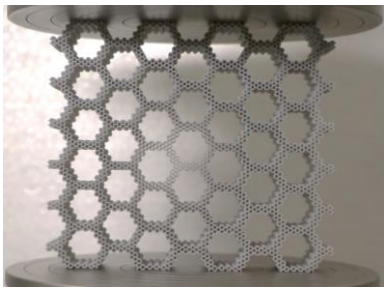	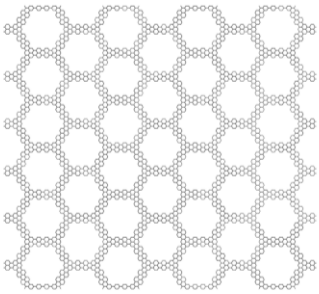
	0.25		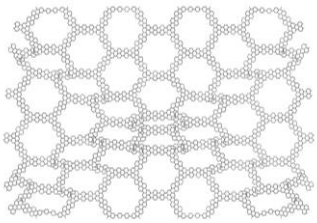
	0.40	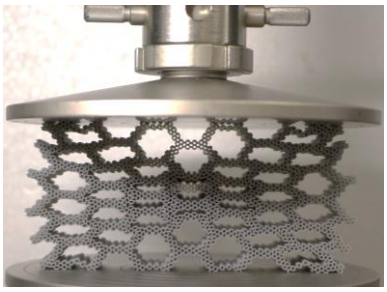	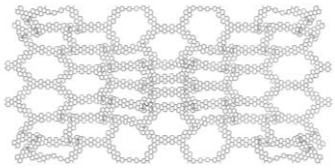
	0.60	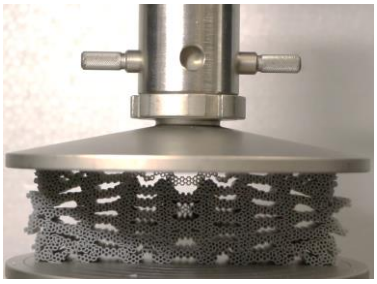	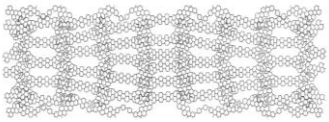
UH-Tri	0.00	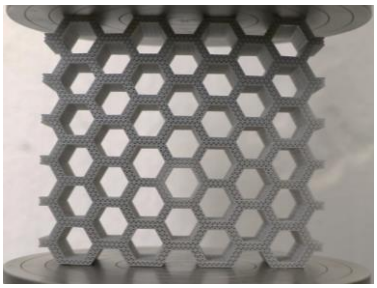	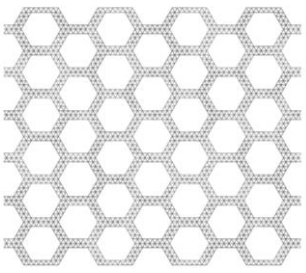

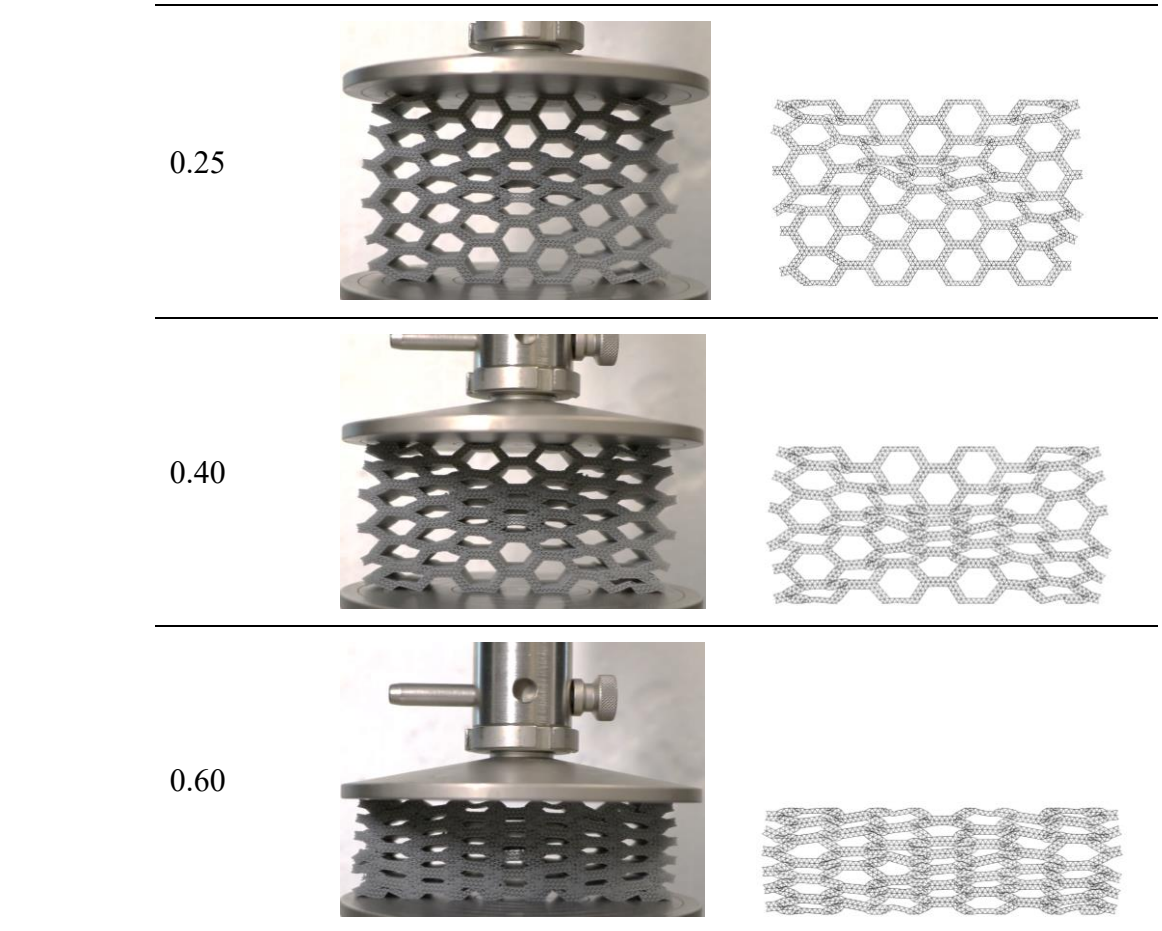

Figure 7.9. Comparison on deformation patterns between results from experiments and FE simulations. A side-by-side comparison had shown strong agreement between experiments and FE simulations in (a) UH-Hex and (b) UH-Tri.

7.3 Results and Discussion

7.3.1 Hierarchical fractal self-similar structure

This section aims to detail the investigation and evaluation of the crashworthiness of graded fractal self-similar honeycomb. The influence of gradient configuration, impact velocity and cell wall thickness on deformation mode and EA are revealed below.

For dynamic crushing under low impact speed of $V = \frac{3m}{s}$ shown in Figure 7.10 and Figure 7.11, both TH and US honeycomb begin to collapse simultaneously at the impact and distal end which resulted in "X" shaped shear band. On the other hand, the collapse started only at the layers with smallest fractal parameter γ for all graded fractal honeycombs. As illustrated in

Figure 7.11, the top and bottom layers of AG-I and AG-II collapsed in the early compression stage, respectively. Whereas, in SG-I, the middle layers is crushed first under impact loading. In contrast, cell of SG-II in the top and bottom layers collapse simultaneously. This drastic difference in deformation pattern provides strong implication that the graded fractal design is influential in controlling the deformation of honeycombs.

7.3.1.1 Influence of gradient configuration

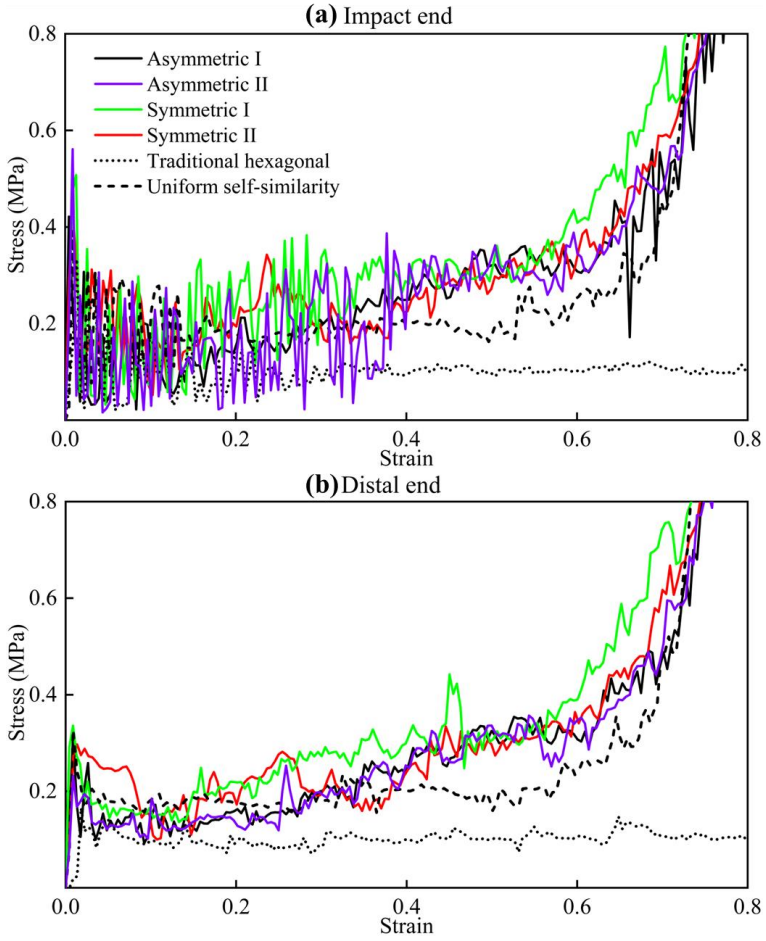

Figure 7.10. SS response of various graded fractal honeycombs under $V = 3m/s$: (a) Impact end and (b) distal end.

Consequently, the influence of graded fractal design on SS relationships is also profound in Figure 7.11, which indicated that the SS relationship can also be controlled via the graded fractal design. An obvious increment of plateau stress is achieved from introducing graded fractal design as compared to its uniform counterparts.

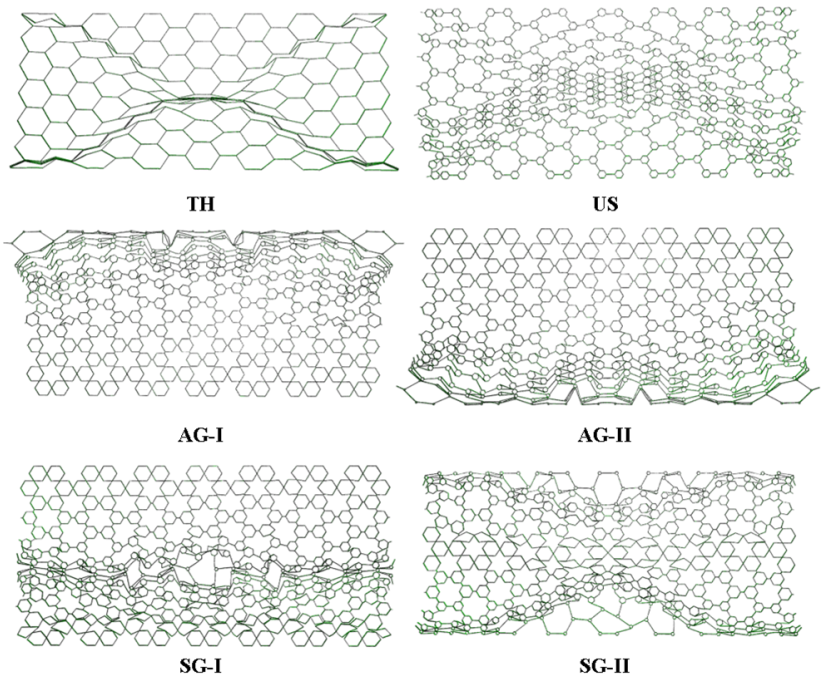

Figure 7.11. Dynamic compressive response of various fractal graded honeycombs under $V = 3m/s$ under strain $\varepsilon = 0.4$.

Among the graded designs, honeycombs with symmetric gradient (SG-I and SG-II) can provide higher plateau stress than asymmetric gradient (AG-I and AG-II) as the amount of material mobilized for deformation during early stage of crushing is more in symmetric than asymmetric gradient. The dynamic stress in the impact and distal end are almost same in magnitude at such a low impact speed.

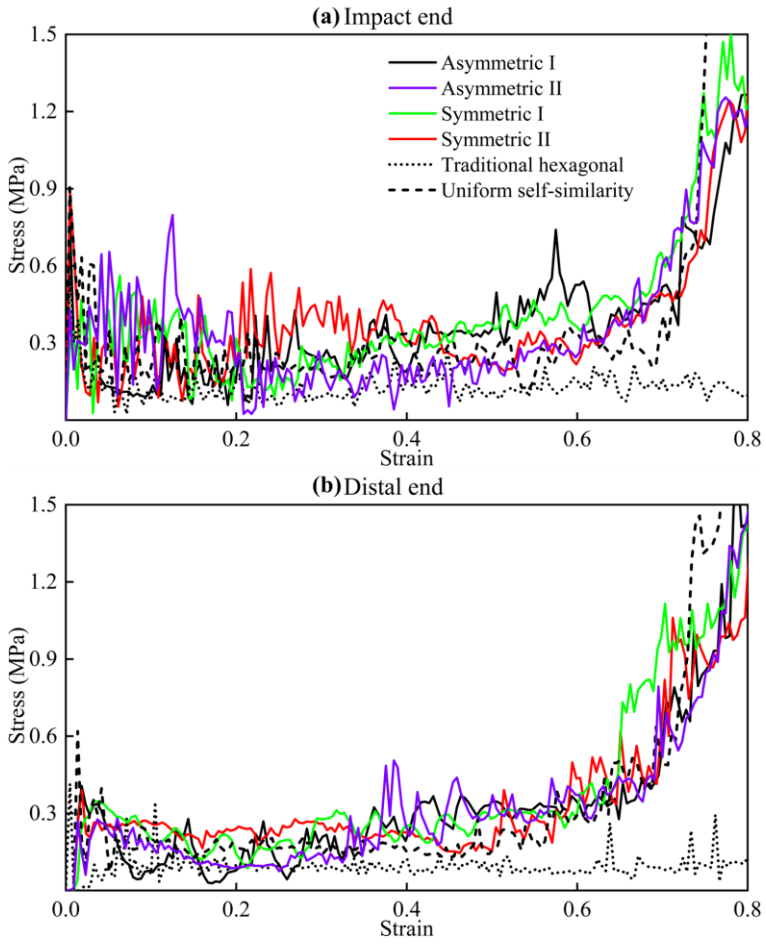

Figure 7.12. Illustration of SS for dynamic crushing responses of various graded fractal designs under impact velocity of $V = 15m/s$. The SS graphs are separated into (a) impact and (b) distal end for comparison.

When the impact velocity increases from $3m/s$ to $15m/s$, a transition in deformation modes is observed as the deformation patterns differs significantly among the graded fractal structures in Figure 7.13 and with the counterparts underwent slower impact speed in Figure 7.11. Starting with TH and US honeycombs, a transition from "X" shaped shear band to "V" shaped shear band located close to impact loaded end. Similar deformation pattern is observed in AG-I and SG-I where most of the lower fractal parameter γ are present. Therefore, for AG-II honeycomb, the "V" shear band actually appeared on the bottom of the structure closer to the distal end due to the smaller fractal parameter in this layer, and the layers near the impact end deformed layer by layer. Only layer by layer deformation is also reproduced in SG-II near the impact end and the lack of shear band is primarily due to the layer with lower fractal parameter is in direct

contact with the impact end. Again, there are significant differences among the deformation patterns among the structures indicating a clear influence and control of graded fractal design over the dynamic characteristics of fractal honeycombs.

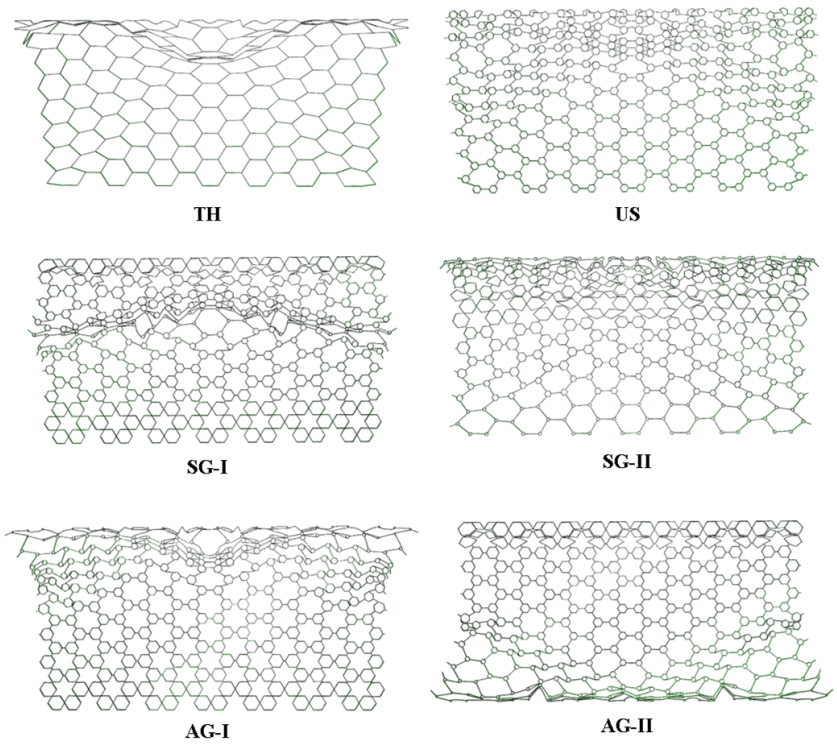

Figure 7.13. Deformation modes under $\varepsilon = 0.40$ under impact velocity of $15m/s$.

From the SS curves in Figure 7.12, the dynamic stress in the impact end is now slightly higher than that of the distal end, implying that the inertia effect is present during medium impact velocity to a certain extent. Both Figure 7.10 and Figure 7.12 had definitively illustrated the advantage of hierarchy over conventional hexagonal honeycomb through the increase in plateau stress. The graded fractal design in turn performed better than the US model especially at the later stage of the compression between $\varepsilon = 0.4$ and 0.6.

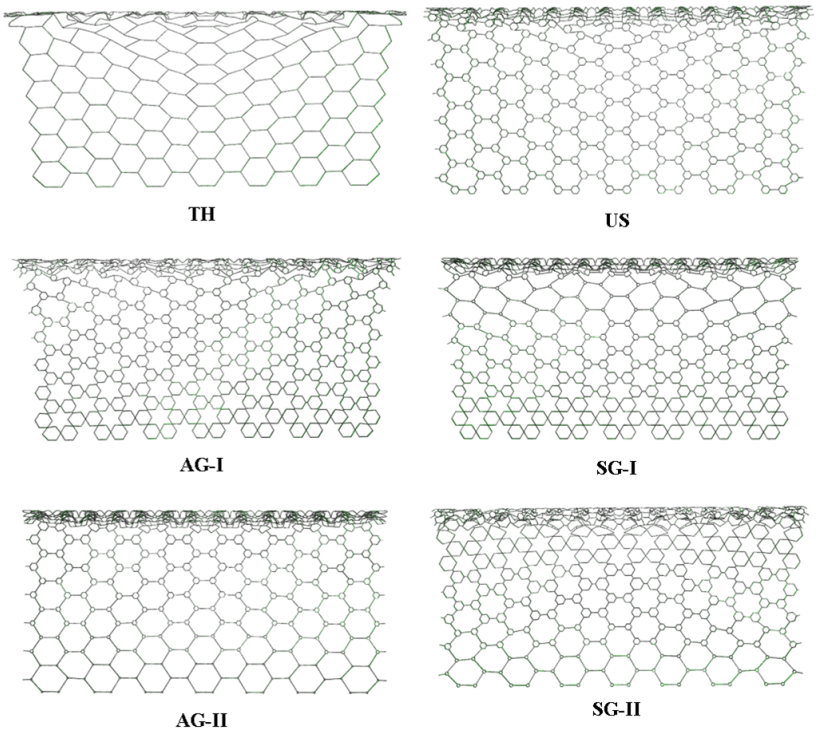

Figure 7.14. Dynamic deformation modes of graded fractal honeycombs under high impact velocity $V = 60m/s$

The typical SS relationship and deformation patterns for various graded fractal structures under high velocity loading are presented in Figure 7.14 and Figure 7.15 above. The deformation modes are completely different from the low and medium impact velocity with no observable transition that was seen between low and medium impact speeds. All honeycombs deform row by row with the crushing starts from the impact end and propagates to the distal end, leading to "I" deformation pattern. Further, a shock front is formed in the densified section located next to the impact end due to high impact velocity. Such deformation mode is insensitive to any gradient distribution because the distinctively greater plateau stress at the impact end over the distal end signifies the predominant presence of inertia effects. No significant difference is observed between the graded fractal structures for the impact end. Apart from deformation modes and SS previously discussed, SEA and MCF are two important indicators of crashworthiness for EA systems.

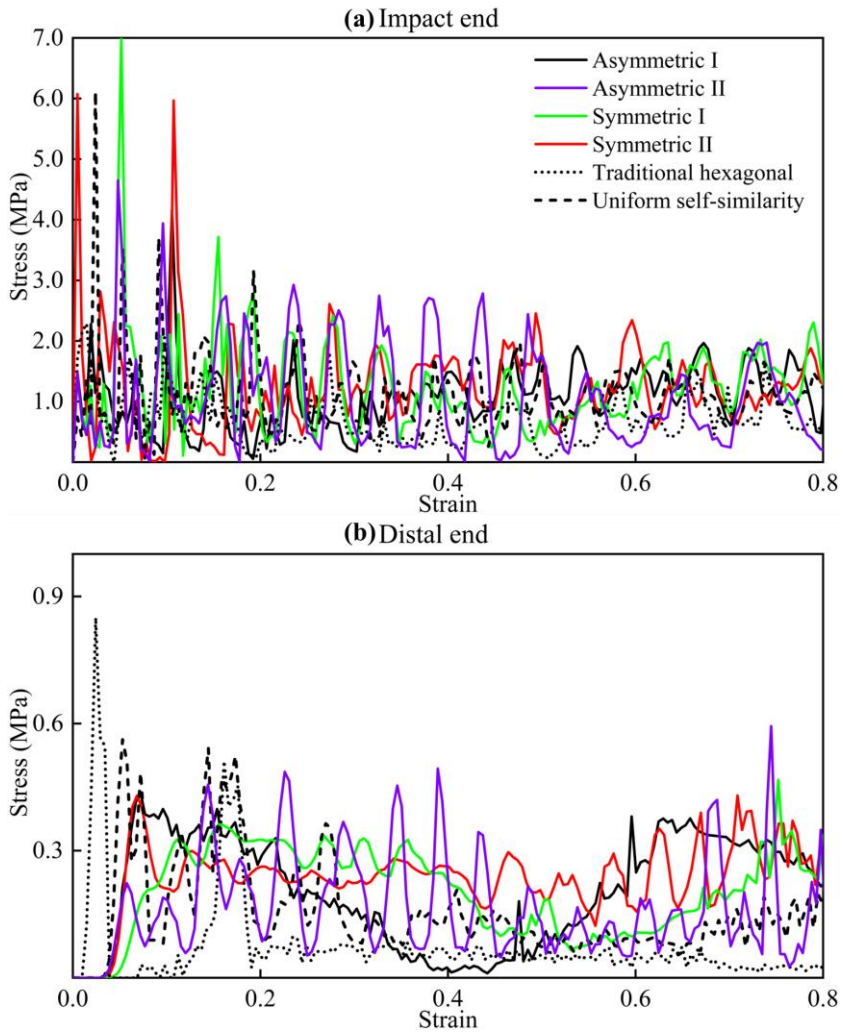

Figure 7.15. SS curve of various graded fractal structures under high impact velocity of $V = 60m/s$.

Shown in Figure 7.16 below, SEA and MCF of different configuration under low impact velocity is demonstrated below. Comparative to traditional hexagonal honeycomb, SEA of all graded fractal designs increase throughout the compression process shown in Figure 7.16(a), indicating significantly better performance in EA capacity. In particular, SG-I has the most profound improvement in EA capacity among the graded designs.

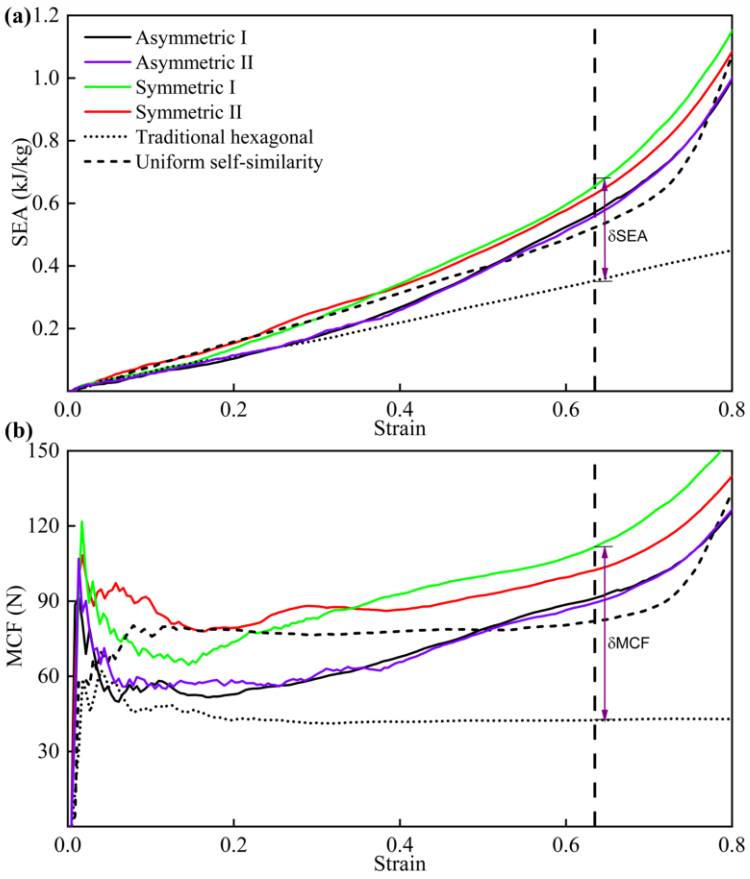

Figure 7.16. (a) SEA and (b) MCF as a function of compressive strain for various fractal honeycomb at $V = 3m/s$.

It is further demonstrated in Figure 7.16(b) that the behavior in MCF varies drastically among the six designs studied in this work. Peaks in MCF are observed at a small compressive strain, which then slightly decreases and then increases with compression strain. At small strain between 0.1 and 0.3, the largest MCF is from SG-II while SG-I honeycombs produce the largest overall MCF at the later stage of the compression at $\varepsilon > 0.4$.

7.3.1.2 Influence of impact velocity

The dynamic SS curve of SG-II honeycombs whose impact and distal end are plotted in Figure 7.17 (a) and (b), respectively. The difference between the plateau stress of the impact and distal end are negligible under low and medium impact velocity from $3m/s$ to $15m/s$. This difference, however, become significant when impact velocity is raised to high impact velocity due to the dominant inertia effect under high impact velocity. The dynamic stress in the distal

end is also fairly similar to that of impact end under low impact velocity as there is sufficient time for impact wave to propagate from impact to distal end. Furthermore, at the distal end, as the velocity is raised to high impact velocity range, there is gap in dynamic stress between the low and the high impact velocity after 0.6 compression strain, which indicates that the impact wave only reach the distal end only at very large deformation and that the densification of structure only concentrates at the impact end at high impact velocity.

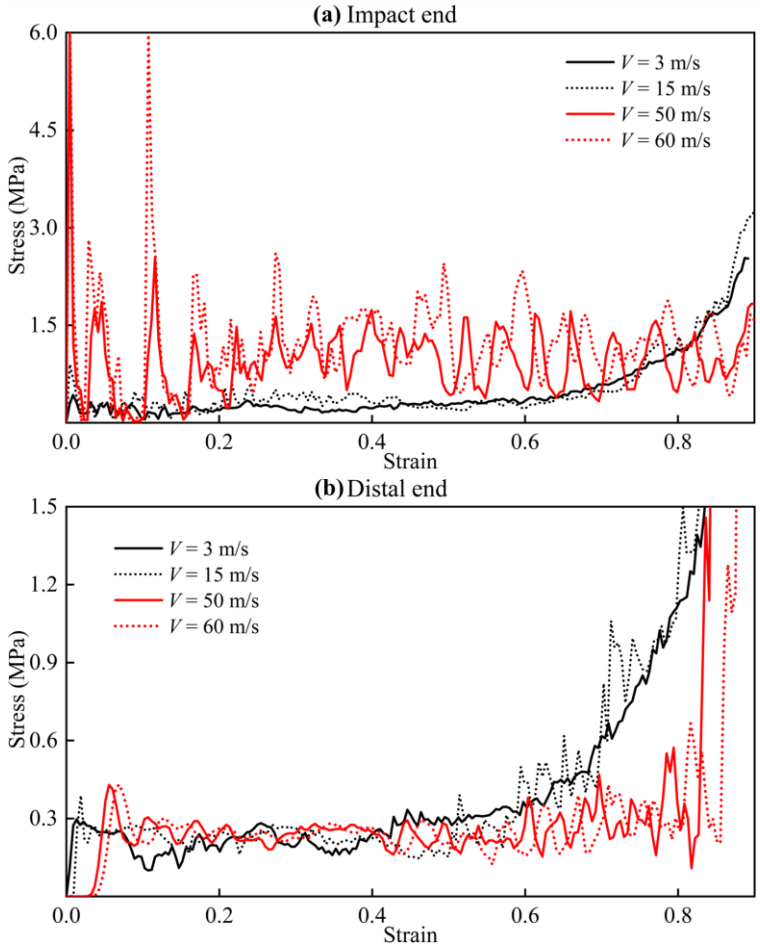

Figure 7.17. SS curve of SG-II honeycombs under various impact velocities for its (a) impact and (b) distal end.

The SEA and MCF of each graded fractal honeycombs are compared between one another among the four impact velocities considered in this study shown in Figure 7.18. The values of SEA and MCF were taken at compressive strain of $\varepsilon = 0.65$ for fair compression. When compared with TH honeycomb, the maximum increment in SEA and MCF achieved by fractal graded honeycombs are 89% and 188%, respectively. The relative increment is reduced as the

impact velocity is increased, with maximum increase of 17% in SEA and 43% in MCF. At low impact velocity of $3m/s$, SG-I honeycomb exhibits the best absorption characteristics while SG-II presents the best performance at medium and high velocities ($15m/s$ and $60m/s$). These findings above indicate the availability of geometric configurations for design for EA at applied impact velocities.

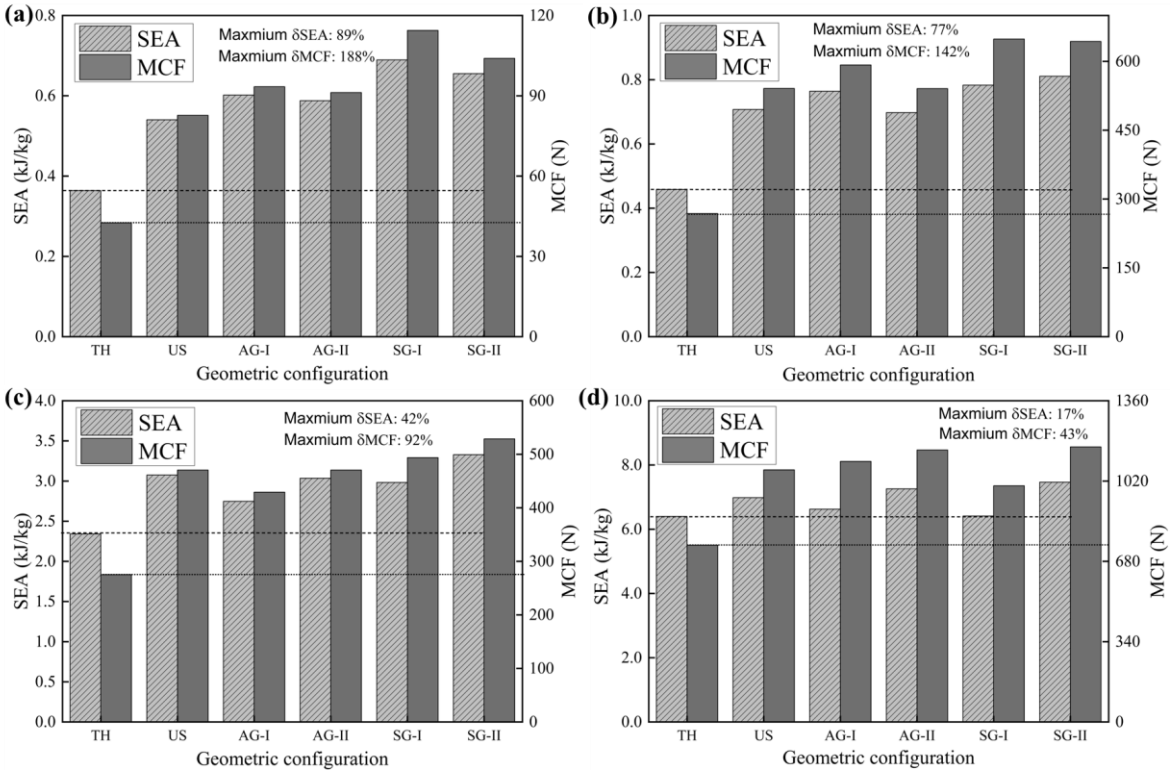

Figure 7.18. Bar Diagram comparison of SEA and MCF between various graded fractal structures under different impact velocity; (a) $3m/s$, (b) $15m/s$, (c) $60m/s$, (d) $100m/s$.

The SEA and MCF of the graded fractal honeycombs as a function of velocity are also compared among the graded fractal structures in Figure 7.19. Generally, graded fractal structures are able to capture more EA and enhance MCF as compared to TH honeycombs in all impact velocities. SG-I has the largest improvement in SEA and MCF at lower impact velocities while SG-II performed best at higher impact velocities. In lower impact velocities, most graded structure is able to perform better in SEA and MCF than US. However, US performed better than some fractal graded structures at higher impact velocity except for SG-

II which had consistently provided better crashworthiness characteristic for all impact velocities considered in this study.

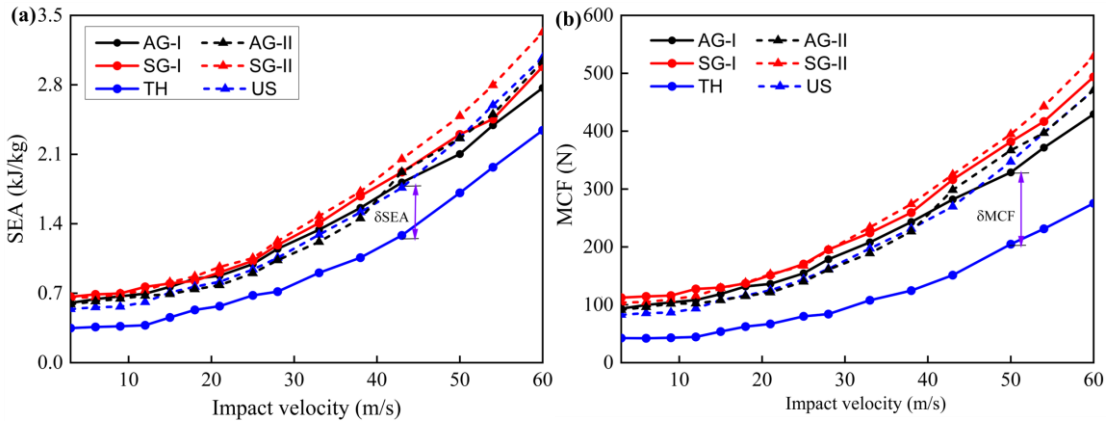

Figure 7.19. (a) SEA and (b) MCF as function of impact velocity for various graded fractal honeycombs.

7.3.1.3 Effect of cell wall thickness

The impact from the cell wall thickness of the graded fractal honeycombs on the SS curves is illustrated in Figure 7.19 below. The influence of cell wall thickness on AG-II honeycomb is analyzed under impact velocity of $V = 15m/s$. The dynamic stress is founded to be enhanced with the increase in the thickness of the cell walls. An obvious increase in plateau stress with the cell wall thickness leads to increase in EA capacity by the graded fractal honeycomb. Further comparison is done on the SESA of different graded fractal honeycombs of cell wall thickness of $t = 0.1mm$ and $0.3mm$ shown in Figure 7.21(a) and (b), respectively.

Figure 7.21 compares the SEA to compression strain of all designs at two different thicknesses. As observed, the values of SEA increase significantly with cell wall thickness for all graded designs in this study. The AG-II honeycomb has the largest SEA at earlier compression strain smaller than 0.4, while SG-II honeycomb exhibits the greatest EA capacity when compressive strain is larger than 0.4.

The influence of cell wall thickness on SEA and MCF of graded fractal honeycombs are further illustrated in Figure 7.22. The positive impact of cell wall thickness on SEA and MCF is clearly

observed and the incremental ratio of SEA for is the largest for SG-II honeycomb which has achieved 57%, 81% and 77% relative to the TH honeycomb for $t = 0.1mm$, $0.3mm$ and $0.5mm$, respectively. On the other hand, the maximum increment with respect to TH honeycomb in MCF are approximately 111%, 145% and 140% for $t = 0.1mm$, $0.3mm$ and $0.5mm$, respectively.

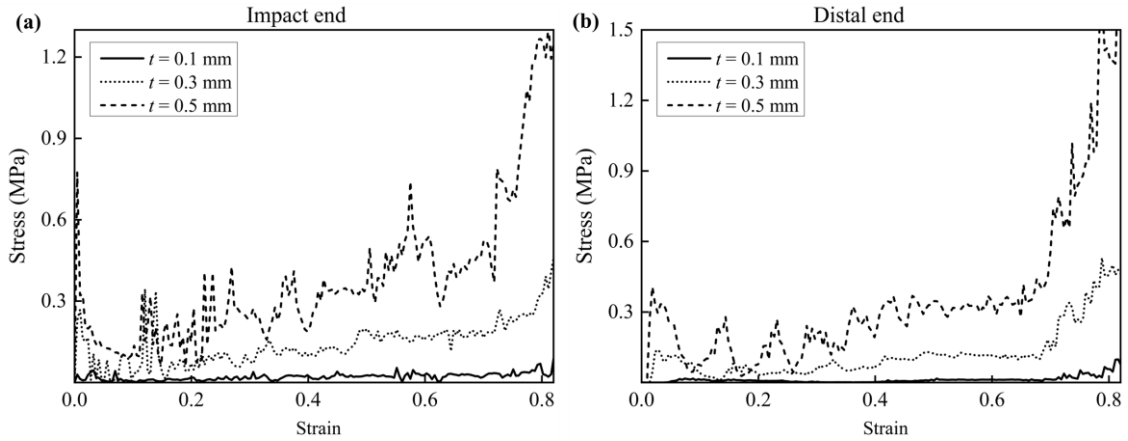

Figure 7.20. SS of AG-II honeycomb of different thickness at (a) impact and (b) distal end.

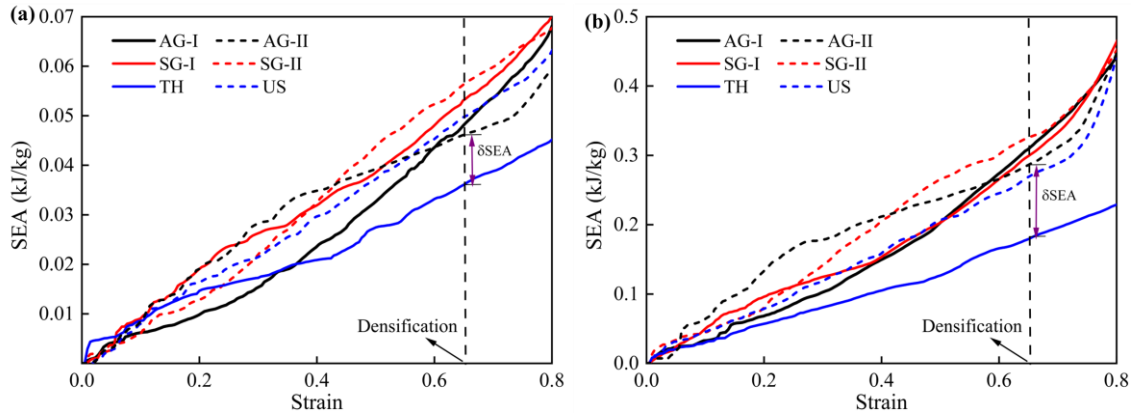

Figure 7.21. Comparison of SEA from different graded fractal honeycombs with different wall thickness for (a) $t = 0.01mm$ and (b) $t = 0.03mm$.

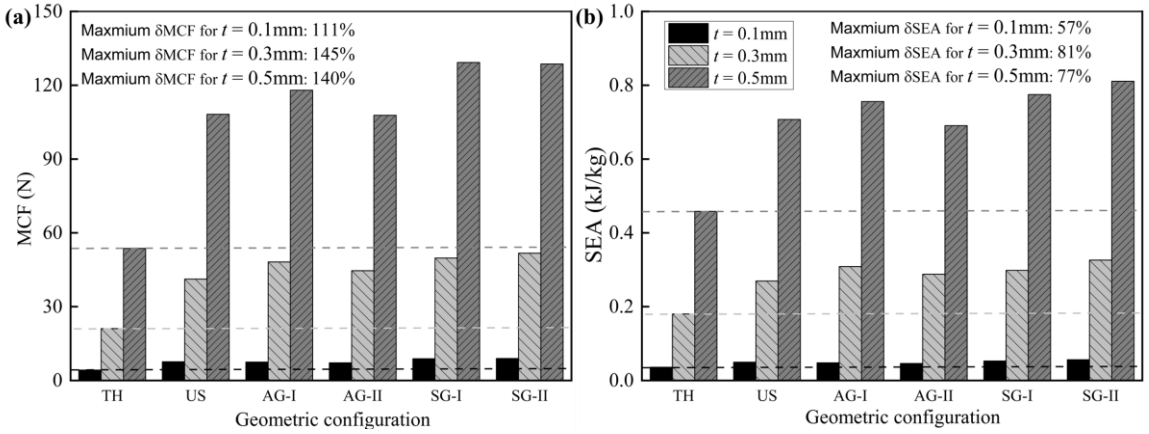

Figure 7.22. Comparison between graded fractal honeycombs of three different thicknesses based on (a) SEA and (b) MCF.

7.3.1.4 Concluding Remarks

To sum up, a series of novel graded fractal honeycombs is introduced by combining fractal self-similarity and functionally graded configurations. Besides uniform self-similarity, two graded fractal honeycombs with asymmetric gradients and another two with symmetric gradients are proposed and their in-plane compressive performance numerically analyzed. A comprehensive parametric study is conducted to evaluate the influence of geometrical gradient configuration, impact velocity and cell-wall thickness on the dynamic responses, SS relationship, SEA and MCF of the honeycombs. Significant findings from this study are summarized as below:

1. The deformation modes are drastically affected by the impact velocity and is controllable by graded fractal design. Three modes can be observed from the analysis; low velocity deformation mode, followed by a transitional deformation mode when impact velocity reaches a moderate value and finally the row-by-row mode at high impact velocity due to presence of inertia and is insensitive to gradient configurations.
2. Generally, the symmetrical gradient designs performed better in SEA at all levels of impact velocity. The SG-I honeycomb provides the best EA capacity for low impact velocity while SG-II honeycomb performed the best in EA at moderate and high impact

velocity. When compared with TH honeycomb, the graded fractal designs are able to absorbed 90% more and 17% more energy at low and high impact velocities, respectively.

3. The plateau stress, SEA and MCF are significantly increased with the impact velocity for all graded fractal honeycombs due to increasing inertia effect. However, the increment ratios of SEA and MCF with respect to TH honeycomb decreased with impact loading velocity. The maximum increment of MCF for graded fractal honeycombs is 188% at low impact velocity and 43% at high impact velocity.
4. The SEA for all graded fractal honeycombs increases significantly with cell wall thickness. Among all the graded fractal designs, AG-II achieved the best EA capacity for low compressive strain below 0.4 while SG-II absorbed more energy at higher compression strain above 0.4.

7.3.2 Graded hierarchical architecture with substructures

7.3.2.1 Low velocity impact performance

The deformation modes for graded hierarchical honeycombs with hexagonal and triangular sub-structures under selected crushing strains are illustrated in Figure 7.23 and Figure 7.24Figure below. In this study, low impact case is represented by an impact velocity of $V = 3m/s$ with thickness set to $t = 0.05mm$. Seen from Figure 7.23 and Figure 7.24, “X” shear band are present in both uniform hierarchical structure with hexagonal and triangular sub-structure. Meanwhile, for graded hierarchical honeycombs, the deformation first occurs in the weak layer with the lowest RD, i.e., the bottom layer of NGH and top layer of PGH honeycomb. The deformation then progressively occur towards the stronger layer of the graded hierarchical honeycombs. The progressive deformations form a “I+V” mode in each gradient layer which is related to the gradient distribution but is independent of the topology of sub-structure. The

independence of sub-structure on deformation pattern is also true for uniform hierarchical structure.

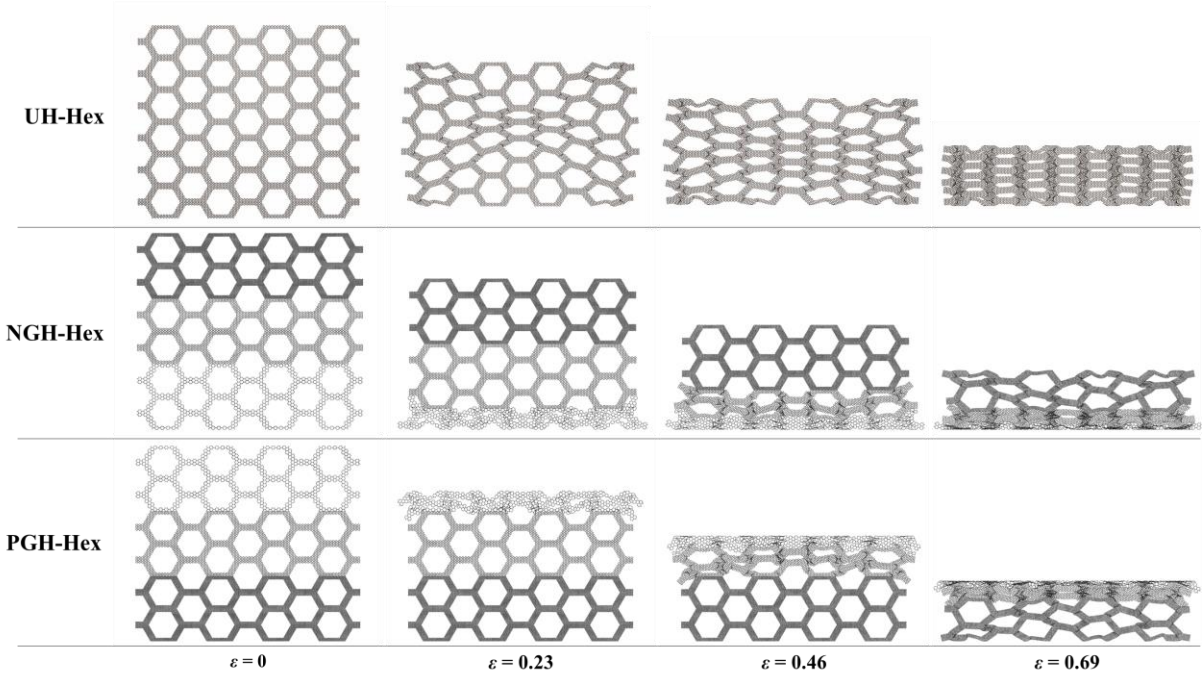

Figure 7.23. Deformation patterns of graded hierarchical structures with hexagonal sub-structures at low impact velocity of $V = 3m/s$. UH-Hex honeycomb being uniform in nature, produces "X" shear band while the graded ones, NGH-Hex and PGH-Hex honeycombs show "I+V" deformation pattern which appears first in the weak layers and then progresses into stronger layers.

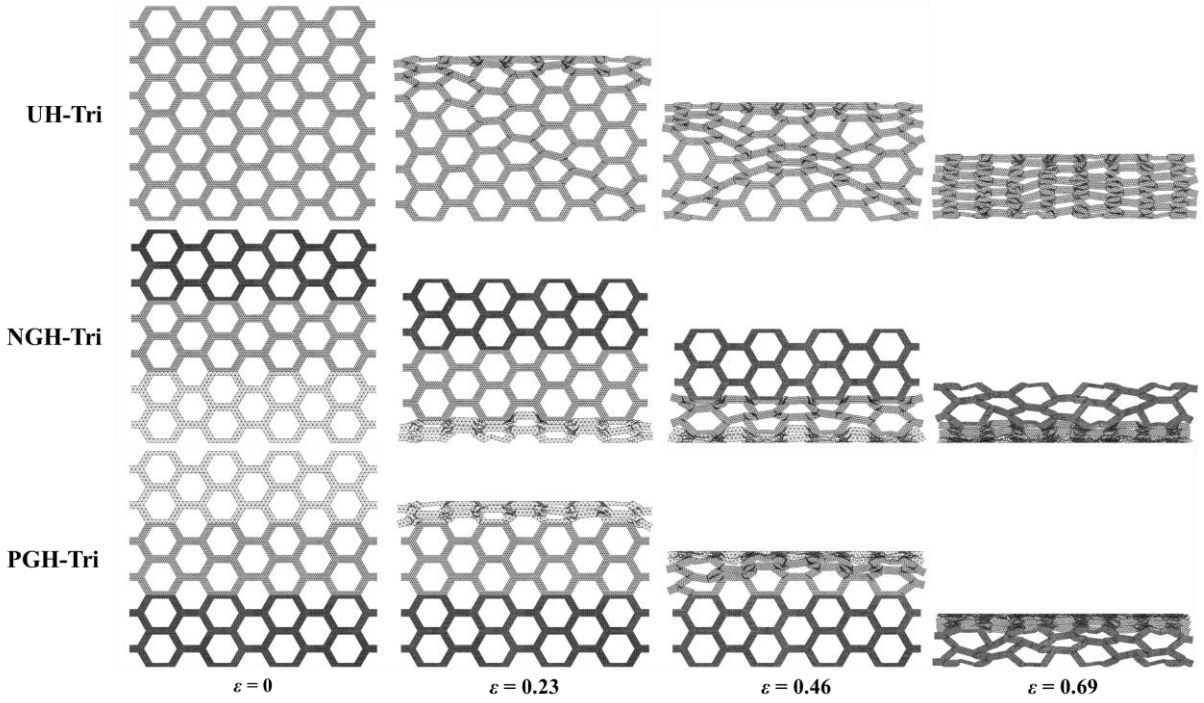

Figure 7.24. Deformation patterns of graded hierarchical structures with triangular sub-structures at low impact velocity of $V = 3m/s$. Similar patterns in Figure 7.23 are observed in hierarchical structures with triangular sub-structures where "X" shear band in UH-tri and "I+V" deformation modes appearing in weak and subsequent strong layers in PGH-Tri and NGH-Tri honeycombs.

The crushing SS relationship in graded hierarchical honeycombs with hexagonal and triangular sub-structures under low velocity impact condition are portrayed in Figure 7.25 below. Seven stages are identified in the SS relationship for the crushing response of graded hierarchical honeycombs under low impact velocity from which, the mechanisms are similar for both hexagonal and triangular sub-structures. Stage I represents the initial linear elastic stage, which is depicted by linear increase in stress over strain and it ends as the initial yield stress is reached. Stage II which is the first plateau region subsequently follows due to the crushing of the weakest layers of NGH and PGH honeycombs which is shown in Figure 7.23 and Figure 7.24. In a plateau stage, the stress is stabilized with increasing strain, which leads to large EA. Stage IV and VI are the second and third plateau region which corresponds to the crushing of medium and strongest layers of NGH and PGH honeycombs presented in Figure 7.23 and Figure 7.24. Stage III and stage V are transitional stage that connects the plateau stages to one another. During the transitional stage, the crushing stress is increased from previous to next plateau stage as the weaker layer is full densified and crushing begins on the next stronger layer. While uniform hierarchy only produces a single plateau region during the compression process, both graded hierarchical structures exhibit three progressively larger plateau stages. Furthermore, the normalized stress for the graded hierarchical structure with triangular sub-structure is approximately 2.5 times than that of graded hierarchical structure with hexagonal sub-structure.

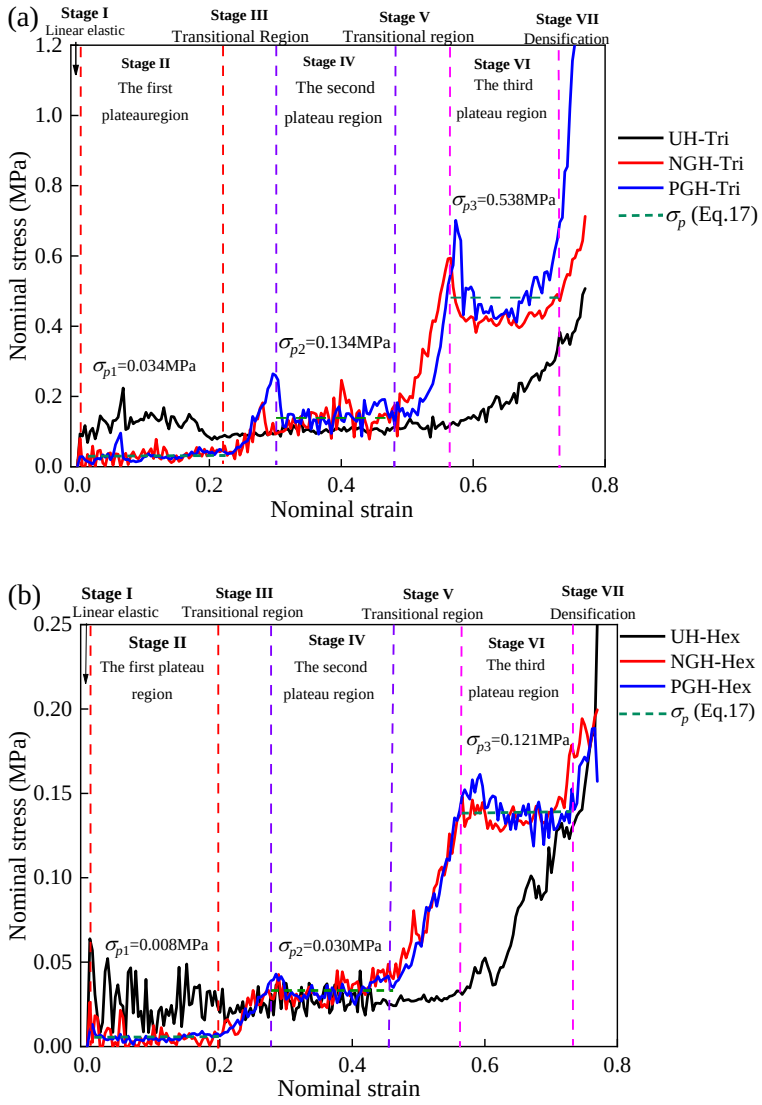

Figure 7.25. Illustration of in-plane crushing SS relationship of graded hierarchical honeycomb with (a) hexagonal and (b) triangular sub-structures under same impact velocity of $V = 3m/s$. A total of seven stages are identified in the SS diagram including two transitional regions and three plateau stages besides elastic and densification regions.

7.3.2.2 Graded hierarchical structures with varying thickness

Under this subsection, given the same low impact velocity of $V = 3m/s$, the response of graded hierarchical honeycombs of varying thickness in each gradient layer is investigated to provide a comparison to the previous subsection. To ensure equivalent total mass between graded and uniform hierarchical honeycombs, $t_1 = 0.0935mm$, $t_2 = 0.05$ and $t_3 = 0.0259mm$ are used for NGH-Tri honeycomb, and $t'_1 = 0.0938mm$, $t'_2 = 0.05mm$ and $t'_3 = 0.0263mm$ for NGH-Hex honeycombs. These values are derived from uniform

hierarchical honeycomb which has a thickness set to $t = 0.05mm$. The deformation pattern of these modified graded hierarchical structure would resemble to those with uniform thickness as presented in Figure 7.23 and Figure 7.24. Five stages comprising of three plateau stages, linear elastic and densification stage are observed for this type of graded hierarchical honeycomb shown in Figure 7.26 below.

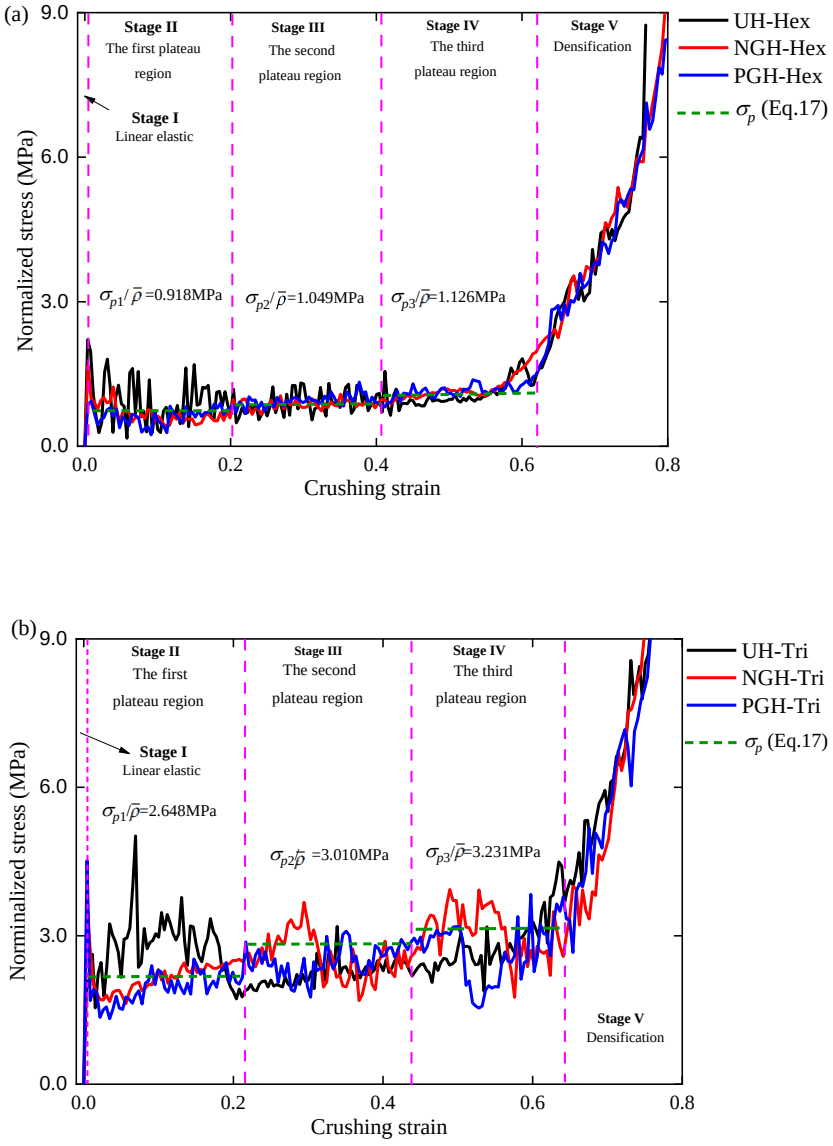

Figure 7.26. In-plane SS curves of graded hierarchical honeycombs with (a) hexagonal and (b) triangular sub-structures of varying thickness. Five stages consisting of three plateau stages, linear elastic and densification stage. Transitional stages are absent due to the equivalence in mass for all graded layers.

Slight difference in plateau stress among various plateau stages are observed which is attributed to the difference in topologies among different gradient layers. Furthermore, plateau stress among all plateau stages is close to that of the uniform hierarchical honeycombs which is consistently proven by the theoretical analysis. This is due to the total mass of each gradient layer being equal to that of uniform hierarchical counterpart.

7.3.2.3 Parametric study

The following parametric study in this section attempts to investigate the influence of impact velocities, topology of sub-structures, gradient distributions and wall thickness on the crushing responses and EA capacity of the graded hierarchical structures.

Three different velocities namely low, medium and high are taken into consideration. Analogically, low velocity is equivalent to velocity attainable by drop hammer which is translated to a strain rate range of about $0.1 - 0.1^3\ s^{-1}$. The medium velocity of strain rate ranging from 10^2 to $10^4\ s^{-1}$ can be realized by Split Hopkinson Bar. And lastly, the high impact velocity is achieved by Taylor impact test with a strain rate range of $10^3 - 10^5\ s^{-1}$ [196]. The graded hierarchical honeycomb with uniform thickness is considered unless otherwise specified in the parametric study which is separate from the uniform mass considered in section 5.2.2.2.

High impact velocity performance

In comparison to low velocity impact deformation mode as discussed in previous section, high velocity impact deformation patterns of graded hierarchical honeycombs under $V = 60m/s$ are presented in Figure 7.27 and Figure 7.28 below. Deformation modes from low velocity impact differs greatly from high impact velocity as it exhibits “I” deformation mode for both uniform and graded hierarchical structure. In this mode, the crushing occurs mainly on the impact end which deform progressively towards the supported end. Thus, shock front is clear

for all honeycombs as impact end is completely crushed or densified whereas the supported end is undeformed during the entire crushing process until the shock front propagates to the end.

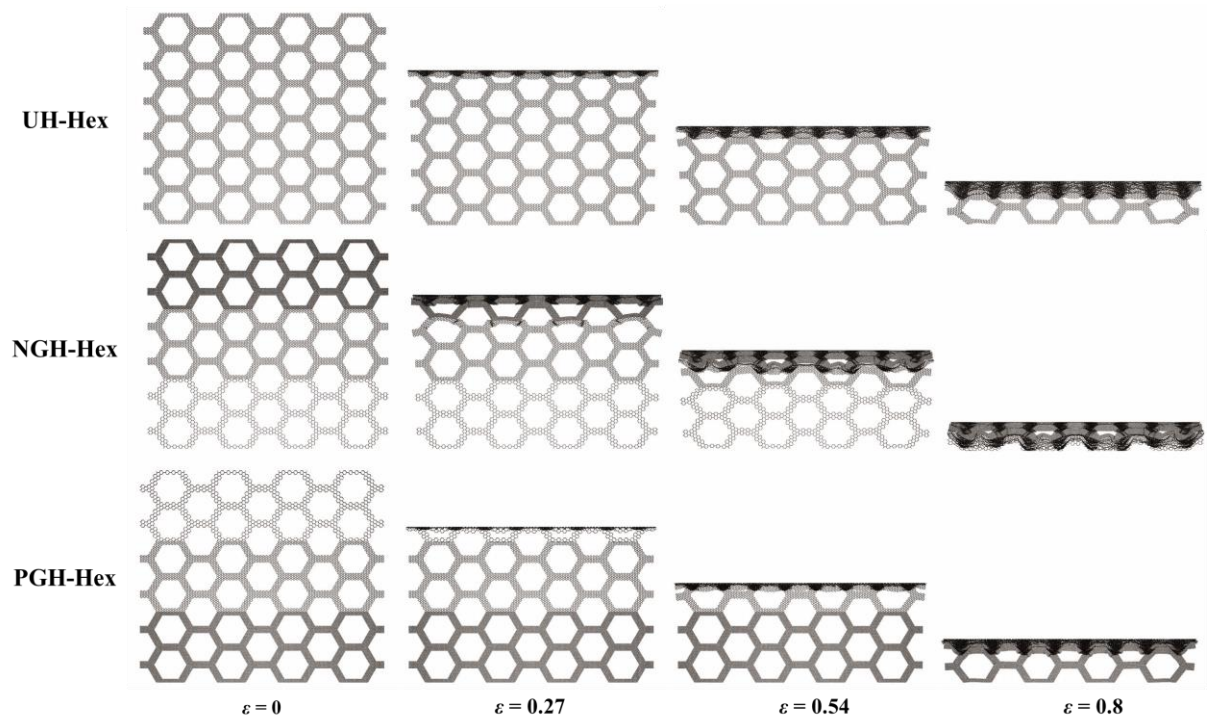

Figure 7.27. Deformation pattern of graded hierarchical honeycomb with hexagonal sub-structures. Figure clearly illustrates the formation of shock front on the impact end leading to crushing and densification on the immediate layer under impact.

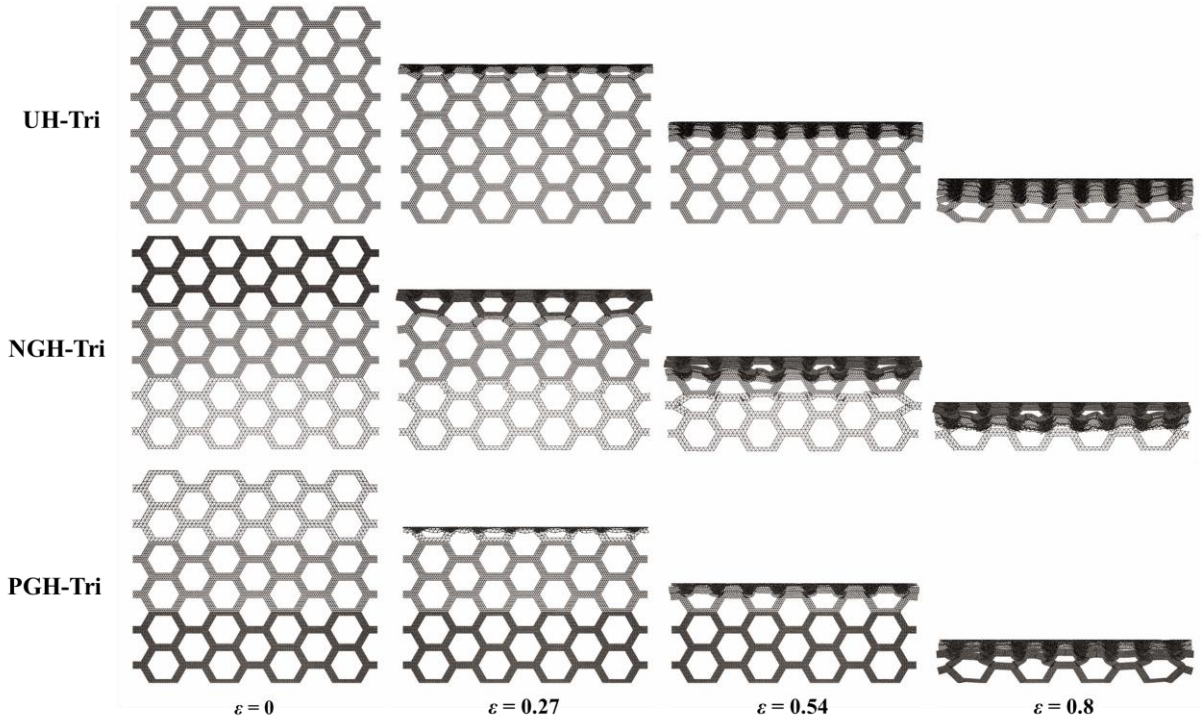

Figure 7.28. Deformation pattern of graded hierarchical honeycomb with triangular sub-structures. Formation of shock front forming "I" deformation mode similar to Figure 7.27.

For honeycomb structures under high impact loading, the dominant presence of inertia will greatly affect the dynamic stress. The observed progressive "I" deformation mode mainly attributed to the hardening phenomenon of cellular material as it densifies and compact itself on impact. This can be physically explained by the shock theory specifically for this type of honeycomb structure discussed in various literature [115][197][139]. As such, the dynamic stress under high velocity impact can thus be approximated by:

$$\sigma_{dy\_i} = \sigma_{st\_i} + \frac{\rho_s \overline{\rho_t}}{\varepsilon_{dy}} v^2$$

where σ_{st_i} and σ_{dy_i} are the static and dynamic plateau stress in the i-th gradient layer of the graded hierarchical honeycomb, respectively. v and ρ_s are the crushing velocity and density of the base material, respectively. $\overline{\rho_t}$ represents the RD of the i-th gradient layer of the graded hierarchical structure. Furthermore, ε_{dy} denotes the densification strain for i-th gradient layer, which in turn can be represented as follows [139]:

$$\varepsilon_{dy} = 0.8(1 - \bar{\rho_t})$$

The dynamic SS responses of graded hierarchical honeycomb with hexagonal and triangular sub-structure are illustrated in Figure 7.29 below. In stark contrast to SS response in low impact velocity shown in Figure 7.25, high impact velocity response lacks two transitional stages due to effect of inertia. Besides linear elastic and densification stage, three distinct plateau stages corresponding to each gradient layer can be observed in the figure. This can be seen that the dynamic stress of NGH and PGH honeycomb is different in the first plateau stage due to the difference in RD in the first gradient layer, i.e., the first crushing region belongs to the strong end of NGH as compared to the weak end of PGH, leading to $\sigma_{d1_{PGH}} > \sigma_{d1_{NGH}}$. The opposite is true for the third plateau stage where the final crushing region now belongs to the weak end of NGH and the strong end of PGH hence $\sigma_{d3_{PGH}} < \sigma_{d3_{NGH}}$. Based on this derivation, the dynamic stress of gradient layer 1 of PGH is equal to that of gradient layer 3 of NGH due to same RD, i.e., $\sigma_{d1_{PGH}} = \sigma_{d3_{NGH}}$ and vice versa $\sigma_{d3_{PGH}} = \sigma_{d1_{NGH}}$. Furthermore, the RD of gradient layer 2 of PGH and NGH is equal to the RD of uniform hierarchical structure hence in the second plateau region, $\sigma_{d2_{PGH}} = \sigma_{d2_{UH}} = \sigma_{d2_{NGH}}$.

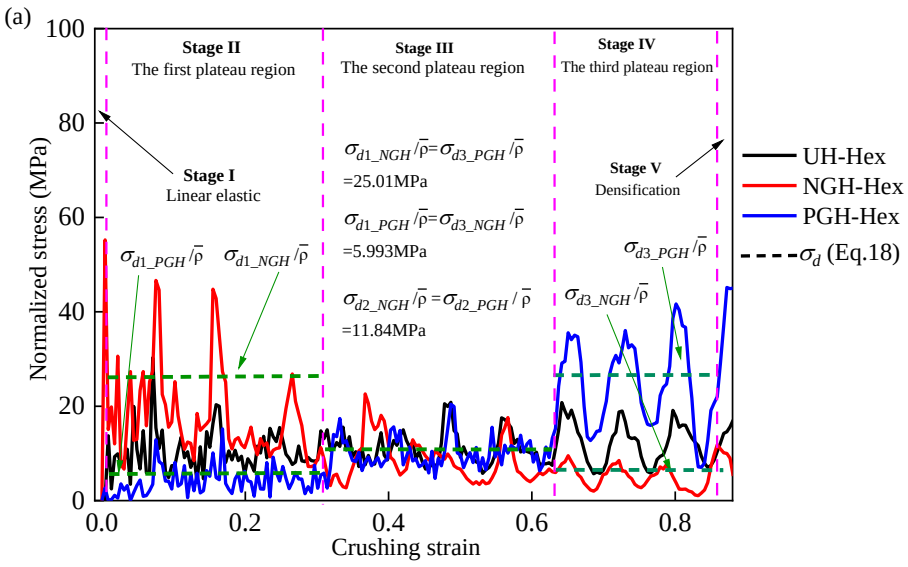

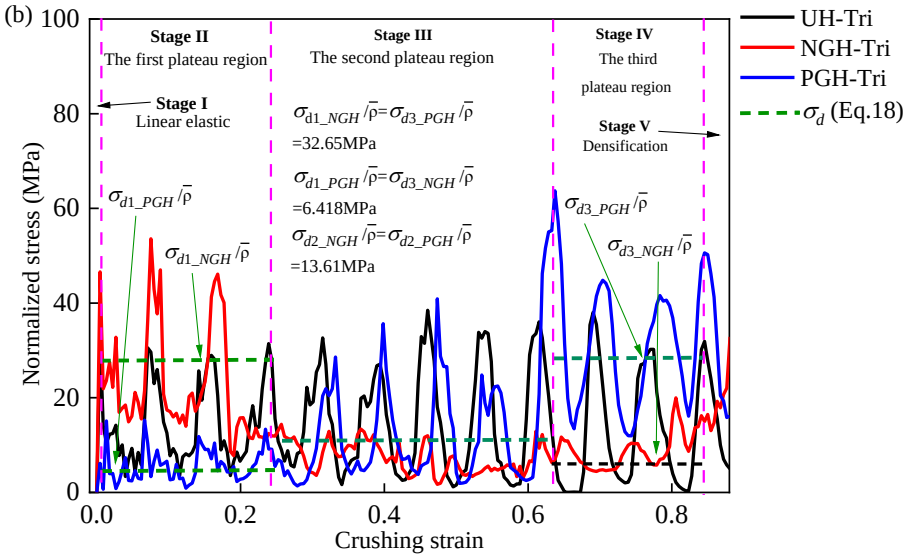

Figure 7.29. SS response of graded hierarchical honeycomb with (a) hexagonal and (b) triangular sub-structure.

Effect of impact velocity

The influence of impact velocities on the SS relationship of graded hierarchical honeycomb with triangular sub-structures is captured and examined by Figure 7.30 below. While the crushing stress is evidently enhanced with the increase with impact velocity, the increase in fluctuation of stress is even more prominent for both graded hierarchical honeycombs. The increase in fluctuation is attributed to the increasing presence of inertia with impact velocity. This oscillation of stress is particularly prevalent in all stages of PGH-Tri honeycomb under impact velocities of $40m/s$ and $60m/s$, but only appears in the first plateau region of NGH-Tri honeycombs. This situation is attributed to processive crushing from weak to strong ends in PGH-Tri honeycomb, leading to oscillation of stress in each region, among which, the magnitude of oscillation is particularly high for crushing of strong end.

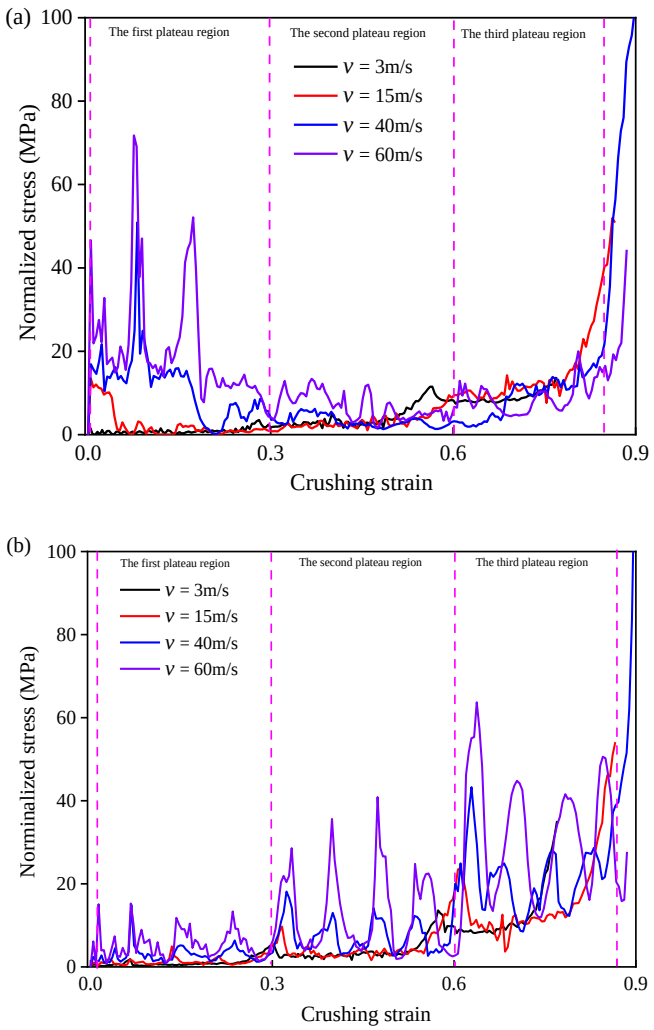

Figure 7.30. In-plane crushing SS response of (a) NGH-Tri and (b) PGH-Tri honeycombs under various impact velocities. The magnitude of plateau stress in each plateau region is dependent on the velocity of impact i.e. the presence of inertia as well as the arrangement of gradient.

Therefore, for NGH-Tri honeycomb, the strong end will be crushed first which leads to strong oscillation in the first plateau region. Subsequently, the crushed material during the first stage reduces the oscillation of the following stages. In low and medium impact velocity, three distinct of plateau stages start from low to high dynamic plateau stress is observed for both honeycombs and given the sufficient time for stress to propagate throughout the structure, the weakest layer regardless of position is always crushed first. At high impact velocities, the layer closest to impact end will always gets crushed first which registers the highest initial plateau stress for NGH-Tri in the first plateau stage as the strongest layer is the first layer to be crushed.

On the other hand, given the weakest layer being the top layer in PGH-Tri, the dynamic plateau stress is always progressively higher for sequential plateau stages.

Further investigation in influence of impact velocity on the crushing stress of the graded hierarchical honeycombs is conducted by examining the relationship of average crushing stress as a function of the impact velocity is presented in Figure 7.31 below. NGH-honeycombs with hexagonal and triangular sub-structure compared with its uniform counterpart are considered. The FE prediction of average crushing stress is calculated over the region between elastic and densification stage. At the same time, theoretical predictions of this stress is obtained by simply taking the average value of the three plateau stresses because the duration of each plateau stage is almost the same:

$$\sigma_{ave} = (\sigma_{d1} + \sigma_{d2} + \sigma_{d3})/3$$

Figure 7.31 clearly illustrates that the average crushing in the entire plateau region increases with impact velocity which ultimately lead to large EA. The average crushing stress for both graded hierarchical honeycombs are consistently larger than its uniform counterpart which implies the inherently better EA capability over uniform honeycombs. The theoretical prediction also agrees fairly well with the numerical method.

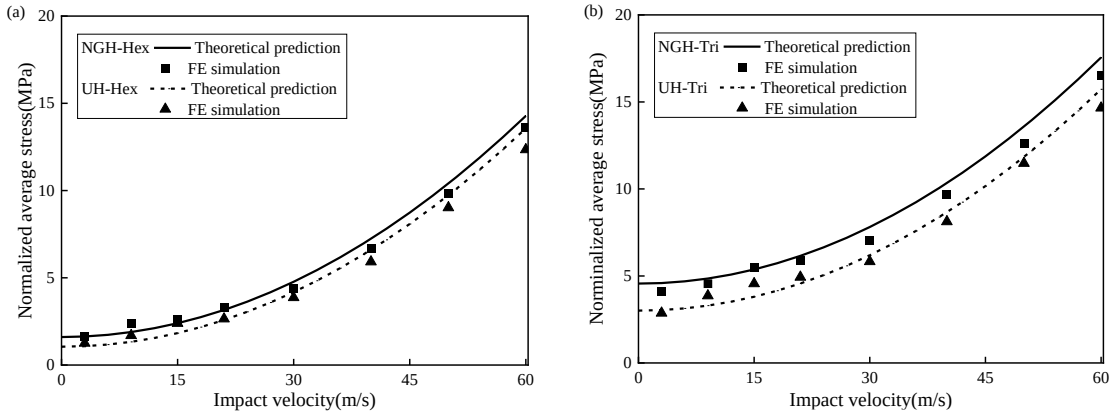

Figure 7.31. Normalized average stress as a function of the impact velocity for uniform and graded hierarchical structure with (a) hexagonal and (b) triangular sub-structures. The average crushing stress increases with impact velocity for all honeycombs.

Energy absorption performance

The EA performances of graded hierarchical honeycomb structures are evaluated in the following section along with Figure 7.32 and Figure 7.33. In low velocity impact, the SEA strain curves of NGH and PGH overlap with each other, while prominent distinction between them is observed when impact velocity is high. From Figure 7.32, the SEA of graded hierarchical honeycomb structure is lower than that of uniform counterpart at low compression strains, but exceeds when compression strain is larger than 0.6 under low-velocity impact. On the other hand, from Figure 7.33, NGH honeycomb exhibits the largest SEA relatively to both PGH and uniform honeycomb at smaller crushing strain as this phenomenon is dependent on the strength of the top region closest to the impact end. Therefore, NGH started with crushing of strong end and ended with the weakest end, the reverse is true for PGH which created an mirror image of SEA-curve to each other. Hence, the SEA of PGH honeycomb is always smaller than uniform structure throughout the crushing process, indicating that positive gradient distribution weaken the EA performance of hierarchical honeycomb with both substructures before densification sets in. With the emphasis on NGH in Figure 7.33, it is clear that NGH-Hex can present larger SEA in all stages of compression than UH-Hex while NGH-Tri is larger than UH-Tri honeycomb only before compression strain of 0.6. This physical performance suggests that the sub-structural configuration also affect the SEA performance of graded hierarchical honeycombs.

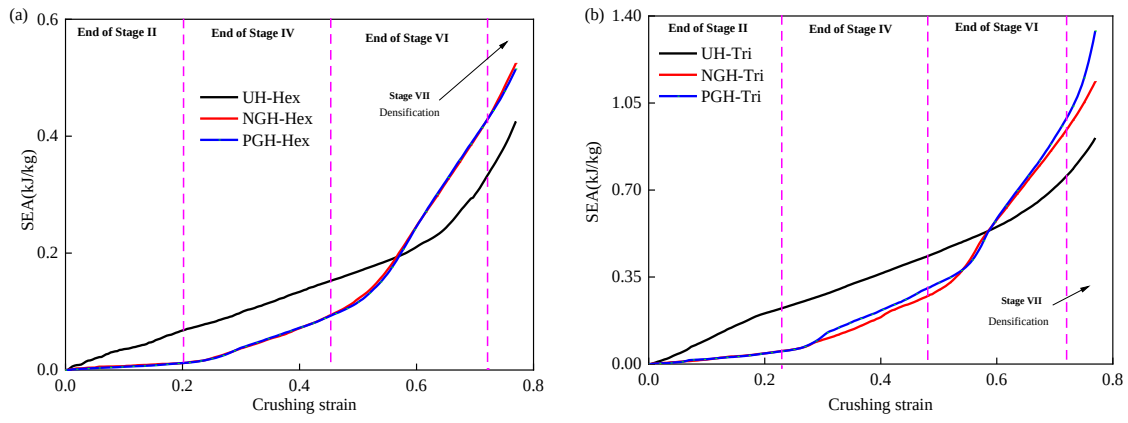

Figure 7.32. SEA to strain curve for graded hierarchical honeycombs with (a) hexagonal and (b) triangular substructures under low velocity impact. The SEA curves of NGH and PGH are very similar to one another because the weakest layer will be crushed first regardless of their gradient direction.

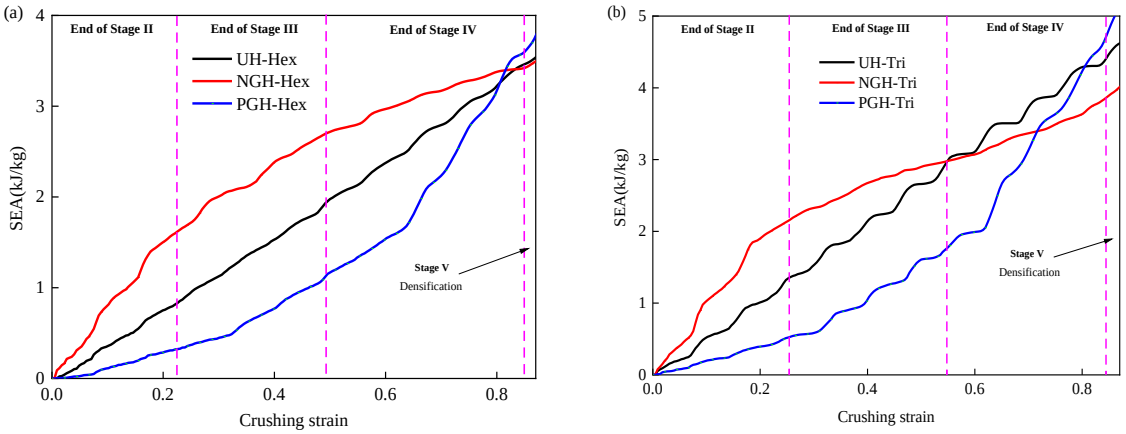

Figure 7.33. SEA to strain curve for graded hierarchical honeycombs with (a) hexagonal and (b) triangular substructures under low velocity impact. As compared with Figure 7.32, NGH and PGH drastically differentiate themselves from one another as gradient direction now has a impact on the SEA in the early and late stage of compression. NGH generally performs better in the early stage as the strongest layer is crushed first.

The influence of sub-structural configuration on EA capacity at densification strain is further illustrated in the following Figure 7.34. In general, triangular sub-structure provides a better SEA performance than hexagonal sub-structure. Given low velocity impact, SEA for graded hierarchical structures with hexagonal and triangular sub-structures are enhanced by 27.9% and 32.2%, respectively with respect to its uniform counterpart. For subsequent velocities, the energy absorbed by the graded hierarchical honeycombs increased due to increasing presence of inertia effect while the enhancement for graded hierarchical honeycombs as compared to its uniform counterpart is reduced which ultimately shows that graded design approach is becoming more independent of SEA as inertia force takes over at higher velocities. Ultimately, under high impact velocities, NHG-Hex honeycomb was only able to provide a 4.04% improvement in SEA when compared to UH-Hex, and 5.25% for NGH-Tri.

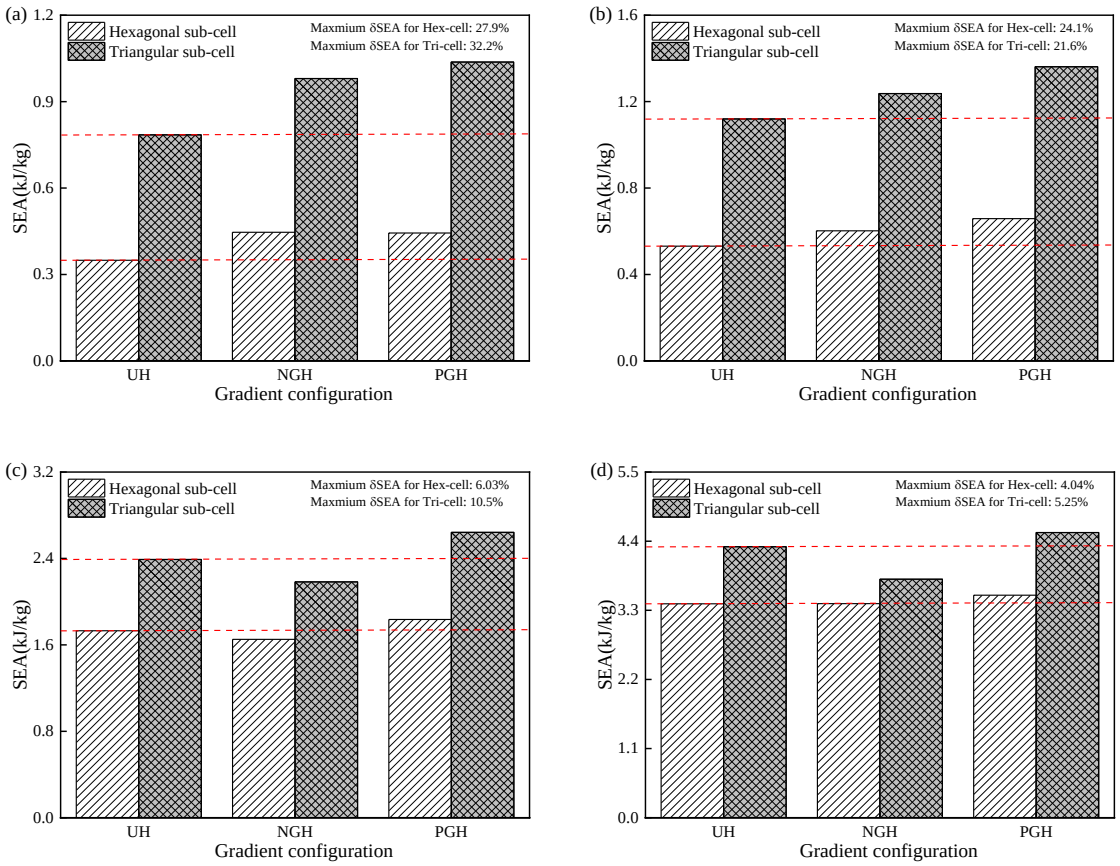

Figure 7.34. Comparison of SEA in graded hierarchical honeycombs of two different sub-structures under various impact velocities (a) $v = 3m/s$, (b) $v = 15m/s$, (c) $v = 40m/s$ and (d) $v = 60m/s$. While increment in SEA is seen for all graded hierarchical structures when compared with uniform honeycombs, the enhancement is reduced with every increase in impact velocity due to the increasing influence of inertia effect.

7.3.2.4 Concluding Remarks

In this study, several novel hexagonal honeycombs with graded hierarchical approach are presented to enhance their impact resistance behaviors. The following design is achieved by replacing the walls of regular honeycombs with sub-structures along with gradient distribution obtained from varying the hierarchical length ratio in each layer. Hexagonal and triangular sub-configurations were chosen as sub-cell structures, and two unidirectional gradient distribution are compared. The crashworthiness and EA of graded hierarchical honeycombs are first validated by experiments and theoretical approaches and numerically analyzed.

Deformation modes are highly dependent on impact velocity, where “I+V” and “I” modes are observed in low and high impact velocities, respectively. Seven stages comprising of standard

linear and densification stages, along with three distinctly different plateau stages and two transitional stages were identified among the graded hierarchical honeycombs under low velocity. The discreteness of transitional stage fades as impact velocities increases with inertia effect whose increasing presence also enhances the crushing stress and SEA.

The gradient distribution provides influence on crashworthiness performance to a great extent. There is no significant difference between SS and SEA curves of NGH and PGH when the velocity impact is low. However, drastic difference emerges can be observed as impact velocity goes higher. Notably for NGH, the largest plateau stage occurs at the third plateau stage under low velocity impact but transforms to the first plateau stage under high-velocity impact which have implication towards large SEA in the early or late stage of impact crushing. On the other hand, the largest plateau stage for PGH always appears in the third plateau stage under all impact velocities. Both configurations can enhance SEA performance under low velocity impact, while only PGH distribution provides greater SEA performance under high velocity impact. Comparatively, PGH has more consistently better performance than NGH configuration.

Sub-cell structure also have a profound impact on the crushing stress and EA of graded hierarchical honeycombs. The triangular sub-structures possess better SEA than hexagonal sub-structures with former providing a 32.3% improvement while the latter 27.9% when compared to uniform counterpart. However, at high velocity impact, the SEA enhancement is drastically reduced to 4.04% and 5.25% for hexagonal and triangular sub-structures respectively.

7.4 Conclusion

Firstly, a series of novel graded fractal honeycombs is introduced. These designs incorporate fractal self-similarity with functionally graded features and are classified into symmetrical and asymmetrical gradient. The study then explored the effects of geometric gradient configuration,

impact velocity, and cell wall thickness on the dynamic crushing behavior, SS relationship, EA, and MCF of these honeycombs. This section of study provides the several findings. Firstly deformation responses varies with impact speed and can be regulated by graded designs but is unaffected as velocity becomes high. Plateau stress, SEA and MCF all increase with impact velocity in all graded fractal honeycombs due to increasing inertia effect. Similarly, SEA improves significantly across all graded fractal honeycombs as cell wall thickness increases. In essence, graded fractal design of honeycombs can significantly enhance EA and deformation control, especially when compared to traditional honeycomb structures. The study's insights into the impact of geometric gradients, impact velocity, and wall thickness provide valuable guidance for optimizing these structures for specific impact scenarios.

Concurrently, new hexagonal honeycombs with graded hierarchical properties were developed to improve crashworthiness. These honeycombs, created by substituting regular cell walls with sub-structures, vary in hierarchical length ratio across layers. Both hexagonal and triangular sub-cell structures were examined, along with negative and positive gradient hierarchies. Likewise, key findings from the study had concluded that there are seven distinct stages in the deformation under low velocity, but only five under high velocity due to the disappearance of two transitional stages. Gradient distribution has an impact on crashworthiness. SS and SEA-strain curves of NGH and PGH are similar at low velocities but diverge at higher velocities. Furthermore, sub-structure also influences the mechanical performance of the honeycombs. Triangular sub-structures outperform hexagonal ones in SEA. Under low-velocity impact, the SEA enhancement is notable for both configurations but is less pronounced at high velocities. Again, the study demonstrated the specificity in design of honeycombs, including gradient distribution and sub-cell configuration, significantly influences their performance in crashworthiness and EA, particularly under varying impact velocities.

Chapter 8 3D Hybrid Hierarchical Auxetic Structure

This chapter focuses on the design and analysis of a new 3D auxetic structure, along with its variant inspired from biological structures of hierarchical configuration. As such, this investigation seeks to develop an auxetic structure with comparable auxetic and energy-absorbing qualities compared to existing 3D structures that evolved from 2D designs. This involves incorporating innovative design elements from 2D auxetics. The primary objective is to optimize the design for superior performance under dynamic loads, while identifying key design factors for auxetics intended for dynamic applications.

This chapter proposes the incorporation of design methods from 2D auxetic structures, which have proven to significantly boost their performance, into the 3D design framework. The aim is to develop a structure that exhibits a more effective response to dynamic loading conditions. This involves designing a structure characterized by its ease of deformation and consistent densification, which in turn enhances its capacity to absorb energy during dynamic impacts.

Since 3D structure are known to be highly anisotropic, two different planes of compression were conducted. Consistent material use ensured that results reflected the design's geometry rather than material properties. Variations in properties due to printing direction were also considered. Each sample underwent identical testing conditions to evaluate properties across different planes and printing directions. As such, a total of 16 experiments were conducted - eight quasi-static and eight dynamic - to analyze and draw conclusions on the performance of auxetic structures. Findings revealed the significant impact of printing direction on the deformation pattern of the structure leading to inconsistency of performances apart from the anistropic nature of 3D structure. However, a more consistent performance and even improved impact behavior is achieved through minor modification to the 3D structure demonstrating the improved ability to efficient response to loading.

8.1 Development and Methodology

In the development of 3D re-entrant auxetic structure with enhanced physical properties, it is insufficient to simply rearrange or reinforce the unit cell in three dimensions [198]. Therefore, it is proposed to integrate innovative design techniques from novel 2D auxetic structures, which have shown to enhance their overall performance, into the 3D model. The objective is to create a structure that responds more efficiently to dynamic loading. This means designing a structure that demonstrates easy deformation and uniform densification, thereby improving its ability to absorb energy from dynamic impacts.

Figure 3.1(a) defines the main auxetic unit cell required to construct the external 3D unit cell. A size of 15mm is selected to ensure that the patterned structure fits on the printing plate of the 3D printer. In addition, a strut diameter of 1mm is chosen in order to ensure the struts are slender and the thickness of the struts do not cause the structure to be overly rigid or overly weak so it will exhibit noticeable deform during dynamic loading conditions. Separately, a re-entrant cell angle of 60° is chosen to achieve a good balance between strength and PR for the structure [199].

Figure 8.1(b) then defines the star sub-unit cell which will serve as both the hybrid aspect and the hierarchical sub support structure for the external re-entrant unit cell. Figure 8.1(d) and (e) features the completed designs. ReC represents the conventional straight struts for its re-entrant unit cells while ReM has its re-entrant unit modified so the straight struts are bent inwards at 45° like the star unit cell so to shift its propensity to deform inwards as compared to ReC. Therefore, based on the following two proposed designs, the objective is to determine whether ReM, which is a structure that deforms more readily and has a lower peak stress is better performing in dynamic loading than ReC, which will have the same deformation mechanism. Both have a star unit strut supporting the re-entrant cell as well as seen in Figure 8.1(d) and (e), which is further ensure the stability of the deformation mechanism [200].

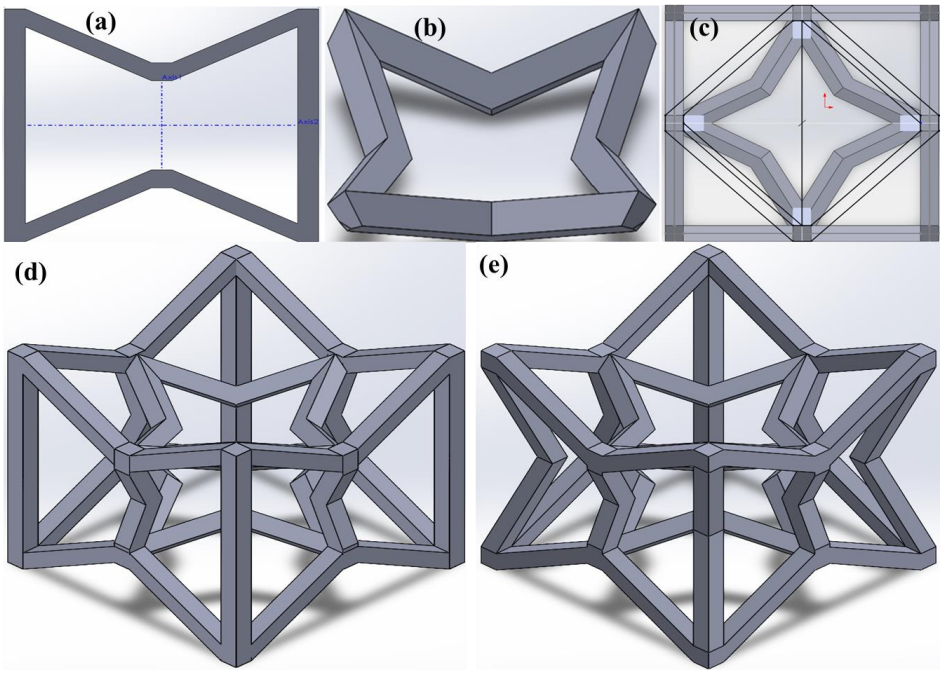

Figure 8.1. (a) Re-entrant unit cell and (b) star sub-unit cell and its placement of star sub-unit cell within re-entrant cube in (c). The assembly of 3D re-entrant and star sub-cell to form two designs namely (d) ReC and (e) ReM.

The 3D unit cells are arranged into a 5x5x5 structure, which is the maximum number of cells that can be arranged horizontally onto the print platform of the printer. It is not necessary to pattern as many cells as possible to fully avoid the size effect which is termed for abnormal localities in the stress concentrations in a 3D auxetic structure due to boundary conditions. Thus, 5 cells per axis is more than enough as the size effect can generally be avoided so long as the number of patterned cells is more than three [199].

Nylon Green, a fairly flexible material, had been identified as a suitable material for manufacturing the samples in this study because the material balances between avoiding easy fracture and maintaining necessary stiffness. This promotes the effective production of the auxetic effect as softer resins might fail to demonstrate the auxetic effect under loading due to inadequate load-bearing capacity, while harder resins are prone to fracture under dynamic loading, hampering the initiation of the structure's deformation mechanism. The samples are printed with the Phrozen Sonic Mighty 4K printer and its affordability for 3D printing applications, allow for the fast and efficient production of numerous experimental samples.

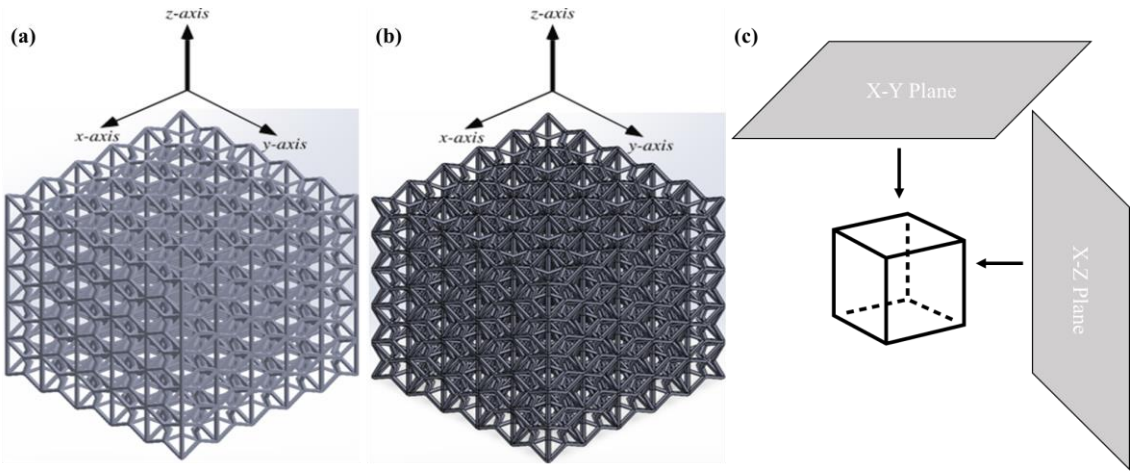

Figure 8.2. illustration of fully assembled model of (a) ReC and (b) ReM and (c) the definition of X-Y and X-Z plane

Given the assembled models shown in Figure 8.2, they were fabricated through 3D printing with Nylon Green and oriented in two different directions. This approach is necessary due to the influence of printing direction on the structural properties. A common issue with this type of 3D printing is the non-uniformity in material properties, caused by the stacking layered approach from the printing process. This problem, aggravated by the inherent anisotropy of the design, necessitates the consideration of both printing orientations in the fabrication. This decision is particularly relevant to dynamic testing scenarios, where the full expression of the auxetic effect and the assessment of EA capabilities are critical. Given the lattice's anisotropic characteristics, the crushing directions are dictated by two planes, X-Y and X-Z planes, which is defined in Figure 8.2(c) based on the contact with the compression plate. Given each crushing direction, further two print directions namely horizontal print (HP) and vertical print (VP) are defined. Horizontal print means that the stacking direction of the print layer is perpendicular to the loading direction while for the vertical print, the orientation of the print layer is perpendicular to the loading direction.

A notable challenge encountered was the simulation of the layer-by-layer print direction in 3D printing processes. Traditional simulation models often assume solids to be fully homogeneous and continuous, which overlooks the layering inherent in 3D printed materials. This assumption

potentially leads to disparities between simulated and actual behavior, particularly in the mechanical response under various loading conditions. Due to these limitations, an experimental methodology was selected for this part of the study.

8.2 Results and Discussion

The results of experiments are presented in form of comparison between the crushing direction on different plane as well as two different printing direction to highlight the significance and importance of ensuring auxetic structure of being capable of maintaining its auxetic deformation mechanism.

Initial investigations into three-dimensional lattice structure exclusively composed of re-entrant unit cells have revealed poor behavior under dynamic load conditions, as evidenced by an excessive magnitude of impact forces and pronounced instability, as depicted in Figure 8.3 (a) and (c), respectively. This phenomenon is largely attributable to the intrinsic hollowness of the 3D structure. Drawing inspiration from biological architectures, such as bone tissue, the re-entrant three-dimensional model has been augmented with smaller hybrid star-shaped unit cells. This integration aims to rectify the previously observed deficiencies in performance.

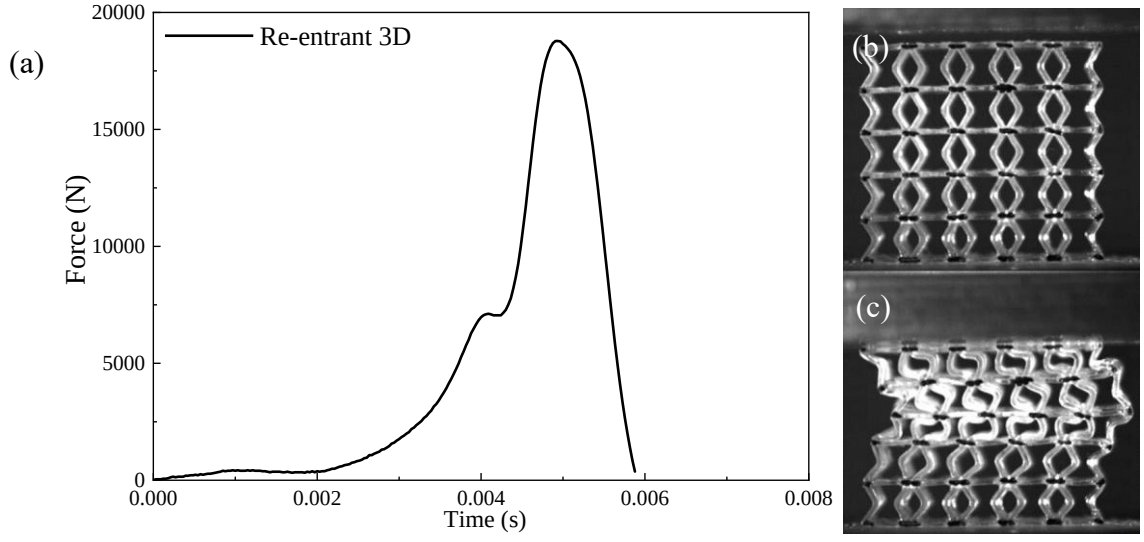

Figure 8.3. (a) Force-time diagram for 3D structure made up of only re-entrant structure along with its (a) undeformed and (b) deformed during dynamic loading.

8.2.1 Quasi-static Analysis

8.2.1.1 ReC

As observed from Table 8.1 below, both print directions had the structure converged towards the centre under quasi-static loading which is prominently shown in Table 8.1-3 where marked in red shows the rotational effect of unit cell towards each other during compression. As Nylon Green is a relatively elastic material, no fracturing of the structure was observed, and the main deformation mechanism was the deformation of the re-entrant unit cell from the struts buckling towards one another in both samples. Print directions had some effect on the deformation mechanism of these structures. ReC-VP showed initial collapse in the middle layers, followed by a gradual collapse of the entire structure. In contrast, ReC-HP led to a more evenly distributed rotation among the 3D unit cells.

Table 8.1. Deformation mechanism of ReC in the X-Y and X-Z plane with two printing directions under quasi-static loading.

ReC	1	2	3
(a) X-Y VP			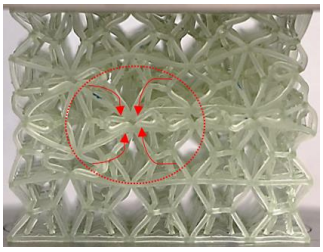
(b) X-Y HP	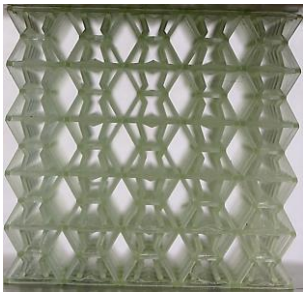		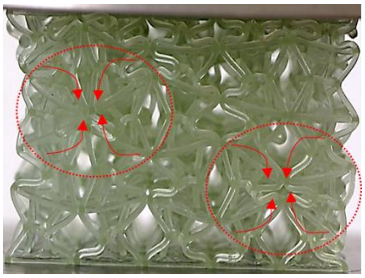

(c) X-Z VP		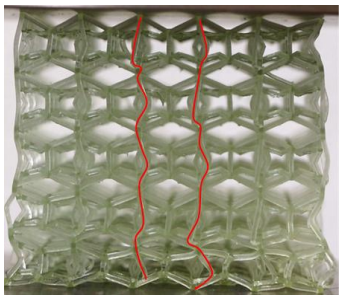	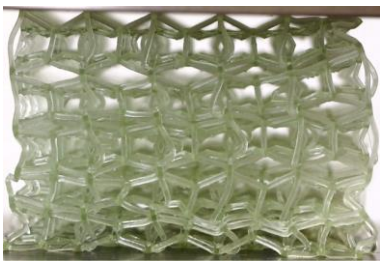
(d) X-Z HP	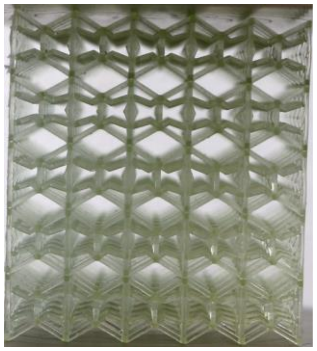	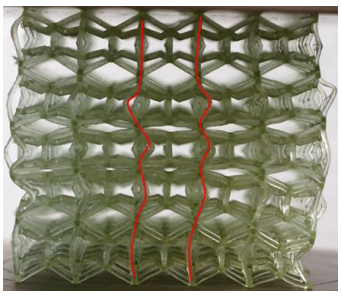	

ReC X-Y VP displayed more variability in its deformation pattern compared to the horizontal print. The layers in HP, being perpendicular to the applied force, allowed for a more uniform deformation compared to VP. This is particularly noticeable in samples X-Y VP-2 and X-Y VP-3 in Table 8.1, where there were more intact cells per layer than in HP samples. Intriguingly, ReC X-Y HP demonstrated a consistently higher resistance to compression than ReC X-Y VP. This finding contrasts with the common assumption that structures perform better when layers are stacked parallel to the loading direction, as layer adhesion is not directly stressed by the load. The key to this observation lies in the stronger and more uniform auxetic deformation of ReC X-Y HP, which effectively engages more material than ReC X-Y VP which is prominently demonstrated in Table 8.1-3. In HP, the layers are parallel to the loading direction. This orientation might allow the layers, and consequently the lattice structure, more flexibility to move or bend laterally when compressed. This increased flexibility can enhance the auxetic behavior of the structure. As such, auxetic effect induced by printing direction has a profound

effect in the SS response as ReC X-Y HP performed consistently better than ReC X-Y VP as seen in Figure 8.4. This is further substantiated by the higher plateau stress which indicate more involvement in deformation caused by increased auxetic effect in ReC X-Y HP.

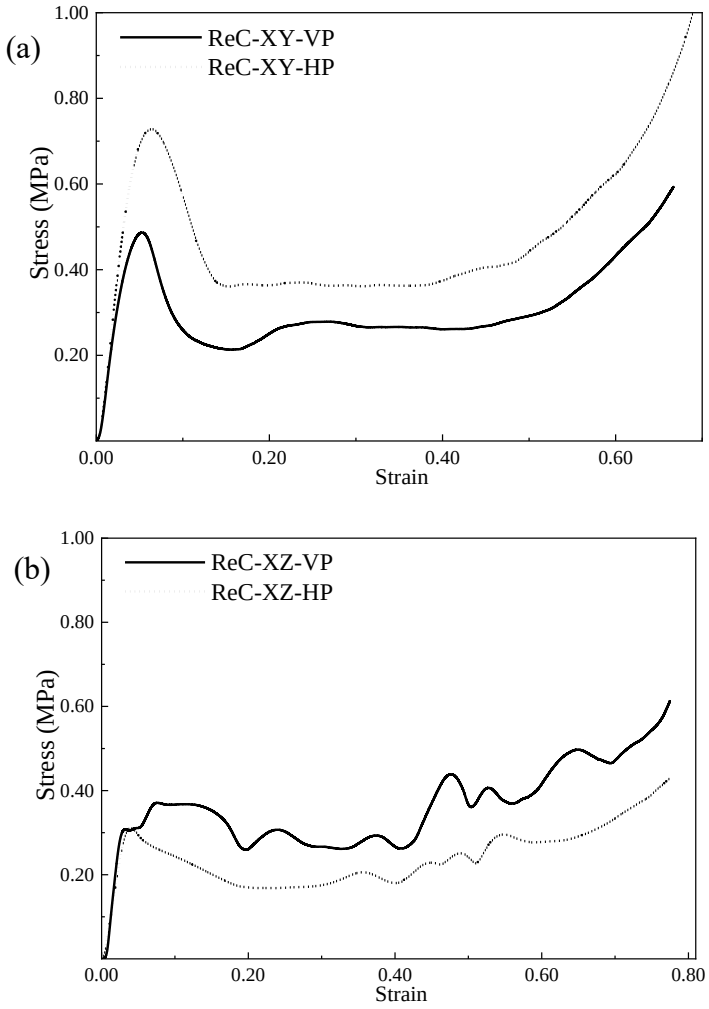

Figure 8.4. SS response of ReC in the (a) X-Y plane between HP and VP and (b) X-Y plane between HP and VP

As compared to ReC X-Y, ReC X-Z predominantly shows buckling during the compression process as marked by red line in Table 8.1 (c) and (d)-2. Negligible amount of auxetic effect is observed in both printing directions as no prominent rotation of unit cells were observed during the compression. Generally, both X-Z VP and X-Z HP underwent similar deformation mechanism, except that the collapse is more concentrated in the center for HP while collapse is more concentrated near the two ends in X-Z VP before densification. The lack of stability in deformation as well as buckling could partially be due to the lack of proper contact area

between the plate and the lattice which could have led to uneven stress distribution and thus ineffective stress propagation through the entire structure causing unstable deformation. Furthermore, the star sub-cell may also not effectively compel the deformation of individual cells as the sub-cell is more resistant to compression loading in X-Z orientation which contributed further to buckling and sliding of the structure.

Apart from the difference in sequence of collapse, both structures exhibit similar deformation which is unaffected by the print direction which is ultimately overshadowed by the buckling effect. The buckling effect is further cemented by Figure 8.4 which showed unstable plateau stress. In ReC X-Y plane, HP is stronger than VP as HP elicited more uniform auxetic effect cross the structure. In stark contrast, X-Z VP is stronger as depicted in Figure 8.4 as the load is applied perpendicular to the layers. This orientation tends to compress the layers against each other, effectively increasing the structure's resistance to buckling. In X-Z HP, however, the load is parallel to the layers, making it easier for these layers to slide or separate under stress, which can lead to earlier buckling. Therefore, in X-Z VP, stresses are distributed across the interfaces of the layers, which can bear compressive loads more effectively. In X-Z HP, the stresses may concentrate at the weaker points between layers, leading to a lower resistance to buckling. In another perspective, in a X-Z VP orientation, the layers can behave more like columns, which are better at resisting compressive forces, whereas in HP, the layers can behave more like beams, which are more susceptible to bending and buckling under similar loads.

8.2.1.2 ReM

In the modified 3D re-entrant structure, ReM X-Y VP shows a more consistent collapse of entire layer with lesser rotation as compared to ReM X-Y HP shown in Table 8.2 (a) and (b). Bending deformation is predominant in ReM X-Y VP as more folding is observed during compression as compared to rotation in ReM X-Y HP as circled in red shown in Table 8.2 (b) -3. As such, the presence of rotation had significantly contributed to the increase in plateau

stress in ReM X-Y HP over ReM X-Y VP. Furthermore, the peak stress in HP is higher than VP, as bending deformation is dominant at the start of the compression in which the bending force will be acting on the weaker bonding layer in the VP as compared to HP. The phenomenon of HP exhibiting more auxetic effect can also be explained by the possibility discussed in section 8.2.1.1 which increased the flexibility of the overall structure in the lateral contraction. Given so, the performance of HP exceeded that of VP in the loading ReM.

Table 8.2. Deformation mechanism of ReM in the X-Y and X-Z plane with two printing directions under quasi-static loading.

ReM	1	2	3
(a) X-Y VP	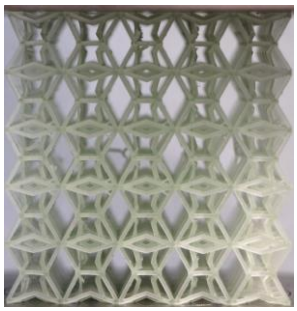	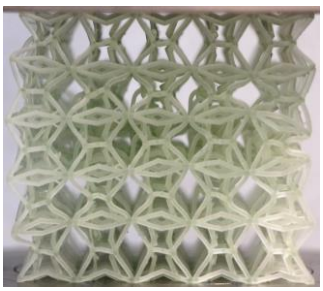	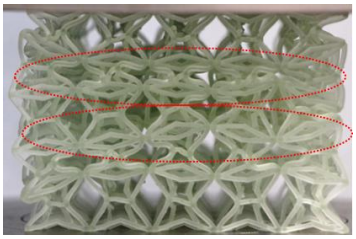
(b) X-Y HP		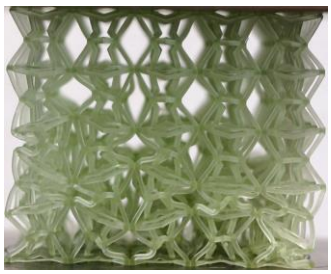	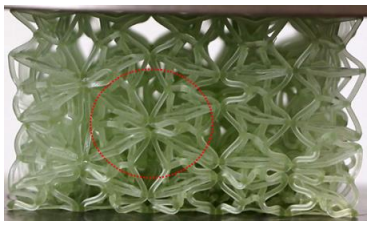
(c) X-Z VP		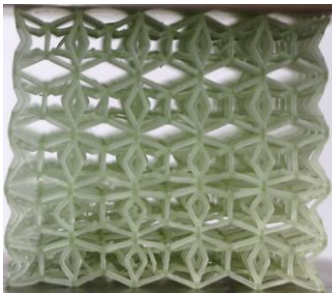	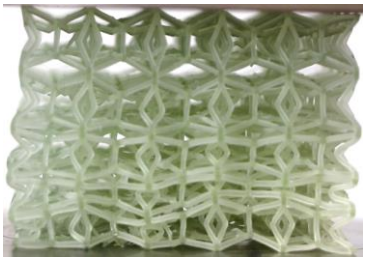

(d) X-Z HP		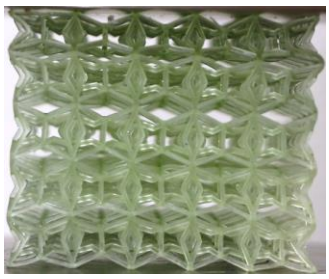	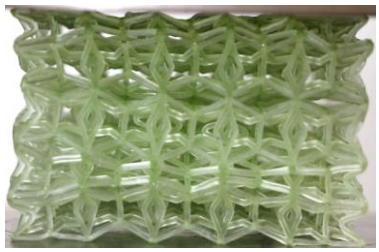

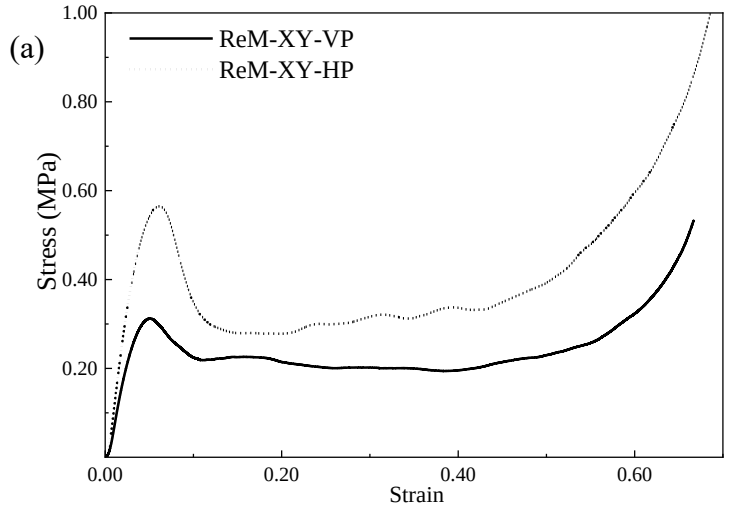

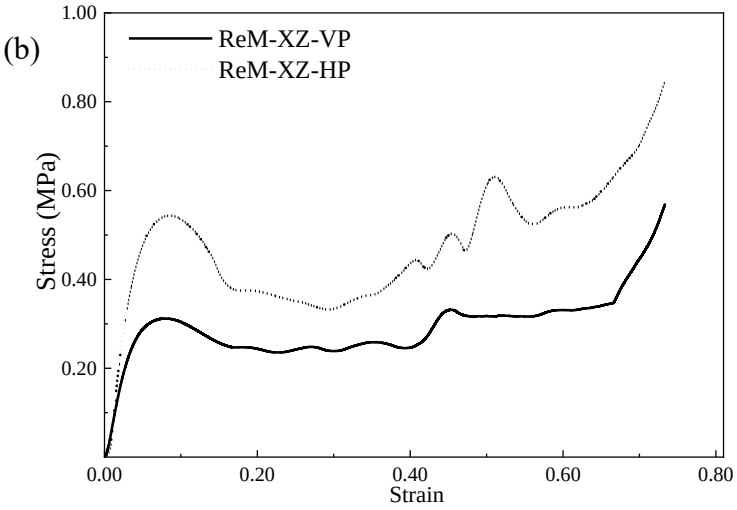

Figure 8.5. SS response of ReM in the (a) X-Y and (b) X-Z plane between HP and VP.

Both X-Z HP and X-Z VP encountered sliding during deformation due to a reduced contact area with the compression plate, leading to unusual stress concentrations within the structure. This issue was also noted in the ReC design under quasi-static loading. However, unlike ReC,

the ReM design did not show outward bending or buckling of struts. The design of ReM, featuring inwardly bent struts, effectively directed deformation towards the center of each 3D unit cell. This allowed both HP and VP samples to maintain some degree of auxetic effect from the onset of loading, in spite of the stress irregularities caused by sliding.

In comparison, X-Z HP exhibited more uniform deformation than X-Z VP. Both print orientations experienced sliding, but it was more pronounced in VP. This can be attributed to the inherent lack of rigidity in the bent struts and the uneven stress distribution, resulting in structural instability due to the print orientation's targeted susceptibility to shearing at the bonding layers. Conversely, HP provided greater flexibility and resistance to bending in the bent struts, leading to a more consistent auxetic effect and uniform deformation. When analyzing SS responses in Figure 8.5, in both planes, ReM-HP outperformed ReM-VP, which contrasts with the ReC model whose performance from printing direction is inconsistent in the two planes. The inclusion of bent struts in the ReM design proved to be beneficial compared to ReC, whose performance was inconsistent under loading in the X-Z plane due to buckling issues.

8.2.2 Dynamic Analysis

8.2.2.1 ReC

During dynamic loading, the rapid nature of the process hinders effective stress distribution across the structure, contributing to the sequential layer collapse observed in ReC X-Y VP detailed in Table 8.3 (a) and (b). The orientation of layers in ReC X-Y VP reduces the bending resistivity of the structure in the loading direction. In contrast, despite similar challenges with stress propagation, ReC X-Y HP exhibited a pronounced auxetic effect and consistent deformation, as depicted in Table 8.3 (a) and (b), characterized by the noticeable rotation of unit cells into petal-like configurations nearing densification. Although the deformation patterns of VP and HP differ, their force-time responses are relatively similar. A notable aspect

is the marginally higher second peak force in HP compared to VP, as shown in in Figure 8.6. This highlights HP's increased compressive resistance induced in the later stages of loading due to its auxetic properties.

Table 8.3. Deformation Mechanism of ReC in the X-Y and X-Z plane under dynamic loading

ReC	1	2	3
(a) X-Y VP	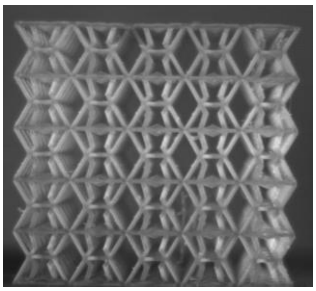	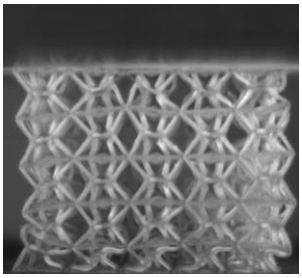	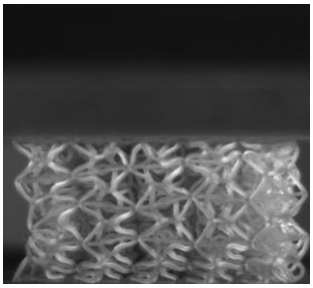
(b) X-Y HP	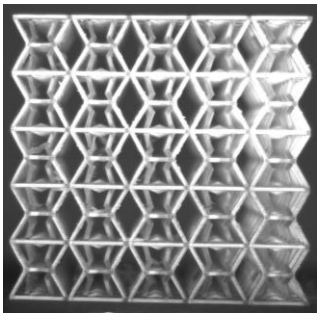	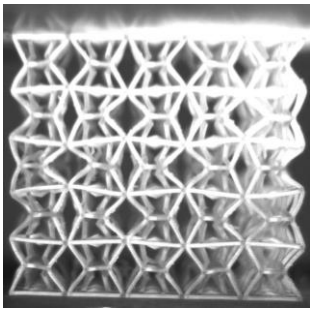	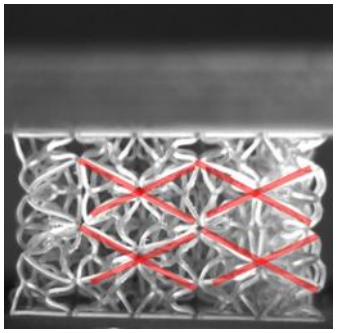
(c) X-Z VP	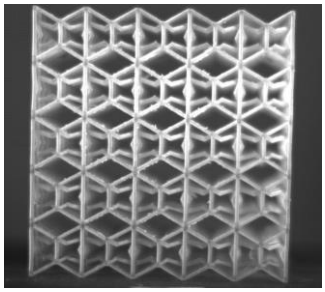	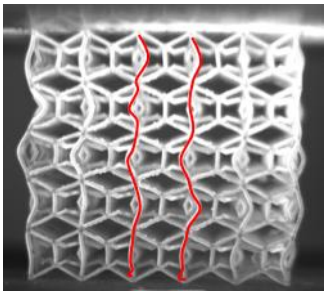	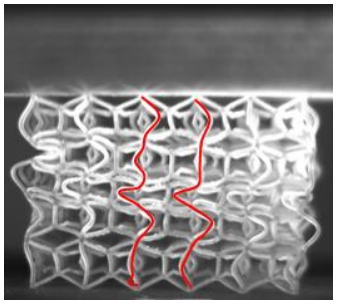

(d) X-Z HP	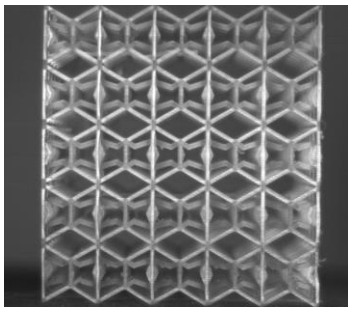	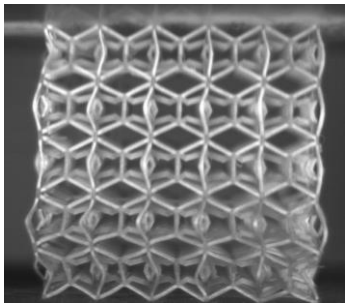	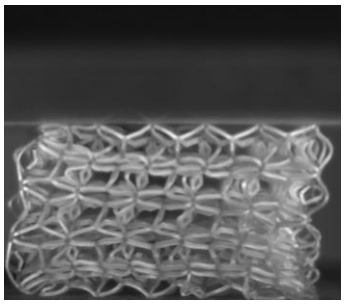

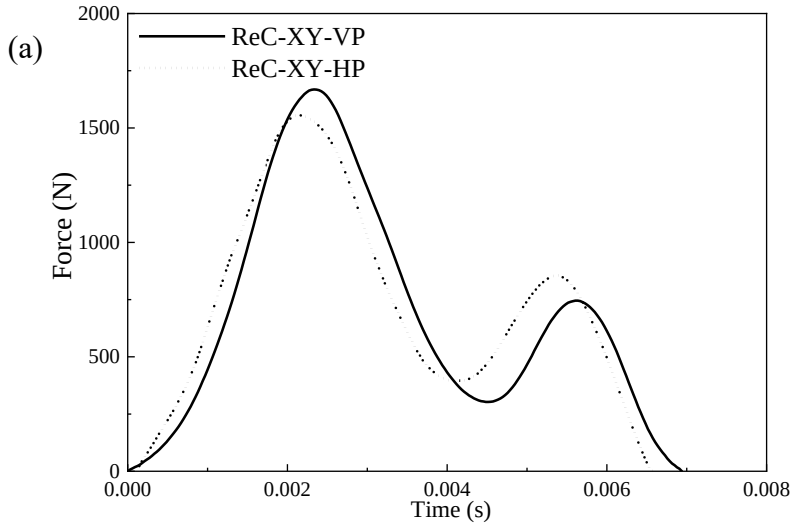

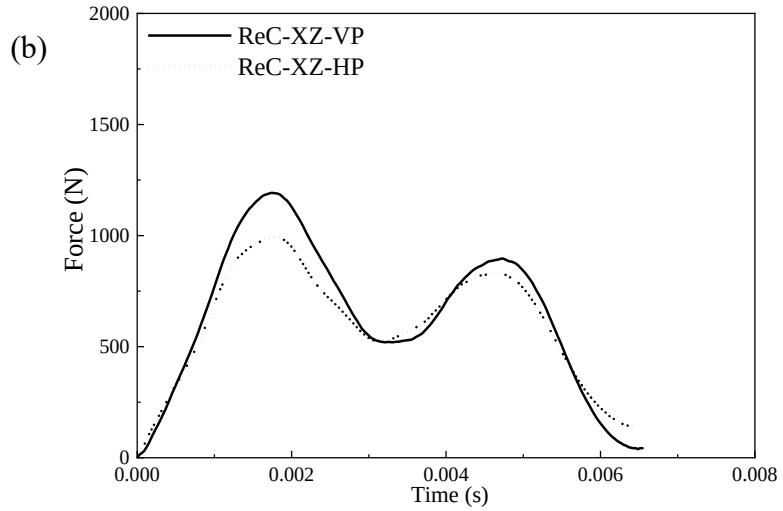

Figure 8.6. Force-Time Response of ReC in the (a) X-Y and (b) X-Z plane under dynamic loading.

Similar deformation progression observed in X-Z plane quasi-static loading Table 8.1 and Table 8.3 (c) and (d) is reproduced in the following dynamic loading. A notable similarity between dynamic and quasi-static loading is evident, particularly how ReC X-Z VP collapses centrally

while ReC X-Z HP shows initial collapse at both ends. In quasi-static loading, ReC X-Z VP outperformed ReC X-Z HP as depicted in Figure 8.5. however, this discrepancy narrows under dynamic loading due to the resemblance in deformation patterns, thereby reducing the impact of print direction on the buckling effect observed in quasi-static loading.

Comparatively, under dynamic loading in the X-Y plane, the force levels are about 50% lower in the X-Z plane, attributed to sliding issues caused by the buckling effect. This buckling-induced instability diminishes compressive resistance, resulting in a lower crushing force. Furthermore, the initial peak force for loading in the X-Y plane, as seen in Figure 8.6, is greater than that in the X-Z plane (Figure 8.5). This difference highlights a reduced capacity for EA and compressive resistance in scenarios where buckling predominates over bending and rotational deformations.

Notably, the impact loading diagrams show two peaks, unlike conventional impact loading, which exhibits only a single, approximately sinusoidal wave. This behavior is attributed to the viscoelastic properties of the base material (nylon green resin), which combines both viscous and inherent damping characteristics, resulting in double peaks during impact. Furthermore, conventional re-entrant structures made of the same material typically exhibit only one peak due to their lack of stability, as shown in Figures 8.3(b) and 8.3(c). This comparison indicates that the modified design's structural layout also contributes to the double peaks observed during dynamic loading.

8.2.2.2 ReM

In the modified 3D re-entrant featuring bent-in struts, a distinct set of deformation mode is observed show in Table 8.4. In ReM-VP, there is an initial collapse and densification of the middle layer, followed by subsequent collapse in the rest of the structure. In contrast, ReM-HP exhibits a more uniform deformation pattern, closely resembling that seen in quasi-static

loading, yet with a less pronounced auxetic effect. This reduced auxetic behavior, despite HP's enhanced flexibility, is linked to the higher loading speeds which created an insufficient time for stress distribution across the structure. As a result, the lateral flexibility's influence on the auxetic behavior becomes less significant compared to the structure's longitudinal compressive resistance. Nonetheless, some degree of auxetic effect is still noticeable in HP at the later stages of loading, leading to an increased second peak force, as depicted in Figure 8.7. Conversely, the higher second peak force observed in VP is primarily due to the initial high compressive resistance generated by the yet-to-deform layers.

Table 8.4. Deformation Mechanism of ReM in the X-Y and X-Z plane under dynamic loading

ReM	1	2	3
(a) X-Y VP	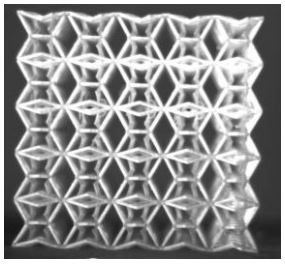	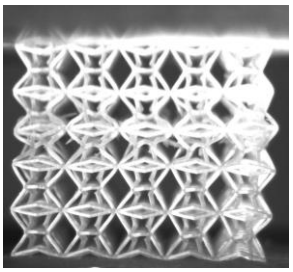	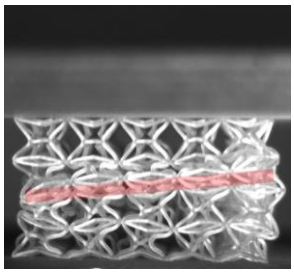
(b) X-Y HP	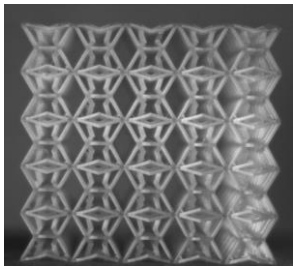	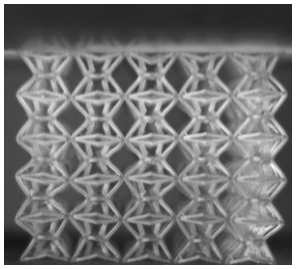	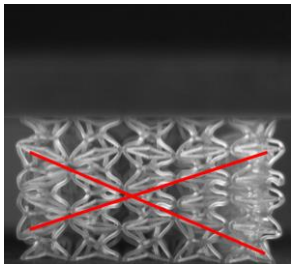
(c) X-Z VP	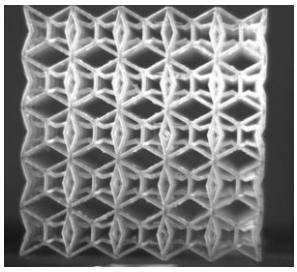	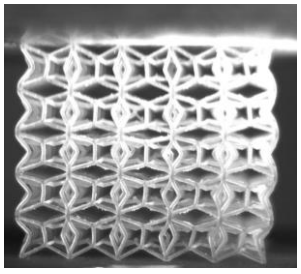	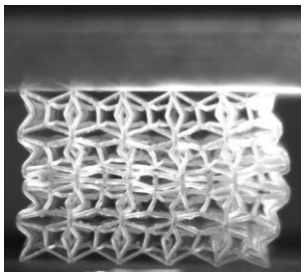

(d) X-Z HP	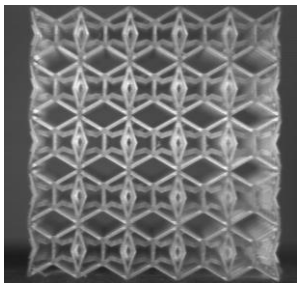	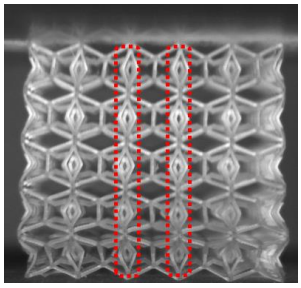	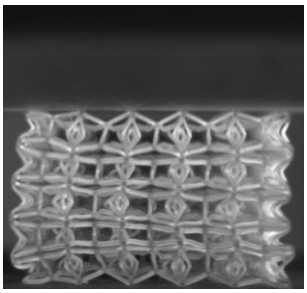

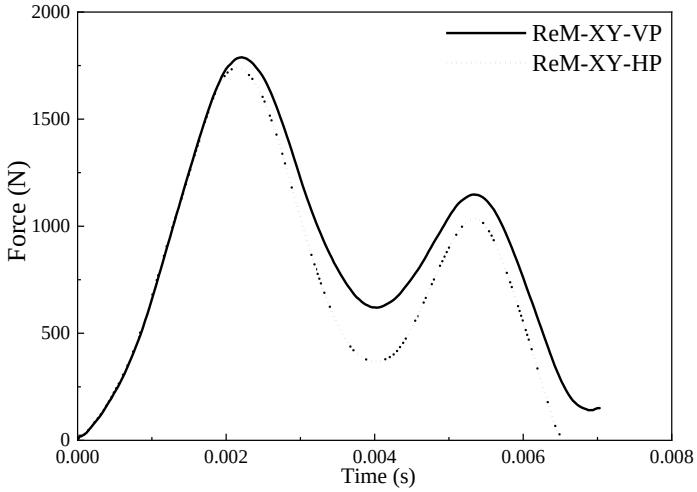

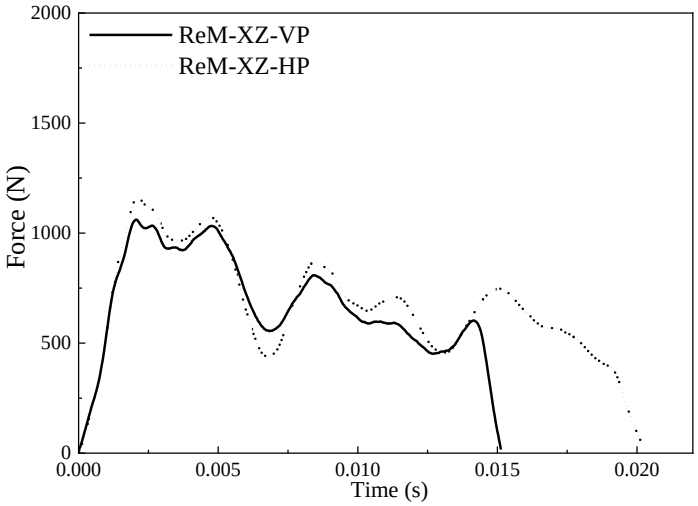

Figure 8.7. Force-Time Response of ReM in the (a) X-Y and (b) X-Z plane under dynamic loading.

Switching from straight to bent-in struts in the ReM design, as depicted in Table 8.4, effectively eradicates the buckling phenomenon observed in the X-Z plane loading. The previously seen wavy strut pattern is now replaced by an expansion of the diamond shapes formed by the bent-

in struts, highlighted in Table 8.4. Although this alteration does not considerably raise the peak force of ReM compared to ReC, the added stability and the role of the bent-in struts significantly enhance the damping effect of the structure. This effect prolongs the impact duration from a typical 0.006 seconds to approximately 0.020 seconds, as illustrated in Figure 8.7. By maintaining a low peak force and prolonging damping, the structure's EA capacity under dynamic loading is notably improved. However, despite these enhancements, no auxetic effect involving the rotation of unit cells was observed, likely due to the X-Z plane loading orientation.

In the context of X-Z plane loading, the diamond configuration of the bent-in struts plays a more active role compared to their function in X-Y loading, where they primarily offer lateral resistance during the compression associated with ReC's auxetic effect, marginally increasing the second peak force. Moreover, as discussed in section 8.2.1, the damping effect is further extended in the HP orientation, which enhances the bending resistance of the struts compared to the VP orientation, where the bonding layers exhibit weaker shear resistance. The gradual reduction in crushing force observed in HP, as opposed to the dual peak forces seen in other loading scenarios, not only demonstrates a robust damping effect but also prevents any abrupt deceleration that could lead to a catastrophic failure of the structure in impact scenarios.

8.3 Conclusion

Drawing inspiration from the multi-tiered organization of diverse materials in bones, the 3D structure employs a similar concept of hybrid unit cells. Thus, the study had conducted a series of quasi-static and dynamic loading tests on two separate hybrid star sub-cell hierarchical 3D re-entrant structures, focusing on two loading directions and two printing orientations. In quasi-static loading, the printing direction significantly impacted the SS response and deformation pattern. The horizontally printed (HP) orientation, aligned parallel to the loading direction, enhanced lateral flexibility and bending resistance, which augmented the auxetic effect. With

unchanged struts in Re-C, buckling and induced instability were prominent, resulting in instability. In stark contrast to Re-C, Re-M, where struts were modified to a bent-in design, HP consistently outperformed vertically printed (VP), enhancing structural predictability.

During dynamic loading, while deformation modes mirrored those in quasi-static loading, structures exhibiting pronounced auxetic effects in quasi-static loading showed reduced auxetic behavior due to stress propagation challenges at higher loading speeds. Notably, the bent-in struts in X-Z loading eliminated buckling and significantly boosted the damping effect, an improvement further enhanced by HP's increased lateral bending resistance.

In summary, printing direction is crucial in enhancing the auxetic effect under quasi-static loading, but it influences different characteristics when the auxetic effect is less pronounced under dynamic loading due to increased loading velocity. Additionally, strut modifications significantly improved dynamic loading performance, transitioning from dual peak loading to a gradual reduction in crushing force, accompanied by a strong damping effect. Despite the initial promise of our bone-structure-inspired design, it has not completely fulfilled our expectations. Consequently, there should be some extent of design modifications to correct any shortcomings and enhance the overall efficacy of the structure.

Chapter 9 Conclusion and Future Work

In this thesis, a variety of auxetic and hybrid structure had been proposed, fabricated, simulated and experimented on. Drawing inspiration from nature, the predominant presence of curved ligament application to harsh environment condition, the concept was first applied onto REAT structure by replacing all straight ligaments with arc shaped ligaments. Significant improvement was discovered due to the increased interaction between cylinders and curved ligaments as well as more profound rotation of ligaments about the cylinders.

Next, a gradient based approach is applied towards two basic geometrical parameters of conventional REAT structure, namely cylindrical size and height. Notably, gradient based approach allows for a gradual increase in plateau stress which translates to a consistent EA efficiency as compared to other efficiency which is momentarily high close to densification.

Then, a combination of gradient based approach is deployed onto arc ligaments in REAT structures. In graded curvature, all four structures incorporate identical gradient layers in their configuration, altering the arrangement of each gradient layer seems to have little to no substantial impact on the overall mechanical performance of the structures. This is due to the lack of drastic difference in mechanical properties between layers. While focus was shifted towards REAT structures with varying cylindrical size, further investigation yielded marginal improvement.

In the next combined study, two innovative honeycomb structures, graded fractal honeycombs and graded hierarchical honeycombs, were developed and analyzed for their crashworthiness and EA capabilities. The graded fractal honeycombs, including symmetric (SG-I & SG-II) and asymmetric gradients (AG-I & AG-II), demonstrated that deformation patterns and EA vary significantly with impact velocity. SG-I honeycombs excelled in EA at low velocities, while SG-II outperformed at higher velocities. The plateau stress, SEA, and MCF for these

honeycombs increased with impact velocity. Additionally, increasing cell wall thickness significantly enhanced SEA across all fractal honeycomb types, with AG-II showing the highest EA capacity at low strain and SG-II excelling at higher strains.

On the other hand, the graded hierarchical honeycombs, featuring hexagonal and triangular sub-cell structures, revealed that their deformation modes and crushing behaviors are also highly dependent on impact velocity. "I+V" deformation mode was observed at low velocities, shifting to an "I" mode at high velocities. These honeycombs showed enhanced crushing stress and SEA with increased impact velocity, influenced by the inertia effect of increasing velocity. The gradient distribution played a crucial role in performance, with PGH providing better SEA than NGH at high velocities. Triangular sub-structures within these honeycombs offered better SEA than hexagonal ones, especially at low velocities. Overall, the study underscores the importance of design configurations, such as gradient distribution and sub-cell structure, in enhancing the performance of honeycombs under varying impact conditions.

And finally, in a comprehensive investigation of two hybrid star sub-cell hierarchical 3D re-entrant structures under quasi-static and dynamic loading, the role of printing direction was established in influencing the structures' SS response and deformation pattern. Specifically, the horizontally printed orientation demonstrated enhanced lateral flexibility and bending resistance, leading to an increased auxetic effect, particularly evident in the 3D re-entrant designs with bent-in struts. Dynamic loading tests revealed that while these structures mirrored quasi-static deformation modes, the pronounced auxetic effect observed under quasi-static conditions diminished at higher loading speeds due to stress propagation challenges. The incorporation of bent-in struts was important in eliminating buckling and enhancing the damping effect, with horizontal printing further boosting this improvement. Ultimately, this research underscores the importance of printing direction and strut configuration in optimizing

the crashworthiness and EA capabilities of 3D re-entrant structures, transitioning from dual peak loading to a more effective, gradual reduction in crushing force under dynamic conditions.

In conclusion, this thesis presents a comprehensive exploration of auxetic and hybrid structures, innovatively blending natural inspirations. By integrating curved ligaments into REAT structures and employing a gradient-based approach to modify geometrical parameters, significant improvements in interaction dynamics and EA efficiency were achieved. The studies on graded fractal and hierarchical honeycombs further highlighted the impact of design configurations on crashworthiness behaviors, demonstrating that varying impact velocities, gradient distributions, and sub-cell structures influence deformation patterns and EA capabilities. Moreover, the examination of printing directions in hybrid star sub-cell hierarchical 3D re-entrant structures revealed that horizontal printing enhances auxetic effects and improves crashworthiness under dynamic loading conditions. Overall, this research not only provides insightful in the structural design of auxetic and hybrid materials but also establishes foundational knowledge for future developments in optimizing material behavior for specific application requirements.

As the research into auxetic and hybrid structures progresses, the scope for exploring an even wider array of design parameters becomes increasingly necessary. Currently, the variation in design parameters has been conducted with other variables being kept constant, which inherently limits the exploration to a certain extent. Therefore, to thoroughly investigate the vast potential of these structures, a more sophisticated approach is needed, one that can handle the complexity and multitude of variable combinations.

Advanced optimization techniques, such as particle swarm optimization and machine learning algorithms, present a promising tool for diving deeper into this field. These methods are particularly apt at navigating extensive and unexplored design spaces, where the number of possible permutations and combinations of parameters is overwhelming. By leveraging these

techniques, it becomes feasible to explore configurations that have yet to be considered or discovered, uncovering novelty and potentially more efficient design solutions.

As mentioned in the beginning of this thesis, the realm of bio-inspired designs offers a rich source of inspiration for future research. One particularly intriguing concept is the development of bio-inspired horseshoe hierarchical honeycombs. This design would integrate the principles of curvature with hierarchical structuring as this multi-scale structuring is a common theme in nature, seen in entities ranging from tiny cellular components to large ecological systems. Each variable – the degree of curvature, the levels of hierarchy, the size and shape of each hierarchical element enriches the design space which will require advanced tools and methods.

References

[1] F. Scarpa and P. J. Tomlin, “On the transverse shear modulus of negative Poisson’s ratio honeycomb structures,” *Fatigue Fract. Eng. Mater. Struct.*, vol. 23, no. 8, pp. 717–720, 2000, doi: 10.1046/j.1460-2695.2000.00278.x.

[2] N. Chan and K. E. Evans, “Indentation resilience of conventional and auxetic foams,” *J. Cell. Plast.*, vol. 34, no. 3, pp. 231–260, 1998.

[3] J. P. Donoghue, K. L. Alderson, and K. E. Evans, “The fracture toughness of composite laminates with a negative Poisson’s ratio,” *Phys. Status Solidi Basic Res.*, vol. 246, no. 9, pp. 2011–2017, Sep. 2009, doi: 10.1002/pssb.200982031.

[4] M. F. Ashby and L. J. Gibson, *Cellular solids: structure and properties*. Cambridge: Cambridge University Press, 1997.

[5] Y. Sun and Q. M. Li, “Dynamic compressive behaviour of cellular materials: A review of phenomenon, mechanism and modelling,” *Int. J. Impact Eng.*, vol. 112, pp. 74–115, 2018, doi: https://doi.org/10.1016/j.ijimpeng.2017.10.006.

[6] W. Wu, W. Hu, G. Qian, H. Liao, X. Xu, and F. Berto, “Mechanical design and multifunctional applications of chiral mechanical metamaterials: A review,” *Mater. Des.*, vol. 180, p. 107950, 2019, doi: 10.1016/j.matdes.2019.107950.

[7] H. M. A. Kolken and A. A. Zadpoor, “Auxetic mechanical metamaterials,” *RSC Adv.*, vol. 7, no. 9, pp. 5111–5129, 2017, doi: 10.1039/c6ra27333e.

[8] D. Mousanezhad *et al.*, “Hierarchical honeycomb auxetic metamaterials,” *Sci. Rep.*, vol. 5, pp. 1–8, 2015, doi: 10.1038/srep18306.

[9] Q. Zhang *et al.*, “Bioinspired engineering of honeycomb structure - Using nature to inspire human innovation,” *Prog. Mater. Sci.*, vol. 74, pp. 332–400, 2015, doi:

10.1016/j.pmatsci.2015.05.001.

[10] R. Yadav, M. Tirumali, X. Wang, M. Naebe, and B. Kandasubramanian, “Polymer composite for antistatic application in aerospace,” *Def. Technol.*, vol. 16, no. 1, pp. 107–118, 2020, doi: 10.1016/j.dt.2019.04.008.

[11] M. Sanami, N. Ravirala, K. Alderson, and A. Alderson, “Auxetic materials for sports applications,” *Procedia Eng.*, vol. 72, pp. 453–458, 2014, doi: 10.1016/j.proeng.2014.06.079.

[12] W. Lee *et al.*, “Effect of auxetic structures on crash behavior of cylindrical tube,” *Compos. Struct.*, vol. 208, pp. 836–846, 2019, doi: https://doi.org/10.1016/j.compstruct.2018.10.068.

[13] F. Robert, “An isotropic three-dimensional structure with Poisson’s ratio =-1,” *J. Elast.*, vol. 15, no. 4, pp. 427–430, 1985, doi: 10.1007/BF00042531.

[14] A. G. Kolpakov, “Determination of the average characteristics of elastic frameworks,” *J. Appl. Math. Mech.*, vol. 49, no. 6, pp. 739–745, 1985, doi: https://doi.org/10.1016/0021-8928(85)90011-5.

[15] L. J. Gibson, M. F. Ashby, G. S. Schajer, and C. I. Robertson, “The mechanics of two-dimensional cellular materials,” *Proc. R. Soc. London. A. Math. Phys. Sci.*, vol. 382, no. 1782, pp. 25–42, Jul. 1982, doi: 10.1098/rspa.1982.0087.

[16] X. C. Zhang, H. M. Ding, L. Q. An, and X. L. Wang, “Numerical investigation on dynamic crushing behavior of auxetic honeycombs with various cell-wall angles,” *Adv. Mech. Eng.*, vol. 7, no. 2, 2015, doi: 10.1155/2014/679678.

[17] Z. Zhou, J. Zhou, and H. Fan, “Plastic analyses of thin-walled steel honeycombs with re-entrant deformation style,” *Mater. Sci. Eng. A*, vol. 688, pp. 123–133, 2017, doi: 10.1016/j.msea.2017.01.056.

[18] Z. Dong, Y. Li, T. Zhao, W. Wu, D. Xiao, and J. Liang, “Experimental and numerical studies on the compressive mechanical properties of the metallic auxetic reentrant honeycomb,” *Mater. Des.*, vol. 182, p. 108036, 2019, doi: 10.1016/j.matdes.2019.108036.

[19] J. Zhang, G. Lu, and Z. You, “Large deformation and energy absorption of additively manufactured auxetic materials and structures : A review,” *Compos. Part B*, vol. 201, no. July, p. 108340, 2020, doi: 10.1016/j.compositesb.2020.108340.

[20] X. Wu, Y. Su, and J. Shi, “In-plane impact resistance enhancement with a graded cell-wall angle design for auxetic metamaterials,” *Compos. Struct.*, vol. 247, p. 112451, 2020, doi: 10.1016/j.compstruct.2020.112451.

[21] D. Xiao, Z. Dong, Y. Li, W. Wu, and D. Fang, “Compression behavior of the graded metallic auxetic reentrant honeycomb: Experiment and finite element analysis,” *Mater. Sci. Eng. A*, vol. 758, pp. 163–171, 2019, doi: https://doi.org/10.1016/j.msea.2019.04.116.

[22] T. Li, Y. Chen, X. Hu, Y. Li, and L. Wang, “Exploiting negative Poisson’s ratio to design 3D-printed composites with enhanced mechanical properties,” *Mater. Des.*, vol. 142, pp. 247–258, 2018, doi: https://doi.org/10.1016/j.matdes.2018.01.034.

[23] Z. Chen, X. Wu, Y. M. Xie, Z. Wang, and S. Zhou, “Re-entrant auxetic lattices with enhanced stiffness: A numerical study,” *Int. J. Mech. Sci.*, vol. 178, 2020, doi: https://doi.org/10.1016/j.ijmecsci.2020.105619.

[24] Z. X. Lu, X. Li, Z. Y. Yang, and F. Xie, “Novel structure with negative Poisson’s ratio and enhanced Young’s modulus,” *Compos. Struct.*, vol. 138, pp. 243–252, 2016, doi: 10.1016/j.compstruct.2015.11.036.

[25] M. H. Fu, Y. Chen, and L. L. Hu, “A novel auxetic honeycomb with enhanced in-plane

stiffness and buckling strength," *Compos. Struct.*, vol. 160, pp. 574–585, 2017, doi: 10.1016/j.compstruct.2016.10.090.

[26] J. Huang, Q. Zhang, F. Scarpa, Y. Liu, and J. Leng, "In-plane elasticity of a novel auxetic honeycomb design," *Compos. Part B Eng.*, vol. 110, pp. 72–82, 2017, doi: 10.1016/j.compositesb.2016.11.011.

[27] A. Alderson, K. L. Alderson, G. Chirima, N. Ravirala, and K. M. Zied, "The in-plane linear elastic constants and out-of-plane bending of 3-coordinated ligament and cylinder-ligament honeycombs," *Compos. Sci. Technol.*, vol. 70, no. 7, pp. 1034–1041, 2010, doi: 10.1016/j.compscitech.2009.07.010.

[28] J. Zhang, G. Lu, and Z. You, "Large deformation and energy absorption of additively manufactured auxetic materials and structures: A review," *Compos. Part B Eng.*, vol. 201, p. 108340, 2020, doi: https://doi.org/10.1016/j.compositesb.2020.108340.

[29] L. L. Hu, Z. R. Luo, Z. Y. Zhang, M. K. Lian, and L. S. Huang, "Mechanical property of re-entrant anti-trichiral honeycombs under large deformation," *Compos. Part B Eng.*, vol. 163, pp. 107–120, 2019, doi: 10.1016/j.compositesb.2018.11.010.

[30] L. L. Hu, Z. R. Luo, and Q. Y. Yin, "Negative Poisson's ratio effect of re-entrant anti-trichiral honeycombs under large deformation," *Thin-Walled Struct.*, vol. 141, pp. 283–292, 2019, doi: https://doi.org/10.1016/j.tws.2019.04.032.

[31] K. Zied, M. Osman, and T. Elmahdy, "Enhancement of the in-plane stiffness of the hexagonal re-entrant auxetic honeycomb cores," *Phys. status solidi*, vol. 252, no. 12, pp. 2685–2692, 2015, doi: https://doi.org/10.1002/pssb.201552164.

[32] Y. Su, X. Wu, and J. Shi, "A novel 3D printable multimaterial auxetic metamaterial with reinforced structure: Improved stiffness and retained auxetic behavior," *Mech. Adv. Mater. Struct.*, pp. 1–11, 2020, doi: 10.1080/15376494.2020.1774690.

[33] X. chun Zhang, C. chao An, Z. feng Shen, H. xiang Wu, W. gang Yang, and J. pan Bai, "Dynamic crushing responses of bio-inspired re-entrant auxetic honeycombs under in-plane impact loading," *Mater. Today Commun.*, vol. 23, 2020, doi: 10.1016/j.mtcomm.2020.100918.

[34] C. Qi *et al.*, "Quasi-static crushing behavior of novel re-entrant circular auxetic honeycombs," *Compos. Part B Eng.*, vol. 197, 2020, doi: 10.1016/j.compositesb.2020.108117.

[35] N. Liu, M. Becton, L. Zhang, and X. Wang, "Mechanical anisotropy of two-dimensional metamaterials: a computational study," *Nanoscale Adv.*, pp. 2891–2900, 2019, doi: 10.1039/c9na00312f.

[36] F. Runkel, G. Ramstein, G. Molinari, A. F. Arrieta, and P. Ermanni, "Mechanics of curved-ligament hexachiral metastructures under planar deformations," *J. Mech. Phys. Solids*, vol. 125, pp. 145–163, 2019, doi: https://doi.org/10.1016/j.jmps.2018.12.001.

[37] H. Wang, Y. Zhang, W. Lin, and Q.-H. Qin, "A novel two-dimensional mechanical metamaterial with negative Poisson's ratio," *Comput. Mater. Sci.*, vol. 171, p. 109232, 2020, doi: https://doi.org/10.1016/j.commatsci.2019.109232.

[38] J. A. J, J. Schneider, A. Schiffer, F. Hafeez, and S. Kumar, "Dynamic crushing of tailored honeycombs realized via additive manufacturing," *Int. J. Mech. Sci.*, vol. 219, 2022, doi: 10.1016/j.ijmecsci.2022.107126.

[39] S. Xie, K. Jing, H. Zhou, and X. Liu, "Mechanical properties of Nomex honeycomb sandwich panels under dynamic impact," *Compos. Struct.*, vol. 235, no. October 2019, p. 111814, 2020, doi: 10.1016/j.compstruct.2019.111814.

[40] Q. Qin, S. Chen, K. Li, M. Jiang, T. Cui, and J. Zhang, "Structural impact damage of metal honeycomb sandwich plates," *Compos. Struct.*, vol. 252, no. July, p. 112719, 2020,

doi: 10.1016/j.compstruct.2020.112719.

[41] S. Ahmad, J. Zhang, P. Feng, D. Yu, Z. Wu, and M. Ke, “Processing technologies for Nomex honeycomb composites (NHCs): A critical review,” *Compos. Struct.*, vol. 250, no. November 2019, 2020, doi: 10.1016/j.compstruct.2020.112545.

[42] L. J. Gibson and M. F. Ashby, *Cellular Solids*. Cambridge University Press, 1997. doi: 10.1017/CBO9781139878326.

[43] J. P. Donoghue, K. L. Alderson, and K. E. Evans, “The fracture toughness of composite laminates with a negative Poisson’s ratio,” *Phys. Status Solidi Basic Res.*, vol. 246, no. 9, pp. 2011–2017, 2009, doi: 10.1002/pssb.200982031.

[44] Y. Sun and Q. M. Li, “Dynamic compressive behaviour of cellular materials: A review of phenomenon, mechanism and modelling,” *Int. J. Impact Eng.*, vol. 112, pp. 74–115, 2018, doi: 10.1016/j.ijimpeng.2017.10.006.

[45] J. Liu, W. Chen, H. Hao, and Z. Wang, “In-plane crushing behaviors of hexagonal honeycombs with different Poisson’s ratio induced by topological diversity,” *Thin-Walled Struct.*, vol. 159, 2021, doi: 10.1016/j.tws.2020.107223.

[46] N. Ahmed and P. Xue, “Governing the In-plane axial crushing of honeycomb with regular hexagonal symmetric division cells using cross-hinge inserts,” *Int. J. Mech. Sci.*, vol. 161–162, 2019, doi: 10.1016/j.ijmecsci.2019.105062.

[47] Y. Chen, Z. Jia, and L. Wang, “Hierarchical honeycomb lattice metamaterials with improved thermal resistance and mechanical properties,” *Compos. Struct.*, vol. 152, pp. 395–402, 2016, doi: 10.1016/j.compstruct.2016.05.048.

[48] D. Sun, W. Zhang, Y. Zhao, G. Li, Y. Xing, and G. Gong, “In-plane crushing and energy absorption performance of multi-layer regularly arranged circular honeycombs,” *Compos. Struct.*, vol. 96, pp. 726–735, 2013, doi: 10.1016/j.compstruct.2012.10.008.

[49] H. Gu, M. Pavier, and A. Shterenlikht, “Experimental study of modulus, strength and toughness of 2D triangular lattices,” *Int. J. Solids Struct.*, vol. 152–153, pp. 207–216, 2018, doi: 10.1016/j.ijsolstr.2018.06.028.

[50] D. Sun and W. Zhang, “Energy Absorption Performance of Staggered Triangular Honeycombs under In-Plane Crushing Loadings,” *J. Eng. Mech.*, vol. 139, no. 2, pp. 153–166, 2013, doi: 10.1061/(asce)em.1943-7889.0000475.

[51] Z. Liu, M. A. Meyers, Z. Zhang, and R. O. Ritchie, “Functional gradients and heterogeneities in biological materials: Design principles, functions, and bioinspired applications,” *Prog. Mater. Sci.*, vol. 88, pp. 467–498, 2017, doi: 10.1016/j.pmatsci.2017.04.013.

[52] N. S. Ha and G. Lu, “A review of recent research on bio-inspired structures and materials for energy absorption applications,” *Compos. Part B Eng.*, vol. 181, 2020, doi: 10.1016/j.compositesb.2019.107496.

[53] A. Alderson, K. L. Alderson, G. Chirima, N. Ravirala, and K. Zied, “Novel tri-coordinated chiral honeycombs,” *ICCM Int. Conf. Compos. Mater.*, 2009.

[54] M. Xu, Z. Xu, Z. Zhang, H. Lei, Y. Bai, and D. Fang, “Mechanical properties and energy absorption capability of AuxHex structure under in-plane compression: Theoretical and experimental studies,” *Int. J. Mech. Sci.*, vol. 159, pp. 43–57, 2019, doi: 10.1016/j.ijmecsci.2019.05.044.

[55] M. F. Guo, H. Yang, and L. Ma, “Design and characterization of 3D AuxHex lattice structures,” *Int. J. Mech. Sci.*, vol. 181, 2020, doi: 10.1016/j.ijmecsci.2020.105700.

[56] Y. Zhu, S. Jiang, Q. Zhang, J. Li, C. Yu, and C. Zhang, “A novel monoclinic auxetic metamaterial with tunable mechanical properties,” *Int. J. Mech. Sci.*, vol. 236, 2022, doi: 10.1016/j.ijmecsci.2022.107750.

[57] D. Attard, P. S. Farrugia, R. Gatt, and J. N. Grima, “Starchirals–A novel class of auxetic hierarchal structures,” *Int. J. Mech. Sci.*, vol. 179, 2020, doi: 10.1016/j.ijmecsci.2020.105631.

[58] H. Wang, Z. Lu, Z. Yang, and X. Li, “In-plane dynamic crushing behaviors of a novel auxetic honeycomb with two plateau stress regions,” *Int. J. Mech. Sci.*, vol. 151, pp. 746–759, 2019, doi: 10.1016/j.ijmecsci.2018.12.009.

[59] L. Shen, Z. Wang, X. Wang, and K. Wei, “Negative Poisson’s ratio and effective Young’s modulus of a vertex-based hierarchical re-entrant honeycomb structure,” *Int. J. Mech. Sci.*, vol. 206, p. 106611, 2021, doi: 10.1016/j.ijmecsci.2021.106611.

[60] Z. Chen, X. Wu, Y. M. Xie, Z. Wang, and S. Zhou, “Re-entrant auxetic lattices with enhanced stiffness: A numerical study,” *Int. J. Mech. Sci.*, vol. 178, 2020, doi: 10.1016/j.ijmecsci.2020.105619.

[61] X. Cheng *et al.*, “Design and mechanical characteristics of auxetic metamaterial with tunable stiffness,” *Int. J. Mech. Sci.*, vol. 223, 2022, doi: 10.1016/j.ijmecsci.2022.107286.

[62] C. Qi, F. Jiang, S. Yang, A. Remennikov, S. Chen, and C. Ding, “Dynamic crushing response of novel re-entrant circular auxetic honeycombs: Numerical simulation and theoretical analysis,” *Aerosp. Sci. Technol.*, vol. 124, 2022, doi: 10.1016/j.ast.2022.107548.

[63] B. Zheng, Y. Liu, J. Liu, S. Yin, and J. Xu, “Novel mechanical behaviors of DNA-inspired helical structures with chirality,” *Int. J. Mech. Sci.*, vol. 161–162, 2019, doi: 10.1016/j.ijmecsci.2019.105025.

[64] K. Lin *et al.*, “Laser powder bed fusion of bio-inspired honeycomb structures: Effect of twist angle on compressive behaviors,” *Thin-Walled Struct.*, 2020, doi:

10.1016/j.tws.2020.107252.

[65] N. S. Ha, G. Lu, and X. Xiang, “Energy absorption of a bio-inspired honeycomb sandwich panel,” *J. Mater. Sci.*, vol. 54, no. 8, pp. 6286–6300, 2019, doi: 10.1007/s10853-018-3163-x.

[66] Y. Wu, Q. Liu, J. Fu, Q. Li, and D. Hui, “Dynamic crash responses of bio-inspired aluminum honeycomb sandwich structures with CFRP panels,” *Compos. Part B Eng.*, vol. 121, pp. 122–133, 2017, doi: 10.1016/j.compositesb.2017.03.030.

[67] H. Jiang, Y. Ren, Q. Jin, G. Zhu, Y. Hu, and F. Cheng, “Crashworthiness of novel concentric auxetic reentrant honeycomb with negative Poisson’s ratio biologically inspired by coconut palm,” *Thin-Walled Struct.*, vol. 154, Sep. 2020, doi: 10.1016/j.tws.2020.106911.

[68] Y. Zhang, M. Lu, C. H. Wang, G. Sun, and G. Li, “Out-of-plane crashworthiness of bio-inspired self-similar regular hierarchical honeycombs,” *Compos. Struct.*, vol. 144, pp. 1–13, 2016, doi: 10.1016/j.compstruct.2016.02.014.

[69] Q. Ma *et al.*, “A nonlinear mechanics model of bio-inspired hierarchical lattice materials consisting of horseshoe microstructures,” *J. Mech. Phys. Solids*, vol. 90, pp. 179–202, 2016, doi: 10.1016/j.jmps.2016.02.012.

[70] Q. Li, L. Zhan, X. Miao, L. Hu, E. Li, and T. Zou, “Morning glory-inspired lattice structure with negative Poisson’s ratio effect,” *Int. J. Mech. Sci.*, vol. 232, 2022, doi: 10.1016/j.ijmecsci.2022.107643.

[71] E. T. Zhang, H. Liu, and B. F. Ng, “Novel arc-shaped ligaments to enhance energy absorption capabilities of re-entrant anti-trichiral structures,” *Compos. Part B Eng.*, vol. 227, 2021, doi: 10.1016/j.compositesb.2021.109366.

[72] N. Reznikov, M. Bilton, L. Lari, M. M. Stevens, and R. Kröger, “Fractal-like

hierarchical organization of bone begins at the nanoscale," *Science (80-.).*, vol. 360, no. 6388, 2018, doi: 10.1126/science.aao2189.

[73] Y. Guo *et al.*, "Functional gradient effects on the energy absorption of spider orb webs," *Appl. Phys. Lett.*, vol. 113, no. 10, 2018.

[74] M. A. Kasapi and J. M. Gosline, "Design complexity and fracture control in the equine hoof wall," *J. Exp. Biol.*, vol. 200, no. 11, pp. 1639–1659, 1997, doi: 10.1242/jeb.200.11.1639.

[75] R. P. Behera and H. Le Ferrand, "Impact-resistant materials inspired by the mantis shrimp's dactyl club," *Matter*, vol. 4, no. 9, pp. 2831–2849, 2021, doi: 10.1016/j.matt.2021.07.012.

[76] Y. Shao *et al.*, "Insight into the negative Poisson's ratio effect of the gradient auxetic reentrant honeycombs," *Compos. Struct.*, vol. 274, p. 114366, 2021, doi: https://doi.org/10.1016/j.compstruct.2021.114366.

[77] Z. Li, H. Sun, T. Wang, L. Wang, and X. Su, "Modularizing honeycombs for enhancement of strength and energy absorption," *Compos. Struct.*, vol. 279, 2022, doi: 10.1016/j.compstruct.2021.114744.

[78] Y. Wang, L. Zhang, S. Daynes, H. Zhang, S. Feih, and M. Y. Wang, "Design of graded lattice structure with optimized mesostructures for additive manufacturing," *Mater. Des.*, vol. 142, pp. 114–123, 2018, doi: 10.1016/j.matdes.2018.01.011.

[79] H. Wu, X. Zhang, and Y. Liu, "In-plane crushing behavior of density graded cross-circular honeycombs with zero Poisson ' s ratio," *Thin-Walled Struct.*, vol. 151, 2020, doi: 10.1016/j.tws.2020.106767.

[80] C. Yang, H. D. Vora, and Y. Chang, "Behavior of auxetic structures under compression and impact forces," *Smart Mater. Struct.*, vol. 27, no. 2, 2018, doi: 10.1088/1361-

665X/aaa3cf.

[81] N. Novak, L. Krstulovi, Z. Ren, and M. Vesenjak, “Mechanics of Materials Compression and shear behaviour of graded chiral auxetic structures,” vol. 148, 2020, doi: 10.1016/j.mechmat.2020.103524.

[82] J. Zhang, B. Song, L. Yang, R. Liu, L. Zhang, and Y. Shi, “Microstructure evolution and mechanical properties of TiB / Ti6Al4V gradient-material lattice structure fabricated by laser powder bed fusion,” *Compos. Part B*, vol. 202, no. 1037, p. 108417, 2020, doi: 10.1016/j.compositesb.2020.108417.

[83] X. Wu, Y. Su, and J. Shi, “In-plane impact resistance enhancement with a graded cell-wall angle design for auxetic metamaterials,” *Compos. Struct.*, vol. 247, p. 112451, 2020, doi: 10.1016/j.compstruct.2020.112451.

[84] Y. Tao, S. Duan, W. Wen, Y. Pei, and D. Fang, “Enhanced out-of-plane crushing strength and energy absorption of in-plane graded honeycombs,” *Compos. Part B Eng.*, vol. 118, pp. 33–40, 2017, doi: 10.1016/j.compositesb.2017.03.002.

[85] C. J. Shen, G. Lu, and T. X. Yu, “Dynamic behavior of graded honeycombs - A finite element study,” *Compos. Struct.*, vol. 98, pp. 282–293, 2013, doi: 10.1016/j.compstruct.2012.11.002.

[86] D. Xiao, Z. Dong, Y. Li, W. Wu, and D. Fang, “Compression behavior of the graded metallic auxetic reentrant honeycomb: Experiment and finite element analysis,” *Mater. Sci. Eng. A*, vol. 758, pp. 163–171, 2019, doi: 10.1016/j.msea.2019.04.116.

[87] X. Liu, X. Tian, T. J. Lu, D. Zhou, and B. Liang, “Blast resistance of sandwich-walled hollow cylinders with graded metallic foam cores,” *Compos. Struct.*, vol. 94, no. 8, pp. 2485–2493, 2012, doi: 10.1016/j.compstruct.2012.02.029.

[88] S. Li, X. Li, Z. Wang, G. Wu, G. Lu, and L. Zhao, “Sandwich panels with layered graded

aluminum honeycomb cores under blast loading," *Compos. Struct.*, vol. 173, pp. 242–254, 2017, doi: 10.1016/j.compstruct.2017.04.037.

[89] X. Jin, Z. Wang, J. Ning, G. Xiao, E. Liu, and X. Shu, "Dynamic response of sandwich structures with graded auxetic honeycomb cores under blast loading," *Compos. Part B Eng.*, vol. 106, pp. 206–217, 2016, doi: 10.1016/j.compositesb.2016.09.037.

[90] Stèphane, "BAMBOO PROPERTIES AND MAINTENANCE." https://bambooimport.com/en/blog-post/bamboe-eigenschappen-en-onderhoud/ (accessed Nov. 05, 2022).

[91] J. Fang, G. Sun, N. Qiu, T. Pang, S. Li, and Q. Li, "On hierarchical honeycombs under out-of-plane crushing," *Int. J. Solids Struct.*, vol. 135, pp. 1–13, 2018, doi: 10.1016/j.ijsolstr.2017.08.013.

[92] Q. He, J. Feng, Y. Chen, and H. Zhou, "Mechanical properties of spider-web hierarchical honeycombs subjected to out-of-plane impact loading," *J. Sandw. Struct. Mater.*, vol. 22, no. 3, pp. 771–796, 2020, doi: 10.1177/1099636218772295.

[93] W. Zhang, S. Yin, T. X. Yu, and J. Xu, "Crushing resistance and energy absorption of pomelo peel inspired hierarchical honeycomb," *Int. J. Impact Eng.*, vol. 125, no. November 2018, pp. 163–172, 2019, doi: 10.1016/j.ijimpeng.2018.11.014.

[94] F. Jiang, S. Yang, Y. Zhang, C. Qi, and S. Chen, "Fabrication and crushing response of graded re-entrant circular auxetic honeycomb," *Int. J. Mech. Sci.*, vol. 242, no. 2, p. 107999, 2023, doi: 10.1016/j.ijmecsci.2022.107999.

[95] H. Liu, E. T. Zhang, G. Wang, and B. F. Ng, "In-plane crushing behavior and energy absorption of a novel graded honeycomb from hierarchical architecture," *Int. J. Mech. Sci.*, vol. 221, p. 107202, 2022, doi: 10.1016/j.ijmecsci.2022.107202.

[96] H. Liu, E. T. Zhang, and B. F. Ng, "In-plane dynamic crushing of a novel honeycomb

with functionally graded fractal self-similarity," *Compos. Struct.*, vol. 270, p. 114106, 2021, doi: 10.1016/j.compstruct.2021.114106.

[97] F. Gao, Q. Zeng, J. Wang, Z. Liu, and J. Liang, "Compressive properties and energy absorption of BCC lattice structures with bio-inspired gradient design," *Acta Mech. Sin. Xuebao*, vol. 38, no. 1, pp. 1–13, 2022, doi: 10.1007/s10409-021-09013-3.

[98] I. Maskery *et al.*, "An investigation into reinforced and functionally graded lattice structures," *J. Cell. Plast.*, vol. 53, no. 2, pp. 151–165, 2017, doi: 10.1177/0021955X16639035.

[99] J. Sienkiewicz, P. Płatek, F. Jiang, X. Sun, and A. Rusinek, "Investigations on the mechanical response of gradient lattice structures manufactured via slm," *Metals (Basel).*, vol. 10, no. 2, 2020, doi: 10.3390/met10020213.

[100] H. Liang, B. Sun, W. Hao, H. Sun, Y. Pu, and F. Ma, "Crashworthiness of lantern-like lattice structures with a bidirectional gradient distribution," *Int. J. Mech. Sci.*, vol. 236, no. September, p. 107746, 2022, doi: 10.1016/j.ijmecsci.2022.107746.

[101] Q. Gao and W. H. Liao, "Energy absorption of thin walled tube filled with gradient auxetic structures-theory and simulation," *Int. J. Mech. Sci.*, vol. 201, no. May, p. 106475, 2021, doi: 10.1016/j.ijmecsci.2021.106475.

[102] W. Hou, X. Yang, W. Zhang, and Y. Xia, "Design of energy-dissipating structure with functionally graded auxetic cellular material," *Int. J. Crashworthiness*, vol. 0, no. 0, pp. 1–11, 2018, doi: 10.1080/13588265.2017.1328764.

[103] H. Yang and L. Ma, "Impact resistance of additively manufactured 3D double-U auxetic structures," *Thin-Walled Struct.*, vol. 169, 2021, doi: 10.1016/j.tws.2021.108373.

[104] J. Plocher and A. Panesar, "Mechanical Performance of Additively Manufactured Fiber-Reinforced Functionally Graded Lattices," *Jom*, vol. 72, no. 3, pp. 1292–1298, 2020,

doi: 10.1007/s11837-019-03961-3.

[105] J. Plocher and A. Panesar, “Effect of density and unit cell size grading on the stiffness and energy absorption of short fibre-reinforced functionally graded lattice structures,” *Addit. Manuf.*, vol. 33, no. February, p. 101171, 2020, doi: 10.1016/j.addma.2020.101171.

[106] L. L. Hu, Z. R. Luo, Z. Y. Zhang, M. K. Lian, and L. S. Huang, “Mechanical property of re-entrant anti-trichiral honeycombs under large deformation,” *Compos. Part B Eng.*, vol. 163, pp. 107–120, 2019, doi: 10.1016/j.compositesb.2018.11.010.

[107] X. Yang, X. Xi, Q. Pan, and H. Liu, “In-plane dynamic crushing of a novel circular-celled honeycomb nested with petal-shaped mesostructure,” *Compos. Struct.*, vol. 226, no. June, p. 111219, 2019, doi: 10.1016/j.compstruct.2019.111219.

[108] L. L. Hu and T. X. Yu, “Dynamic crushing strength of hexagonal honeycombs,” *Int. J. Impact Eng.*, vol. 37, no. 5, pp. 467–474, 2010, doi: 10.1016/j.ijimpeng.2009.12.001.

[109] L. L. Hu and T. X. Yu, “Mechanical behavior of hexagonal honeycombs under low-velocity impact - Theory and simulations,” *Int. J. Solids Struct.*, vol. 50, no. 20–21, pp. 3152–3165, 2013, doi: 10.1016/j.ijsolstr.2013.05.017.

[110] T. Wierzbicki, “Crushing analysis of metal honeycombs,” *Int. J. Impact Eng.*, vol. 1, no. 2, pp. 157–174, 1983, doi: 10.1016/0734-743X(83)90004-0.

[111] W. Goldsmith and J. L. Sackman, “An experimental study of energy absorption in impact on sandwich plates,” *Int. J. Impact Eng.*, vol. 12, no. 2, pp. 241–262, 1992, doi: 10.1016/0734-743X(92)90447-2.

[112] G. Cricrì, M. Perrella, and C. Calì, “Honeycomb failure processes under in-plane loading,” *Compos. Part B Eng.*, vol. 45, no. 1, pp. 1079–1090, 2013, doi: 10.1016/j.compositesb.2012.07.032.

[113] S. D. Papka and S. Kyriakides, “Experiments and full-scale numerical simulations of in-plane crushing of a honeycomb,” *Acta Mater.*, vol. 46, no. 8, pp. 2765–2776, 1998, doi: 10.1016/S1359-6454(97)00453-9.

[114] L. Hu, F. You, and T. Yu, “Effect of cell-wall angle on the in-plane crushing behaviour of hexagonal honeycombs,” *Mater. Des.*, vol. 46, pp. 511–523, 2013, doi: 10.1016/j.matdes.2012.10.050.

[115] D. Ruan, G. Lu, B. Wang, and T. X. Yu, “In-plane dynamic crushing of honeycombs - A finite element study,” *Int. J. Impact Eng.*, vol. 28, no. 2, pp. 161–182, 2003, doi: 10.1016/S0734-743X(02)00056-8.

[116] M. Montemurro, A. Catapano, and D. Doroszewski, “A multi-scale approach for the simultaneous shape and material optimisation of sandwich panels with cellular core,” *Compos. Part B Eng.*, vol. 91, pp. 458–472, 2016, doi: 10.1016/j.compositesb.2016.01.030.

[117] A. Catapano and M. Montemurro, “A multi-scale approach for the optimum design of sandwich plates with honeycomb core. Part I: Homogenisation of core properties,” *Compos. Struct.*, vol. 118, no. 1, pp. 664–676, 2014, doi: 10.1016/j.compstruct.2014.07.057.

[118] A. Catapano and M. Montemurro, “A multi-scale approach for the optimum design of sandwich plates with honeycomb core. Part II: The optimisation strategy,” *Compos. Struct.*, vol. 118, no. 1, pp. 677–690, 2014, doi: 10.1016/j.compstruct.2014.07.058.

[119] F. N. Habib, P. Iovenitti, S. H. Masood, and M. Nikzad, “Cell geometry effect on in-plane energy absorption of periodic honeycomb structures,” *Int. J. Adv. Manuf. Technol.*, vol. 94, no. 5–8, pp. 2369–2380, 2018, doi: 10.1007/s00170-017-1037-z.

[120] X. Yang, Y. Sun, J. Yang, and Q. Pan, “Out-of-plane crashworthiness analysis of bio-

inspired aluminum honeycomb patterned with horseshoe mesostructure," *Thin-Walled Struct.*, vol. 125, no. September 2017, pp. 1–11, 2018, doi: 10.1016/j.tws.2018.01.014.

[121] W. Liu, H. Li, J. Zhang, and Y. Bai, "In-plane mechanics of a novel cellular structure for multiple morphing applications," *Compos. Struct.*, vol. 207, no. May 2018, pp. 598–611, 2019, doi: 10.1016/j.compstruct.2018.08.096.

[122] D. Zhang, Q. Fei, and P. Zhang, "In–plane dynamic crushing behavior and energy absorption of honeycombs with a novel type of multi-cells," *Thin-Walled Struct.*, vol. 117, no. April, pp. 199–210, 2017, doi: 10.1016/j.tws.2017.03.028.

[123] M. Bodaghi and W. H. Liao, "4D printed tunable mechanical metamaterials with shape memory operations," *Smart Mater. Struct.*, vol. 28, no. 4, 2019, doi: 10.1088/1361-665X/ab0b6b.

[124] M. Bodaghi, A. Serjouei, A. Zolfagharian, M. Fotouhi, H. Rahman, and D. Durand, "Reversible energy absorbing meta-sandwiches by FDM 4D printing," *Int. J. Mech. Sci.*, vol. 173, no. January, p. 105451, 2020, doi: 10.1016/j.ijmecsci.2020.105451.

[125] C. Zeng, L. Liu, W. Bian, J. Leng, and Y. Liu, "Compression behavior and energy absorption of 3D printed continuous fiber reinforced composite honeycomb structures with shape memory effects," *Addit. Manuf.*, vol. 38, no. September 2020, p. 101842, 2021, doi: 10.1016/j.addma.2021.101842.

[126] M. Montemurro, G. Bertolino, and T. Roiné, "A general multi-scale topology optimisation method for lightweight lattice structures obtained through additive manufacturing technology," *Compos. Struct.*, vol. 258, no. November 2020, p. 113360, 2021, doi: 10.1016/j.compstruct.2020.113360.

[127] G. Bertolino, M. Montemurro, and G. De Pasquale, "Multi-scale shape optimisation of lattice structures: an evolutionary-based approach," *Int. J. Interact. Des. Manuf.*, vol. 13,

no. 4, pp. 1565–1578, 2019, doi: 10.1007/s12008-019-00580-9.

[128] H. L. Tan, Z. C. He, K. X. Li, E. Li, A. G. Cheng, and B. Xu, “In-plane crashworthiness of re-entrant hierarchical honeycombs with negative Poisson’s ratio,” *Compos. Struct.*, vol. 229, no. September, 2019, doi: 10.1016/j.compstruct.2019.111415.

[129] H. L. Tan, Z. C. He, E. Li, X. W. Tan, A. G. Cheng, and Q. Q. Li, “Energy absorption characteristics of three-layered sandwich panels with graded re-entrant hierarchical honeycombs cores,” *Aerosp. Sci. Technol.*, vol. 106, 2020, doi: 10.1016/j.ast.2020.106073.

[130] H. Yin, X. Huang, F. Scarpa, G. Wen, Y. Chen, and C. Zhang, “In-plane crashworthiness of bio-inspired hierarchical honeycombs,” *Compos. Struct.*, vol. 192, no. March, pp. 516–527, 2018, doi: 10.1016/j.compstruct.2018.03.050.

[131] Y. Chen, T. Li, Z. Jia, F. Scarpa, C. W. Yao, and L. Wang, “3D printed hierarchical honeycombs with shape integrity under large compressive deformations,” *Mater. Des.*, vol. 137, pp. 226–234, 2018, doi: 10.1016/j.matdes.2017.10.028.

[132] Y. Tao *et al.*, “Mechanical properties and energy absorption of 3D printed square hierarchical honeycombs under in-plane axial compression,” *Compos. Part B Eng.*, vol. 176, no. January, p. 107219, 2019, doi: 10.1016/j.compositesb.2019.107219.

[133] H. Fan, Y. Luo, F. Yang, and W. Li, “Approaching perfect energy absorption through structural hierarchy,” *Int. J. Eng. Sci.*, vol. 130, pp. 12–32, 2018, doi: 10.1016/j.ijengsci.2018.05.005.

[134] Y. Sha, L. Jiani, C. Haoyu, R. O. Ritchie, and X. Jun, “Design and strengthening mechanisms in hierarchical architected materials processed using additive manufacturing,” *Int. J. Mech. Sci.*, vol. 149, no. September, pp. 150–163, 2018, doi: 10.1016/j.ijmecsci.2018.09.038.

[135] G. Sun, H. Jiang, J. Fang, G. Li, and Q. Li, “Crashworthiness of vertex based hierarchical honeycombs in out-of-plane impact,” *Mater. Des.*, vol. 110, pp. 705–719, 2016, doi: 10.1016/j.matdes.2016.08.032.

[136] G. Sun, J. Zhang, S. Li, J. Fang, E. Wang, and Q. Li, “Dynamic response of sandwich panel with hierarchical honeycomb cores subject to blast loading,” *Thin-Walled Struct.*, vol. 142, no. October 2018, pp. 499–515, 2019, doi: 10.1016/j.tws.2019.04.029.

[137] A. Ajdari, B. H. Jahromi, J. Papadopoulos, H. Nayeb-Hashemi, and A. Vaziri, “Hierarchical honeycombs with tailorable properties,” *Int. J. Solids Struct.*, vol. 49, no. 11–12, pp. 1413–1419, 2012, doi: 10.1016/j.ijsolstr.2012.02.029.

[138] Q. He, J. Feng, and H. Zhou, “A numerical study on the in-plane dynamic crushing of self-similar hierarchical honeycombs,” *Mech. Mater.*, vol. 138, no. August, 2019, doi: 10.1016/j.mechmat.2019.103151.

[139] J. Qiao and C. Chen, “In-plane crushing of a hierarchical honeycomb,” *Int. J. Solids Struct.*, vol. 85–86, pp. 57–66, 2016, doi: 10.1016/j.ijsolstr.2016.02.003.

[140] Y. Zhang, J. Wang, C. Wang, Y. Zeng, and T. Chen, “Crashworthiness of bionic fractal hierarchical structures,” *Mater. Des.*, vol. 158, pp. 147–159, 2018, doi: 10.1016/j.matdes.2018.08.028.

[141] Y. Zhang, T. Liu, H. Ren, I. Maskery, and I. Ashcroft, “Dynamic compressive response of additively manufactured AlSi10Mg alloy hierarchical honeycomb structures,” *Compos. Struct.*, vol. 195, no. August 2017, pp. 45–59, 2018, doi: 10.1016/j.compstruct.2018.04.021.

[142] D. Zhang, Q. Fei, D. Jiang, and Y. Li, “Numerical and analytical investigation on crushing of fractal-like honeycombs with self-similar hierarchy,” *Compos. Struct.*, vol. 192, no. December 2017, pp. 289–299, 2018, doi: 10.1016/j.compstruct.2018.02.082.

[143] Q. Chen and N. M. Pugno, “In-plane elastic buckling of hierarchical honeycomb materials,” *Eur. J. Mech. A/Solids*, vol. 34, pp. 120–129, 2012, doi: 10.1016/j.euromechsol.2011.12.003.

[144] Z. Li, Z. Wang, X. Wang, and W. Zhou, “Bending behavior of sandwich beam with tailored hierarchical honeycomb cores,” *Thin-Walled Struct.*, vol. 157, no. August, p. 107001, 2020, doi: 10.1016/j.tws.2020.107001.

[145] H. Liu, Z. Zhang, H. Liu, J. Yang, and H. Lin, “Theoretical investigation on impact resistance and energy absorption of foams with nonlinearly varying density,” *Compos. Part B Eng.*, vol. 116, pp. 76–88, 2017, doi: 10.1016/j.compositesb.2017.02.012.

[146] Z. Li, D. Liu, Y. Qian, Y. Wang, T. Wang, and L. Wang, “Enhanced strength and weakened dynamic sensitivity of honeycombs by parallel design,” *Int. J. Mech. Sci.*, vol. 151, no. December 2018, pp. 672–683, 2019, doi: 10.1016/j.ijmecsci.2018.12.013.

[147] X. chun Zhang, L. qiang An, and H. min Ding, “Dynamic crushing behavior and energy absorption of honeycombs with density gradient,” *J. Sandw. Struct. Mater.*, vol. 16, no. 2, pp. 125–147, 2014, doi: 10.1177/1099636213509099.

[148] Z. Li, Y. Jiang, T. Wang, L. Wang, W. Zhuang, and D. Liu, “In-plane crushing behaviors of piecewise linear graded honeycombs,” *Compos. Struct.*, vol. 207, no. September 2018, pp. 425–437, 2019, doi: 10.1016/j.compstruct.2018.09.036.

[149] D. Mousanezhad, R. Ghosh, A. Ajdari, A. M. S. Hamouda, H. Nayeb-Hashemi, and A. Vaziri, “Impact resistance and energy absorption of regular and functionally graded hexagonal honeycombs with cell wall material strain hardening,” *Int. J. Mech. Sci.*, vol. 89, pp. 413–422, 2014, doi: 10.1016/j.ijmecsci.2014.10.012.

[150] S. A. Galehdari, M. Kadkhodayan, and S. Hadidi-Moud, “Low velocity impact and quasi-static in-plane loading on a graded honeycomb structure; experimental, analytical

and numerical study," *Aerosp. Sci. Technol.*, vol. 47, pp. 425–433, 2015, doi: 10.1016/j.ast.2015.10.010.

[151] J. Zhang, Z. Wang, and L. Zhao, "Dynamic response of functionally graded cellular materials based on the Voronoi model," *Compos. Part B Eng.*, vol. 85, pp. 176–187, 2015, doi: 10.1016/j.compositesb.2015.09.045.

[152] M. Mahbod and M. Asgari, "Elastic and plastic characterization of a new developed additively manufactured functionally graded porous lattice structure: Analytical and numerical models," *Int. J. Mech. Sci.*, vol. 155, no. September 2018, pp. 248–266, 2019, doi: 10.1016/j.ijmecsci.2019.02.041.

[153] S. R. G. Bates, I. R. Farrow, and R. S. Trask, "Compressive behaviour of 3D printed thermoplastic polyurethane honeycombs with graded densities," *Mater. Des.*, vol. 162, pp. 130–142, 2019, doi: 10.1016/j.matdes.2018.11.019.

[154] J. Zhang, G. Lu, D. Ruan, and X. Huang, "Experimental observations of the double shock deformation mode in density graded honeycombs," *Int. J. Impact Eng.*, vol. 134, no. May, p. 103386, 2019, doi: 10.1016/j.ijimpeng.2019.103386.

[155] M. Liang, Z. Li, F. Lu, and X. Li, "Theoretical and numerical investigation of blast responses of continuous-density graded cellular materials," *Compos. Struct.*, vol. 164, pp. 170–179, 2017, doi: 10.1016/j.compstruct.2016.12.065.

[156] B. Chang, Z. Zheng, Y. Zhang, K. Zhao, S. He, and J. Yu, "Crashworthiness design of graded cellular materials: An asymptotic solution considering loading rate sensitivity," *Int. J. Impact Eng.*, vol. 143, no. May, p. 103611, 2020, doi: 10.1016/j.ijimpeng.2020.103611.

[157] D. Chen, S. Kitipornchai, and J. Yang, "Dynamic response and energy absorption of functionally graded porous structures," *Mater. Des.*, vol. 140, pp. 473–487, 2018, doi:

10.1016/j.matdes.2017.12.019.

[158] B. T. Cao, B. Hou, H. Zhao, Y. L. Li, and J. G. Liu, “On the influence of the property gradient on the impact behavior of graded multilayer sandwich with corrugated cores,” *Int. J. Impact Eng.*, vol. 113, no. November 2017, pp. 98–105, 2018, doi: 10.1016/j.ijimpeng.2017.11.017.

[159] L. Bai *et al.*, “Mechanical properties and energy absorption capabilities of functionally graded lattice structures: Experiments and simulations,” *Int. J. Mech. Sci.*, vol. 182, no. February, p. 105735, 2020, doi: 10.1016/j.ijmecsci.2020.105735.

[160] L. Xiao, W. Song, and X. Xu, “Experimental study on the collapse behavior of graded Ti-6Al-4V micro-lattice structures printed by selective laser melting under high speed impact,” *Thin-Walled Struct.*, vol. 155, no. December 2019, p. 106970, 2020, doi: 10.1016/j.tws.2020.106970.

[161] H. Rahman, E. Yarali, A. Zolfagharian, A. Serjouei, and M. Bodaghi, “Energy absorption and mechanical performance of functionally graded soft–hard lattice structures,” *Materials (Basel).*, vol. 14, no. 6, 2021, doi: 10.3390/ma14061366.

[162] T. Tancogne-Dejean and D. Mohr, “Elastically-isotropic truss lattice materials of reduced plastic anisotropy,” *Int. J. Solids Struct.*, vol. 138, pp. 24–39, 2018, doi: 10.1016/j.ijsolstr.2017.12.025.

[163] X. Ren, J. Shen, P. Tran, T. D. Ngo, and Y. M. Xie, “Design and characterisation of a tuneable 3D buckling-induced auxetic metamaterial,” *Mater. Des.*, vol. 139, pp. 336–342, 2018, doi: 10.1016/j.matdes.2017.11.025.

[164] I. Maskery *et al.*, “A mechanical property evaluation of graded density Al-Si10-Mg lattice structures manufactured by selective laser melting,” *Mater. Sci. Eng. A*, vol. 670, pp. 264–274, 2016, doi: 10.1016/j.msea.2016.06.013.

[165] M. Leary *et al.*, “Inconel 625 lattice structures manufactured by selective laser melting (SLM): Mechanical properties, deformation and failure modes,” *Mater. Des.*, vol. 157, pp. 179–199, 2018, doi: 10.1016/j.matdes.2018.06.010.

[166] T. Zhong, K. He, H. Li, and L. Yang, “Mechanical properties of lightweight 316L stainless steel lattice structures fabricated by selective laser melting,” *Mater. Des.*, vol. 181, p. 108076, 2019, doi: 10.1016/j.matdes.2019.108076.

[167] Z. Xiao, Y. Yang, R. Xiao, Y. Bai, C. Song, and D. Wang, “Evaluation of topology-optimized lattice structures manufactured via selective laser melting,” *Mater. Des.*, vol. 143, pp. 27–37, 2018, doi: 10.1016/j.matdes.2018.01.023.

[168] C. Ling, A. Cernicchi, M. D. Gilchrist, and P. Cardiff, “Mechanical behaviour of additively-manufactured polymeric octet-truss lattice structures under quasi-static and dynamic compressive loading,” *Mater. Des.*, vol. 162, pp. 106–118, 2019, doi: 10.1016/j.matdes.2018.11.035.

[169] T. Tancogne-Dejean, A. B. Spierings, and D. Mohr, “Additively-manufactured metallic micro-lattice materials for high specific energy absorption under static and dynamic loading,” *Acta Mater.*, vol. 116, pp. 14–28, 2016, doi: 10.1016/j.actamat.2016.05.054.

[170] S. Duan, W. Wen, and D. Fang, “Additively-manufactured anisotropic and isotropic 3D plate-lattice materials for enhanced mechanical performance: Simulations & experiments,” *Acta Mater.*, vol. 199, pp. 397–412, 2020, doi: 10.1016/j.actamat.2020.08.063.

[171] S. Wang, Z. Zheng, C. Zhu, Y. Ding, and J. Yu, “Crushing and densification of rapid prototyping polylactide foam: Meso-structural effect and a statistical constitutive model,” *Mech. Mater.*, vol. 127, no. September, pp. 65–76, 2018, doi: 10.1016/j.mechmat.2018.09.003.

[172] T. Tancogne-Dejean, M. Diamantopoulou, M. B. Gorji, C. Bonatti, and D. Mohr, "3D Plate-Lattices: An Emerging Class of Low-Density Metamaterial Exhibiting Optimal Isotropic Stiffness," *Adv. Mater.*, vol. 30, no. 45, pp. 1–6, 2018, doi: 10.1002/adma.201803334.

[173] M. Zhao, D. Z. Zhang, F. Liu, Z. Li, Z. Ma, and Z. Ren, "Mechanical and energy absorption characteristics of additively manufactured functionally graded sheet lattice structures with minimal surfaces," *Int. J. Mech. Sci.*, vol. 167, no. September 2019, 2020, doi: 10.1016/j.ijmecsci.2019.105262.

[174] Y. Wang *et al.*, "Numerical and experimental studies on compressive behavior of Gyroid lattice cylindrical shells," *Mater. Des.*, vol. 186, p. 108340, 2020, doi: 10.1016/j.matdes.2019.108340.

[175] H. Jiang, A. Coomes, Z. Zhang, H. Ziegler, and Y. Chen, "Tailoring 3D printed graded architected polymer foams for enhanced energy absorption," *Compos. Part B Eng.*, vol. 224, no. February, p. 109183, 2021, doi: 10.1016/j.compositesb.2021.109183.

[176] L. Zhang, Z. Hu, M. Y. Wang, and S. Feih, "Hierarchical sheet triply periodic minimal surface lattices: Design, geometric and mechanical performance," *Mater. Des.*, vol. 209, p. 109931, 2021, doi: 10.1016/j.matdes.2021.109931.

[177] L. R. Meza, A. J. Zelhofer, N. Clarke, A. J. Mateos, D. M. Kochmann, and J. R. Greer, "Resilient 3D hierarchical architected metamaterials," *Proc. Natl. Acad. Sci. U. S. A.*, vol. 112, no. 37, pp. 11502–11507, 2015, doi: 10.1073/pnas.1509120112.

[178] W. Lv, D. Li, and L. Dong, "Study on mechanical properties of a hierarchical octet-truss structure," *Compos. Struct.*, vol. 249, no. January, p. 112640, 2020, doi: 10.1016/j.compstruct.2020.112640.

[179] J. W. Gooch, "Astm D638," in *Encyclopedic Dictionary of Polymers*, J. W. Gooch, Ed.,

New York, NY: Springer New York, 2011, pp. 51–51. doi: 10.1007/978-1-4419-6247-8_856.

[180] H. Liu, E. T. Zhang, and B. F. Ng, “In-plane dynamic crushing of a novel honeycomb with functionally graded fractal self-similarity,” *Compos. Struct.*, vol. 270, p. 114106, 2021, [Online]. Available: https://www.sciencedirect.com/science/article/pii/S0263822321005687

[181] X. Zhang and H. Zhang, “Axial crushing of circular multi-cell columns,” *Int. J. Impact Eng.*, vol. 65, pp. 110–125, 2014, doi: 10.1016/j.ijimpeng.2013.12.002.

[182] D. Hu, Y. Wang, B. Song, L. Dang, and Z. Zhang, “Energy-absorption characteristics of a bionic honeycomb tubular nested structure inspired by bamboo under axial crushing,” *Compos. Part B Eng.*, vol. 162, no. June 2018, pp. 21–32, 2019, doi: 10.1016/j.compositesb.2018.10.095.

[183] S. A. Meguid, J. C. Stranart, and J. Heyerman, “On the layered micromechanical three-dimensional finite element modelling of foam-filled columns,” *Finite Elem. Anal. Des.*, vol. 40, no. 9, pp. 1035–1057, 2004, doi: https://doi.org/10.1016/j.finel.2002.02.001.

[184] M. Kucewicz, P. Baranowski, J. Małachowski, A. Popławski, and P. Płatek, “Modelling, and characterization of 3D printed cellular structures,” *Mater. Des.*, vol. 142, pp. 177–189, 2018, doi: https://doi.org/10.1016/j.matdes.2018.01.028.

[185] G. Sun, G. Li, S. Zhou, H. Li, S. Hou, and Q. Li, “Crashworthiness design of vehicle by using multiobjective robust optimization,” *Struct. Multidiscip. Optim.*, vol. 44, no. 1, pp. 99–110, 2011, doi: 10.1007/s00158-010-0601-z.

[186] P. Patpatiya, K. Chaudhary, A. Shastri, and S. Sharma, “A review on polyjet 3D printing of polymers and multi-material structures,” *Proc. Inst. Mech. Eng. Part C J. Mech. Eng. Sci.*, vol. 236, no. 14, pp. 7899–7926, 2022, doi: 10.1177/09544062221079506.

[187] A. Alomarah, S. H. Masood, I. Sbarski, B. Faisal, Z. Gao, and D. Ruan, “Compressive properties of 3D printed auxetic structures: experimental and numerical studies,” *Virtual Phys. Prototyp.*, vol. 15, no. 1, pp. 1–21, 2020, doi: 10.1080/17452759.2019.1644184.

[188] D. Sharma and S. S. Hiremath, “Bio-inspired repeatable lattice structures for energy absorption: Experimental and finite element study,” *Compos. Struct.*, vol. 283, no. December 2021, p. 115102, 2022, doi: 10.1016/j.compstruct.2021.115102.

[189] R. Hamzehei, J. Kadkhodapour, A. P. Anaraki, S. Rezaei, S. Dariushi, and A. M. Rezadoust, “Octagonal auxetic metamaterials with hyperelastic properties for large compressive deformation,” *Int. J. Mech. Sci.*, vol. 145, no. April, pp. 96–105, 2018, doi: 10.1016/j.ijmecsci.2018.06.040.

[190] R. Johnston and Z. Kazancı, “Analysis of additively manufactured (3D printed) dual-material auxetic structures under compression,” *Addit. Manuf.*, vol. 38, no. November 2020, p. 101783, 2021, doi: 10.1016/j.addma.2020.101783.

[191] C. Ge, L. Priyadarshini, D. Cormier, L. Pan, and J. Tuber, “A preliminary study of cushion properties of a 3D printed thermoplastic polyurethane Kelvin foam,” *Packag. Technol. Sci.*, vol. 31, no. 5, pp. 361–368, 2018, doi: 10.1002/pts.2330.

[192] S. R. G. Bates, I. R. Farrow, and R. S. Trask, “3D printed polyurethane honeycombs for repeated tailored energy absorption,” *Mater. Des.*, vol. 112, pp. 172–183, 2016, doi: 10.1016/j.matdes.2016.08.062.

[193] S. Yuan, F. Shen, J. Bai, C. K. Chua, J. Wei, and K. Zhou, “3D soft auxetic lattice structures fabricated by selective laser sintering: TPU powder evaluation and process optimization,” *Mater. Des.*, vol. 120, pp. 317–327, 2017, doi: 10.1016/j.matdes.2017.01.098.

[194] S. Higuera, R. Miralbes, and D. Ranz, “Mechanical properties and energy–absorption

capabilities of thermoplastic sheet gyroid structures," *Mech. Adv. Mater. Struct.*, vol. 29, no. 25, pp. 4110–4124, 2022, doi: 10.1080/15376494.2021.1919803.

[195] X. M. Qiu, J. Zhang, and T. X. Yu, "Collapse of periodic planar lattices under uniaxial compression, part I: Quasi-static strength predicted by limit analysis," *Int. J. Impact Eng.*, vol. 36, no. 10–11, pp. 1223–1230, 2009, doi: 10.1016/j.ijimpeng.2009.05.011.

[196] Y. Sun and Q. M. Li, "Dynamic compressive behaviour of cellular materials: A review of phenomenon, mechanism and modelling," *Int. J. Impact Eng.*, vol. 112, no. February 2017, pp. 74–115, 2018, doi: 10.1016/j.ijimpeng.2017.10.006.

[197] S. Li *et al.*, "In-plane compression of 3D-printed self-similar hierarchical honeycombs – Static and dynamic analysis," *Thin-Walled Struct.*, vol. 157, no. April, p. 106990, 2020, doi: 10.1016/j.tws.2020.106990.

[198] Y. Xue, P. Gao, L. Zhou, and F. Han, "An enhanced three-dimensional auxetic lattice structure with improved property," *Materials (Basel).*, vol. 13, no. 4, 2020, doi: 10.3390/ma13041008.

[199] L. Yang, O. Harrysson, H. West, and D. Cormier, "Mechanical properties of 3D re-entrant honeycomb auxetic structures realized via additive manufacturing," *Int. J. Solids Struct.*, vol. 69–70, pp. 475–490, 2015, doi: 10.1016/j.ijsolstr.2015.05.005.

[200] E. Heiml, A. Hössinger-Kalteis, and Z. Major, "Experimental characterization of 3D printed cellular structures," *Mater. Today Proc.*, vol. 62, pp. 2528–2532, 2022, doi: 10.1016/j.matpr.2022.03.124.

Appendix

The geometric properties of all 9 models are defined in Table A- 1.

Table A- 1. Table illustrating configurations of graded honeycombs.

Model	**Geometric properties**
Ungraded REAT Honeycomb(Control Model) 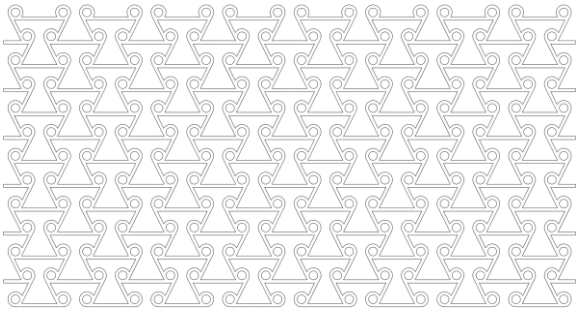	Geometric properties constant for all layers. $d = 3\ mm$ $h = 12mm$
Unidirectional Graded Chiral (Decreasing) UC-P 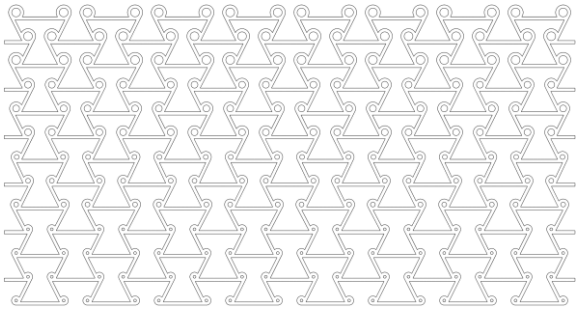	Chiral diameter at chiral layer 1, $d_1 = 3.0\ mm$ Chiral diameter decreases by constant intervals of $0.5\ mm$ every 3 subsequent chiral layers. Chiral diameter at chiral layer 13, $d_{13} = 1.5\ mm$ L_2 and h constant for all layers.
Unidirectional Graded Chiral (Increasing) UC-N 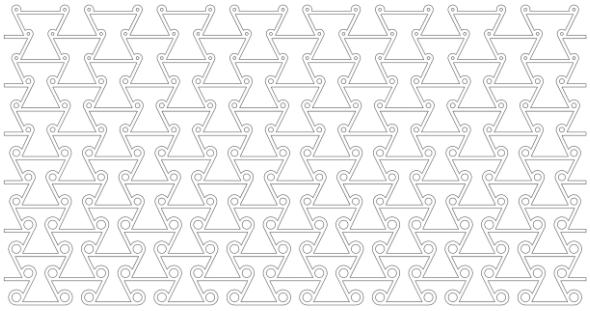	Chiral radius at chiral layer 1, $d_1 = 1.5\ mm$ Chiral diameter increases by constant intervals of $0.5\ mm$ every 3 subsequent chiral layers. Chiral diameter at chiral layer 13, $d_{13} = 3.0\ mm$ L_2 and h constant for all layers.

Bidirectional Graded Chiral (Decreasing) BC-N 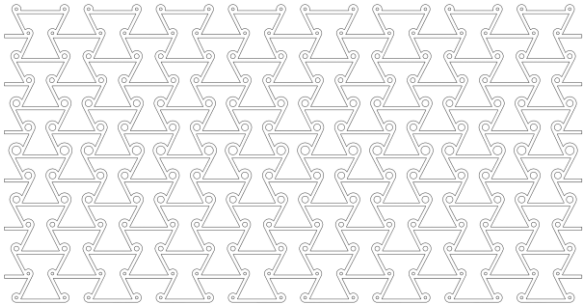	Chiral radius at chiral layer 7, $d_7 = 3.0\ mm$ Chiral diameter decreases by constant intervals of $0.5\ mm$ from middle chiral layer towards both proximal and distal end every 2 subsequent chiral layers. Chiral diameter at layers 1 and 13, $d_{1,13} = 1.5\ mm$ L_2 and h constant for all layers.
Bidirectional Graded Chiral (Increasing) BC-P 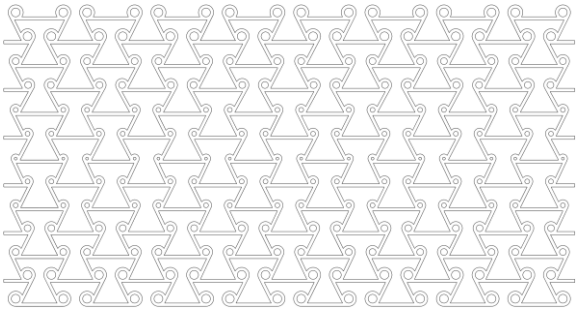	Chiral radius at chiral layer 7, $d_7 = 1.5\ mm$ Chiral diameter decreases by constant intervals of $0.5\ mm$ from middle chiral layer towards both proximal and distal end every 2 subsequent chiral layers. Chiral radius at chiral layers 1 and 13, $d_{1,13} = 3.0\ mm$ L_2 and h constant for all layers.
Unidirectional Graded Height (Decreasing) UH-P 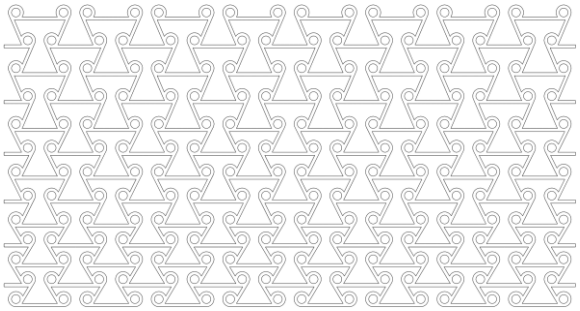	Unit layer height at layers 1, $h_1 = 14mm$ h decreases by constant intervals of $2\ mm$ every 2 subsequent height layers. Unit layer height at layers 6, $h_6 = 10mm$ L_2 and r constant for all layers.

Unidirectional Graded Height (Increasing) UH-N 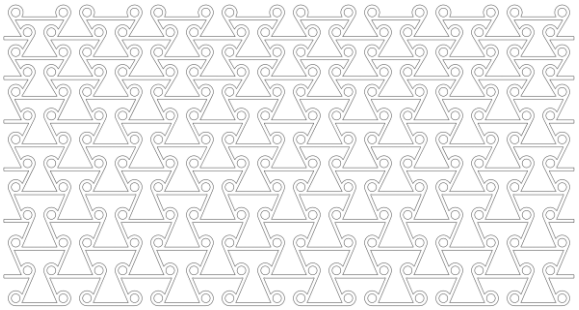	Unit layer height at layers 1, $h_1 = 10mm$ *h* increases by constant intervals of 2 mm every 2 subsequent height layers. Unit layer height at layers 6, $h_6 = 14mm$ L_2 and *r* constant for all layers.
Bidirectional Graded Height (Decreasing) BH-N 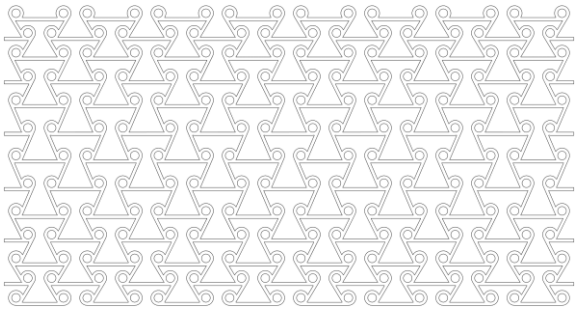	Unit layer height at layers 3 or 4, $h_{3,4} = 14mm$ *h* decreases by constant intervals of 2 mm in each adjacent height layer. Unit layer height at layers 5 or 6, $h_{1,6} = 10mm$ L_2 and *r* constant for all layers.
Bidirectional Graded Height (Increasing) BH-P 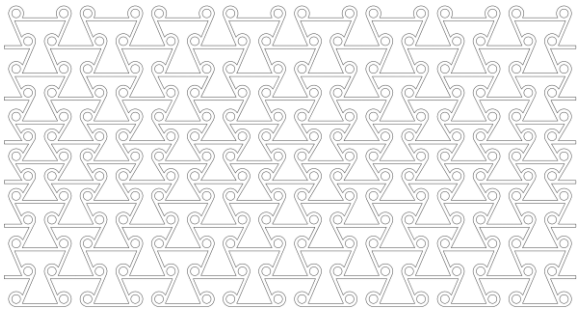	Unit layer height at layers 3 or 4, $h_{3,4} = 10mm$ *h* increases by constant intervals of 2 mm in each adjacent height layer. Unit layer height at layers 5 or 6, $h_{1,6} = 14mm$ L_2 and *r* constant for all layers.

The following figures contain the stress-strain curves of each design with three specimens to show the consistency in the 3D printed samples and their respective results.

Base Model

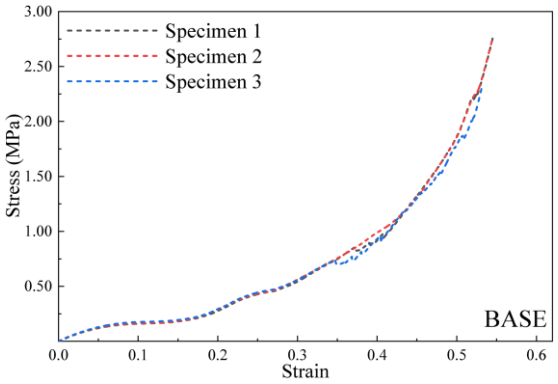

Figure A-1. Stress-strain of uniform REAT or control model.

UC-P

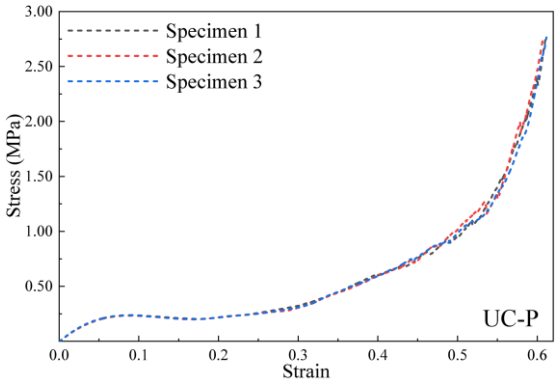

Figure A-2. Stress-strain of uniform UC-P.

UC-N

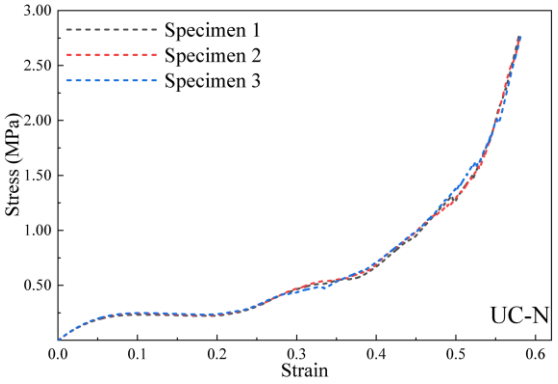

Figure A-3. Stress-strain of uniform UC-N.

BC-N

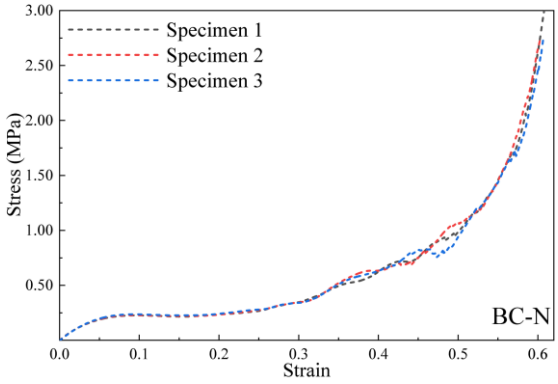

Figure A-4. Stress-strain of uniform BC-N.

BC-P

UH-P

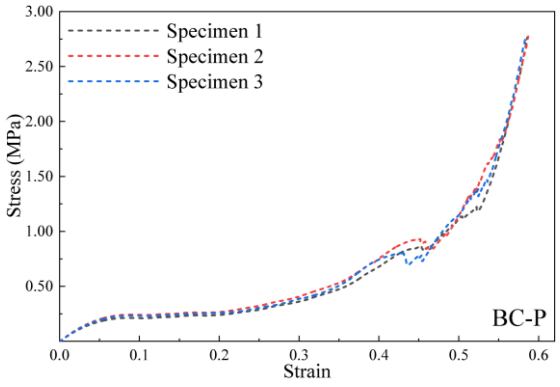

Figure A-5. Stress-strain of uniform BC-P.

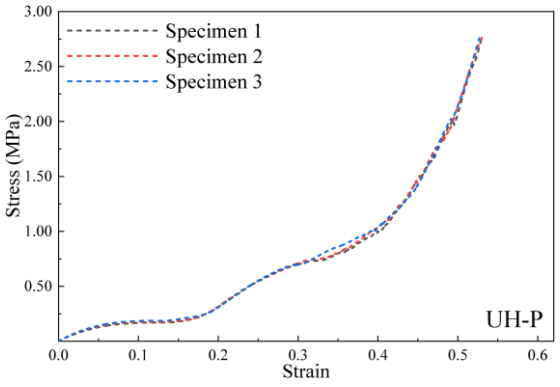

Figure A-6. Stress-strain of uniform UH-P.

UH-N

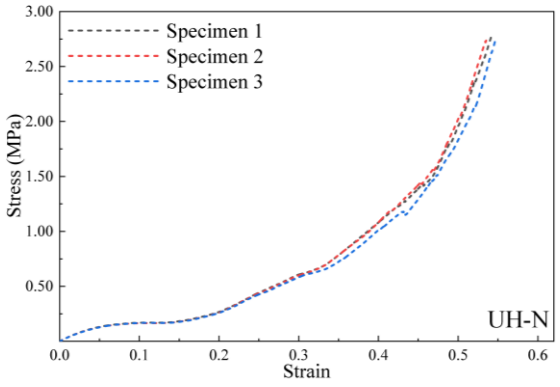

Figure A-7. Stress-strain of uniform UH-N.

BH-P

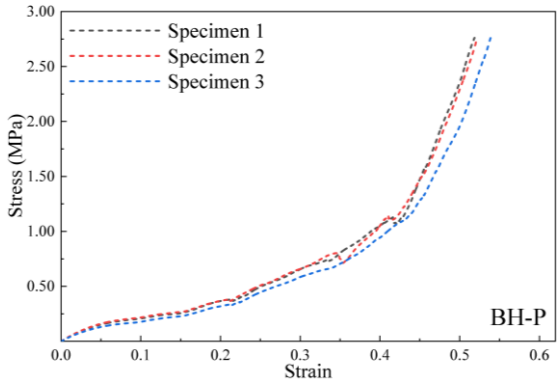

Figure A-8. Stress-strain of uniform BH-P.

BH-N

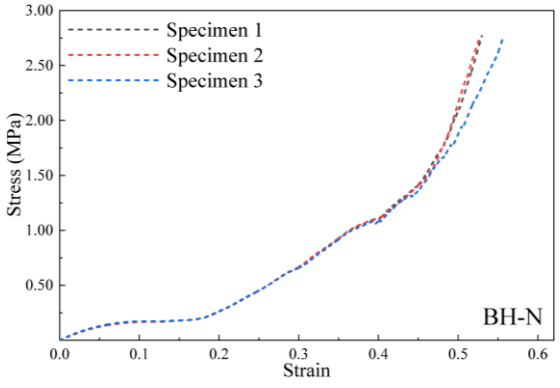

Figure A-9. Stress-strain of uniform BH-N.

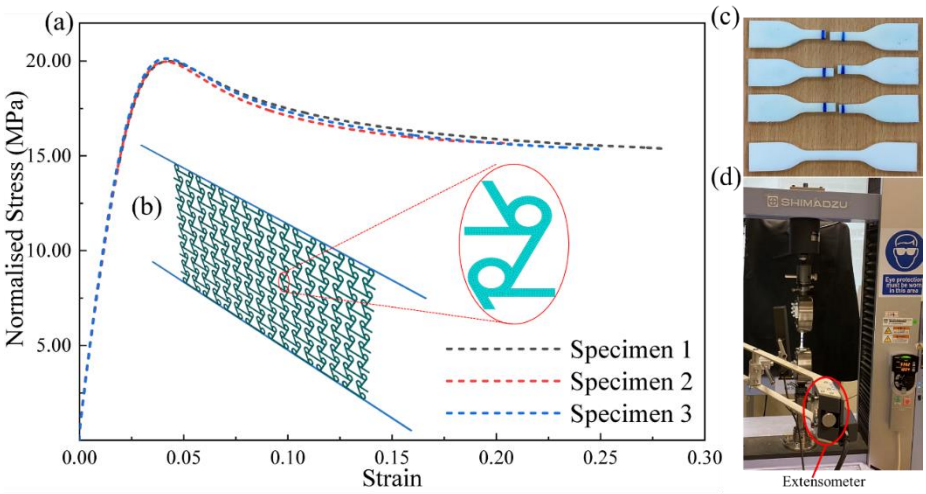

Figure A-10. (a) stress-strain curve of RGD-8530DM. (b) simulation setup with C3D8R solid mesh. (c) Tensile samples printed with RGD-8530DM with (d) the experimental setup.

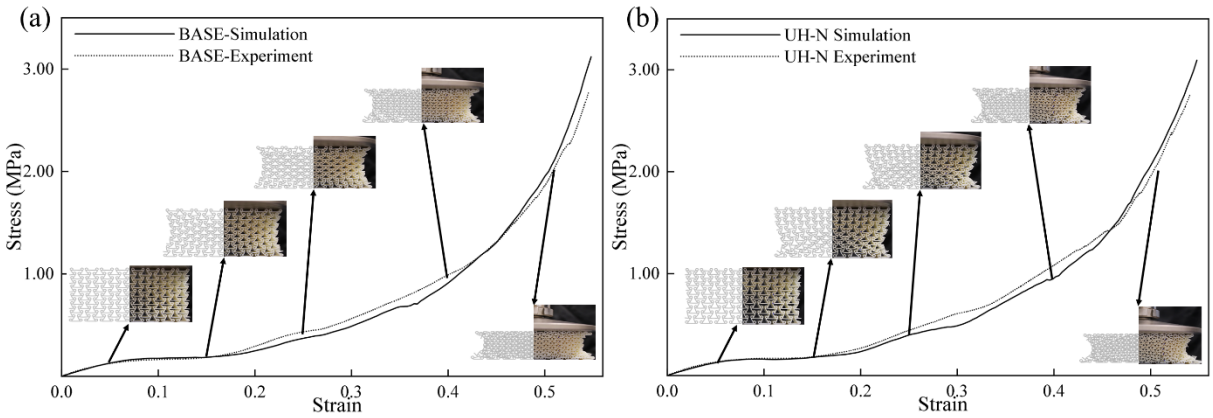

Figure A-11. Experimental validation with simulation for (a) Base model and (b) UH-N. Deformation and stress-strain curve are in substantial agreement.